UNIVERSITÀ DEGLI STUDI DELL'INSUBRIA

Facoltà di Scienze Matematiche, Fisiche e Naturali - Como

Anno Accademico 2011-2012

Dottorato di ricerca in Fisica

THE MICE ELECTRON MUON RANGER: A FUNDAMENTAL STEP TOWARDS A NEUTRINO FACTORY

Dottorando: Davide Bolognini
Matricola 610319

Coordinatore:	Prof. Philip G. Ratcliffe *Università degli Studi dell'Insubria*
Tutor:	Dr.ssa Michela Prest *Università degli Studi dell'Insubria*
Co-tutor:	Dr. Erik Vallazza *INFN - Sezione di Trieste*

Clover, whose eyes are failing in her old age,
asks Benjamin to read the writing on the barn wall
where the Seven Commandments were originally inscribed.
Only the last commandment remains: "all animals are equal."
However, it now carries an addition:
"but some animals are more equal than others."

Animal Farm - George Orwell

a Laura

Contents

Introduction

Nowadays neutrino physics is one of the most important research fields in particle physics: almost 100 years of studies and discoveries have produced a huge amount of information, but, at the same time, have left a lot of questions unanswered. Although neutrino is probably the most abundant particle in the universe, its study is complicated by its nature: its mass, the mixing and oscillation processes, the lepton CP violation are just an example of the open issues related to this particle. Dealing with neutrinos requires to solve two different problems: the necessity of a neutrino beam (that can be controlled in terms of geometry, flux and energy) and, given its weak nature, the development of large and heavy detectors.

In recent years a new source has been proposed: a Neutrino Factory. In such a factory these particles are generated by the decay of muons in a beam that can be tuned in terms of energy and intensity, allowing the optimization of the detector. However, the Neutrino Factory idea has a limitation: in order to have a large flux, muons must be stored, thus cooling is required. Because of its lifetime, standard cooling techniques (electron, stochastic, laser, etc.) applied to a muon beam are not effective. The Muon Ionization Cooling Experiment (MICE) is being commissioned at the Rutherford Appleton Laboratory (RAL, UK) and intends to study the feasibility of a Neutrino Factory based on a muon storage ring using for the muon cooling an innovative technique called *ionization cooling*. The ionization cooling has been proposed in the early '80s and consists of two different phases: a muon beam crosses a light absorber and loses transversal and longitudinal momentum via the interactions with atomic electrons; the longitudinal energy loss is then restored by accelerating cavities. The net result is a reduction of the phase-space volume, mathematically described by the emittance.

In MICE the cooling is evaluated measuring (with a precision of the order of 0.1%) the emittance before and after the cooling section, requiring a precision on the emittance reduction measurement of the order of 1%. In order to achieve this result, a performing particle identification system is foreseen to discriminate muons (with a momentum in the range 140-240 MeV/c) from the background (mainly pions, electrons and gammas). The experiment consists of three parts: the muon cooling is performed in a dedicated section with three absorbers (liquid

hydrogen in a focusing cavity) and two radiofrequency cavities; the emittances are measured by two 4 T spectrometers based on scintillating fiber trackers; the particle identification is covered in the first part of the line by Time-Of-Flight (TOF) and Cherenkov detectors to distinguish muons from pions (from which the muons are produced) and by a TOF and an electromagnetic calorimeter (EMcal) system at the end of the line to discriminate the electrons (the muon decay products). This last system consists of a pre-shower (a KLOE-Light calorimeter) and a fully active tracker-calorimeter detector, the Electron Muon Ranger (EMR).

The large sensitive area combined with the good energy resolution and low cost led to the choice of scintillator for the EMR detector. EMR, in fact, consists of 48 planes of extruded scintillating plastic bars arranged in a x-y geometry; each plane is made of 59 1.1 m long bars with a triangular shape whose scintillator light is brought out by a 1.2 mm wavelength shifter (WLS) fiber. The bars are readout on both sides: on one side by a single photomultiplier to measure the energy loss in the whole plane, while on the other the fibers are connected to a 64 channel multi-anode PMT (MAPMT), readout by a dedicated frontend electronics based on a 64 channel ASIC.

The final design of the detector has required the assembly of several prototypes, evaluating their performance by means of radioactive sources, beams or cosmic rays: in particular, tests on the shape of the plastic bars and the frontend electronics have been performed. Moreover, the performance of EMR has been simulated with the help of dedicated Monte Carlo codes: the results have supplied a feedback to the detector design and to the operational phase.

This thesis deals with the EMR detector, from the construction to the results obtained with the prototypes and during the first commissioning phase. Chapter 1 is devoted to the physical motivation beyond the detector: after a brief introduction on the neutrino field, from a historical review to the different sources (in particular the Neutrino Factory), the ionization cooling and the MICE experiment are approached. The Electron Muon Ranger is described in chapter 2, focusing on the MAPMT frontend and readout electronics, under the responsibility of the Insubria group. Two prototypes have been developed in order to test the mechanical solutions and the electronics: the first (a small scale prototype) has been used like a tracker, while the second (Large EMR Prototype - LEP) as a calorimeter. The results obtained with cosmic rays and in a beamtest at CERN are presented in chapter 3. The experimental data obtained with LEP with a 1 GeV/c beam have been used to tune a GEANT4 simulation that has then been improved to include the whole EMR detector. The first part of chapter 4 describes the muon/electron discrimination based on the algorithms applied by the MICE collaboration, while in the second part a new possible method is presented. The last chapter deals with the commissioning phase of 4 EMR complete modules that have been first tested with cosmic rays at the University of Geneva (UNIGE) and then with a 200 MeV/c

mixed beam at RAL.

Finally a brief outlook on the future applications is given: while MICE is the first step towards the neutrino factory, EMR can be considered the first step towards the totally active scintillator detectors (TASD) with huge dimensions for the future neutrino beam experiments.

Chapter 1

Neutrino physics and MICE

This chapter deals with the physical motivation behind the EMR detector, from neutrino physics to the MICE experiment. Neutrinos are nowadays one of the keys of the physics of (and beyond) the Standard Model (SM) and, in general, they represent the frontier of particle physics. Although postulated in 1930, neutrinos are still the least understood of the fundamental particles given their elusive nature: from their mass to the oscillation phenomenon, there are a lot of open questions. To solve the neutrino puzzle, two important ingredients are necessary: a neutrino source and a dedicated detector. Among the sources, an innovative hypothesis is represented by the Neutrino Factory based on a muon storage ring: in such a factory neutrinos are produced by the decays of muons, and this guarantees the control of the beam in terms of energy, flux and geometry and a good prediction of the neutrino energy spectrum. However, in order to accumulate muons in a storage ring, these charged leptons must be cooled: since the standard techniques are not effective, the only possibility is represented by the ionization cooling. The aim of the Muon Ionization Cooling Experiment (MICE) is to investigate this technique and to develop muon beams for a future Neutrino Factory.

1.1 Neutrino physics

After almost 100 years of studies, neutrino is known as a $\hbar/2$-spin electrically neutral lepton which interacts weakly with matter. Its birthday dates in 1930, when W. Pauli postulated its existence to explain the continuum spectrum of β-decays; however, only in 1956 the first experimental observation was performed. Although neutrinos are probably among the most abundant particles in the universe, their nature is still not completely known: the mixing and oscillation phenomena and the leptonic CP (charge-parity) violation are just an example of the open questions. In this section an overview on neutrino is given: after a brief

introduction on the history and the phenomenology of this particle, the present neutrino sources are described focusing the attention on the Neutrino Factory.

1.1.1 Neutrino history and phenomenology

Differently from the great majority of the elementary particles, the neutrino was first theoretically postulated to solve the problem of the energy spectrum in the β-decays and then experimentally found [1]. In their studies on the β-decay, O. Hahn and L. Meitner in 1911 and J. Chadwick in 1914 discovered a continuous energy spectrum of the emitted electron: this result was utterly puzzling given the α and γ decays of the atomic nuclei showed discrete lines. Two interpretations were given [2]: C. D. Ellis foresaw that the spectrum was the result of a primary process in which an electron was ejected from the outer shells of a radioactive atom, while Meitner (according to α, γ and some β processes) suggested that a primary electron had a discrete energy spectrum and, in a secondary process, could emit more electrons from outer shells with smaller energies.

The solution was found thanks to a calorimetric measurement of the ^{210}Bi β-decay, that, nowadays, can be written as follows:

$$\mathrm{M}(A, Z) \rightarrow \mathrm{D}(A, Z+1) + \mathrm{e}^- + \overline{\nu_e} \tag{1.1}$$

where $\mathrm{M}(A, Z)$ and $\mathrm{D}(A, Z+1)$ are the mother and daughter nuclei, while A and Z are the mass and the atomic number; in the process, no gammas are emitted. It was known from counting experiments that one electron was emitted from the nucleus per decay: according to Ellis' explanation, the energy measured in the calorimeter per decay had to be the mean value of the energy spectrum; following Meitner's one, the spectrum upper limit value had to be measured. Ellis and W. A. Wooster in 1922 and Meitner herself in 1924 (with an improved calorimeter) measured a value corresponding to the mean energy of the beta spectrum, confirming Ellis' explanation [2].

The continuous energy spectrum was explained by two important physicists: N. Bohr supposed that the energy conservation law in β-decays was only statistically valid, while W. Pauli suggested ("as a desperate remedy") the presence of a new (not detectable) particle that carried away the additional energy and spin and allowed to reach the angular momentum conservation in the decay process. In Pauli's famous letter of 1930 [3], the neutrino was described as a 1/2-spin[1] particle produced together with the electron but not detected. In fact Pauli's idea was that of a particle (called neutron) without mass, or with a mass smaller than the electron one. After the discovery of the neutron by Chadwick in 1932 [4], E. Fermi called *neutrino* the particle involved in the β-decay [5]. The possibility

[1] In the thesis $\hbar = c = 1$, if not otherwise indicated.

to detect neutrinos was suggested by B. Pontecorvo in 1946 [6, 7] by means of the inverse β process:

$$\overline{\nu_e} + \mathrm{p} \rightarrow \mathrm{e}^+ + \mathrm{n} \tag{1.2}$$

His idea was to use ^{37}Cl atoms which transform into ^{37}Ar and can be detected by means of their radioactive decay. Following a similar idea, in 1956 C. L. Cowan and F. Reines demonstrated experimentally for the first time the neutrino existence at the Savannah River reactor [8]. The detectors (presented in figure 1.1(a)) consisted in a water tank with dissolved $CdCl_2$ surrounded by two liquid scintillators (for a total of 4200 l). The scintillators detected both the 511 keV photons due to the positron annihilation and the one produced by the neutron capture in cadmium[2]: the two slightly separated (in time) signals on the photomultipliers represent the signature of the inverse β-decay process (figure 1.1(b)); the certainty of the measurement was given by the absence of events when the reactor was shut down [9]. For the first time they measured an interaction cross section of 6×10^{-44} cm^2.

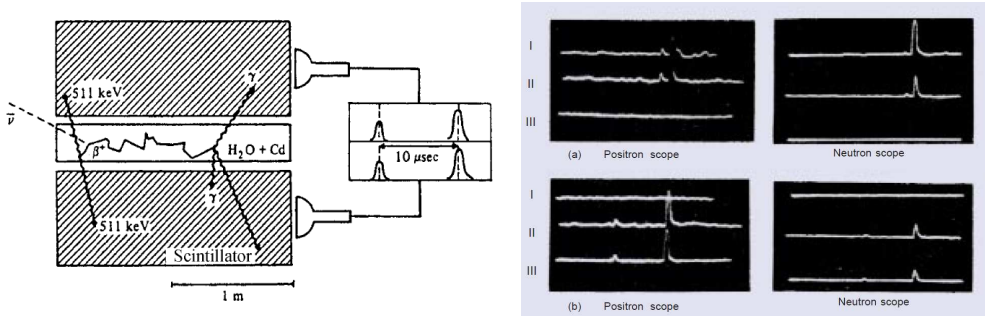

(a) (b)

Figure 1.1: a) The schematic illustration of the setup of the Cowan & Reines' experiment: the 511 keV annihilation photons and the ones produced by the neutron capture in Cd are detected by liquid scintillator [1]. b) The signature of the inverse β-decay process is given by the positron annihilation gamma rays and the Cd neutron capture (followed by a delayed gamma emission). The two slightly separated signals on the photomultipliers are presented in the scope shots [10].

After the experimental observation, a series of important results was achieved: in 1958 the neutrino chirality[3] was measured by M. Goldhaber [11] finding that, as predicted by the V-A electroweak theory, the antineutrino is "right-handed", while

[2]The neutron capture reaction is ^{113}Cd(n,γ)^{114}Cd.

[3]The chiral projectors are operators defined as:

$$P_{L,R} = \left[\frac{1 \mp \gamma^5}{2}\right] \tag{1.3}$$

the neutrino is "left-handed". This fundamental result implied that neutrinos are massless. In fact if one supposes that the neutrino has mass, according to the special relativity it cannot travel at the speed of light; so an observer that travels at the speed of light could see the neutrino (which is supposed to be left-handed) moving in the opposite direction, resulting right-handed. Since right-handed neutrinos had never been detected, the neutrino had to be massless [11]. Moreover the zero-mass is in general supposed by the Standard Model: the Quantum Field Theory (QFT) and Lorentz invariance foresee that when a massive particle interacts with a Higgs boson to acquire mass, its handedness changes. Again, since such a state has never been seen for a neutrino, left-handed neutrinos cannot interact with the Higgs boson and acquire mass [12]. However, as presented later on, the oscillation phenomenon is due to the presence of non-zero neutrino masses, and this complicates the SM predictions on the neutrino experiments: the solution is given by the assumption that free neutrinos propagate as mixtures of left- and right-handed helicity states, but this does not significantly affect the experiments since neutrinos are nearly always ultrarelativistic.

As far as flavors are concerned, similarly to the quark case under the SU(2)$_L$ gauge symmetry, the SM foresees that the left-handed neutrino and the corresponding charged part are doublets:

$$L_l \equiv \begin{pmatrix} \nu_{lL} \\ l_L \end{pmatrix} \tag{1.4}$$

where $l = e, \mu, \tau$. The muonic neutrino (ν_μ) was predicted by K. Inouë and S. Sakata in 1943 [13] and observed at the Brookhaven Alternating Gradient Synchrotron (AGS) by means of a muon beam produced by pion decays [14]. The third flavor (ν_τ) was discovered at Fermilab in 1991 by the DONUT collaboration [15] after a series of indirect measurements in 1974 and 1977 at SLAC (USA).

In the neutrino history the most crucial result is represented by the discovery of the oscillation phenomenon. In 1968 the Homestake experiment (see section 1.1.2.1 for further details) was the first to show a difference between the expected electron neutrino flux from the Sun and the measured flux: during its journey the neutrino changes its flavor with a probability that intrinsically requires the particle to have mass.

There are two possible ways to include the mass term in the SM: either the neutrino is a *Dirac particle* (that is the particle does not correspond to its anti-particle) or a *Majorana particle* (that is the particle coincides with its anti-particle) [16, 17]. The puzzle has not been solved yet. According to the SM (and in particular the Higgs mechanism that generates the mass for charged leptons and quarks) and allowing right-handed neutrinos in the model, the Dirac mass term (m_D) in

where the chiral operator γ^5 is the product $i\gamma_0\gamma_1\gamma_2\gamma_3$ of Dirac matrices.

the particle interaction Lagrangian is (see Ref. in [18, 19]):

$$L_D = -m_D(\overline{\nu_L}\nu_R + h.c.) \tag{1.5}$$

where $h.c.$ is the hermitian conjugate and the left-handed (ν_L) and right-handed (ν_R) neutrino components are defined as:

$$\nu_L = \begin{pmatrix} \nu_{eL} \\ \nu_{\mu L} \\ \nu_{\tau L} \end{pmatrix} \quad \nu_R = \begin{pmatrix} \nu_{eR} \\ \nu_{\mu R} \\ \nu_{\tau R} \end{pmatrix} \tag{1.6}$$

If only the Dirac mass term were considered and supposing a neutrino mass of the order of 0.05 eV (suggested by experiments [18]) and the vacuum expectation value of the Higgs field $\langle\phi\rangle_0$ of 250 GeV, the coupling constant f_ν should be of the order of 10^{-13}, given the relation $m_D = f_\nu \langle\phi\rangle_0$. This value is very small and it is possible just considering a new physics at energies $\gg$TeV.

In 1937 E. Majorana [20] postulated that a massive neutral fermion can obey to the so-called Majorana condition:

$$\Psi = \Psi^C = C\overline{\Psi}^T \tag{1.7}$$

where Ψ is the two independent component spinor which describes the fermion, C is the charge conjugation matrix and T identifies the transposition. Since massive fermions can be described by the sum of two spinors, $\Psi = \Psi_L + \Psi_R$, the Majorana condition makes the two neutrino components dependent:

$$\Psi = \Psi_L + \Psi_L^C = \Psi_R + \Psi_R^C \tag{1.8}$$

Therefore the left (m_L) and right (m_R) Majorana mass terms can be included in the interaction Lagrangian:

$$L_{M_L} = -\frac{m_L}{2}\overline{\nu_L}^C\nu_L + h.c. \tag{1.9}$$

$$L_{M_R} = -\frac{m_R}{2}\overline{\nu_R}^C\nu_R + h.c. \tag{1.10}$$

The Majorana condition is clearly valid only for neutral fermions, since in the charged case the electric charge conservation would be violated.

Since the Majorana mass term for ν_L is not allowed because it is not invariant under the SU(2)$_L\times$U(1)$_Y$ gauge symmetry [21] and supposing that the neutrino mass is due both to the Dirac (equation 1.5) and Majorana (equation 1.10) terms, the interaction Lagrangian becomes:

$$\begin{aligned} L_{m_\nu} &= -m_D\overline{\nu_R}\nu_L - \frac{m_R}{2}\overline{\nu_R}^C\nu_R + h.c. \\ &= -\frac{1}{2}[\overline{\nu_L}^C, \overline{\nu_R}] \begin{bmatrix} 0 & m_D \\ m_D & m_R \end{bmatrix} \begin{bmatrix} \nu_L \\ \nu_R^C \end{bmatrix} + h.c. \end{aligned} \tag{1.11}$$

where the second line is due to the Majorana two-component fermion theory and

$$M_\nu = \begin{bmatrix} 0 & m_D \\ m_D & m_R \end{bmatrix} \tag{1.12}$$

is the neutrino mass matrix. M_ν can be diagonalized using the following transformation:

$$Z^T M_\nu Z = D_\nu \tag{1.13}$$

where Z is a unitary matrix and D_ν is a diagonal matrix:

$$D_\nu = \begin{bmatrix} m_1 & 0 \\ 0 & m_2 \end{bmatrix} \tag{1.14}$$

$m_{1,2}$ are the positive-definite eigenvalues of M_ν.

Since in the SM m_R can assume any value, one can choose $m_R \gg m_D$; thus the parameter $\rho \equiv m_D/m_R$ is very small. At the first order in ρ, Z is:

$$Z = \begin{bmatrix} 1 & \rho \\ -\rho & 1 \end{bmatrix} \begin{bmatrix} i & 0 \\ 0 & 1 \end{bmatrix} \tag{1.15}$$

while at the order ρ^2, D_ν is equivalent to:

$$D_\nu = \begin{bmatrix} m_D^2/m_R & 0 \\ 0 & m_R \end{bmatrix} \tag{1.16}$$

Therefore, expressing L_{m_ν} in terms of mass eigenfields, the following eigenvalues appear:

$$\begin{aligned} \lambda_\pm &= \frac{m_R}{2} \pm \sqrt{m_R^2 + 4m_D^2} \\ \lambda_+ &\approx m_R \\ \lambda_- &\approx -\frac{m_D^2}{m_R^2} \end{aligned} \tag{1.17}$$

Considering λ_-, the larger the m_R value, the smaller the neutrino mass; this fact is known as the *See-Saw Mechanism*. If the neutrino mass is explained under the Grand Unified Theory (GUT), one can assume m_R of the order of the higher mass scale ($\approx 10^{15}$ GeV) and m_D of the order of the top quark mass (≈174 GeV), thus the neutrino mass is approximately $\lambda_- \approx 3 \times 10^{-2}$ eV. As far as the other eigenvalue is concerned, the existence of a heavy neutral lepton with a mass m_R could explain the baryon-antibaryon asymmetry of the Universe [18].

In order to explain the oscillation phenomenon, the neutrino mixing had to be introduced considering the three weakly-interacting neutrinos ($l = e, \mu, \tau$) as a linear combination of the mass eigenstates (ν_i):

$$|\nu_l\rangle = \sum_{i=1}^{n} U_{li}^{*} |\nu_i\rangle \tag{1.18}$$

where U_{li}^{*} is a unitary matrix called Pontecorvo-Maki-Nakagawa-Sakata matrix [22, 23], analogous to the CKM matrix in the quark sector. If a sterile neutrino[4] is considered, this does not interact weakly but another mass eigenstate can be introduced, so n can be more than three. However the case $n = 3$ is considered here. The matrix can be parametrized with the introduction of three mixing angles (θ_{12}, θ_{23} and θ_{13}), a δ phase (called Dirac phase), responsible of the leptonic charge-parity (CP) violation, and two Majorana phases (α_1 and α_2), that appear only if the neutrino is a Majorana particle:

$$U = \begin{pmatrix} c_{12}c_{13}e^{i\alpha_1/2} & s_{12}c_{13}e^{i\alpha_2/2} & s_{13}e^{-i\delta} \\ (-s_{12}c_{23} - c_{12}s_{23}s_{13}e^{i\delta})e^{i\alpha_1/2} & (c_{12}c_{23} - s_{12}s_{23}s_{13}e^{i\delta})e^{i\alpha_2/2} & s_{23}c_{13} \\ (s_{12}s_{23} - c_{12}c_{23}s_{13}e^{i\delta})e^{i\alpha_1/2} & (-c_{12}s_{23} - s_{12}c_{23}s_{13}e^{i\delta})e^{i\alpha_2/2} & c_{23}c_{13} \end{pmatrix} \tag{1.19}$$

where

$$c_{ij} \equiv \cos\theta_{ij} \tag{1.20}$$

$$s_{ij} \equiv \sin\theta_{ij} \tag{1.21}$$

The oscillation phenomenon is explained considering a time evolution in the Hamiltonian:

$$|\nu_i\rangle_t = \sum_{i} U_{li}^{*} e^{-iE_i t} |\nu_i\rangle \tag{1.22}$$

where E_i is the energy of the mass-eigenstate i. Reconsidering the flavor eigenstate basis, the previous equation becomes:

$$|\nu_i\rangle_t = \sum_{m} \sum_{i} U_{li}^{*} e^{-iE_i t} U_{im} |\nu_i\rangle \tag{1.23}$$

For relativistic neutrinos the momentum p is $\gg m_i$, so the energy can be defined as:

$$E_i \simeq p + \frac{m_i^2}{2E} \tag{1.24}$$

In the two flavor case:

$$U = \begin{bmatrix} \cos\theta & \sin\theta \\ -\sin\theta & \cos\theta \end{bmatrix} \tag{1.25}$$

[4] A sterile neutrino is a hypothetical neutrino that can interact only via gravity.

and the oscillation probability can be described as:

$$P_{\nu_l \to \nu_l} = |\langle \nu_l | \nu_l \rangle_t|^2 = 1 - \sin^2 2\theta \sin^2 \frac{m_i^2 - m_j^2}{4E} t \tag{1.26}$$

Indicating $\Delta m_{ij}^2 = m_i^2 - m_j^2$, in the two flavor ($l \neq m$) case the previous equation becomes:

$$P_{\nu_l \to \nu_m} = \sin^2 2\theta \sin^2 \Delta m_{ij}^2 4Et \tag{1.27}$$

A schematic view of the oscillation probability for a muonic neutrino as a function of time is presented in figure 1.2.

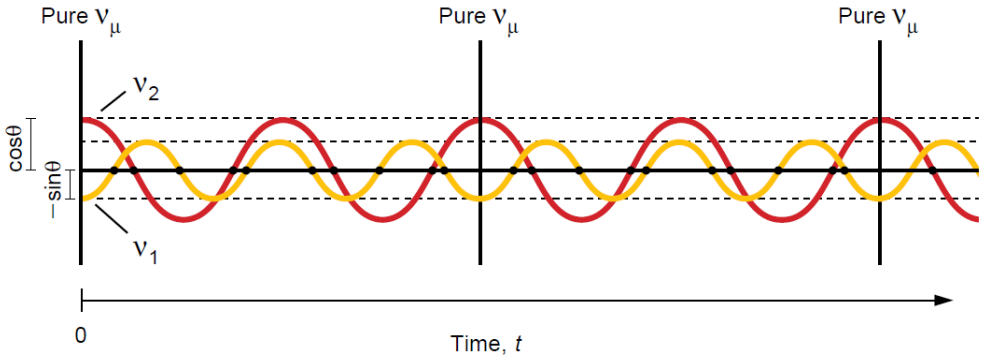

Figure 1.2: The time-evolution of the mixing probability of a muonic neutrino [24].

Equation 1.27 can be rewritten including in the time-dependent Hamiltonian (equation 1.22) the space term given by the so-called baseline L, defined as the distance between the production and the detection points, which is equivalent to the time for relativistic neutrinos:

$$P_{\nu_l \to \nu_m} = \sin^2 2\theta \sin^2 \frac{1.267 \Delta m_{ij}^2 L}{E} \tag{1.28}$$

where Δm_{ij}^2 is expressed in eV^2, E in GeV and L in km. Starting from equation 1.28, the following remarks hold [25]:

- the transition probability is a function of the oscillation length $L^{osc} = \frac{4\pi E}{\Delta m_{ij}^2}$ while the amplitude is proportional to the mixing matrix elements;
- the experiments which measure the neutrino oscillation are sensitive to the squared-mass difference of two eigenstates, so no direct mass measurement can be performed;

- a neutrino oscillation experiment is characterized by the baseline L and the energy E. Since a neutrino beam is not monochromatic, the oscillation probability is a function of the E average value;
- in order to study the oscillation phenomenon with a sensitivity of the order of Δm^2_{ij}, an experiment has to be developed with $E/L \approx \Delta m^2_{ij}$.

When neutrinos cross matter, they can interact coherently or incoherently. In the second case, the probability of an inelastic $\nu - p$ scattering is very small, with a cross section of the order of 10^{-43} cm^2 (E/[MeV])^2 [25]. On the other hand, coherent scattering can modify the oscillation pattern: the effect is known as the Mikheyev-Smirnov-Wolfenstein (MSW) effect [26, 27]. A simplified version of the MSW theory is presented considering only two flavors [18]. It is possible to describe a neutrino as the column vector in the flavor space:

$$\begin{bmatrix} a_e(t) \\ a_\mu(t) \end{bmatrix} \tag{1.29}$$

where $a_x(t)$ corresponds to the amplitude of the neutrino of a certain flavor at a time t. The matter effect theory can be developed starting from the vacuum case whose mixing matrix for two flavors is:

$$U_V = \begin{bmatrix} \cos\theta_V & \sin\theta_V \\ -\sin\theta_V & \cos\theta_V \end{bmatrix} \tag{1.30}$$

where the subscript V indicates vacuum. As before, the time evolution is described by the Schrödinger equation in which the Hamiltonian H_V in vacuum is:

$$H_V = \frac{\Delta m^2_V}{4E} \begin{bmatrix} -\cos 2\theta_V & \sin 2\theta_V \\ \sin 2\theta_V & \cos 2\theta_V \end{bmatrix} \tag{1.31}$$

and the corresponding probability is:

$$P_{\nu_e \to \nu_\mu} = \sin^2 2\theta \sin^2 \left(\Delta m^2_V \frac{L}{4E} \right) \tag{1.32}$$

The neutrino can interact with matter via charged or neutral currents (figure 1.3): the charged current is allowed only for electron neutrinos, while the neutral current is flavor-independent. Assuming matter as electrically neutral, the contribution of the electrons and protons to the coherent forward scattering via the Z^0 exchange can be neglected. Considering the W^--exchange due to the ν_e charged current, the interaction energy E_I is equal to:

$$E_I = \sqrt{2} G_F N_e \tag{1.33}$$

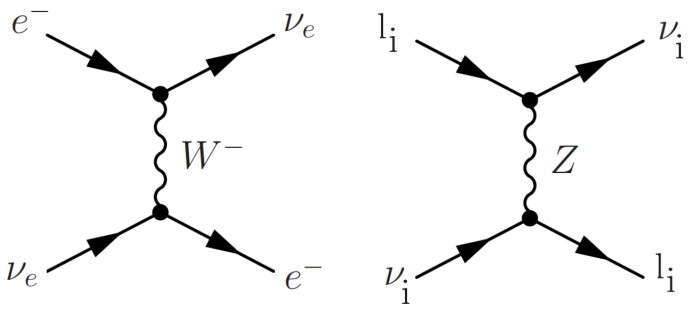

Figure 1.3: The Feynman diagrams of charged (left) and neutral (right) currents neutrino interactions with matter.

where G_F is the Fermi constant and N_e is the number of electrons per unit of volume. Thus the 2×2 Hamiltonian in matter becomes:

$$H_M = \frac{\Delta m_V^2}{4E} \begin{bmatrix} -\cos 2\theta_V & \sin 2\theta_V \\ \sin 2\theta_V & \cos 2\theta_V \end{bmatrix} + \begin{bmatrix} E_I & 0 \\ 0 & 0 \end{bmatrix} \tag{1.34}$$

In order to compare the matter and vacuum cases, H_M has to be expressed like equation 1.31 adding the product "$\mathbb{1} \times -E_I/2$" (where $\mathbb{1}$ denotes the unitary matrix), and obtaining:

$$H_M = \frac{\Delta m_M^2}{4E} \begin{bmatrix} -\cos 2\theta_M & \sin 2\theta_M \\ \sin 2\theta_M & \cos 2\theta_M \end{bmatrix} \tag{1.35}$$

where the effective mass splitting in matter is:

$$\Delta m_M^2 = \Delta m_V^2 \sqrt{\sin^2 2\theta_V + (\cos 2\theta_V - x)^2} \tag{1.36}$$

and the effective mixing angle in matter is:

$$\sin^2 2\theta_M = \frac{\sin^2 2\theta_V}{\sin^2 2\theta_V + (\cos 2\theta_V - x)^2} \tag{1.37}$$

and x is defined as:

$$x \equiv \frac{2EE_I}{\Delta m_V^2} \tag{1.38}$$

The matter effect can be very strong: if, for example, the mixing angle in vacuum (θ_V) is very small, x assumes the value $x \approx \cos 2\theta_V$, so the mixing angle in matter becomes very large ($\sin^2 2\theta_M \cong 1$).

1.1.2 The neutrino sources

As already stated, neutrino is probably among the most abundant particle in the universe. The reason lies in the large number of sources where several processes involved in the neutrino production take place. Just to make an example, the human body produces up to 4×10^3 neutrinos per second in the following β reaction:

$$^{40}\mathrm{K} \rightarrow \ ^{40}\mathrm{Ca} + \mathrm{e}^- + \overline{\nu_e} \tag{1.39}$$

The sources used for neutrino studies can be divided in natural and artificial. The first group consists of the Sun, the atmosphere, cosmological objects and natural radioactivity; the artificial sources are nuclear reactors and particle accelerators.

A neutrino experiment is usually designed to study particular neutrino features: oscillation experiments are devoted to the study of the mixing of the particle, while mass measurements are performed by dedicated experiments such as the neutrinoless double beta decay. The design of an oscillation experiment is constrained by the expected oscillation parameters. Table 1.1 summarizes the parameters of the different oscillation experiments in terms of baseline length, energy and sensitivity over the squared-mass difference Δm^2.

Experiment	L (m)	E (MeV)	Δm^2 (eV^2)
Solar	10^{10}	1	10^{-10}
Atmospheric	10^4-10^7	10^2-10^5	10^{-1}-10^{-4}
Reactor	SBL 10^2-10^3	1	10^{-2}-10^{-3}
	LBL 10^4-10^5		10^{-4}-10^{-5}
Accelerator	SBL 10^2	10^3-10^4	> 0.1
	LBL 10^5-10^6	10^4	10^{-2}-10^{-3}

Table 1.1: The oscillation parameters for solar, atmospheric, reactor and accelerator neutrino experiments. LBL defines the Long BaseLine experiments, while SBL the Short BaseLine ones [25].

The Neutrino Factory has been proposed as a particular source for future oscillation experiments. In fact, even in presence of a variety of available sources, the uncertainty on the parameters of the neutrino mixing and oscillation (the mixing angle, the CP phase, the matter effect) is still large. This section describes the main features of the present sources for oscillation experiments and the most recent results. Moreover, given the fundamental importance of the neutrino mass, the Neutrinoless Double Beta Decay (and the related results) is briefly presented.

1.1.2.1 Solar neutrinos

The Sun produces energy via thermonuclear reactions where the hydrogen burning happens through two main chains: the pp chain (figure 1.4(a)), responsible of the Be neutrino production (see later on), consists of 5 reactions, while the CNO one of three [1, 25, 28]. In both cases, the net result is :

$$4\mathrm{p} \rightarrow {}^{4}\mathrm{He} + 2\mathrm{e}^{+} + 2\nu_e + \gamma \tag{1.40}$$

The expected solar neutrino flux of the eight reactions can be computed taking into account some solar observables: the surface luminosity, the age, the radius and the mass. The fluxes predictions are summarized in the so-called *Standard Solar Model* (SSM): figure 1.4(b) presents the expected solar neutrino flux from the different production chains [29]. The first experiment which measured the

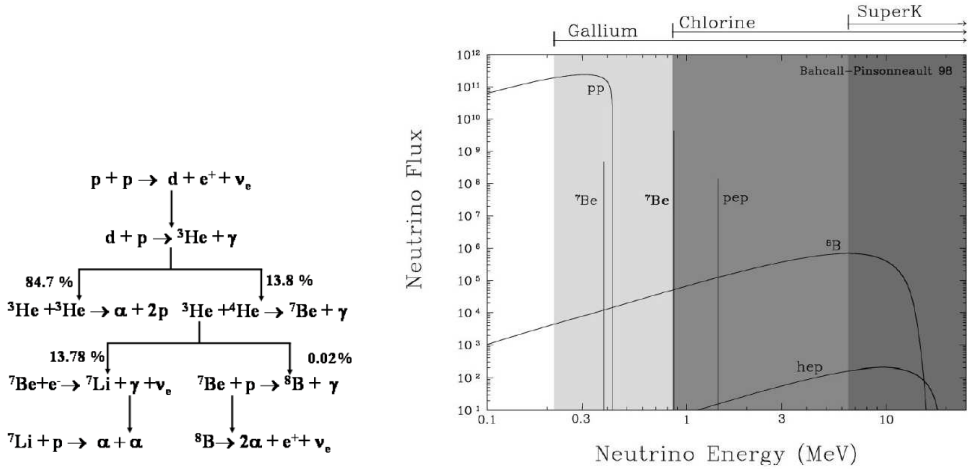

(a) (b)

Figure 1.4: Solar neutrinos: a) the proton-proton chain is one of the major responsible of the heavy elements production from thermonuclear fusion. These processes produce a huge quantity of ν_e [28]. b) Expected energy spectrum of the 5 pp and 3 CNO reactions [29]: in the early life of the solar experiment a key role was played by the ^{8}B neutrinos.

solar neutrino flux was proposed by R. Davis Jr. and performed in the Homestake Gold Mine in South Dakota (USA) [30]. Like all the neutrino experiments, it was installed deeply underground (in a mine) to reduce the cosmic ray background contribution. It was based on a radiochemical measurement performed using 615 tons of perchloroethylene (C_2Cl_4), in which the neutrino flux was computed by the number of radioactive Argon atoms in the reaction:

$$\nu_e + \mathrm{Cl}^{37} \rightarrow \mathrm{Ar}^{37} + \mathrm{e}^{-} \tag{1.41}$$

The neutrino energy threshold of this process is $E_\nu \gtrsim 0.814$ MeV, so in practice only the ^{8}B (and only electron) neutrinos were measured. The Homestake experiment was the first to compute the solar neutrino flux obtaining a value which was only one-third of the expected one [25]:

$$R = 2.56 \pm 0.16 \pm 0.16 \text{ SNU} \Longrightarrow \frac{R}{SSM} = 0.30 \pm 0.03 \tag{1.42}$$

with 1 SNU=10^{-36} captures/atom/sec. This difference was defined as the *problem of the solar neutrinos*, which in fact is the first experimental evidence of the neutrino oscillation.

The Homestake experiment was followed by other two radiochemical experiments based on a gallium detector: GALLEX/GNO at LNGS (Italy) [31] and SAGE (Russia) [32]. Gallium was chosen because it is more sensitive to the lower energy range ($E_\nu \gtrsim 0.23$ MeV). Both the experiments confirmed the deficit in the solar neutrino flux. Later on the Kamiokande experiment (Japan) [33] obtained the same result with a water Cherenkov detector, where the energy threshold was $E_\nu \gtrsim 7$ MeV.

Together with the results of Kamiokande, the puzzle was solved by the Sudbury Neutrino Observatory (SNO) experiment (Canada), a 1 kton heavy water Cherenkov detector sensitive to all the three neutrino flavors. Neutrinos can interact with matter in three ways:

$$\begin{aligned} \text{Charged Current } (CC): &\ \nu_e + \mathrm{d} \to \mathrm{p} + \mathrm{p} + \mathrm{e}^- \\ \text{Neutral Current } (NC): &\ \nu_x + \mathrm{d} \to \mathrm{p} + \mathrm{n} + \nu_x \\ \text{Electron Scattering } (ES): &\ \nu_x + \mathrm{e}^- \to \nu_x + \mathrm{e}^- \end{aligned} \tag{1.43}$$

where $x = e, \mu, \tau$. Thus, thanks to the heavy water (D_2O), SNO was able to measure the three flavors. The experiment consisted in three phases focusing on the different interactions; the final results were [34]:

$$\begin{aligned} \Phi_{CC} =& 1.68 \pm 0.06^{+0.08}_{-0.09} \times 10^6 \mathrm{cm}^{-2}\mathrm{s}^{-1} \\ \Phi_{NC} =& 4.94 \pm 0.21^{+0.38}_{-0.34} \times 10^6 \mathrm{cm}^{-2}\mathrm{s}^{-1} \\ \Phi_{ES} =& 2.35 \pm 0.22 \pm 0.15 \times 10^6 \mathrm{cm}^{-2}\mathrm{s}^{-1} \end{aligned} \tag{1.44}$$

The experimental data were in perfect agreement with the ones predicted by the SSM; a clear deficit in the electron neutrino flux was confirmed by the ratio:

$$\frac{\Phi_{CC}}{\Phi_{NC}} = 0.340 \pm 0.023^{+0.29}_{-0.31} \tag{1.45}$$

The experimental fluxes combined with the energy spectrum allowed to measure the so-called Large Mixing Angle (LMA), whose present best fit value (obtained from several experiments) is [35]:

$$\Delta m^2_{12} = (7.58 \pm 0.21) \times 10^{-5}\mathrm{eV}^2, \ \tan^2\theta_{12} = 0.484 \pm 0.048 \tag{1.46}$$

1.1.2.2 Atmospheric neutrinos

Atmospheric neutrinos are produced in the hadronic showers generated by the interaction of primary cosmic rays (mainly protons) with the nitrogen and oxygen nuclei in the atmosphere. These processes produce pions and kaons that then decay in the following way [28]:

$$\begin{aligned} \pi^+ &\rightarrow \mu^+ + \nu_\mu \\ \mu^+ &\rightarrow \mathrm{e}^+ + \nu_e + \overline{\nu_\mu} \end{aligned} \tag{1.47}$$

The most important results in this field have been achieved by the Super-Kamiokande (Super-K) experiment [36]. The detector (figure 1.5) consists of a 50 kton water tank placed in the Kamioka mine (Japan), surrounded by 2700 MWE (Meter Water Equivalent) of rock. The charged counter-part of the neutrino produces Cherenkov light that is readout by about 11500 50 cm diameter PhotoMultiplier Tubes (PMTs). The neutrino flavor is identified by the Cherenkov ring: the μ-like events are identified by the presence of a sharp ring, while the e-like ones by a broader one, since electrons generate a shower in water.

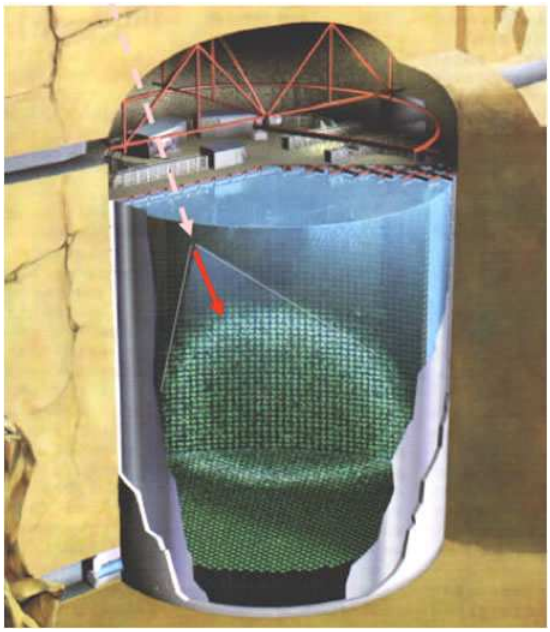

Figure 1.5: A sketch of the Super-K experiment.

At low energy (the *sub-GeV* range, $E_\mu \leq 1.33$ GeV) all muons decay in atmosphere: considering the pion and muon decays, the detector should measure a muon/electron event ratio ($R_{\mu/e}$) equal to 2. For *multi-GeV* muons ($E_\mu > 1.33$ GeV), the ratio should be larger. $R_{\mu/e}$ is typically expressed as a function

of the same quantity evaluated by a Monte Carlo simulation in the hypothesis of no oscillation [37]:

$$R_{sub-GeV} = \frac{R^{meas}_{\mu/e}}{R^{MC}_{\mu/e}} = 0.638 \pm 0.016 \pm 0.050 \tag{1.48}$$

$$R_{multi-GeV} = \frac{R^{meas}_{\mu/e}}{R^{MC}_{\mu/e}} = 0.658 \pm 0.030 \pm 0.078 \tag{1.49}$$

The ratios should be of the order of 1: given that $R^{meas}_{\mu/e}$ is model independent, this value is a clear indication of the ν_μ oscillation. Moreover the Super-K collaboration measured the zenith angle distribution (θ_z, the angle between the vertical direction and the neutrino momentum) for high energy muon events: the results (figure 1.6) show a clear deficit in the muon events, but not in the electron ones. The larger the $\cos\theta$ value, the stronger the suppression of the μ-like events: this ef-

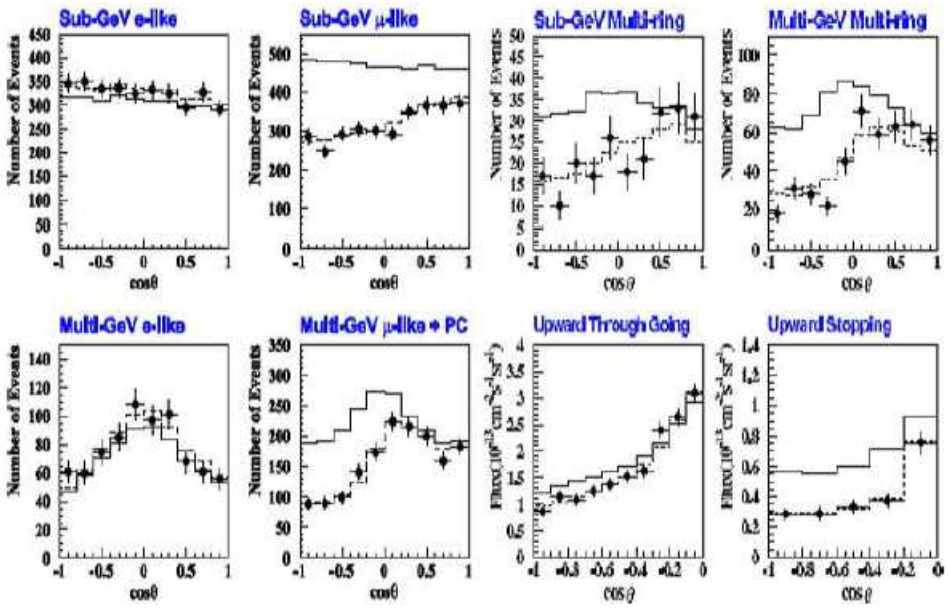

Figure 1.6: The Super-K zenith angle distribution: $\cos\theta$=1(-1) identifies the so-called down (up) events, that are muonic neutrinos going downwards (upwards). The points are the experimental data, while the dashed histograms the Monte Carlo simulations without oscillation.

fect is more evident in multi-GeV events where the charged lepton is more aligned with the neutrino momentum and can be quantitatively described by the up-down asymmetry [25]:

$$A_\mu = \frac{U - D}{U + D} = -0.29 \pm 0.03 \tag{1.50}$$

Since no difference occurs between experimental and expected data in electron events (first top plot in figure 1.6), the deficit in the flux can be only explained by the $\nu_\mu \rightarrow \nu_\tau$ oscillation. Given the fluxes measured in several experiments, the θ_{23} mixing angle value is assumed to be [35]:

$$\Delta m^2_{23} = (2.40 \pm 0.15) \times 10^{-3}\text{eV}^2,\ \tan^2\theta_{23} = 1.02 \pm 0.04 \tag{1.51}$$

1.1.2.3 Neutrinos from nuclear reactors

Reactors produce a huge amount of low energy electron antineutrinos from nuclear reactions: the neutrino energy is low, so only the electron flavor is generated. KamLAND (Kamioka Liquid scintillator AntiNeutrino Detector) was the first LBL experiment devoted to such a neutrino study [28, 38]. Similarly to the solar experiments, an estimation of the LMA due to the $\overline{\nu_e}$ disappearance in reactors neutrino beams can be performed thanks to the long baseline (~ 200 km) and to the energies in the MeV region [18]. The detector consists of 1000 tons of liquid scintillator placed 1000 m underground in the Kamioka mine (Japan). The antineutrinos are detected via the inverse β decay:

$$\overline{\nu_e} + p \rightarrow e^+ + n \tag{1.52}$$

The energy threshold is $E_{\overline{\nu_e}} = 1.8$ MeV. The KamLAND collaboration measured an absolute event rate of:

$$\frac{N_{obs} - N_{bg}}{N_{expected}} = 0.611 \pm 0.085 \pm 0.041 \tag{1.53}$$

The deficit is shown in figure 1.7, where the neutrino disappearance as a function of the energy (as requested by the oscillation theory) is clearly visible.

The LMA estimation obtained from the KamLAND data is [28]:

$$\Delta m^2_{12} = 7.1 \times 10^{-5}\text{eV}^2,\ \tan^2\theta_{12} \sim 0.41 \tag{1.54}$$

in agreement with the best fit value (within 1σ) presented in equation 1.46. Given the short baseline with respect to the solar experiments, this result is important because it is independent from the matter effect: a comparison between solar neutrinos and KamLAND allows a verification of the MSW theory.

Another fundamental reactor neutrino experiment is CHOOZ [40], a 5 ton liquid scintillator detector placed 300 MWE under the two Chooz reactors (France); the measurement was based on the inverse β decay. The experiment had a baseline of 1 km and an energy of a few MeV, providing a sensitivity better than 10^3 eV^2. CHOOZ measured no electronic antineutrino disappearance, fixing the ratio between the measured and the expected fluxes to be:

$$\frac{N_{obs}}{N_{expected}} = 1.01 \pm 0.04 \tag{1.55}$$

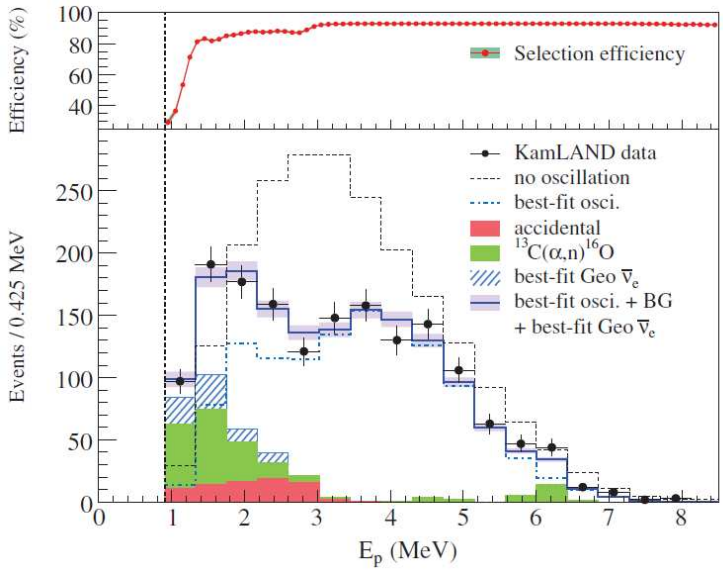

Figure 1.7: The KamLAND results present a clear deficit in the experimental data (dots) with respect to the predicted ones without oscillation [39].

As shown in section 1.1.2.2, the atmospheric neutrino anomaly (the measured flux ratio ν_μ/ν_e is roughly half of the expected one) can be explained by the possible $\nu_\mu \leftrightarrow \nu_\tau$ and $\nu_\mu \leftrightarrow \nu_e$ oscillations. Super-K showed that $\nu_\mu \leftrightarrow \nu_\tau$ caused the anomaly, but the experiment was not able to set a limit on the $\nu_\mu \leftrightarrow \nu_e$ oscillations such as those produced by solar neutrino oscillations or by a small mixing angle θ_{13} at the atmospheric frequency Δm^2_{atm}. In principle both atmospheric and solar neutrino oscillations are sensitive to θ_{13}. But in CHOOZ the solar oscillations and matter effect can be neglected, so in conclusion the experiment removed the possibility to explain the atmospheric anomaly with the $\nu_\mu \leftrightarrow \nu_e$ case, allowing to fix the θ_{13} value [25, 35, 40]. Considering the mass hierarchy (see later on for further details), in CHOOZ the oscillation probability can be approximated as [25]:

$$P_{ee}^{CHOOZ} \cong 1 - \sin^2 2\theta_{13} \sin^2 \left(\frac{\Delta m^2_{31} L}{4E} \right) \tag{1.56}$$

Thus a fundamental CHOOZ result is a limit on the θ_{13} mixing angle and Δm_{13} [25, 40]:

$$\Delta m_{13} \gtrsim 2 \times 10^{-3}\text{eV}, \ \sin^2 \theta_{13} = 0.07 \pm 0.04 \tag{1.57}$$

1.1.2.4 Neutrinos from accelerators

The θ_{23} mixing angle (associated to atmospheric neutrinos) can also be studied with LBL accelerator experiments where the neutrino production is associated to

the following processes [25]:

$$\begin{aligned} p + \ target \rightarrow & \pi^{\pm} + X \\ & \pi^{\pm} \rightarrow \mu^{\pm} + \nu_{\mu}(\overline{\nu_{\mu}}) \\ & \mu^{\pm} \rightarrow e^{\pm} + \nu_{e}(\overline{\nu_{e}}) + \overline{\nu_{\mu}}(\nu_{\mu}) \end{aligned} \tag{1.58}$$

The first LBL accelerator experiment was K2K, developed in Japan in 1999 [28, 41]: a ν_{μ} beam is generated by the decays of the muons produced at the KEK laboratory with a mean energy of 1.3 GeV and is detected 250 km away in the Kamioka mine. The beam properties are measured at KEK by a Near Detector (ND) placed 300 m after the target. The main detector is a 1 kiloton water Cherenkov detector, a scaled version of the Super-Kamiokande one.

Another important experiment was NuMI/MINOS [42], that exploited the 3-18 GeV muon neutrino beam produced at Fermilab and detected 730 km far away in the Soudan mine (USA). The measurement is similar to the K2K one: a near detector is placed in Fermilab to identify the beam characteristics, while the far one is placed in the mine. Both detectors are steel-scintillator sampling calorimeters made of alternating planes of magnetized steel and plastic scintillators.

Both the experiments confirmed the atmospheric anomaly and the results are in good agreement with the oscillation theory. The best fit MINOS value (figure 1.8) is:

$$\Delta m^2_{23} = 2.74^{+0.44}_{-0.26} \times 10^{-3}\mathrm{eV}^2, \ \sin^2 2\theta_{23} > 0.87 \tag{1.59}$$

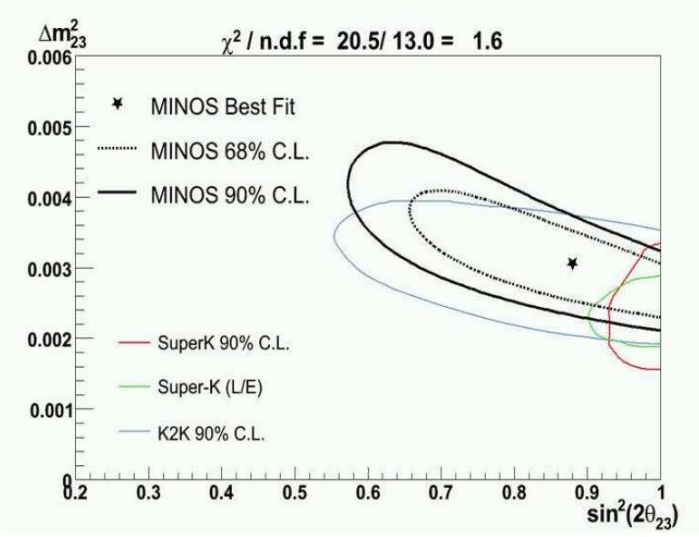

Figure 1.8: θ_{23} allowed region at the 68% and 90% confidence level. The MINOS best fit point is $\Delta m^2_{23} = 2.74^{+0.44}_{-0.26} \times 10^{-3}\mathrm{eV}^2$; $\sin^2 2\theta_{23} > 0.87$ [28].

On the other hand, the OPERA experiment (placed at LNGS, 732 km far from CERN where neutrinos are produced) uses a higher energy ν_μ beam in order to generate τ particles in the detector and directly confirm the oscillation phenomenon. The events are observed in 150000 "bricks" of photographic emulsion films interleaved with lead plates complemented by electronic detectors (trackers and spectrometers). On May 31st 2010, the OPERA Collaboration announced the observation of the first tau neutrino candidate event in a muon neutrino beam [43].

1.1.2.5 Cosmological neutrinos

Cosmological neutrinos can be divided in two categories: the relic neutrinos produced in the early life of the universe and the ones produced by cosmological objects (supernovae, Active Galactic Nuclei, Gamma Ray Bursts, micro-quasars, etc.) [18, 25].

As far as the first type is concerned, when the universe temperature T was greater than 1 MeV, weak interactions occurred thanks to the large density [18]. When the temperature decreased ($T < 1$ MeV), neutrinos decoupled from plasma and gammas; only after 100000 years the radiation decoupled from matter, generating the so-called Cosmic Microwave Background (CMB), a fundamental instrument to evaluate the matter distribution of that period. The CMB and the present matter distribution are a function of the presence of massive neutrinos in the early universe. From the comparison of the CMB power spectrum and density fluctuation, the Wilkinson Microwave Anisotropy Probe (WMAP) experiment has estimated the mass of the heaviest neutrino to be lower than 0.6 eV [44].

An important example of the neutrinos produced in a supernova explosion is the one provided by the SN1987A case (which earned to M. Koshiba the Nobel prize). A star produces energy if its core elements are lighter than iron: ^{56}Fe is the element with the maximum nuclear binding energy, so no more fusion processes can occur. A star exists thanks to the balance of two forces: gravity and the pressure of degenerated electrons. When a star has an iron core of 1.4 solar masses, gravity wins and the star collapses. The collapsing stops when the iron core reaches the nuclear density: a pressure discontinuity in the core generates a sonic point which creates an outgoing shock wave. This last phase of the stellar evolution is called supernova. The neutrino production is the result of the electron capture and the pair production processes [1]:

$$\begin{aligned} \mathrm{e}^- + \mathrm{p} &\rightarrow \nu_e + \mathrm{n} \\ \gamma &\rightarrow \mathrm{e}^- + \mathrm{e}^+ \rightarrow \nu_x + \overline{\nu_x} \end{aligned} \tag{1.60}$$

where $x = e, \mu, \tau$.

In 1987 the neutrinos of a blue super-giant star exploded in the Large Magellanic Cloud at a distance of about 55 kpc[5] were detected. The resulting neutrino flux was measured by 4 experiments, among which Kamiokande [45]. Figure 1.9 presents the scatter plot of the number of events as a function of time: a burst of neutrinos is clearly visible in plot (e).

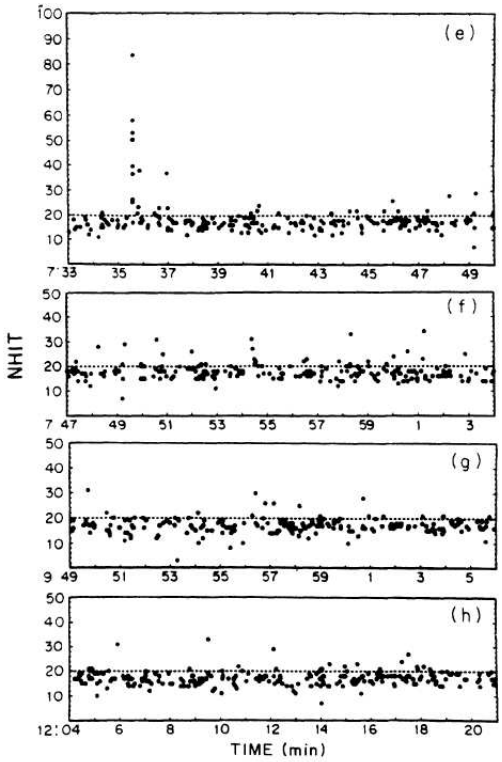

Figure 1.9: Scatter plots of the number of hits as a function of time. A clear burst is visible in plot (e) [45].

Although the number of neutrino events is very small (12), the following remarks hold [45]:

- taking into account the supernova distance (55 kpc), the ν_μ and $\overline{\nu_\mu}$ lifetime lower limit has been estimated to be 1.7×10^{15} [m/E];
- the neutrino mass upper limit has been evaluated to be 24 eV.

[5] 1 kpc=3.09×10^{19} m

1.1.2.6 Natural radioactivity: the $0\nu\beta\beta$ decay

In the experiments described in the previous sections, the source and the detector are separated: whenever possible, the distance between the two components has been chosen taking into account the neutrino oscillation phenomenon, which depends on the squared-mass differences. The neutrino mass is directly measured evaluating the endpoint of the kinematic spectrum of the β decay. An other possibility, that also allow to identify the neutrino as a Dirac or a Majorana particle, exploiting a particular β process (the neutrinoless double beta decay - $0\nu\beta\beta$ decay) where the source and the detector are in practice the same. The basic process is described by the following reaction [25]:

$$(\mathrm{A}, \mathrm{Z}) \rightarrow (\mathrm{A}, \mathrm{Z}+2) + 2\mathrm{e}^- \tag{1.61}$$

schematically represented by the Feynman diagram shown in figure 1.10.

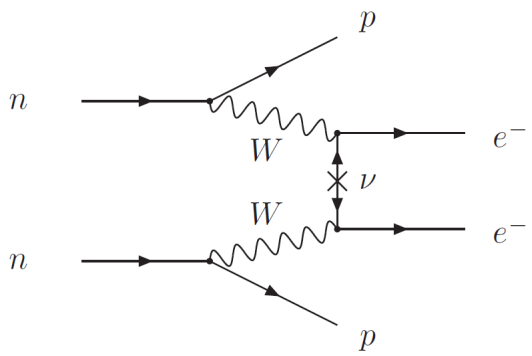

Figure 1.10: The neutrinoless double beta decay Feynman diagram [25].

This process amplitude is proportional to the product of the two leptonic currents:

$$M_{\alpha\beta} \propto [\overline{e}\gamma_\alpha(1-\gamma_5)\nu_e][\overline{e}\gamma_\beta(1-\gamma_5)\nu_e] \tag{1.62}$$

(where γ_x are the Dirac matrices) which can only lead to a neutrino propagator based on the contraction $\langle 0|\nu_e(x)\nu_e^T(y)|0\rangle$. This contraction is fundamental to understand the ultimate nature of the neutrino: if ν_e annihilates and creates a different antineutrino state, it is a Dirac particle, thus $\langle 0|\nu_e(x)\nu_e^T(y)|0\rangle$=0 and $M_{\alpha\beta}$=0; otherwise if the neutrino is a Majorana particle, neutrino and antineutrino are the same state and $\langle 0|\nu_e(x)\nu_e^T(y)|0\rangle \neq$0.

If the neutrino mass is caused only by the Majorana mass terms, the rate of the

$0\nu\beta\beta$ decay is proportional to the *effective neutrino Majorana mass* defined as:

$$m_{ee} = \left| \sum_i m_i U_{ei}^2 \right| \tag{1.63}$$

The process signature is given by the energy measured in the detector: if the value corresponds to the Q-value, a $0\nu\beta\beta$ decay has occurred; otherwise a broader spectrum is measured, identifying the $2\nu\beta\beta$ decay process. The mass is measured starting from the decay half-life defined as:

$$(T_{1/2}^{0\nu})^{-1} = G^{0\nu} |M^{0\nu}|^2 \left(\frac{m_{ee}}{m_e} \right)^2 \tag{1.64}$$

where $G^{0\nu}$ is the phase space integral and $|M^{0\nu}|^2$ is the nuclear matrix element of the transition. The half-life is expected to be of the order of 10^{20} years, so the experiments must be very sensitive. The Heidelberg Moscow experiment has used 11 kg of enriched Ge obtaining a limit on the half-life of [25]:

$$T_{1/2}^{0\nu} > 1.9 \times 10^{25} \text{ yr} \ \ (90\% \text{ C.L.}) \tag{1.65}$$

Therefore, the effective Majorana mass is assumed to be:

$$m_{ee} \leq 0.26 \ (0.34) \text{ eV} \quad \text{at } 68\% \ (90\%) \text{ C.L.} \tag{1.66}$$

1.1.3 Results, open issues and the Neutrino Factory

In the previous sections the most important neutrino sources and experiments have been described. The results of these last 50 years of activity are summarized in table 1.2 [46]. A schematic representation of the neutrino mixing matrix with the

parameter	best fit	2σ	3σ	4σ
$\Delta m^2_{21}[10^{-5}]$ eV^2	7.9	7.3-8.5	7.1-8.9	6.8-9.3
$\Delta m^2_{31}[10^{-5}]$ eV^2	2.6	2.2-3.0	2.0-3.2	1.8-3.5
$\sin^2\theta_{12}$	0.30	0.26-0.36	0.24-0.40	0.22-0.44
$\sin^2\theta_{23}$	0.50	0.38-0.63	0.34-0.68	0.31-0.71
$\sin^2\theta_{13}$	0.000	$\leq$0.025	$\leq$0.040	$\leq$0.058

Table 1.2: The best fit values at 2, 3 and 4σ for the three flavor oscillation parameters [46].

experimental results is presented in figure 1.11.

However a large number of problems have to be solved, among which one can list [9, 19, 28]:

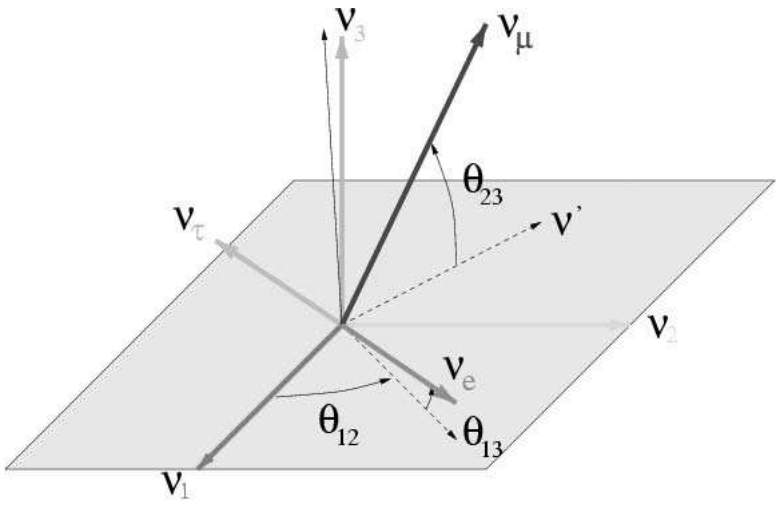

Figure 1.11: A schematic representation of the mixing matrix results obtained in oscillation experiments: $\theta_{23} \cong 45°$, $\theta_{12} \cong 30°$, $\theta_{13} \lesssim 13°$ [1].

- **the absolute mass value**: the oscillation experiments have discovered that the neutrino has a mass; however they are sensitive to the squared-mass difference, so no absolute mass value can be measured. The only way to obtain a direct mass value is to evaluate the endpoint of the kinematic spectrum in the β decay or to measure the flux of the (very) rare neutrinoless double beta decay;

- **Dirac-Majorana particle**: the mechanism which generates the small neutrino mass has not been confirmed. Dirac's explanation (and the Higgs mechanism) seems not to be the only responsible of such a small mass; on the other hand in the See-Saw mechanism (derived from Majorana's theory) the leptonic number would be no longer conserved. The Dirac-Majorana nature can be only confirmed in the $0\nu\beta\beta$ decay evaluating if neutrino and antineutrino are the same particle or not;

- **mass hierarchy**: the neutrino mass eigenstates hierarchy is still not confirmed. At present two possible cases are suggested: in the *normal* hierarchy the two lightest eigenvalues are separated by a small difference while the third is heavier than the other two; in the *inverted* one the third eigenstate is lighter than the other two. A schematic view is presented in figure 1.12: the small difference is measured by solar experiments (that also ensure that $m_2 > m_1$), while the large difference is computed in the atmospheric ones;

- $\boldsymbol{\theta_{13}}$: the θ_{13} mixing angle has been measured in the CHOOZ experiment but a better precision is requested;

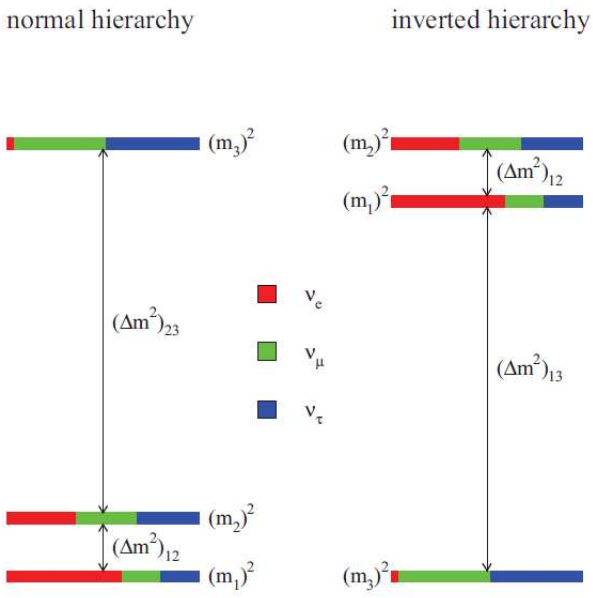

Figure 1.12: The normal (left) and inverted (right) mass hierarchies: the small difference ($\nu_1 - \nu_2$) is evaluated in solar neutrino experiments, while the large one (ν_3-others) in the atmospheric ones [19].

- **CP violation**: if $\theta_{13} \neq 0$, a complex phase factor (δ in the PMNS matrix, equation 1.19) would cause the CP violation. It can be evaluated by measuring the following asymmetry:

$$A_{CP} = \frac{P(\nu_\alpha \to \nu_\beta) - P(\overline{\nu_\alpha} \to \overline{\nu_\beta})}{P(\nu_\alpha \to \nu_\beta) + P(\overline{\nu_\alpha} \to \overline{\nu_\beta})} \tag{1.67}$$

- **leptogenesis**: the matter-antimatter asymmetry in the Universe was previously associated to the GUT baryogenesis where heavy gauge baryons decoupled from equilibrium in the early time. However the mass of the gauge bosons resulted too small to be the ultimate responsible of the problem. A possible solution could come from the broken lepton number conservation that causes an asymmetry in the baryon-antibaryon number.

Even if neutrinos are available in such large numbers, their weak nature results in the need of large and heavy detectors and in the fact that neutrino beams with well defined features do not exist at the moment. A possible solution to simplify these studies is represented by the Neutrino Factory based on a muon storage ring: such a factory would provide a well known neutrino beam to (at least) three independent experiments with different baselines. The intrinsic features of the beam in terms of energy and geometry would allow to develop optimized detectors.

1.1.3.1 The conceptual layout of a Neutrino Factory

In a Neutrino Factory, neutrinos are produced by the decay of a high intensity muon beam [47]; a possible schematic view is presented in figure 1.13. There are

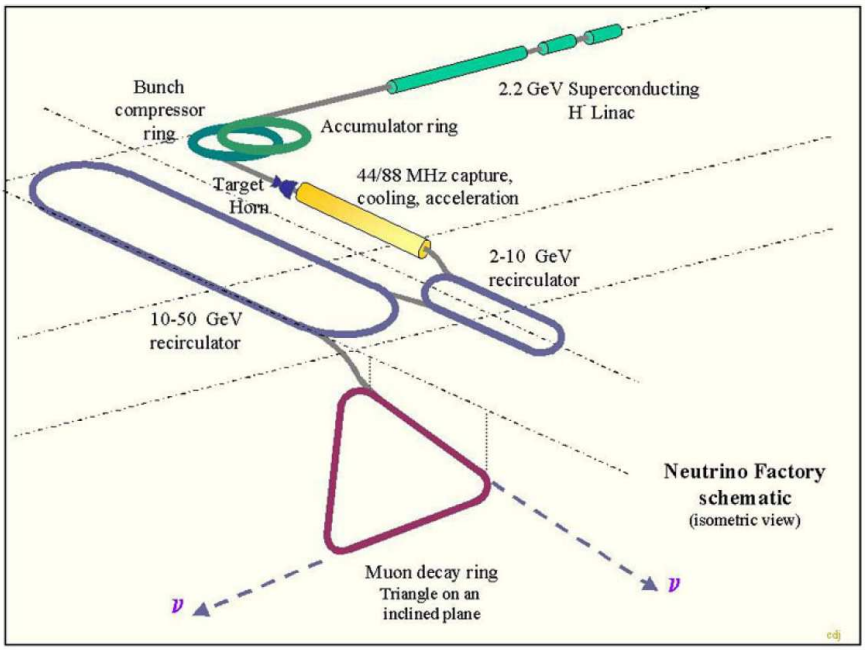

Figure 1.13: A possible conceptual layout of a Neutrino Factory [47].

several designs for such a source with a common goal: the generation of up to 10^{21} muons per year from a proton beam.

In a Neutrino Factory an accelerator provides the required energy to a very high power proton beam (4 MW); in order to minimize the longitudinal phase space volume, the proton bunches must be at least of the order of a few nanoseconds. The proton beam impinges on a target of 2-3 nuclear interaction lengths to create pions: given the beam high intensity, the target must be extremely robust and resistant. Two solutions have been suggested: a liquid-jet and a rotating target [48, 49]. The pions can be captured in three different ways: superconducting and warm magnets, magnetic horns or wide-aperture bending magnets. In figure 1.14 the pion production and capture is presented: a proton with an energy in the range 16-30 GeV impinges on a liquid (e.g. Hg) target producing pions; the target is placed inside a solenoid field which guides pions to the decay and phase rotation line.

Pions decay in muons in a 30-40 m dedicated line. Since a high intensity muon beam is needed, the beamline must have a large acceptance for pions; therefore wide apertures and strong magnetic fields (granted by solenoid magnets) are

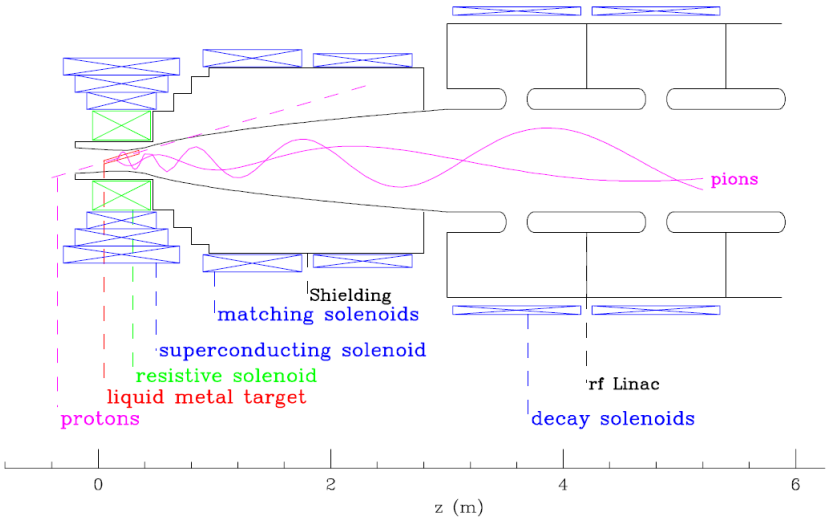

Figure 1.14: A possible schematic view of the pion production in a Neutrino Factory: 16-30 GeV protons impinge on a liquid-jet target inside a high-field solenoid magnet followed by a decay and phase rotation channel [49].

necessary. In order to store them, muons must be cooled via an innovative technique called *ionization cooling* (described in detail in section 1.2.1): muons lose transversal and longitudinal momenta in a light element absorber (e.g. liquid hydrogen), then radiofrequency cavities restore the longitudinal momentum, with the net result of a phase space volume reduction. Muons are accelerated to 20-50 GeV and then stored in a triangular muon decay storage ring. Here muons can decay in the three straight lines, generating three neutrino beams that can be sent to different baseline experiments. Such an accelerator guarantees a very high neutrino flux given the large apertures and very soft focusing magnets.

A storage muon ring is also the first step towards a muon collider, a complex that combines the advantages of a $e^{\pm}$ collider (point-like structure of the probes) with the ones of a hadronic accelerator (less energy loss given the suppression of the radiative processes) [48].

1.1.3.2 Physics at the Neutrino Factory

In a Neutrino Factory for each muon decay two flavor neutrinos are produced [46]:

$$\mu^{\pm} \rightarrow e^{\pm} + \nu_e(\overline{\nu_e}) + \overline{\nu_\mu}(\nu_\mu) \tag{1.68}$$

The physics at a Neutrino Factory is based on the oscillation phenomenon, although also a non-oscillation physics program has been proposed. The basic

goal is the precise measurement of the elements of the mixing matrix, a result that could be achieved exploiting the natural advantages of such a source [47]:

- the neutrino beam energy spectrum can be precisely evaluated starting from the muon one;
- the flavor composition is well known: two different flavors with opposite leptonic number are generated for each muon decay;
- it is possible to change the polarity of the stored muons to obtain a charge-conjugate neutrino beam;
- it delivers the same beam to different baseline experiments.

The oscillation physics is granted by the availability of different oscillation channels that can be summarized in the following way:

- *golden channel*: it is based on $\nu_e \rightarrow \nu_\mu$ and it can be tagged via the so-called "wrong-sign muons", in which muons in the detector have an opposite charge with respect to the ones in the accelerator complex;
- *silver channel*: the oscillation $\nu_e \rightarrow \nu_\tau$ occurs and, given the high energy, a τ particle appears in the detector. The tagging is performed requiring a "wrong-sign" event and identifying the τ decay vertex;
- *platinum channel*: the $\nu_\mu(\overline{\nu_\mu}) \rightarrow \nu_e(\overline{\nu_e})$ oscillation is studied. This process is the T and CP-conjugate of the golden one, even if with different matter effects. The channel signature depends on the identification of the electron charge.

According to the previous considerations, the following measurements have been proposed [47]:

- **determination of Δm^2_{23}, its sign, the θ_{23} mixing angle and the leptonic CP violation**: the oscillation $\nu_e \rightarrow \nu_\mu$ allows a precise measurement of Δm^2_{23} and θ_{23}. Moreover an evaluation of the CP violation and the mass hierarchy can be made considering the effect of matter in the oscillation probability. The CP violation can be measured considering the ratio:

$$R = \frac{N(\overline{\nu_e} \rightarrow \overline{\nu_\mu})}{N(\nu_e \rightarrow \nu_\mu)} \tag{1.69}$$

  that is represented as a function of the baseline in figure 1.15. If $L = 0$ and no effects of CP violation occur, the ratio is 0.5, given the neutrino/antineutrino cross sections. If L increases, the ratio becomes larger

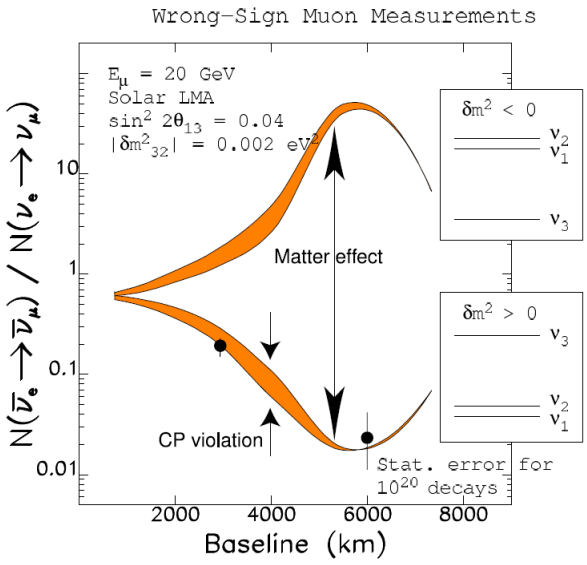

Figure 1.15: The predicted ratio of the wrong sign muon events as a function of the baseline considering both the Δm^2_{23} signs. The band in the figure represents the CP violation [50].

(smaller) if the Δm^2_{23} sign is positive (negative). Sufficiently large baseline experiments (even better if the baselines are different) allow a precise measurement of the R ratio, determining the Δm^2_{23} sign and the δ phase.

- **determination of the θ_{13} mixing angle**: figure 1.16 presents the sensitivity of the Neutrino Factory (NuFact) compared with other present and future experiments. An entry-level (10^{19} muon decays per year without cooling) and high-performance (2.4×10^{20} muon decays per year) Neutrino Factory (NuFact I & II, respectively) have been compared with the J-PARC-SK experiment, a higher-energy off-axis project (NuMi) and a future J-PARK experiment in which the detector is a megaton water Cherenkov system (HyperKamiokande). The statistical sensitivity limit can be reduced taking into account other oscillation parameters and degeneracy errors. The sensitivity of NuFact II is almost two orders of magnitude better than the other experiments.

Neutrino Factory non-oscillation physics studies like Deep Inelastic Scattering (DIS) and non-neutrino science can be also performed. As far as the first type is concerned, present neutrino DIS experiments require large and dense nuclear targets to generate neutrinos from pion decays and the energy spectrum is not well defined. In a Neutrino Factory this problem does not exist given the well-defined original muon beam: the expected event rates would be an order of magnitude

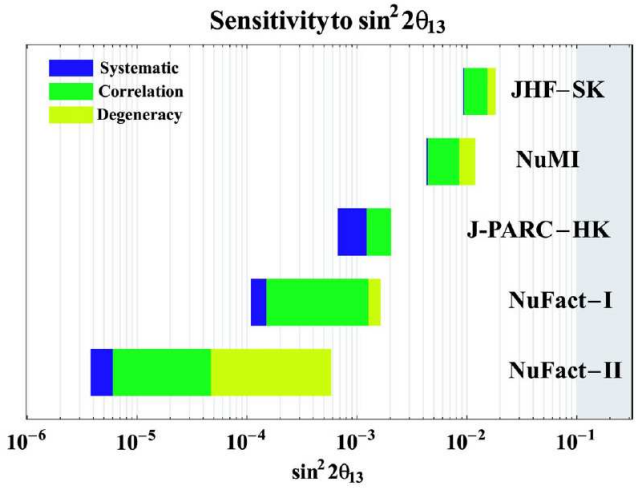

Figure 1.16: The sensitivity of an entry-level (I) and high-performance (II) Neutrino Factory on the mixing angle $\sin^2\theta_{13}$ compared with present and future experiments. JHF is the former name of J-PARK [51].

better than the present available experiments. Precise measurements of the CKM matrix elements and the electroweak fundamental parameters (like $\sin^2\theta_W$) are also possible [47, 50].

Moreover non-neutrino physics researches can be also performed: the physics of slow muons and the muon lifetime are just a couple of examples.

1.2 MICE: Muon Ionization Cooling Experiment

The Muon Ionization Cooling Experiment has been proposed in 2003 to study the feasibility of a Neutrino Factory based on a muon storage ring, a tool that represents the frontier for neutrino oscillation and CP violation studies and for $\mu^+\mu^-$ colliders [47]. More precisely, MICE intends to evaluate the most crucial task in a Neutrino Factory: the muon cooling. Since standard techniques like electron, stochastic or laser cooling are not effective enough because of the muon lifetime, a possible solution is represented by the ionization cooling. This technique consists of two parts: in a first phase muons lose transversal and longitudinal momenta by means of scattering in a low density absorber, while in a second one the longitudinal component is restored by radiofrequency cavities. The net result is a reduction of the phase space volume, mathematically described by the emittance. MICE is being commissioned at RAL in order to test the ionization cooling measuring the emittance before and after a cooling section with a large precision which requires a performing particle ID.

In this section the ionization cooling is described together with its implementation in the MICE experiment.

1.2.1 The ionization cooling

In high energy physics, electrons and protons have been always considered as the basic tools to study the SM and go beyond it. However, with higher energies, both have some limits [52]: electrons are perfect probes because of their "point-like" nature but lose a large amount of energy because of synchrotron radiation; on the other hand, protons are complex objects. A possible alternative is provided by muons: they are leptons with a mass m_μ of 105.66 MeV [53] (about 200 times larger than the electron mass, m_e), so they can be accelerated and stored in a ring and their energy loss due to radiation emission and beamstrahlung[6] is negligible. Focusing on neutrino physics, a muon storage ring is the basic component of a Neutrino Factory.

However a muon storage ring requires that muons are first cooled which is a hard task since, given the muon mean life ($\tau_\mu = 2.2 \times 10^{-6}$ s [53]), the standard techniques are not effective [47] and, given the fact that muons are generated by pions produced in a target, the initial phase-space volume is very large. The only solution is represented by the *ionization cooling*.

1.2.1.1 The emittance

In order to better understand this technique, it is important to describe it in terms of *emittance*. The emittance (ϵ) defines the beam volume in the phase-space and it is expressed as $\epsilon_{6,n} = \sqrt{V}/(m_\mu c)^6$, where V is the determinant of the covariance matrix of the muons in the 6D coordinate system (x, y, z, p_x, p_y, p_z) and c the speed of light; z is set along the particle motion, x and y define the orthogonal transversal directions. If there are no correlations among the 6D coordinates, it is possible to express the 6D volume by $(\sigma_x \sigma_{p_x} \sigma_y \sigma_{p_y} \sigma_z \sigma_{p_z})$, where σ_i is the RMS width of the ith variable distribution [48]. Under the hypothesis that the off-diagonal (correlation) terms of V are negligible, it is possible to express the emittance as:

$$\epsilon_{6,n} \approx \epsilon_{x,n} \epsilon_{y,n} \epsilon_{z,n} \tag{1.70}$$

where $\epsilon_{i,n} = \sigma_i \sigma_{p_i} / m_\mu c$. The n subscript identifies the normalized emittance, to distinguish it with respect to the non-normalized one, defined as:

$$\epsilon_i = \epsilon_{i,n} / \gamma\beta \tag{1.71}$$

[6] In a storage ring, the beamstrahlung of a charged particle beam is the radiation emitted because of the interaction with the electric field of the other beam.

where $i = (x, y, z)$, while γ and β are the Lorentz factor and the velocity in terms of speed of light.

In a cylindrical coordinate system, the emittance can be defined as:

$$\epsilon_{6,n} \approx \epsilon_{\perp n}^2 \epsilon_{\parallel n} \tag{1.72}$$

where $\epsilon_{\perp n}$ ($\epsilon_{\parallel n}$) is the normalized transverse (longitudinal) emittance.

The ionization cooling has been proposed in the early '80s [52] and consists in two different phases, as shown in figure 1.17 [54, 55]: first a muon beam with a large emittance crosses an absorber and loses transversal and longitudinal momentum via the interactions with atomic electrons (the dE/dx described by the Bethe-Bloch theory [53]); then accelerating cavities restore the longitudinal energy loss.

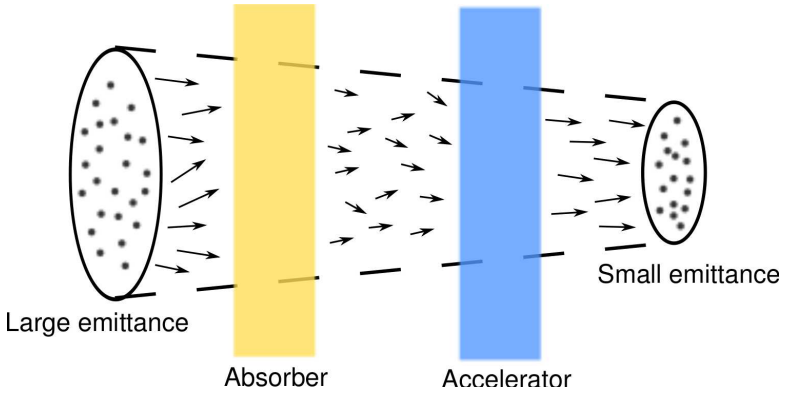

Figure 1.17: A schematic overview of the ionization cooling technique [54].

The interaction with an absorber causes multiple scattering[7] which in turn

[7]The multiple scattering effect describes the deflection (over small angles) of a charged particle due to Coulomb scattering with nuclei [53]. For small deflection angles, it is described by a Gaussian distribution: the RMS in a plane is defined as:

$$\theta_{plane}^{RMS} = \theta_0 = \frac{13.6 \text{ MeV}}{\beta cp} z \sqrt{x/X_0}[1 + 0.038 \ln(x/X_0)] \tag{1.73}$$

where p, βc and z are the momentum, velocity and charge number of the incoming particle, while x/X_0 is the thickness of the material (absorber in this case) in radiation lengths. At larger scattering angles the phenomenon is the same of a Rutherford scattering, with tails larger than the ones given by a Gaussian distribution. The radiation length is defined as the mean distance over which an electron loses $1/e$ of its energy via bremsstrahlung. Empirically it can be expressed in the following way:

$$X_0 = \frac{716.41 \cdot A}{Z(Z+1) \ln \frac{287}{\sqrt{Z}}} \text{ g} \cdot \text{cm}^{-2} \tag{1.74}$$

where A and Z are the mass and atomic numbers.

results in the increase of the emittance (a kind of heat source); according to equation 1.73, the cooling effect dominates for low Z materials like liquid hydrogen, helium, lithium and beryllium since the multiple scattering contribution is smaller.

1.2.1.2 The transverse emittance cooling

According to figure 1.18(a), the transverse emittance cooling in the momentum space can be schematically described in the following way [55]:

1. *t1 to t2*: muons cross an absorber reducing the transversal and longitudinal emittance; looking at the Bethe-Bloch curve (an example is presented in figure 1.18(b) for the lithium and beryllium cases), the minimum (Minimum Ionizing Particle, MIP) is located at $\sim$ 300 MeV/c, so both the regions before and after this value can be used, even if the lower momenta are favourite. Because of the multiple scattering, the emittance is quite large with respect to the theoretical one;
2. *t2 to t3*: the accelerator cavities restore the longitudinal momentum.

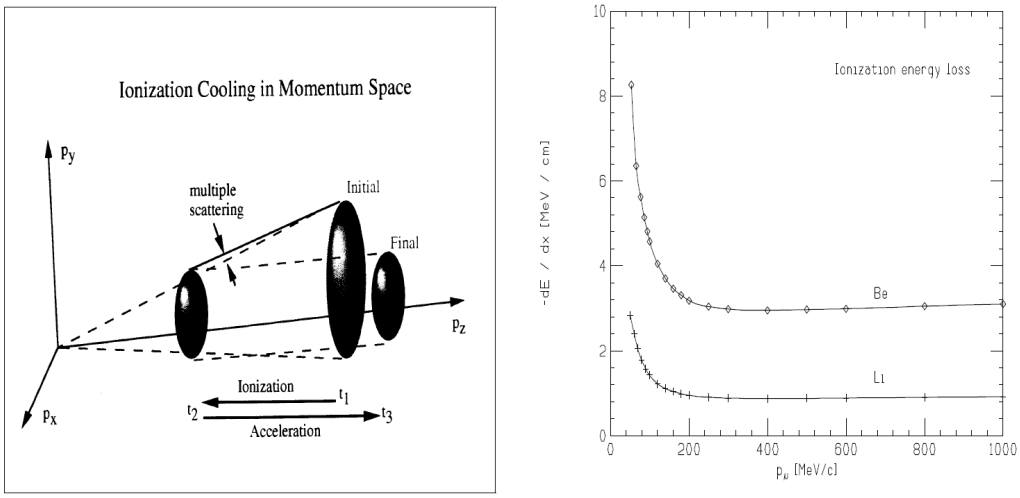

(a) (b)

Figure 1.18: a) The ionization cooling technique in the momentum space [55] and b) the Bethe-Bloch curve for muons in Li and Be [55].

Since only the longitudinal momentum is restored, the beam divergence is smaller.

Mathematically the transversal ionization cooling is described starting from equation 1.71: the normalized emittance in a given direction (e.g. x) is:

$$\epsilon_{x,n} = \gamma\beta\epsilon_x \tag{1.75}$$

where ϵ_x can be statistically expressed as:

$$\epsilon_x^2 = \left\langle x^2 \right\rangle \left\langle \theta^2 \right\rangle - \left\langle x\theta \right\rangle^2 \tag{1.76}$$

where θ is the divergence angle of the particle trajectory projected in the x-z plane.

The emittance variation along the travel motion z is:

$$\frac{d\epsilon_{x,n}}{dz} = \epsilon_x \frac{d(\gamma\beta)}{dz} + \gamma\beta \frac{d\epsilon_x}{dz} \tag{1.77}$$

The first term describes the cooling, while the second the heating:

$$\frac{d\epsilon_{x,n}}{dz}(cool) = -\frac{1}{\beta^2}\frac{\epsilon_{x,n}}{E}\left\langle \frac{dE}{dz} \right\rangle \tag{1.78}$$

$$\frac{d\epsilon_{x,n}}{dz}(heat) = \frac{\beta\gamma}{2\epsilon_x}\left[\left\langle x^2 \right\rangle \frac{d}{dz}\left\langle \theta^2 \right\rangle + \left\langle \theta^2 \right\rangle \frac{d}{dz}\left\langle x^2 \right\rangle - 2\left\langle x\theta \right\rangle \frac{d}{dz}\left\langle x\theta \right\rangle\right] \tag{1.79}$$

where E is the muon energy and the angle brackets indicate a mean value.

Assuming that the cooling occurs near the beam core and the focusing is strong enough, the effects of the correlation among the beam parameters and the growth in the transverse size of the beam are negligible, thus the heat term becomes:

$$\frac{d\epsilon_{x,n}}{dz}(heat) \approx \frac{\beta\gamma}{2\epsilon_x}\left\langle x^2 \right\rangle \frac{d}{dz}\left\langle \theta^2 \right\rangle \tag{1.80}$$

According to the betatron[8] focusing theory in the cylindrical symmetric coordinate system (where $\beta_x = \beta_y \equiv \beta_\perp$):

$$\left\langle x^2 \right\rangle = \beta_\perp \epsilon_x \tag{1.81}$$

thus:

$$\frac{d\epsilon_{x,n}}{dz}(heat) \approx \beta\gamma\frac{\beta_\perp}{2}\frac{d}{dz}\left\langle \theta^2 \right\rangle \tag{1.82}$$

Considering the multiple scattering theory and an approximation of equation 1.73 (without the term in the squared brackets), the heat term becomes:

$$\frac{d\epsilon_{x,n}}{dz}(heat) \approx \frac{\beta_\perp}{2}\frac{E_S^2}{\beta^3 Emc^2}\frac{1}{X_0} \tag{1.83}$$

where $E_S = 13.6$ MeV.

[8]The β-function is the envelope around all the trajectories of the particles circulating in the focusing-defocusing (FODO) lattice [56].

From equations 1.78 and 1.83 it is possible to note that the cooling decreases as a function of the absorber length, while the heating term increases; equaling the two terms, the minimum achievable emittance value is:

$$min\ \epsilon_{x,n} \approx \frac{\beta_\perp E_S^2}{2\beta mc^2 X_0 \left\langle \frac{dE}{dz} \right\rangle} \tag{1.84}$$

where the dependence on the focusing is described by $\beta_\perp$, while the one on the absorbing material by $X_0 \left\langle \frac{dE}{dz} \right\rangle$.

Table 1.3 presents the most important parameters of some materials that can be used in the ionization cooling [55]: the dE/dx is expressed for relativistic particles ($\beta \approx 1$) and it is possible to note that the best cooler is liquid hydrogen.

Material	ρ [g/cm^3]	dE/dx [MeV/cm]	X_0 [cm]	$\beta_\perp$ [mm mr/cm]
liq. H_2	0.071	0.286	890.	42
liq. He	0.125	0.242	756.	59
LiH	0.82	1.34	102.	78
Li	0.534	0.875	155.	79
Be	1.848	2.95	35.3	103
CH_2	0.93	1.93	47.9	116
C	2.265	3.95	18.8	144
liq. N_2	0.807	1.47	47.	155
Al	2.70	4.36	8.9	275

Table 1.3: Parameters of materials for the ionization cooling [55].

1.2.1.3 The longitudinal emittance cooling

The beam longitudinal component is also cooled during the absorption. The normalized longitudinal emittance can be defined as [55]:

$$\epsilon_{z,n} = \beta_z \gamma \delta \sigma_z \tag{1.85}$$

where σ_z is the beam bunch length and

$$\delta = \frac{\sigma_{p_z}}{p_z} \tag{1.86}$$

As before, the emittance variation in a step dz in an absorber is given by:

$$\frac{d\epsilon_{z,n}}{dz} = \beta\gamma\delta\frac{d\sigma_z}{dz} + \beta\gamma\sigma_z\frac{d\delta}{dz} + \delta\sigma_z\frac{d(\beta\gamma)}{dz} \tag{1.87}$$

In this equation it is assumed that the motion is predominant along the z direction. In the hypothesis of relativistic beams, the changes in the bunch length (σ_z) are very small, so the first term can be neglected; therefore the previous equation becomes:

$$\frac{d\epsilon_{z,n}}{dz} \approx \frac{\beta\gamma\sigma_z}{p_z}\frac{d\sigma_{p_z}}{dz} \tag{1.88}$$

The energy spread term $\left(\frac{d\sigma_{p_z}}{dz}\right)$ can be generated by three factors:

- dE/dx: because of the curvature of the dE/dx (figure 1.18(b)), particles with different momenta lose a different amount of energy. The energy loss term is given by:

  $$\frac{d\sigma_{p_z}}{dz} = \frac{\sigma_E}{\beta c}\frac{d}{dE}\left(\frac{dE}{dz}\right) \tag{1.89}$$

  The term increases (decreases) for a momentum smaller (larger) than the minimum ionization value. However the rate of cooling is very small since the dE/dx is very small (in the relativistic region): as an example, in the range 600-800 MeV the dE/dx term varies from 0.4×10^{-4}/cm for hydrogen to 4.5×10^{-4}/cm for aluminum;

- straggling: the statistical fluctuation in the energy loss in a given distance is defined *straggling*. Straggling adds another term to the energy spread:

  $$\frac{d\sigma_{p_z}}{dz} = \frac{K_s}{2\beta c\sigma_E}\gamma^2\left(1 - \frac{1}{2}\beta^2\right) \tag{1.90}$$

  where the constant K_s is defined as:

  $$K_s = 4\pi(r_e m_e c^2)^2\frac{N_A Z\rho}{A} \tag{1.91}$$

  where r_e is the classic radius of the electron and N_A the Avogadro number. Given the γ^2 factor, the cooling at lower energy has to be preferred;

- the absorber density: the longitudinal cooling is a function of the density or thickness of the absorber in a region of non-zero dispersion. Considering a wedge absorber (figure 1.19), the energy dispersion term becomes:

  $$\frac{d\sigma_{p_z}}{dz} \approx \frac{1}{\beta c}\frac{dE}{dz}\frac{\eta\delta}{\alpha L_0} \tag{1.92}$$

  where the dispersion is defined by $\eta = dx/d\delta$, the wedge angle $\alpha = dx/dz$ and L_0 is the wedge absorber thickness.

The longitudinal cooling is typically associated to the heating in the transverse component due to the multiple scattering effects, and viceversa: this effect is called *emittance exchange* [55].

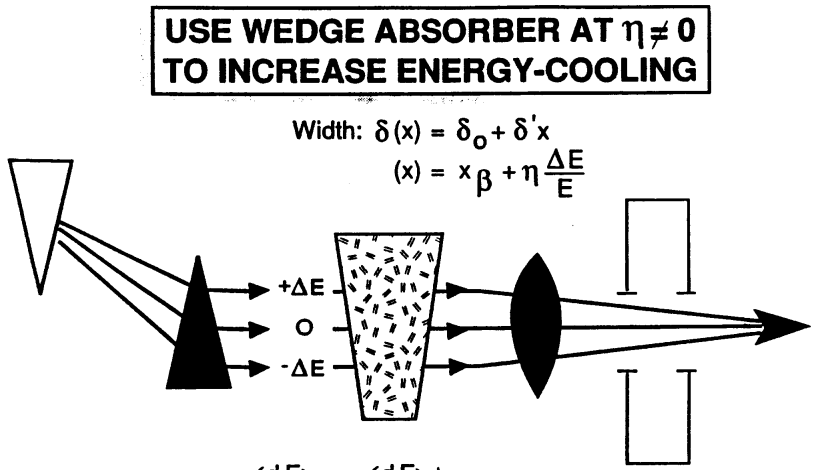

Figure 1.19: The longitudinal cooling using a wedge absorber [55].

1.2.2 MICE: goals and setup

The Muon Ionization Cooling Experiment is being built to study the ionization cooling technique for future Neutrino Factory and Muon Collider applications [47]. More in detail, the MICE goals are:

1. to design and build a cooling section for a Neutrino Factory;

2. to tune and characterize the muon beam produced in the section.

Figure 1.20 presents a 3D model of the MICE line: the basic elements are the cooling section, two spectrometers (to measure the emittance reduction) and the particle ID system. MICE intends to reduce by a factor of 10% the transverse emittance of a muon beam with a momentum in the range 140-240 MeV/c and an emittance from 1π to 10π mm rad. Just for a comparison, a transverse RMS emittance of 1500 mm mrad and a longitudinal RMS emittance of 30 mm are needed for a Neutrino factory [58].

As in the case of a Neutrino Factory, in MICE muons are produced by the decay of pions generated by protons impinging on a target. The protons are accelerated by the ISIS synchrotron at the Rutherford Appleton Laboratory (RAL, Didcot, UK, figure 1.21(a)) to an energy of 800 MeV. A part of the primary beam halo interacts with a titanium target and produces pions (figure 1.21(b)). Since MICE must not disturb the normal ISIS operation, the target is inserted into the proton beam only once per ISIS cycle. The ISIS cycle is divided in micro-structures (bunches) of 100 ns (separated by 224 ns) for 1 ms per second: for the MICE purpose, only one good muon per bunch is requested. It has been estimated that

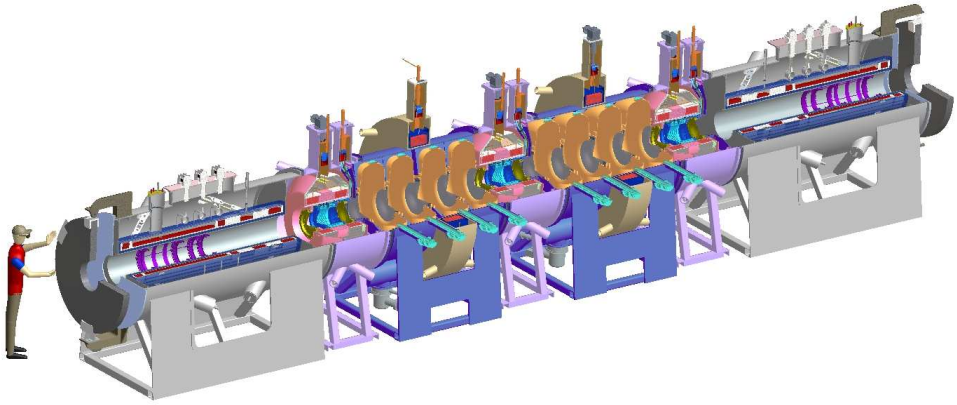

Figure 1.20: A 3D model of the MICE line: the muon beam comes from the left [57].

in order to have 500 good muons per spill in the cooling channel, up to 1.4×10^{12} must impinge on the target [9].

Pions are then captured by a triplet of quadrupole magnets (figure 1.22(a)), while bending magnets send them to the MICE hall (figure 1.22(b)), selecting the particles with the highest momenta. In the MICE hall pions can decay in a 5 m long superconducting 5 T solenoid that was contributed by the Paul Scherrer Institute (PSI, Switzerland). After the decay solenoid, a polyethylene absorber is placed to capture the remaining protons. Finally, a second dipole and two quadrupole magnets are used to select muons from pions, to address them towards the MICE line and to focus the beam itself.

A representation of the MICE line layout is given in figure 1.23: a muon beam is cooled by three liquid hydrogen absorbers while the longitudinal momentum is restored by two radiofrequency cavities; the emittance is measured by two 4 T spectrometers before and after the cooling channel; a particle identification system (made of TOF and Cherenkov detectors and a calorimetric system) is used to discriminate muons from the background (mainly pions and electrons).

1.2.2.1 Cooling section

A cooling section is based on three fundamental parts: low-Z absorbers, high-gradient radiofrequency (RF) cavities and focusing systems to squeeze the beam. A possible schematic view is presented in figure 1.24. The design of a cooling channel depends on several factors [47]:

1. **cooling factor**: the largest reduction factor in the transversal emittance is

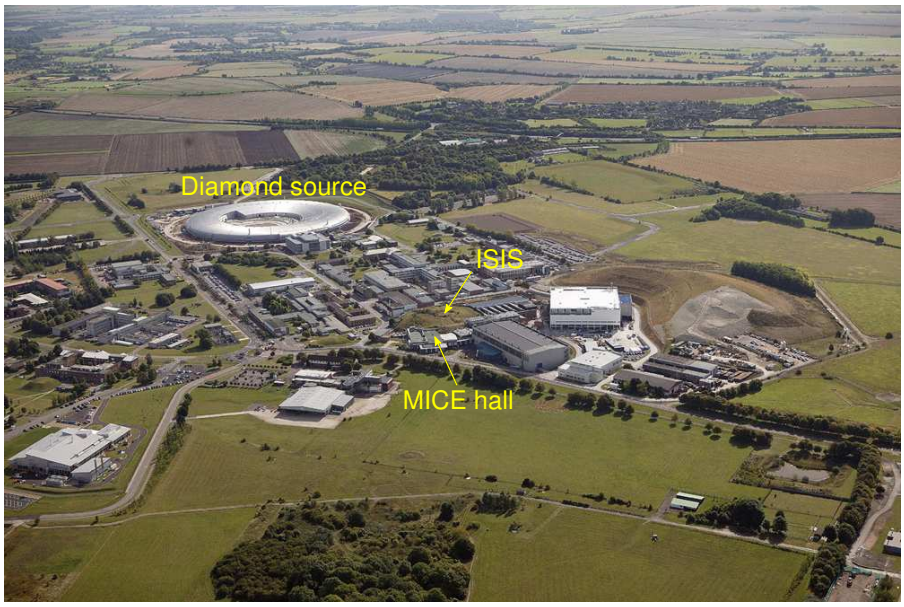

(a)

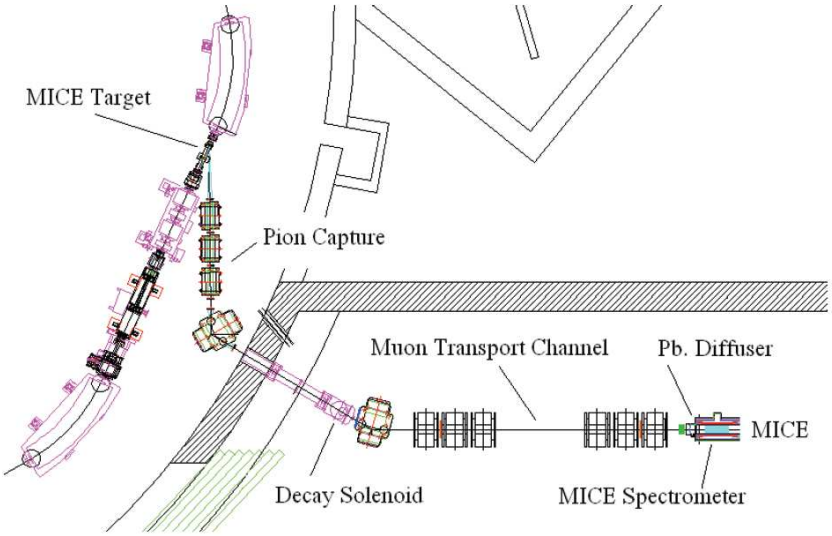

(b)

Figure 1.21: MICE at RAL: a) a photo of the Rutherford Appleton Laboratory and b) a drawing of the pion extraction line [9].

given by:

$$\frac{\Delta\epsilon}{\epsilon} = \frac{\Delta E}{E} \tag{1.93}$$

For a muon beam of 200 MeV/c, a 10% reduction request corresponds to

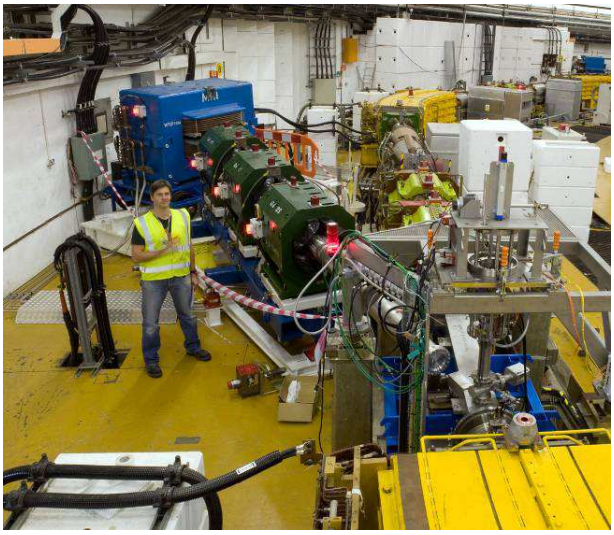

(a)

(b)

Figure 1.22: Muon production at RAL: a) the ISIS proton beam halo impinges on a titanium target (bottom right); pions are generated and captured by three quadrupoles (in green). High momentum pions are selected by a bending magnet which transports them to the b) MICE hall where they decay in a 5 m long solenoid.

20 MeV of energy loss and a similar value of momentum restoring in the RF cavities;

2. **absorbing material**: the best absorber material is selected considering the pros and cons of each of the elements presented in table 1.3;

3. **RF cavity frequency**: the RF cavities are characterized by their frequency: some studies have suggested to use 88 MHz, while some others 201 MHz. Since the first ones occupy more space, need more power and provide less gradient, the second ones have been chosen by the MICE collaboration;

4. **beam**: a typical incoming muon beam could have the following features:

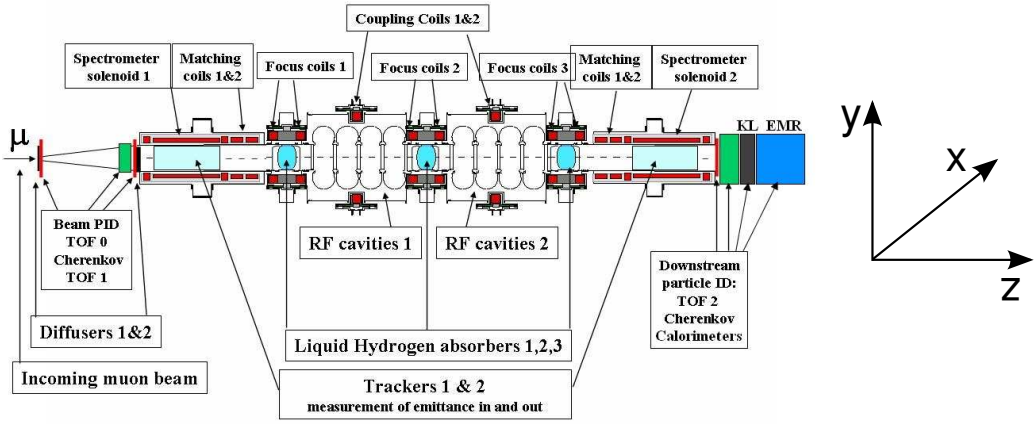

Figure 1.23: The MICE experiment layout [47]: a muon beam is cooled by three liquid-H_2 absorbers and the momentum is restored by two radiofrequency cavities. 4 T spectrometers before and after the cooling channel measure the emittance reduction, while a particle identification system (based on TOF, Cherenkov detectors and a calorimetric system) is used to discriminate muons from background. The z direction is defined along the beam, while the x and y coordinates are the transversal ones.

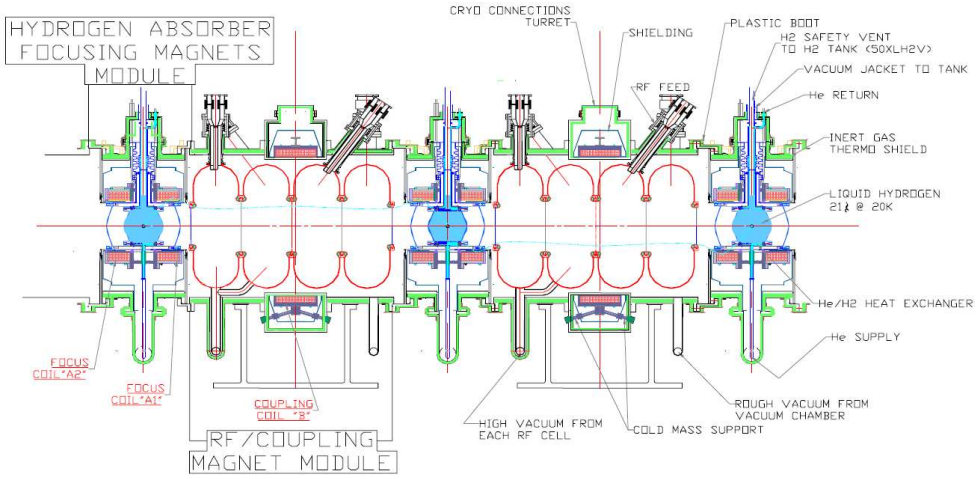

Figure 1.24: A schematic view of a possible cooling channel: three low-Z absorbers are enclosed in focusing coils (to squeeze the beam); two RF cavities restore the longitudinal momentum [47].

- momentum: 200 MeV/c;

- momentum spread: 10%
- beam size RMS: 5 cm in both the transversal directions;
- beam divergence RMS: 150 mrad in both the transversal directions.

5. **focusing**: in order to reduce the emittance growth due to the increase of the beam size, different focusing methods have been proposed [55]:

   - a solenoid, that produces a central longitudinal magnetic field, causing the particle to follow a helicoidal trajectory;
   - a solenoid FOFO cell, made of short solenoids separated by a certain distance that can focus in both the transversal directions at the same time.

According to the previous constraints, the MICE section is made of three Absorber Focusing Coils (AFCs) and two RF cavity and Coupling Coils (RFCCs). An AFC module consists of two parts: the liquid hydrogen absorber (but other materials, like helium, can be also used) and solenoid magnets [59, 60]; a 3D model is presented in figure 1.25(a).

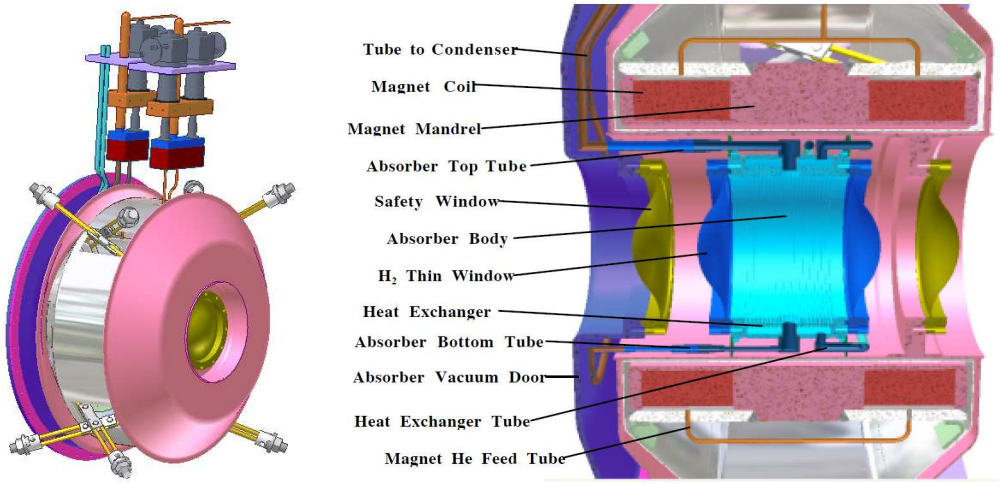

(a) (b)

Figure 1.25: A 3D [61] and a cross sectional view [62] of an Absorber Focusing Coil.

The absorber consists in a 21 l vessel that contains 1.5 kg of liquid hydrogen (or 2.63 kg of liquid helium); in order to reduce the multiple scattering, a pair of 300 mm diameter 0.18 mm thick windows are used in the beam aperture

(figure 1.25(b)). The hydrogen, supplied by a 1.5 W cryocooler at 4.5 K, is explosive when mixed with air, thus some safety precautions like the double window (the vacuum is pumped between the windows) and the coverage of all the vacuum chambers with argon gas (to avoid the air condensation) have been taken into account.

The absorber is placed in the center of a superconducting focusing solenoid (with a magnetic field of 4-6 T [47]) which has a bore diameter of 470 mm; the total length along the beam motion is 844 mm.

A RFCC module (figure 1.26(a)) consists of 4 201 MHz normal conducting RF cavities and one superconducting coupling coil magnet [63]. The cavity resonant

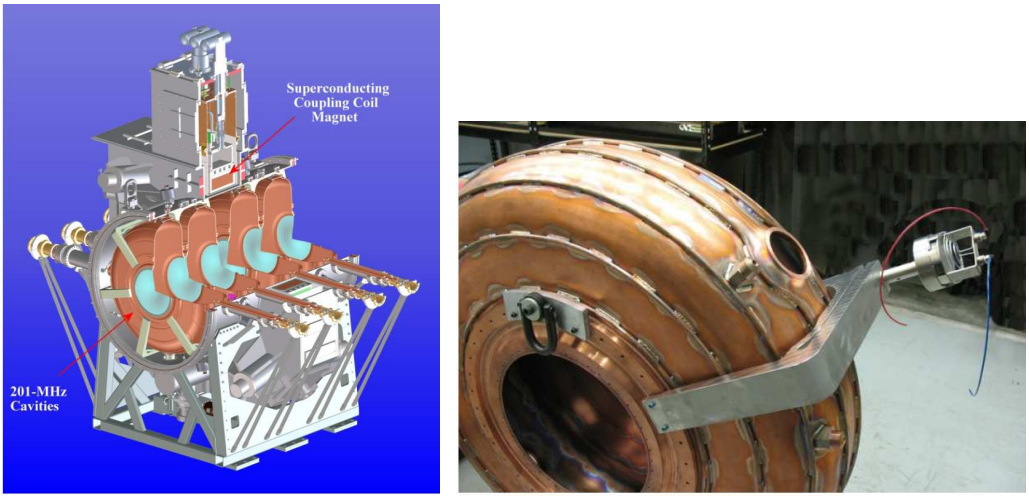

(a) (b)

Figure 1.26: a) A representation of a RFCC module and b) a photo of a 201 MHz cavity [63].

frequency is set shaping the cavities by means of six stainless steel flexure tuners (figure 1.26(b)); a very thin Be window or an Al grid (both transparent to muons) are installed on the beam aperture [47]. The coupling coil magnet is made of Al and Cu and is cooled with liquid helium at 4 K.

1.2.2.2 Spectrometers

The muon cooling is evaluated through the measurement of the emittance reduction of each single particle; the emittance before and after the cooling channel is computed using six coordinates $(x, y, t, p_x/p_z, p_y/p_z, E/p_z)$. These coordinates are measured by spectrometers consisting of a scintillating fiber tracker [64] and a 4 T solenoid magnet [65]: the muon trajectories are circular in the transver-

sal plane, providing the transversal momentum from the radius and p_z from the number of the orbit and the TOF measurements [47].

The 10% emittance reduction in MICE has to be measured with an accuracy of 1%, so a precision of 0.1% on the single particle emittance is required. Therefore the amount of the tracker material must be small not to increase the multiple scattering effect. A scintillating fiber tracker (SciFi, figure 1.27(a)) has been developed for this goal: it consists of 5 stations with a 40 cm diameter carbon-fiber frame and three scintillating fiber doublets glued at a 120° angular spacing. A fiber

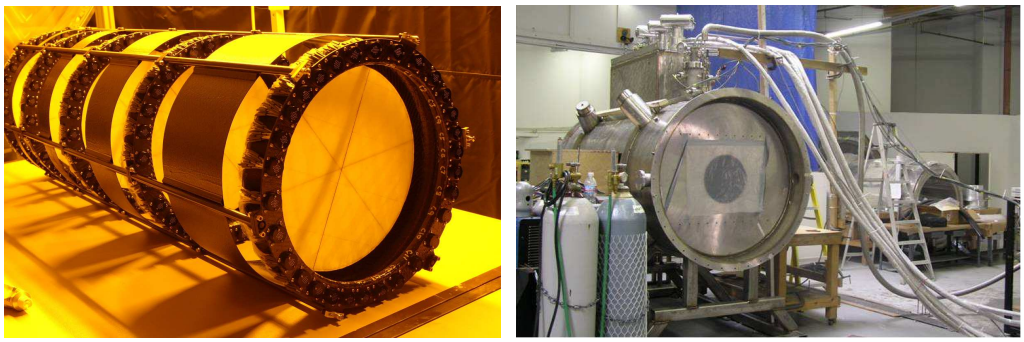

(a) (b)

Figure 1.27: The spectrometer: a) the SciFi tracker [66] and b) its solenoid [67].

doublet is made of two layers of 350 μm of diameter scintillating fibers. The scintillating light is readout by Visible Light Photon Counters (VLPCs) maintained at a temperature of 9 K. The overall number of channels of the two spectrometers is 6400 [64]. The spatial resolution has been measured to be (682$\pm$1) μm with cosmic rays at RAL with a detection efficiency of 99.7%.

The fiber detectors are placed in two 2.9 m long solenoid magnets (presented in figure 1.27(b)): since the ranges of momentum and $\beta_\perp$ are very large, the solenoid must be tuned over a very large range of currents. A tracker solenoid is made of two matching coils and three spectrometer ones. The spectrometer coils guarantee a uniform magnetic field over a length of 1 m and a diameter of 30 cm, while the two matching ones are used to match the β of the adjacent AFC with the one in the spectrometer. The overall magnetic field is 4 T.

1.2.2.3 Particle ID: TOF, CKOV and EMCal

In MICE a performing particle identification is necessary to identify muons from the background which consists mainly in pions and electrons. Upstream of the cooling channel, two Time-Of-Flight (TOF) stations and two Cherenkov (CKOV) detectors are used to distinguish muons from the remaining pions; downstream,

another TOF station and an electromagnetic calorimeter (EMcal) are devoted to the muon electron separation [47].

The upstream TOF detectors are not only used for particle identification, but also to generate the experiment trigger and a precise timing reference with respect to the accelerating RF cavities [68]. Each TOF station consists of two layers of 1 inch scintillator counters arranged in a x-y geometry (to increase the redundancy, figure 1.28(a)) readout on both sides by two fast R4998 Hamamatsu photomultipliers; TOF0 has a sensitive area of 40×40 cm^2, TOF1 of 42×42 cm^2, while TOF2 of 60×60 cm^2 [68, 69]. TOF0 is placed at the beginning of the channel,

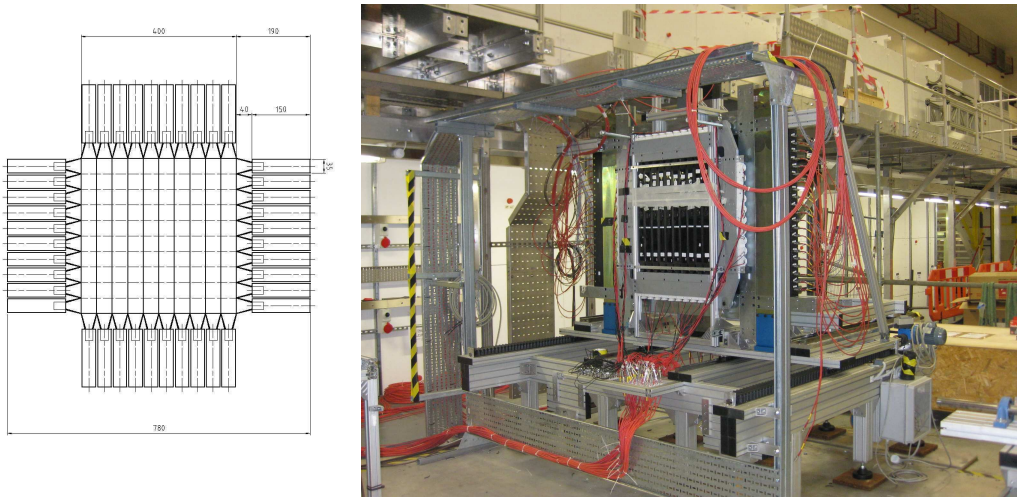

(a) (b)

Figure 1.28: a) A TOF schematic view: the scintillator slabs are arranged in a x-y geometry and are readout on both sides by fast PMTs [70]. b) TOF2 in its shielding cage [69].

about 10 m upstream of the first AFC, while TOF1 and TOF2 are placed at the beginning and at the end of the cooling channel respectively.

To determine the timing with respect to the RF phase with a precision better than 5°, a time resolution of 50 ps for TOF0 is required, while for a 99% pion rejection a resolution of 100 ps is enough. These performances must be provided in critical conditions: TOF0 must support an incoming beam rate of about 1.5 MHz (0.5 MHz per PMT), while the other two must work with a residual magnetic field that can reach 1300 G. The PMTs of the first station are shielded with conventional mu-metal shielding, while the other two TOFs are enclosed in 100 mm iron shielding cages (figure 1.28(b)). As far as the readout electronics is concerned, the time measurement is based on the CAEN V1290 time-to-digital converters (TDCs), while flash analog-to-digital converters (FADC) are used for

the time-walk corrections.

For higher momenta, the particle identification with only the TOF system becomes critical: from 220 to 340 MeV/c the muon/pion time difference goes from 2.4 to 1 ns [71]. Therefore two aerogel threshold Cherenkov detectors (named CKOVa and CKOVb) have been assembled: the first has an aerogel reflection index equal to n_1=1.07 (which corresponds to a momentum threshold for muons of $P_{\mu,1}$=278 MeV/c and for pions of $P_{\pi,1}$=367 MeV/c), while the second has n_2=1.12 ($P_{\mu,2}$=210 MeV/c, $P_{\pi,2}$=277 MeV/c) [9, 72]. Experimentally, for a 140 MeV/c beam both CKOVs do not provide a signal; 200 MeV/c muons are above threshold in CKOVb, while pions are below threshold in both; at 280 MeV/c, pions are above the CKOVb threshold, while muons are above both thresholds.

A CKOV station (figure 1.29) is based on two 2.3 cm thick layers of aerogel that cover a sensitive area of 46×46 cm^2: the light is readout by 4 8-inch PMTs. Since the expected rate is very high, the PMT signals are digitized by a high

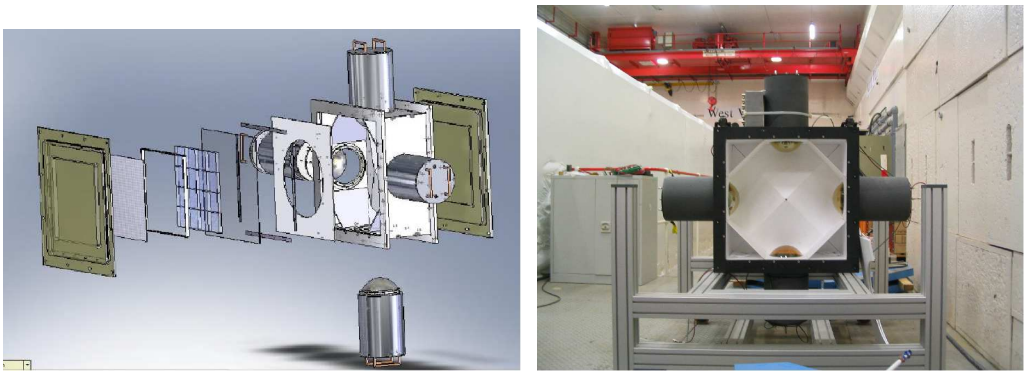

(a) (b)

Figure 1.29: a) An exploded view of a CKOV detector. From left to right a muon/pion crosses: the entrance window, the mirror, the aerogel mosaic, the acetate window, the GORE-TEX reflector panel, the exit window. The gray cylinders are the 8-inch PMTs in the iron shield. b) A photo of an Aerogel Cherenkov station [73].

frequency sampling waveform digitizer (CAEN V1731).

The last particle identification device is the Electron Muon calorimeter (EMcal): this electromagnetic system is based on a pre-shower (KLOE-Light front layer) and the Electron Muon Ranger (EMR) and has been developed to discriminate muons from electrons[9]. Since EMR is the heart of this thesis work, it is extensively described in chapter 2.

[9]MICE can work with both negative and positive particles; in this thesis, if not otherwise indicated, electron is used both for electron and positron.

The KLOE-Light (KL) pre-shower is a sampling calorimeter based on the KLOE one [74]: it is made of extruded 80×80 cm^2 Pb foils transversally segmented with 1 mm scintillating fibers that are inserted and glued in the lead holes. The energy is lower with respect to the KLOE one, so the lead foils are thinner.

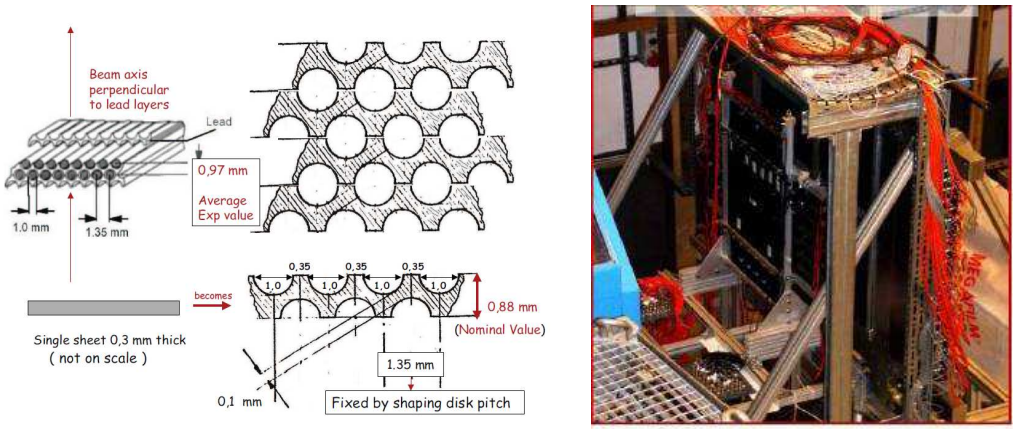

(a) (b)

Figure 1.30: The KLOE-Light layer: a) the "spaghetti" structure requires that the scintillating fibers are glued in grooved lead foils [9]. b) The KL is placed downstream of TOF2.

The overall detector (placed downstream of the TOF2 station (figure 1.30(b)) consists of 7 modules for a total of 2.5 X_0. The scintillator light is readout on both sides by Hamamatsu R1335 PMTs. The energy resolution has been measured to be σ_E/E=7%/$\sqrt{E(\mathrm{GeV})}$, while the time resolution is σ_t=70 ps/$\sqrt{E(\mathrm{GeV})}$ [71].

1.2.2.4 MICE time schedule

The MICE experiment is planned to be commissioned in six main stages [47]: figure 1.31 presents the schedule updated in 2010 [75].

The six steps can be described as follows:

1. characterization of the beamline, calibration of the detectors and evaluation of the beam composition; for this step the first two TOFs, the CKOVs and the KL are installed;

2. installation of the first spectrometer and TOF2;

3. installation of the second spectrometer: since no material is present between the two spectrometers, they must provide the same results, allowing a good calibration of the system. Installation of EMR;

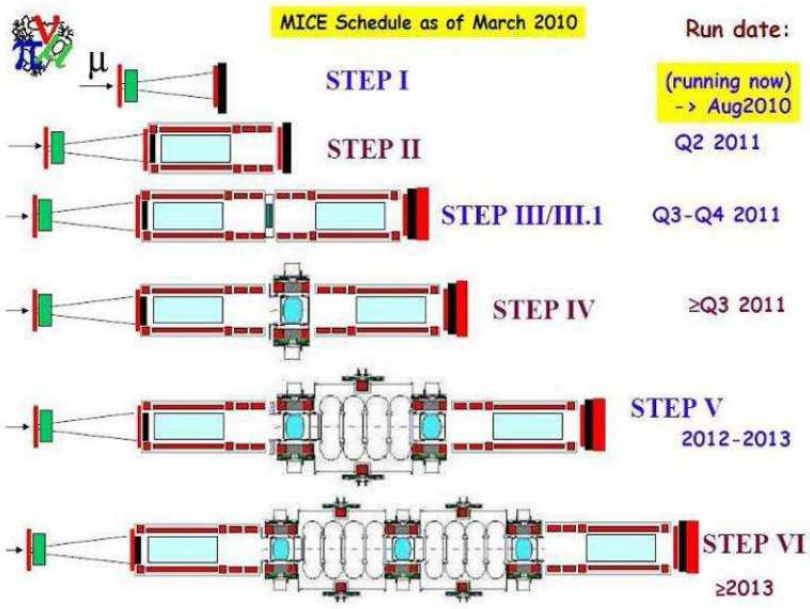

Figure 1.31: The MICE time schedule is divided in 6 stages. The present schedule has been fixed in March 2010 [75].

4. installation of the first AFC to measure the energy loss and the multiple scattering in different focusing conditions;

5. installation of the first cooling cell (two AFCs and one RFCC); the noise due to the RFCC is evaluated for the first time;

6. installation of the second cooling cell (one AFC and one RFCC) and final measurements.

At the time of this work, Step I has been completed, TOF2 has been installed and part of EMR has been commissioned (see chapter 5).

Chapter 2

The Electron Muon Ranger: how & why

The Electron Muon Ranger (EMR) is a fully active scintillator detector that is being assembled to discriminate (together with KL) muons from electrons. The necessity to use two devices is explained in the first part of this chapter, while the second one deals with a full description of this tracker-calorimeter based on 2832 scintillating bars. EMR, in fact, is made of 48 layers arranged in a x-y geometry; each layer consists in 59 1.1 m long extruded scintillating bars with a triangular shape whose light is carried out by one wavelength shifter (WLS) fiber and readout on both sides by single or multi-anode PMTs. A particular attention is devoted to the readout electronics of the whole system: the single PMT signals are readout by multi-channel waveform digitizers (WFDs), while the multi-anode ones are managed by a dedicated ASIC system.

Last but not least, the description of two EMR prototypes is given: the first (the small scale prototype) is devoted to the study of the tracker capability of the EMR detector while the second one (Large EMR Prototype) has been used to investigate its potential as a calorimeter. The muon/electron identification in MICE in fact is based on kinematic cuts (TOF system) and on a couple of variables depending on the energy measured by each EMR plane and the number of particle tracks in the detector itself.

2.1 The μ/e discrimination in MICE

As stated in section 1.2.2.3, in MICE muons are separated from the background by a performing particle identification (particle-ID) system: pions are identified upstream of the cooling channel by means of two TOF stations and two aerogel Cherenkov detectors, while electrons are discriminated by a third TOF and

EMcal. As far as the upstream particle-ID is concerned, figure 2.1(a) presents the time-of-flight spectrum (obtained with the TOF0 and TOF2 detectors during the commissioning phase of the TOF2) of a low emittance 300 MeV/c beam [75]. This beam is used for detector studies and it is composed of positrons (represented by the first small peak), muons (second peak) and pions (third peak).

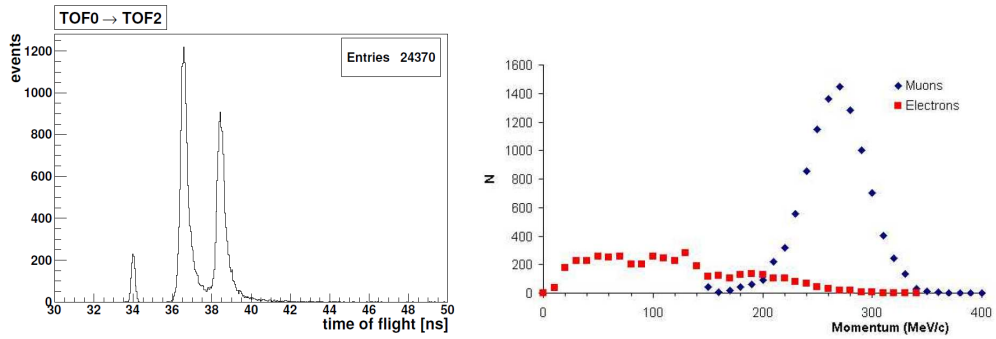

(a) (b)

Figure 2.1: a) The TOF system spectrum of a 300 MeV/c pion beam [69]: the small peak (at 34 ns) is the one corresponding to positrons, the peak in the range [36-38] ns to muons while the last one to pions. b) The number of survived muons (blue) and electrons (red) as a function of momentum downstream of the second spectrometer [47].

The downstream particle-ID is necessary since 1% of the muons are expected to decay in the cooling channel: this small fraction of electrons has a significant difference in momentum and it can introduce a bias in the emittance measurement. As presented in figure 2.1(b), the lower the momentum value, the larger the number of electrons after the second solenoid.

In order to achieve a 0.1% precision on the emittance measurement, a muon identification purity of 99.993% is required [9]: with kinematic cuts (based on the TOF system, in a way similar to the one presented in figure 2.1(a)) a rejection of 80% of the events is granted; the rest was originally achieved using KL and a second CKOV detector [47]. However the system costs were considerable and, more in general, the calorimeter was not optimized for MICE. So a fully active scintillator detector was proposed: SandWich (SW, figure 2.2(a)) consisted in 12 layers with different thickness which had to be placed just after KL, replacing the CKOV [9]. The layer thickness was chosen in order to optimize the energy resolution by means of G4MICE [76], a simulation toolkit based on GEANT4 [77]: the simulation results (presented in figure 2.2(b)) clearly indicated that such a device was optimal to reach the required purity.

Later on, the SW design evolved in EMR: because of the simplification in

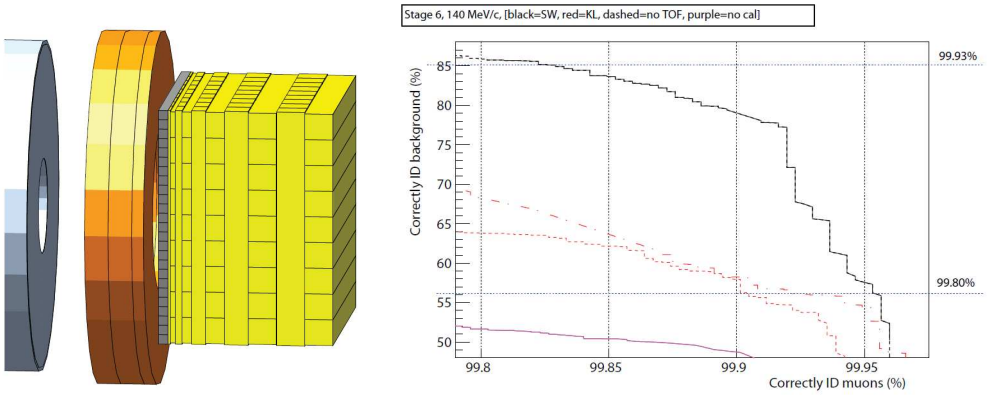

(a) (b)

Figure 2.2: a) The SandWich detector (in gray and yellow) has been designed by means of a G4MICE simulation. b) The background rejections for a 140 MeV/c beam: the black solid line is related to the use of SW and TOF, while the dash-dotted red line indicates KL+TOF. KL and SW without TOF are given by the red and black dashed lines, while the purple line is the one corresponding to TOF only [9].

the manufacturing and the good performances over a large range of momenta and of the experience in the MINERνA detector[1], a multi-layer system based on long scintillating bars was proposed. Moreover, after some prototype studies, the original rectangular bar shape was substituted with the final triangular one.

2.2 EMR: design and manufacturing

The Electron Muon Ranger is a fully active scintillator detector placed at the end of the MICE line, just behind the KL calorimeter (figure 2.3(a)). EMR consists in 48 planes of extruded scintillating bars arranged in a x-y geometry. The bars are provided by the Fermi National Accelerator Laboratory (FNAL) and are made of blue-emitting DOW Styron 663 polystyrene with 1% PPO and 0.03% POPOP dopants [79]; the emission peak corresponds to 420 nm. The bar shape has been chosen after some prototype studies [80]: originally the bars had a rectangular shape (1.5×1.9 cm^2), but this caused an inefficiency due to the non perfect planarity of the contiguous edges. Therefore the triangular shape (base=3.3 cm, height=1.7 cm, figure 2.3(b)) has been adopted.

[1]MINERνA (Main INjector ExpeRiment for ν-A) is a neutrino scattering experiment placed on the NuMI beamline at Fermilab [78]. The tracking system is based on long plastic scintillating bars.

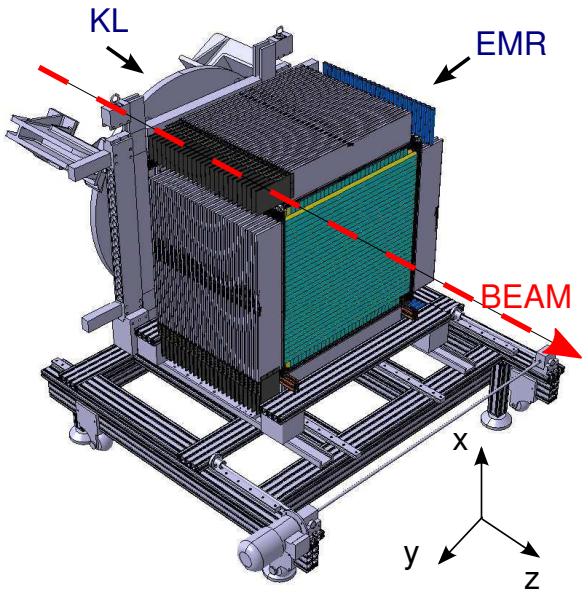

(a)

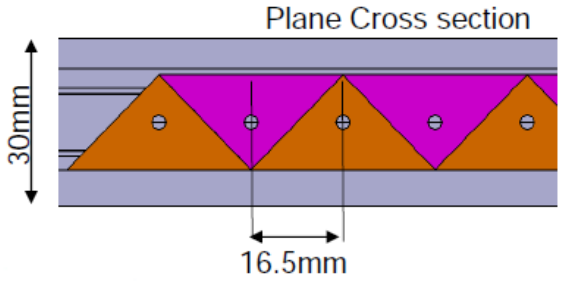

(b)

Figure 2.3: a) The Electron Muon Ranger is a fully active detector placed at the end of the MICE line, just behind KL. The z direction is defined along the beam, while the x and y coordinates are the transversal ones. b) The scintillating bars have a triangular cross section in order to reduce the inefficiency in the dead region among the bars themselves [Courtesy of the UNIGE group].

The scintillator light is brought out by one 1.2 mm diameter Saint-Gobain[2] BCF-92 wavelength shifter (WLS) fiber; the main features of the WLS fibers are presented in table 2.1. The original design foresaw that a unique 3.5 m WLS fiber (glued in the bar) carried out the light on both sides to two PMTs; however some prototype tests [81] demonstrated that the mechanical stress could cause micro-

[2]Saint-Gobain Crystals: www.detectors.saint-gobain.com

Manufacture reference	BFC-92
Physical property	Fast blue to green shifter
Diameter	1.2 mm
Core material	Polystyrene
Core refractive index	1.6
Density	1/05
1^{st} cladding material	PMMA (PolyMethylMethAcrylate)
1^{st} cladding refractive index	1.49
1^{st} cladding thickness	3% of fiber diameter
2^{nd} cladding material	Fluor-Acrylie
2^{nd} cladding refractive index	1.42
2^{nd} cladding thickness	1% of fiber diameter
Numerical aperture	0.74
Trapping efficiency	5.6% minimum
Decay time	2.7 ns
Peak emission	492 nm (green)

Table 2.1: The main features of the BFC-92 WLS fiber.

fractures that reduce the light transmission. For this reason, a new fiber system has been suggested: one WLS fiber is glued in the scintillator bar and fixed at the edge of the bar itself with two connectors; two separate clear fibers (one per side) carry out the light from the connectors to the PMT coupling masks. In this way all the bars are assembled with their own fiber and independently tested; in presence of a failure in the transmission of the light in the bar+external fibers chain, only these last ones have to be changed.

The Département de Physique Nucléaire et Corpuscolaire (DPNC) of the University of Geneva (UNIGE) is responsible of the EMR design and mechanics. The bar assembly procedure is schematically presented in figure 2.4 and it is the result of the steps studied in the prototype phase that can be summarized as follows:

- the original bars (from FNAL) have a length of 3-4 m, so they are cut at 1.1 m grouping 4 bars together to simplify the procedure (figure 2.4(a));
- the bar edges are polished and fine milled (figure 2.4(b));
- a WLS fiber is inserted in the bar (figure 2.4(c)), fixed on one side to a connector and glued in the bar with transparent glue. Then the second connector is placed on the other edge, before polishing both the fiber edges;
- 60 clear fibers (per PMT) are prepared: 59 fibers are used to readout the bars, while one for the calibration with a LED system. On one side they are

polished and fixed to a connector, while the other side is free. They are then covered with a dark plastic to avoid the fiber cross-talk effect and to protect the fibers themselves (figure 2.4(d));

- the fibers are interfaced to the PMT coupling masks and then glued, cut and polished.

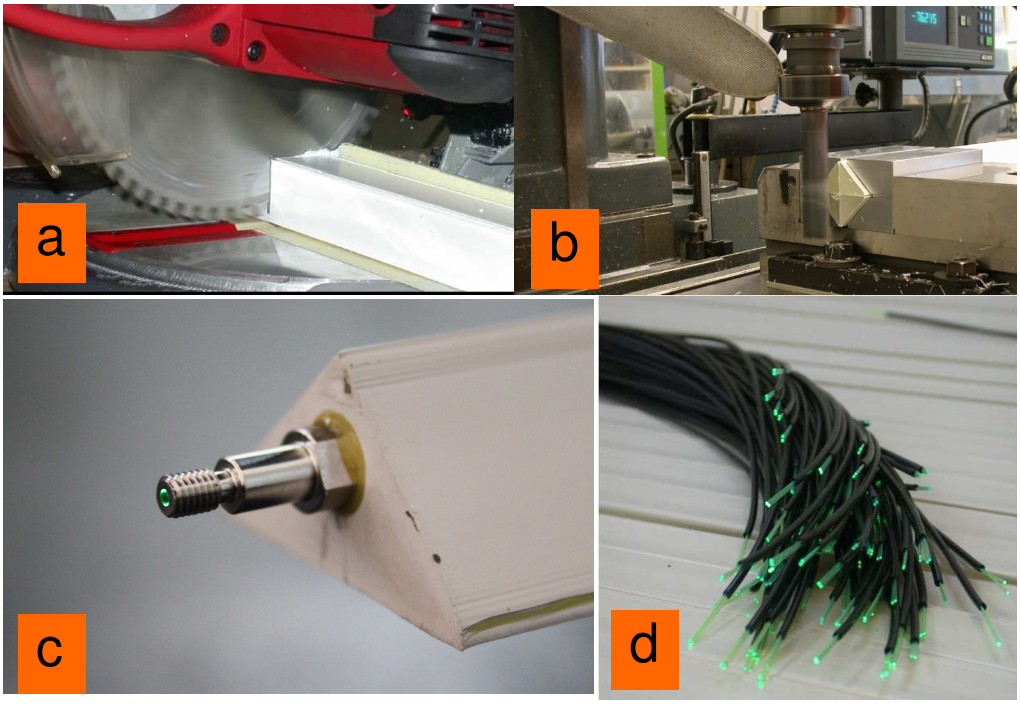

Figure 2.4: The bar assembly procedure: a) the original bars (3-4 m long) are cut to the right length and b) milled. c) A WLS fiber is inserted and glued in the bar and a connector is placed at the edge. d) The clear fibers that connect the edge of the bars and the PMTs are covered by a dark plastic foil [Courtesy of the UNIGE group].

Figure 2.5(a) shows the drawing of an EMR plane made of 59 1.1 m long scintillating bars: an EMR module (1x+1y layers) covers a sensitive area of nearly 1 m^2. Each layer is supported by an aluminum frame, while an aluminum box is used to guarantee the light tightness of the WLS fibers (figure 2.5(b)); the electronics supports are directly connected to the frame.

The EMR planes are placed one after the other (figure 2.6(a)) in an outer box that is integrated with the KL frame (figure 2.6(b)). The box also hosts 4 patch panels for the high voltage, the configuration and the data transmission signals. In total EMR consists in 2832 bars: since a single layer weights about 30 kg, the

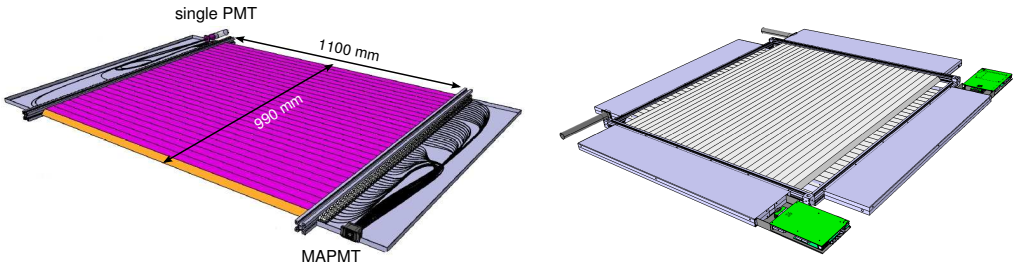

(a) (b)

Figure 2.5: a) An EMR plane: the scintillator light of each of the 59 1.1 m long bars is carried out by a fiber system made of one 1.2 mm WLS fiber and a clear one. On one side the light is readout by a single PMT to measure the whole plane charge, while on the other side by a 64 channel PMT (MAPMT) for the tracking. b) A module consists in 1x and 1y layers: each layer is supported by an aluminum frame, while the fiber light tightness is ensured by metallic boxes. The electronics supports are directly connected to the aluminum frame [Courtesy of the UNIGE group].

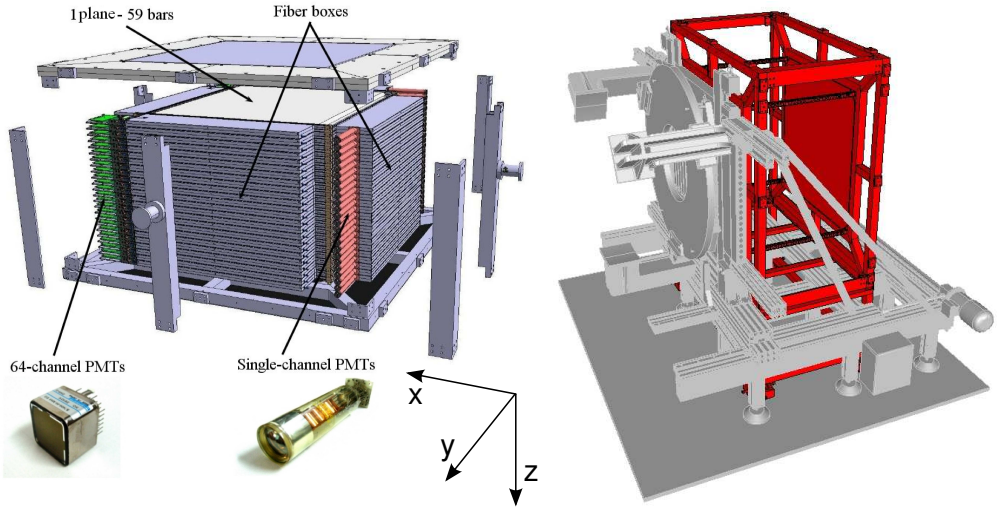

(a) (b)

Figure 2.6: a) The EMR layers are positioned one after the other and are enclosed in a metallic external frame which also hosts the patch panels. b) The EMR outer box is integrated in the KL frame [Courtesy of the UNIGE group].

whole detector weight is about 1.5 tons.

The scintillator light is readout on both sides by two different photomultiplier tubes (PMTs): on one side the 59 bars are interfaced to a single anode PMT to measure the overall energy loss in the whole plane; on the other side each bar is

coupled to one of the 64 channels of a multi-anode PMT (MAPMT).

As far as the PMTs are concerned, the major problem is represented by the residual magnetic field due to the last spectrometer: in the worst case (close to KL) the residual field is expected to reach 1200 G and to decrease to 300 G in the last EMR plane. The shielding has been designed considering a 5 cm soft iron reflector in front of EMR and a 1 mm thick Armco tube around the PMTs [75]: figure 2.7(a) presents the single PMT and its cylindrical frame that is fixed to the aluminum frame of each plane.

(a) (b)

Figure 2.7: a) The single anode PMT consists mainly of the glass (bottom right) and the voltage divider (bottom left) that are inserted in a 1 mm thick cylindrical shielding tube (top) fixed to the plane frame. b) The 59 fibers and the PMT are connected through a dedicated plastic mask [Courtesy of the UNIGE group].

The single channel PMT is a Photonics XP2972[3] whose main features are presented in table 2.2. The coupling between the 59 fibers and the PMT is obtained

Diameter	29 mm
Material	lime glass
Photo-cathode	bi-alkali
Spectral range	290-650 nm
Maximum sensitivity at	420 nm
HV	-1300 V
Gain	9.3×10^5

Table 2.2: The main features of the Photonics XP2972 single anode PMT.

thanks to the plastic mask presented in figure 2.7(b): after the gluing into the mask, the fibers are polished with a dedicated machine.

[3]Laurin Publishing Co., Inc.: *www.photonics.com*

A 64 channel multi-anode PMT (MAPMT) is used to measure the energy deposited in each bar: it is the green enhanced version of the Hamamatsu H7546B[4] (figure 2.8(a)) integrated in the device R7600-00-M64, whose main features are summarized in table 2.3. The MAPMT is coupled to the WLS fibers by means of

Number of anodes	8×8
Anode effective area	1.81×1.81 mm^2
Dynode stages	12
Photo-cathode material	bi-alkali
Window material	borosilicate glass
Spectral range	185-650 nm
Peak wavelength	420 nm
Cross-talk among channels	2%
Maximum HV	-1000 V
Gain	3×10^5

Table 2.3: The main features of the 64 channel Hamamatsu R7600-00-M64 MAPMT.

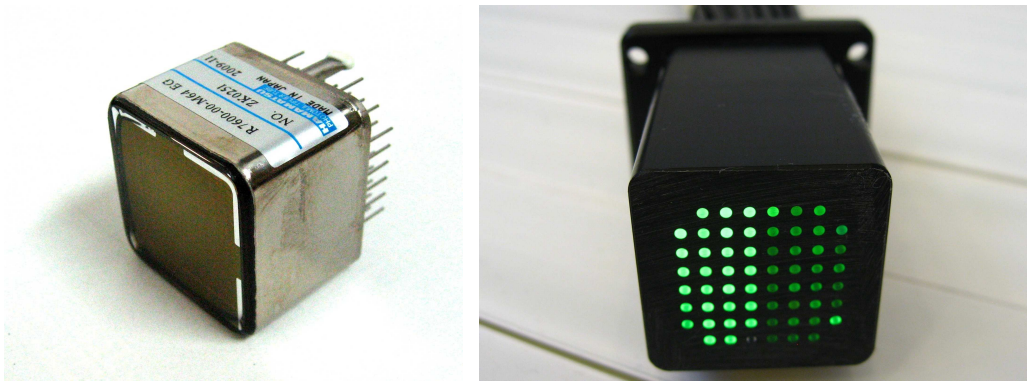

(a) (b)

Figure 2.8: a) The Hamamatsu R7600-00-M64 64 channel MAPMT and b) the fiber-PMT coupling mask [Courtesy of the UNIGE group].

the plastic mask shown in figure 2.8(b). As in the single PMT case, the fibers are glued in the mask and then polished; the system is inserted in a 1 mm thick iron shielding tube. In order to reduce the cross-talk effect, for each plane the odd bars are readout by the first half of the MAPMT, while the even ones by the second half.

[4]Hamamatsu Photonics K.K.: *www.hamamatsu.com*

In the prototype phase several tests have been performed to arrive to the final design of the mechanics and the assembly fixtures of the PMTs [80, 82]:

- PMT model. Two PMTs have been used: the R7600-03-M64 is more sensitive to the UV wavelengths, while the R7600-00-M64 to the green region. In the EMR case, the difference in the quantum efficiency should be of the order of 20%. Laboratory tests have confirmed that the EMR plane efficiency with the second device is better;

- optical grease. In order to reduce the light dispersion in the contact between the fibers and the PMT glass, an optical grease has been adopted. Although the detection efficiency increases, the same happens to the cross-talk effect given the high density of channels. In the final setup the optical grease is not used;

- flex cable. For mechanical constraints the MAPMT signals are addressed to the frontend board by means of a flexible kapton cable (see section 2.3.1 for further details). Laboratory tests have demonstrated that such a device is not a source of electromagnetic noise, although further studies need to be performed at RAL with the RF cavities in place.

2.3 Electronics

The EMR electronics scheme is shown in figure 2.9; it is based on a Versa Module Eurocard (VME) system which hosts six 8 channel WaveForm Digitizers (CAEN WFD 1731[5]) to digitize the single PMTs signal, three configuration boards and eight readout ones for the MAPMTs. The MAPMT signals are processed by the FrontEnd Boards (FEBs) and are sampled, buffered in memory, and sent via a gigabit link by the Digitizer and Buffer Boards (DBBs) to a readout board; a configuration board (VCB) is foreseen to configure and send the trigger signal to a group of 16 FEBs in parallel (3 VCBs in total).

More in detail, and referring to the block diagram presented in figure 2.10, the overall EMR electronics can be divided as follows:

1. the MAPMT data acquisition (DAQ) software is developed on a PC which communicates with the VME bus via a PCI card (CAEN V2818). The software is developed within the MICE DAQ framework (DATE, designed for the ALICE[6] experiment [83]);

[5] CAEN Spa; *www.caen.it*

[6] ALICE (A Large Ion Collider Experiment) is one of the four experiments of the Large Hadron Collider (LHC, CERN).

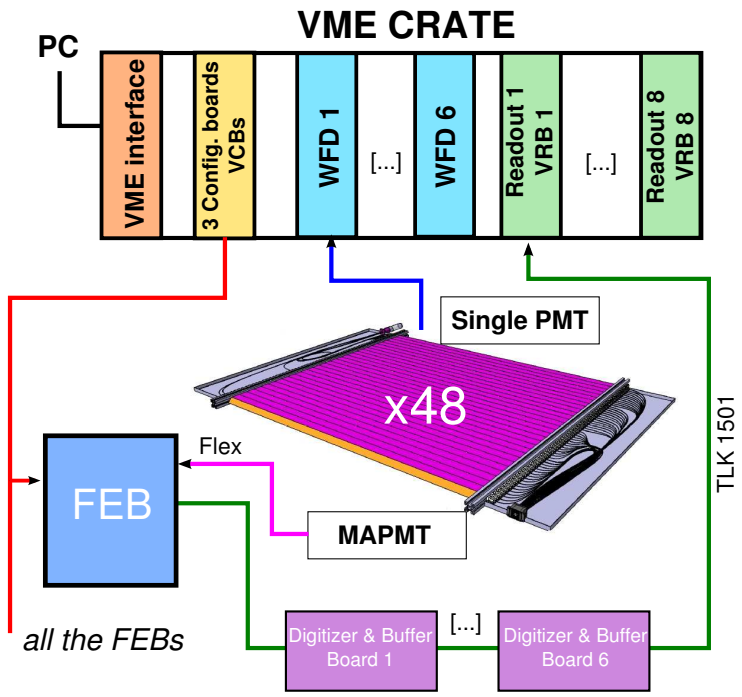

Figure 2.9: The EMR electronics scheme: the single-anode PMT signals are readout by 8 channel WFDs, while the MAPMT ones are processed by the FEBs and are sampled and sent to the VME system via a gigabit link by the DBBs. A configuration board is foreseen to configure and send the trigger signal to a group of 16 FEBs in parallel.

2. 3 VME Configuration Boards (VCBs) are inserted in a VME crate equipped with a VME/PCI interface (CAEN V2718) and they are used to configure three groups of 16 FEBs in parallel at the beginning of the run;

3. a VME Readout Board (VRB) is responsible of the data transmission with the DBB: since 6 DBBs are daisy-chained, 8 VRBs are used;

4. a Trigger Receiver board addresses the MICE triggers to the system: the "DAQ trigger", which arrives about 100 ms after the end of the spill and is responsible of the readout of all the MICE systems, and the "Particle trigger", which identifies the passage of a particle through the detectors in MICE. According to the MICE specifications (section 1.2.2), a maximum number of 500 particle triggers per spill are expected; typically muons generate 2 hits per layer, while electrons can generate more.

The other two fundamental elements of the EMR electronics are the FEB and the DBB, which will be extensively discussed in the next sections.

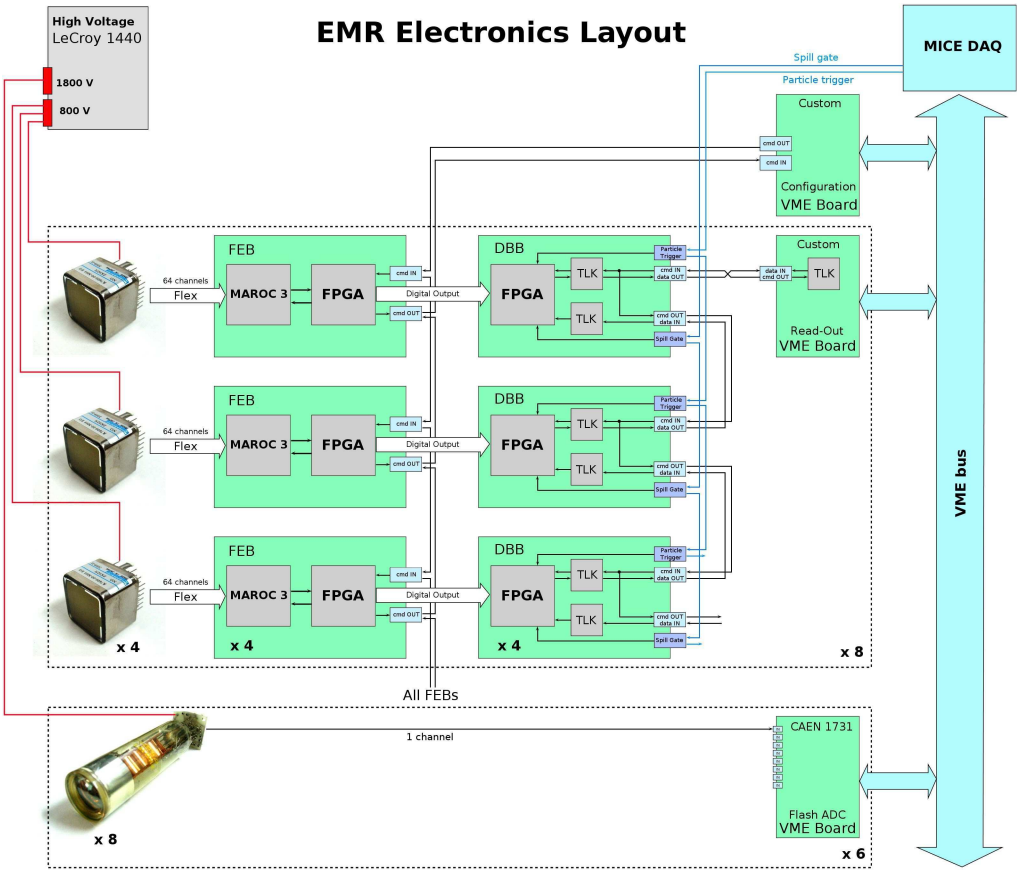

Figure 2.10: The block diagram of the overall EMR electronics [Courtesy of the UNIGE group].

The PC PCI card and the VME interface are connected through an optical link. The connection between the VRB and the first DBB of the chain is performed by 4 coaxial cables that have SMA (SubMiniature version A) connectors on the DBB side and LEMO[7] connectors on the VRB one. One pair of cables is used for the input (DATA IN) and one pair for the output (CMD OUT), since each pair forms a differential transmission line.

2.3.1 The FrontEnd Board

The FrontEnd Board (FEB) is being developed to process the MAPMT signals: the core is represented by the MAROC (Multi Anode ReadOut Chip) ASIC (Application Specific Integrated Circuit) [84], that is able to process 64 channels in

[7]LEMO S.A.; *www.lemo.com*.

parallel, and the control FPGA (Field Programmable Gate Array). The final FEB version has been developed starting from a prototype one used for all the preliminary tests (chapter 3); the block diagram of both versions is presented in figure 2.11.

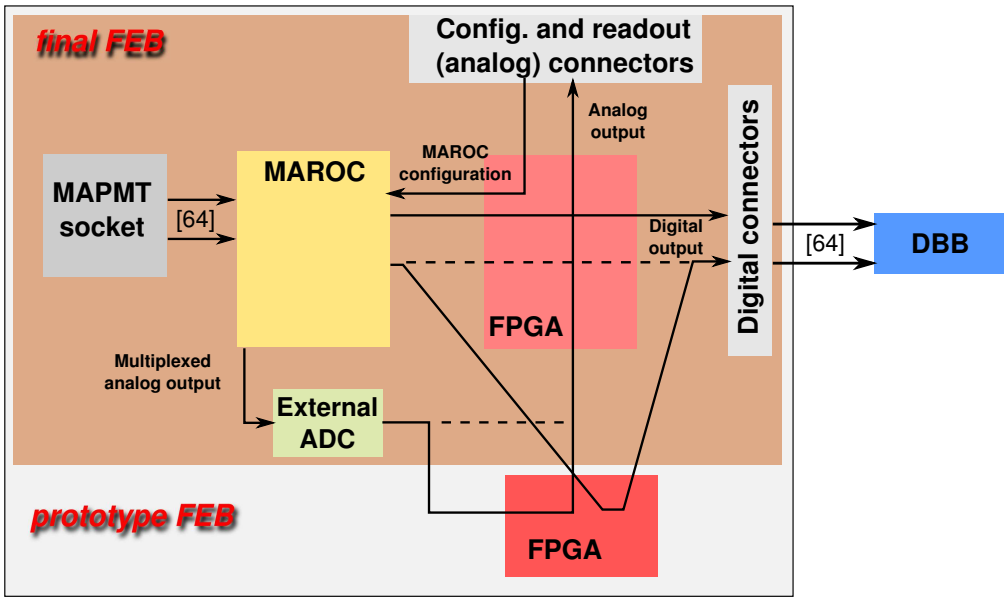

Figure 2.11: The FrontEnd Board schematic view: the MAPMT signals are managed by the MAROC ASIC; the analog output is digitized by an external ADC, while the digital ones are addressed to the DBB via the FPGA that is responsible of the configuration and readout. The brown region identifies the components of the final FEB.

The MAPMT is connected to the FEB through a socket: in the prototypes the PMTs are directly plugged in the boards, while in the final detector a 4 layer flexible kapton cable (figure 2.12(a)) is used because of geometrical constraints; in this case the high voltage is provided by an external cable.

The PMT outputs are processed in parallel by the MAROC ASIC, a chip designed in the AMS SiGe 0.35 μm technology. The choice of this ASIC was given by the first electronics requests of a pure digital provided by this commercial ASIC which had large advantages in terms of costs and knowhow.

Each MAROC channel (figure 2.12(b)) consists in a pre-amplifier with a variable gain, a tunable slow shaper and a sample & hold circuit for the analog readout, a tunable fast shaper and a discriminator for the digital one. The analog shaper provides a signal with a tunable peak value between 50 and 150 ns, while the digital ones of the order of a few tens of ns.

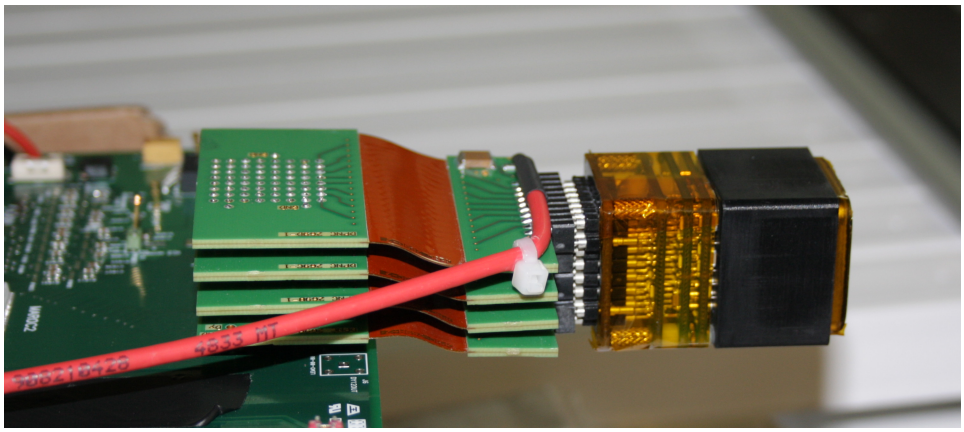

(a)

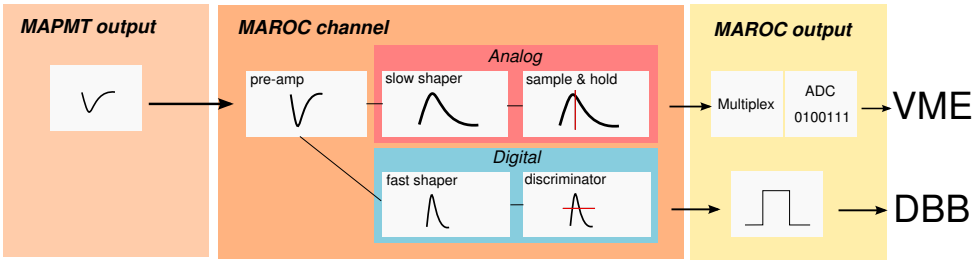

(b)

Figure 2.12: a) The flex cable connecting the MAPMT to the FEB. b) A schematic view of the MAROC ASIC channel: each MAPMT channel output is pre-amplified, shaped, sampled or discriminated, depending on the readout mode. The ASIC provides one multiplexed analog output and 64 parallel digital ones.

The ASIC (inserted in a plastic package) provides one multiplexed analog output which is digitized by an external analog-to-digital converter (ADC AD9220, Analog Devices[8]) and 64 parallel digital ones that are sent to the DBB. At the beginning of each run the ASIC has to be configured through the VCB: this operation consists in sending a string of bits to the MAROC in order to set all the parameters like the gain, the threshold, the shaper feedback capacitors. Further details are presented in appendix A, together with the performances of the ASIC with the prototype FEB. Among the tests, a special attention is devoted to the ones related to the Time over Threshold (ToT) architecture implemented in the ASIC, that ensures a correlation between the digital and the analog outputs since the digital output width is a function of the input amplitude.

A Field Programmable Gate Array (FPGA, Altera Cyclone II[9]) is used to con-

[8] Analog Devices Inc.; *www.analog.com*
[9] Altera Corporation; *www.altera.com*

figure the MAROC ASIC and to perform the readout sequence; the analog connectors are used for the configuration and the analog readout, while the MAROC digital outputs are addressed by the FPGA and the digital connectors to the DBB. Since the experimental duty cycle foresees one particle every 5 μs during a spill of 1 ms per second, the analog readout can be used in MICE only in the commissioning phase and for tests: in fact, the readout requires 12.8 μs (64 channels with a multiplexing clock of 5 MHz), which does not comply with the duty cycle. Thus the final readout will be based on the digital mode. The possibility to store some analog data in the FPGA and transmit them during the interspill period to the VCB is being studied.

The major changes in the FEB final version (figure 2.13(a)) with respect to the prototype one (figure 2.13(b)) are the following:

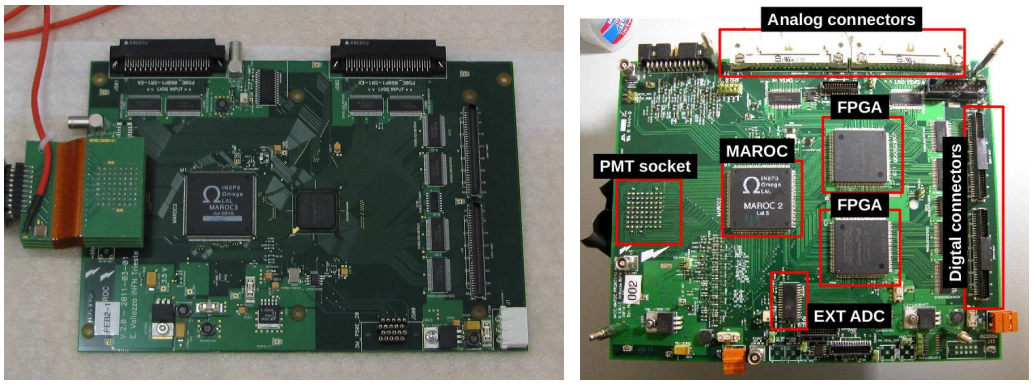

(a) (b)

Figure 2.13: A photo of the a) final and b) prototype versions of the FrontEnd Board.

- it supports just the version 3 of the MAROC ASIC. Version 3 has minor improvements with respect to version 2: the most important one is the presence of an embedded 12 bit ADC to digitize the analog output, that anyway is not used in EMR. The prototype FEB can host both versions 2 and 3;

- it has a single FPGA (in light red in figure 2.11), that is the Ball Grid Array (BGA) version of the Altera Cyclone II, while the prototype board hosts two Plastic Quad Flat Pack (PQFP) FPGAs. One PQFP FPGA has not enough connections to perform all the FEB tasks; thus in the prototype FEB another FPGA is housed (in dark red in figure 2.11) to address part of the 64 channels to the digital connectors and the analog data from the ADC to the control FPGA;

- the analog and power connectors are high-density and TE CONNECTIVITY / AMP connectors respectively to optimize the component area;

- a lot of connectors and test points have been removed.

2.3.2 The Digitizer and Buffer Board

The main tasks of the Digitizer and Buffer Board (DBB) are to sample the 64 channels coming from the FrontEnd Board and to transmit the event data upon receiving the DAQ trigger. The DBB is presented in figure 2.14(a): it is organized around a single FPGA (Altera Stratix II) that performs the data sampling, buffering and data-flow control functions of the board. The sampling rate is 400 MHz (2.5 ns of resolution); the data are stored in the internal memory (First In First Out - FIFO) together with the timestamp of the leading and trailing edges of the FEB digital signals and other information and sent to the VRB by means of two gigabit trans-receivers (TLK 1501, Texas Instruments[10]). Considering the maximum duration of the experimental spill (that is 1 ms but it can extended up to 10 ms) and the clock rate (400 MHz), the timestamp corresponding to a hit can always be stored in a 22 bit word.

Each DBB is configured by a dual-in package (DIP) switch to have a unique board ID in the system. In the final configuration, six DBBs are grouped together and daisy-chained with Cat 5 (Category 5) cables equipped with RJ 45 connectors: a DBB in the middle of the chain receives the DATA IN signal from the upstream DBB and transmits the DATA OUT signal to the downstream one; at the same time it receives CMD IN signals from the downstream DBB and transmits CMD OUT signals to the upstream DBB.

The DBB works like a TDC in the following way:

- a DBB continuously receives the 64 discriminated outputs from the FEB and the particle and spill gate signals from the MICE DAQ system;

- it counts the clock edges between the beginning of the spill gate and the leading edge of the hit signal from the FEB; in the same way, the trailing edge is considered;

- the data are stored in a local memory together with other information (e.g. timestamp and number of particle triggers) until the end of the spill, when they are sent to the VRB. The number of particle triggers in a spill gate is compared with the one sent by the general DAQ system in order to verify the DBB (EMR) readout.

[10] Texas Instruments Inc.; *www.ti.com*

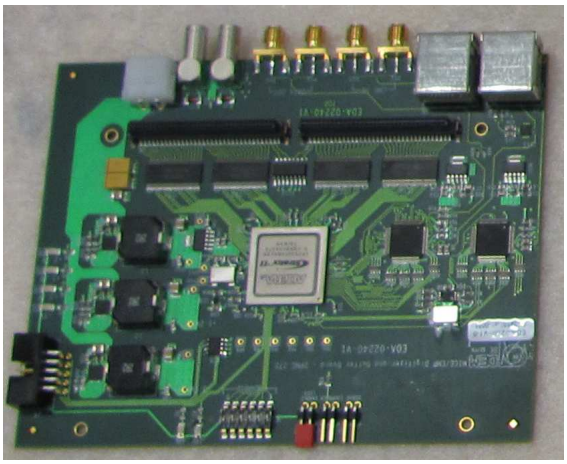

(a)

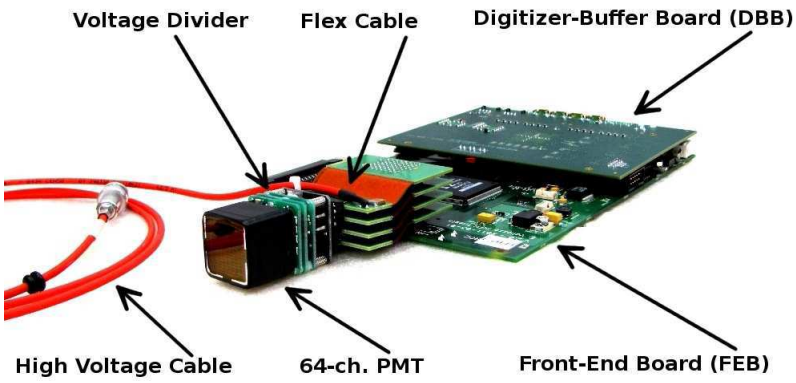

(b)

Figure 2.14: a) A photo of the DBB. b) The MAPMT electronics: the FEB and the DBB are plugged together; the flex cable is connected to the FEB via the socket [Courtesy of the UNIGE group].

Figure 2.14(b) presents the final MAPMT electronics: the DBB is plugged on the FEB with a couple of 68 pin Erni connectors; the MAPMT signals are sent to the FEB through the flexible kapton cable.

2.4 The prototypes

In 2007 the SandWich detector (section 2.1) based on scintillating layers of different thickness was proposed, studied and optimized (with a GEANT4 simulation). The design optimization in the desired momentum range, the cost reduction and the manufacturing procedure made the project evolve to EMR, a detector able to

combine the advantages of a calorimeter with the capabilities of a tracker.

Both the tracking and calorimetric features are required to apply the algorithm developed by MICE to distinguish muons from electrons. Focusing only on EMR and not considering the kinematic cuts provided by the TOF system, the algorithm is based on two observables:

1. **the ratio between the energy of the layer with the largest value and the energy of the first layer**. Muons lose energy with a Bragg-peak behavior generating a ratio characterized by the presence of a peak with a mean value larger than the one generated by the electrons which release their energy continuously in the detector;

2. **tracking**: the KL pre-shower generates a shower in presence of an electron, while a single track is visible in EMR in the case of a muon.

EMR has been optimized with the studies performed with two prototypes: the small scale prototype has been assembled to measure the tracking performance; the Large EMR Prototype (LEP) is devoted to the muon/electron discrimination exploiting the calorimeter capabilities. Both the prototypes consist in planes of bars with a rectangular shape whose scintillating light is carried out on both sides by WLS fibers and readout by MAPMTs.

The small prototype performance with a particle beam at CERN has led to the design of the final EMR: a triangular shape has been chosen for the bars in order to reduce the dead region between two contiguous bars; the light is carried out by a single 1.2 mm diameter WLS fiber (instead of 4 0.8 mm ones) inserted and glued in the bar, that guarantees to reduce the cross-talk effect maintaining the light yield; the MAROC readout ASIC has been preferred to a couple of ASICs (VA64TAP2.1 + LS64, Gamma Medica - IDEAS[11]) because of its being more performing, of its having both the analog and digital features in a single chip and, last but not least, of its being less expensive [80].

In the next sections, a description of the main features of both the prototypes is given. The results obtained in the final prototype phase are presented in chapter 3.

2.4.1 The small scale prototype

The small scale prototype has been assembled at the end of 2006 to become the test bench of different electronics chains. In practice it is responsible of the major changes between the original and the final EMR design (bar shape, number and diameter of the WLS fibers) [9, 80]. The prototype has been assembled to study the tracking performance of the detector. It consists in 8 planes of plastic

[11] Gamma Medica - IDEAS; *http://www.gm-ideas.com/*

scintillator bars arranged in two blocks and in a x-y geometry (figure 2.15); each plane has ten 19.1 cm long extruded scintillating bars with a rectangular shape (1.9×1.5 cm^2). The scintillator light is carried out by 4 0.8 mm WLS fibers to two

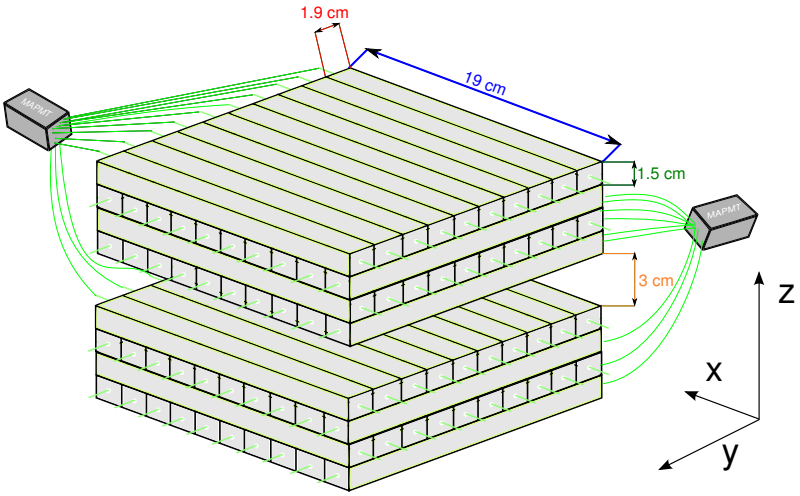

(a)

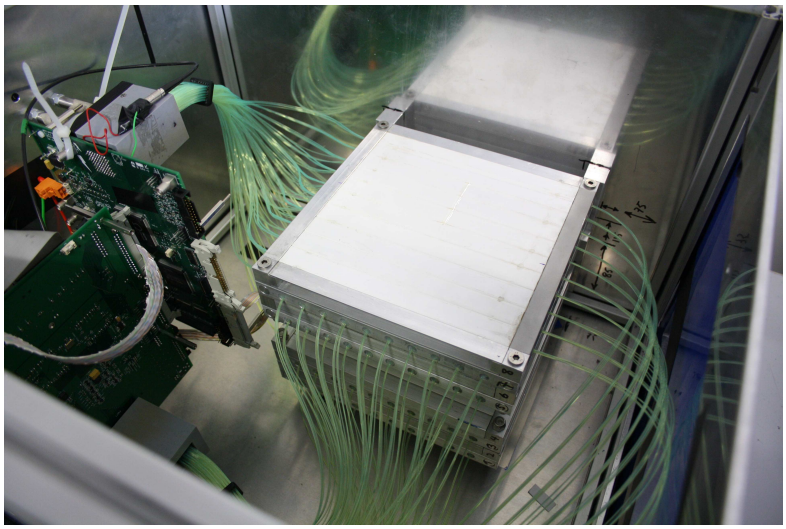

(b)

Figure 2.15: a) A drawing and b) a photo of the EMR prototype. The z direction is along the particle motion, while x and y are the transversal ones.

MAPMTs: the 4 Y planes are readout by MAPMT 1, while the X direction by MAPMT 2. Figure 2.16 shows the MAPMT pads and the corresponding readout bars: given this map, the light of one channel can be readout by another because of the cross-talk effect among the pads themselves.

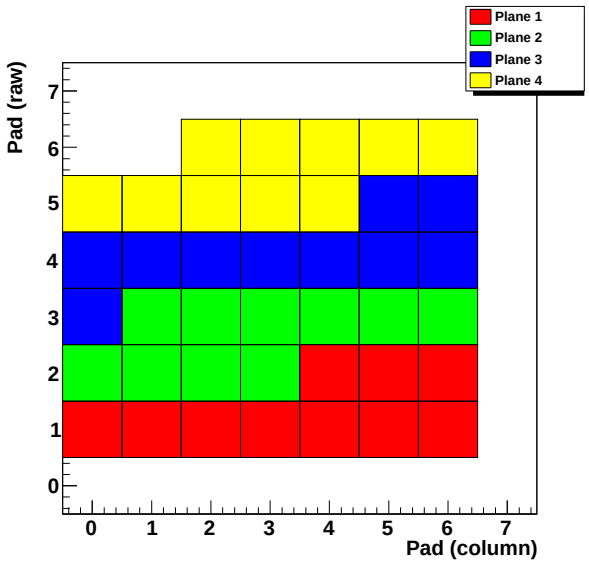

Figure 2.16: The MAPMT pads: each MAPMT reads 40 bars arranged in 4 planes.

The presence of cross-talk could cause a non correct identification of the hit position: the phenomenon is one of the main problems in tracking systems read-out by MAPMTs because of the misalignment of the fiber-PMT coupling mask. The cross-talk has been studied with the prototype (see section 3.2.5) where no optimization of the mechanics was possible; starting from these studies a new fiber-PMT coupling system has been implemented in EMR. In fact, in the final design the alignment is mechanically tuned moving the PMT; moreover the odd bars are readout by the first half of the MAPMT, while the even ones by the second half. This should allow to identify and reduce the cross-talk in the commissioning phase.

2.4.2 The Large EMR Prototype detector

The calorimeter capability of EMR has been studied with a second prototype called Large EMR Prototype. To be more precise, the aim of LEP is twofold:

- to exploit its calorimeter capability to discriminate muons and electrons in a high momentum (1 GeV/c) negative mixed beam and to compare the experimental data with the ones produced by a Monte Carlo simulation;

- to study the same quantities with a Silicon PhotoMultiplier (SiPM) readout system.

LEP (figure 2.17) consists in 48 planes of scintillating bars; each plane is made of 4 rectangular bars (the ones used for the small scale prototype). The whole detector measures about 2 X_0, which roughly corresponds to the EMR extension. The scintillator light is brought out by two 0.8 mm WLS fibers (glued in the bar) and readout on both sides: on one side by three 64 channel MAPMTs (one every 16 layers), while on the other by 192 2.8 mm diameter SiPMs. The test with the

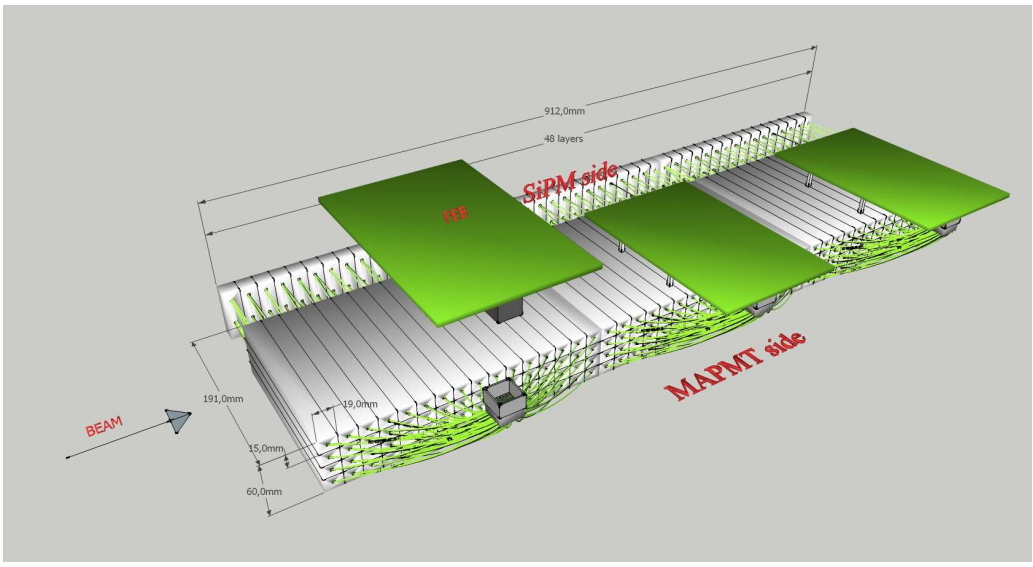

Figure 2.17: A sketch of LEP: the detector consists in 48 layers of scintillating bars; each layer is made of 4 19.1 cm long bars. The light is brought out by two WLS fibers to a channel of a MAPMT on one side and to one SiPM on the other. In the prototype the FEBs are placed in the vertical direction instead of the horizontal one, as presented in this sketch.

SiPMs is the first step towards the Totally Active Scintillator Detector (TASD, an example can be found in [85]), a new detector proposed for neutrino studies and based on very long scintillating bars (up to 15 m).

A few photos of LEP are presented in figure 2.18: the WLS fibers are coupled to a plastic mask connected to a holder which hosts the MAPMT. For mechanical constraints the detector is divided in three blocks of 16 layers each; among the blocks a 1 cm air gap is present.

(a)

(b)

Figure 2.18: A few photos of LEP: in a) the MAPMT glasses are clearly visible in the MAPMT holders; b) the FEBs are placed vertically instead of the original horizontal position foreseen in figure 2.17. On the opposite side the SiPM readout boards are placed.

Chapter 3

The prototype phase

The EMR prototype phase started in 2006 and it has required the assembly of two devices: the first, the small scale prototype, to study the EMR tracking capability; the second, LEP, with the same number of radiation lengths of EMR, to be used as a calorimeter.

The small scale prototype is based on the first EMR design, for a total of 8 planes of rectangular bars whose scintillating light is carried out by 4 0.8 mm diameter WLS fibers; its frontend electronics is based on a couple of ASICs (VA64TAP2+LS64) [9]. Since the prototype was assembled to evaluate the tracking capability of EMR, the spatial resolution and the efficiency have been measured in a test with an external beam at CERN. The results led to the final EMR design, in which the bar shape and the number and diameter of the WLS fibers changed [80]. This thesis work considers the last part of the prototype phase that is the tests of the prototype with the final EMR electronics both in the analog and digital readout modes. The final electronics is based on the MAROC ASIC which combines in a single chip both the functionalities of the VA64TAP+LS64 pair (that is the analog and digital working modes), is less expensive and has shown a great stability.

The second part of the chapter is devoted to the second prototype, LEP (Large EMR Prototype), developed to study the calorimeter features with an external beam at CERN. The main goal was to study the discrimination of muons and electrons in a high momentum (1 GeV/c) negative mixed beam; the experimental data have been compared with the ones generated by a Monte Carlo simulation and some predictions at lower momenta are also presented.

In the first part of the chapter the general setup of the small scale prototype and LEP tests is presented: the tests have been performed either with cosmic rays or particle beams and the driving idea was to track (with high spatial resolution silicon detectors) each single particle and measure the prototype response.

3.1 Test setup: design and detectors

The two prototypes tests have been performed either with cosmic rays or with a particle beam at CERN. Although the test main goals are different, the basic elements of the setup are the same (figure 3.1): each particle is tracked by a couple of high resolution silicon detectors and the trigger is provided by plastic scintillators. The silicon detectors and plastic scintillators are described in the following, while

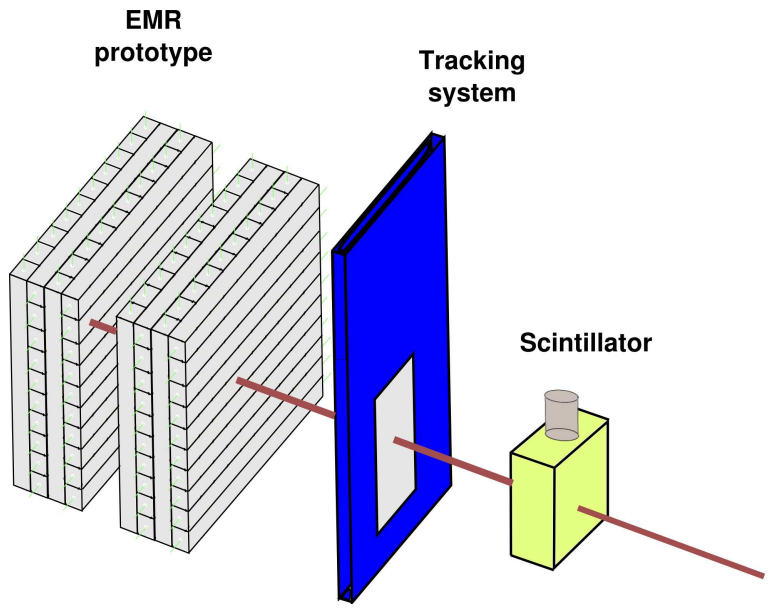

Figure 3.1: The basic elements of the prototypes test setup: each particle (either a cosmic ray or a particle beam) is tracked by a couple of high resolution silicon detectors; the trigger is generated by plastic scintillators.

the DAQ features and the setup modifications in each of the prototype sections.

3.1.1 The Silicon Beam Chambers

The tracking system is based on a pair of large area silicon detectors: the AGILE beam chambers (BC) have been built for the test phase of the AGILE[1] satellite [86, 87]. Each chamber is made of two single side silicon tiles of $9.5 \times 9.5\ \mathrm{cm}^2$ and 410 μm thickness arranged in a x-y scheme. The physical pitch is 121 μm, while the readout one is 242 μm: thus a one floating strip readout scheme is adopted to obtain a spatial resolution better than 30 μm [88]. Each tile is readout by three

[1]The Astro-rivelatore Gamma a Immagini LEggero (AGILE) satellite is an ASI (Italian Space Agency) project.

128 channel self-triggering ASICs (TA1, Gamma Medica-IDEAS, figure 3.2(a)); the readout is a multiplexed one with a maximum clock frequency of 10 MHz.

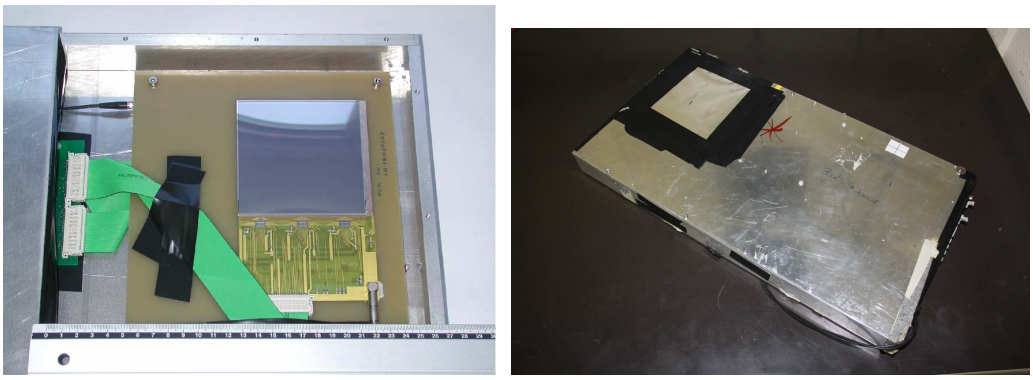

(a) (b)

Figure 3.2: The AGILE silicon beam chamber: a) each silicon tile is readout by three self-triggering TA1 ASICs; b) one of the chambers (which consists of two modules arranged in a x-y geometry) in its aluminum box.

An aluminum box (figure 3.2(b)) hosts two modules and part of the frontend electronics consisting of a printed-circuit board (PCB) for the ASICs and a repeater board to distribute the ASIC bias voltage and the silicon one (typically 54 V), to transform the digital inputs from standard RS422 to single ended and to amplify the multiplexed analog output with a NE592.

The readout electronics and DAQ systems for the BCs are different in the two tests, so they are described in detail in the dedicated sections.

3.1.2 The plastic scintillators

The DAQ trigger is provided by a pair of plastic scintillators. Different types have been used:

1. a 10×10 cm^2 1 cm thick polystyrene tile (figure 3.3(a)) whose light is readout by a photomultiplier tube directly connected to the scintillator;

2. a tile of $20\times30\times1$ cm^3 NE120 (Nuclear Enterprises) scintillator readout by a P30CW5 photomultiplier (Electron Tubes[2]) directly coupled to the scintillator. The module (figure 3.3(b)) is hosted in a PVC box;

3. a $10\times20\times1$ cm^3 tile made of polystyrene (figure 3.3(c)) readout by a 931B photomultiplier tube (by Hamamatsu).

[2]Now Sens-Tech Ltd.; *www.senstech.com*

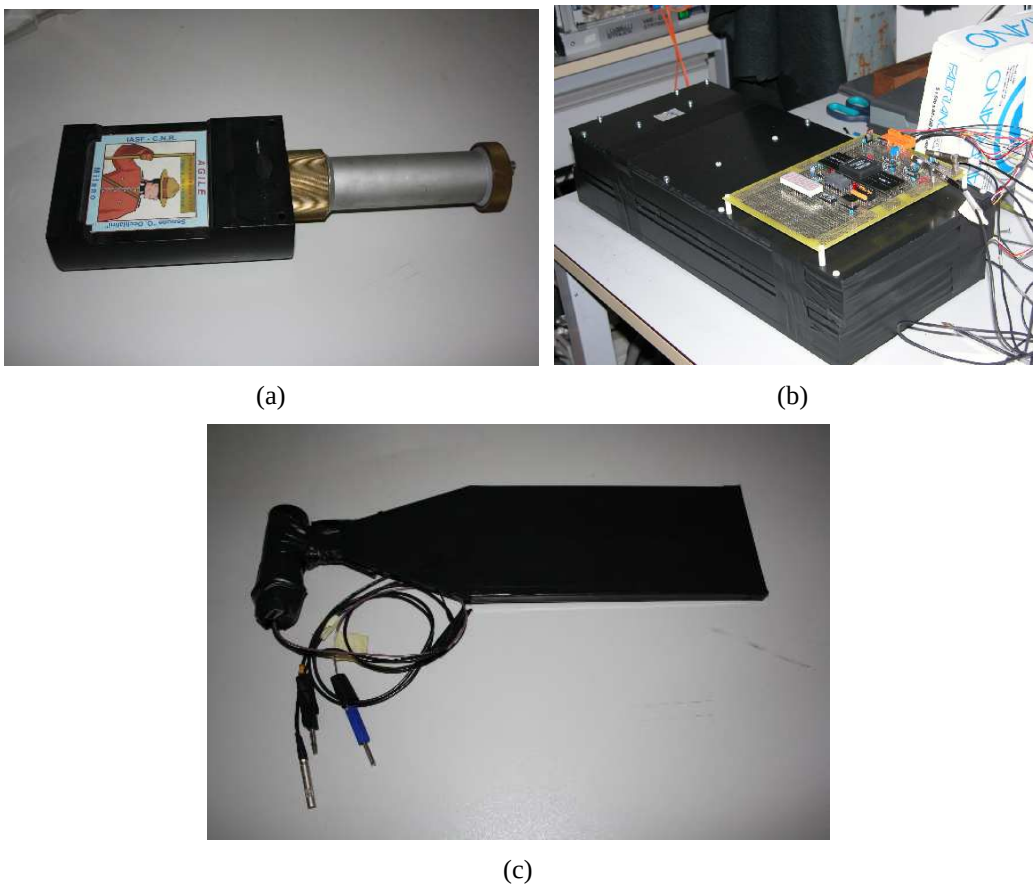

(a) (b)

(c)

Figure 3.3: The trigger scintillators with a dimension of a) $10\times10\times1$ cm^3, b) $20\times30\times1$ cm^3 and c) $10\times20\times1$ cm^3.

3.2 The small scale prototype

The EMR tracking capability has been studied with the small scale prototype, assembled on the basis of the original EMR design. The device, presented in section 2.4.1, consists of 8 planes of rectangular bars arranged in a x-y geometry. The scintillator light is readout by two MAPMTs whose frontend electronics is based on the MAROC ASIC.

This section deals with the tests of this electronics focusing on the tracking purpose: the spatial resolution and the efficiency have been evaluated with cosmic rays using both the analog and digital readout modes [89]. In MICE only the digital readout can be used because of the experimental duty cycle. The results obtained with the digital mode are compared with the analog ones considered as a benchmark. Moreover the problem of the cross-talk effect is also approached.

3.2.1 Setup and DAQ

The spatial resolution and the efficiency of the small scale prototype planes have been measured by means of cosmic rays. The setup (figure 3.4) consists of a couple of 20×30 cm^2 plastic scintillators used in coincidence for the trigger generation, a couple of silicon beam chambers for the particle tracking and the EMR prototype.

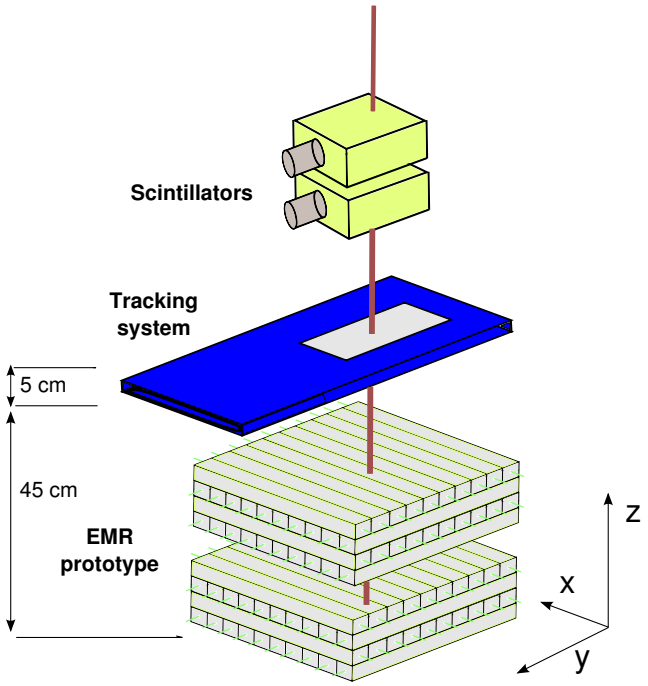

Figure 3.4: The setup for the cosmic ray tests.

The scheme of the readout electronics is presented in figure 3.5 and it is based on a VME system consisting of the following items:

- a SBS[3] Bit3 620 board optically connected to a PC;
- a MAROC control board (a VME I/O custom board and a piggy-back one called daughter) to configure and readout the analog signals of the FEBs and of the so-called ADC boards (one per BC);
- two shift register boards to readout the MAROC digital outputs.

The ADC board is based on an Altera Cyclone II FPGA: it receives the trigger signal from the MAROC control board and starts the readout sending dedicated

[3]SBS Technologies, Inc., *http://www.sbs.com*

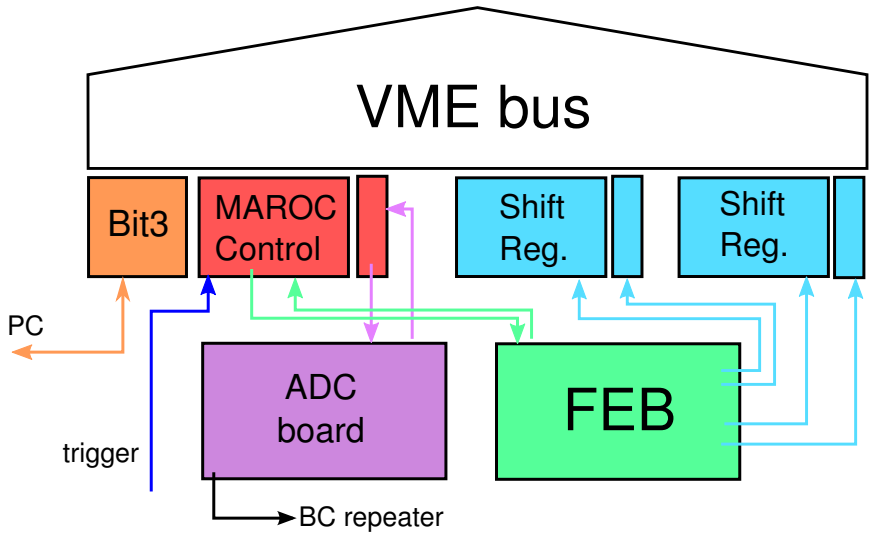

Figure 3.5: The scheme of the readout electronics: the VME system is optically connected to a PC through a SBS Bit3 620 system. A MAROC control board is used to configure and readout the analog outputs of the MAPMTs and BCs. The shift register boards are needed for the digital readout.

signals to the BC repeaters (one per module); the corresponding analog output is digitized by an external ADC (AD9220), stored in the FPGA internal memory and then sent back to the VME system. As far as the shift register boards are concerned, a full description is given in section 3.2.3.

The DAQ software is written in C with Tcl/Tk[4] for the user graphical interface; it allows to configure the ASIC and perform the readout. The output data are written as PAW[5] ntuples which are processed to obtain an ASCII file with all the relevant information.

The test procedure is organized in three different phases:

1. configuration: a string of bits is loaded in the MAROC ASIC to set all the parameters (see appendix A for further details);

2. pedestal run: a run with 200 events generated by a random trigger is acquired to measure the electronics baseline and noise;

3. cosmic run: in this case the trigger is provided by the scintillators.

The analysis of the prototype performances with the prototype FEBs hosting the MAROC2 ASIC in the analog and digital working modes is presented in the

[4]Tcl (Tool command language) is a dynamic programming language and Tk is its graphical user interface toolkit; *http://www.tcl.tk/*

[5]Physics Analysis Workstation, *http://paw.web.cern.ch/paw/*

following sections. To simplify the analysis, only single particle events have been considered, that is only the events with a single hit in all the BC planes have been taken into account. As far as the ASIC is concerned, there are no differences between the two MAROC versions in terms of performance, but only from the operational point of view[6].

3.2.2 The analog readout

The analog readout provides typically more information with respect to the digital readout mode but there are cases in which it cannot be used. In MICE, for example, it can be exploited only in the commissioning phase because it requires a readout time of 12.8 μs (64 channels with a multiplexing clock of 5 MHz), which is incompatible with the experimental duty cycle foreseeing an event every 5 μs within a spill of 1 ms per second. However in the prototype tests the analog results have been used as a benchmark for the digital ones: the spatial resolution and the efficiency of the prototype planes have been computed with both the readout modes and the comparison is presented in section 3.2.4.

In order to study the analog readout mode, the pulse height distribution of the bar with the maximum signal for each event has been considered to evaluate the signal to noise ratio of the system. Given that the bars of the 4 Y planes are readout by MAPMT 1 and the X ones by MAPMT 2, the bar with the maximum has been considered for each plane type. The distributions for one Y and one X planes are shown in figure 3.6: if not otherwise indicated, from now on just a single plane per MAPMT is considered given the performances of all the planes are equivalent.

An event has been considered good (that is corresponding to a particle) if the pulse height is larger than 110 ADC counts (blue lines). In a similar way it is possible to compute directly the signal to noise ratio (pull): the pull distributions are shown in figure 3.7. The pull has been computed considering the noise as the pedestal RMS.

3.2.2.1 Spatial resolution

The particle hit position on each plane has been reconstructed considering the bar cluster that consists of a group of contiguous bars which have a signal larger than the analog threshold (110 ADC units). The hit position is obtained with the charge centroid method. The distribution of the number of clusters per plane (considering one X and one Y plane) is shown in figure 3.8.

[6]MAROC2 has been used for the small scale prototype, while the version 3 for LEP and for the final modules (chapter 5): the performances are very similar. The differences consist in the ASIC settings (in MAROC2, for example, the pre-buffer capacitance cannot be set).

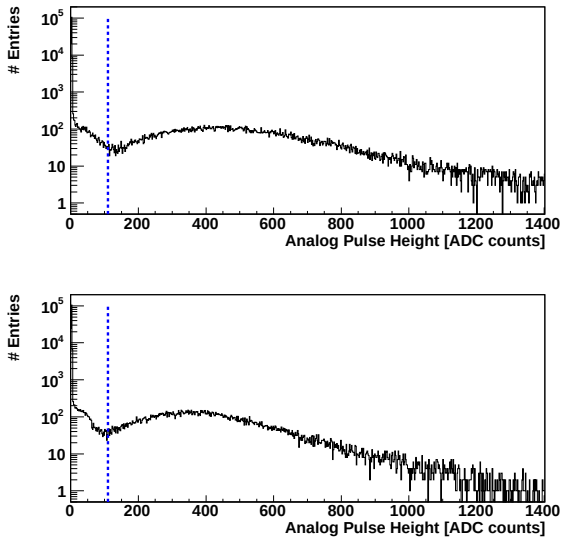

Figure 3.6: The analog pulse height of one Y (MAPMT 1, top) and one X (MAPMT 2, bottom) plane. The blue lines indicate the so called analog threshold (110 ADC).

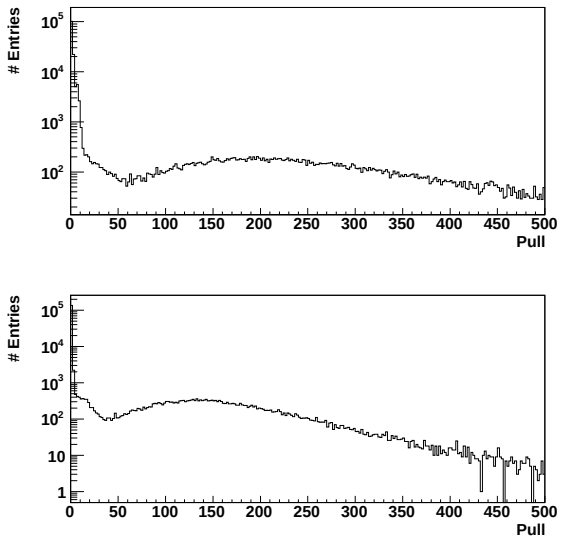

Figure 3.7: The pull distribution of one Y (top) and one X (bottom) plane.

Since in the analysis just the single particle events have been taken into account, a number of clusters larger than one per plane can be explained in two ways:

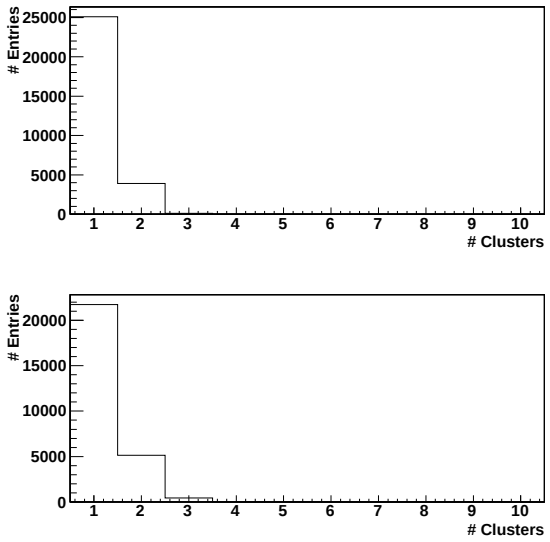

Figure 3.8: The number of clusters per plane for the Y (top) and X (bottom) directions.

1. a different particle which hits the prototype (but not the trigger and the tracking system) at the same time of the trigger one (lower probability, given the Poissonian arrival time distribution[7]);

2. cross-talk: the scintillator light is spread on several MAPMT pads and can cause a wrong position reconstruction (the evidence of the cross-talk effect will be shown later in detail).

The number of bars per cluster is presented in figure 3.9: as before, the data are collected considering the direction. Given the rectangular shape, the expected number of bars per cluster is 1: a larger number can be due to the particles which hit the prototype with a large impact angle and (most probably) to the cross-talk effect.

The prototype spatial resolution has been computed using the residual method and the silicon tracking system. The residual method consists in measuring the difference between the position detected by EMR and the one reconstructed by the silicon chambers. The distributions for all the planes are presented in figure 3.10 and have been fitted with a Gaussian function: the “Sigma” parameters indicate the spatial resolutions, which are of the order of 7-8 mm. Since the silicon spatial

[7]Considering a muon flux of about 100 m^{-2} s^{-1} sr^{-1} [53], the probability of two events is of the order of 10^{-10}. A larger probability occurs considering a shower caused by the enviromental material.

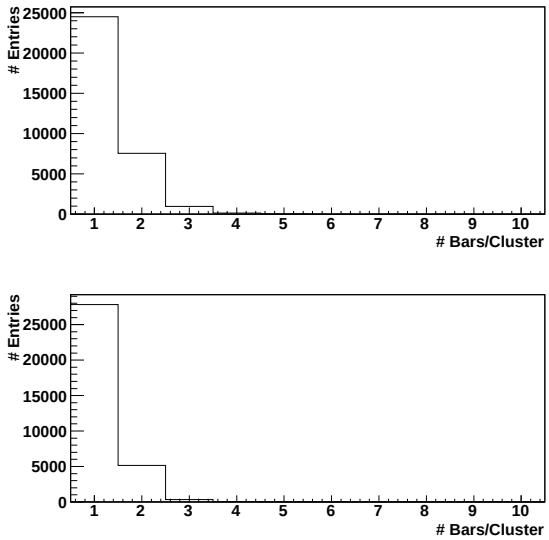

Figure 3.9: The number of bars per cluster for one Y (top) and one X (bottom) plane.

resolution is of the order of 30 μm, and taking into account the distances presented in figure 3.4, the expected error on the extrapolated position on the last plane should be of the order of a few hundreds of μm: thus its contribution to the spatial resolution is negligible.

A residual uncertainty is also given by the distance between the BCs and the prototype planes. A precise value can be extrapolated via the residual minimization method which consists in the following procedure:

- the residual of each plane is evaluated varying the BC-prototype distance;
- the sigma value obtained from the Gaussian fit of the residual is plotted as a function of the distance as presented in figure 3.11(a);
- in order to identify the distance where the residual value is minimum, a power-of-2 law is used to fit the new distribution: $-\frac{\mathrm{p1}}{2 \cdot \mathrm{p2}}$ provides the required distance.

To make an example, the distance between the second BC and the first prototype plane (Y4) has been measured to be 30.4 cm, while the one with the last plane 44.7 cm. The residual distributions presented in figure 3.10 are the ones obtained with the distances computed with this method.

A proof of the cross-talk effect is given by the residual distributions considering all the clusters: these plots (an example is presented in figure 3.11(b)) show

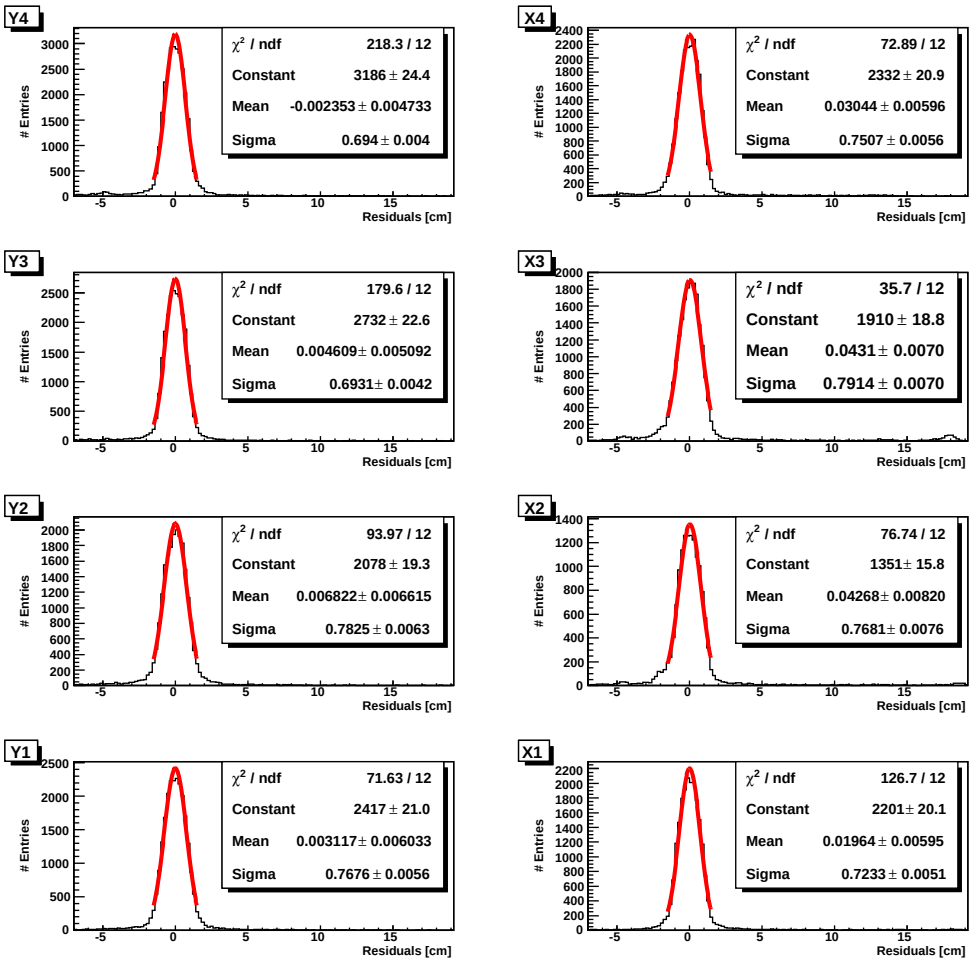

Figure 3.10: The residual distribution for all the planes, from top to bottom as they are positioned in the prototype (Y4 is the first module, X1 the last one): the spatial resolutions (Sigma parameter) are of the order of 7-8 mm.

small peaks due to the light spreading among the MAPMT pads. The lateral peaks with respect to the one on 0 are due to "false" clusters generated by the cross-talk; the smaller the peaks, the better the MAPMT-fiber alignment. The last plot can be understood taking into account the MAPMT-pad mask presented in figure 3.12.

If one assumes for geometrical considerations that a particle hits perpendicularly the last bar of each plane (for plane 4 the pad in column 2, raw 6; for plane 3: column 5, raw 5), because of the cross-talk effect, a fake signal could be registered in the pad in column 5 and raw 6, three pads ($\sim$5 cm) far from the original position: this corresponds to the "negative" peak in figure 3.11(b). Viceversa, if a particle hits the bar in column 2, raw 5, this can cause a fake signal in the pad in

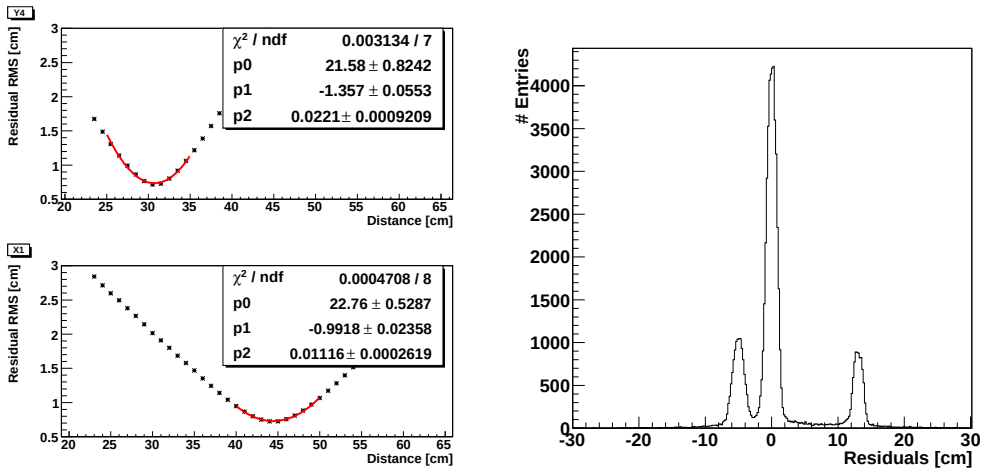

(a) (b)

Figure 3.11: a) The residual RMS for the first (Y4) and last (X1) prototype planes varying the distance between the second BC and the planes themselves in the analysis. b) The residual distribution for one plane considering all the clusters: the small lateral peaks are due to the cross-talk effect.

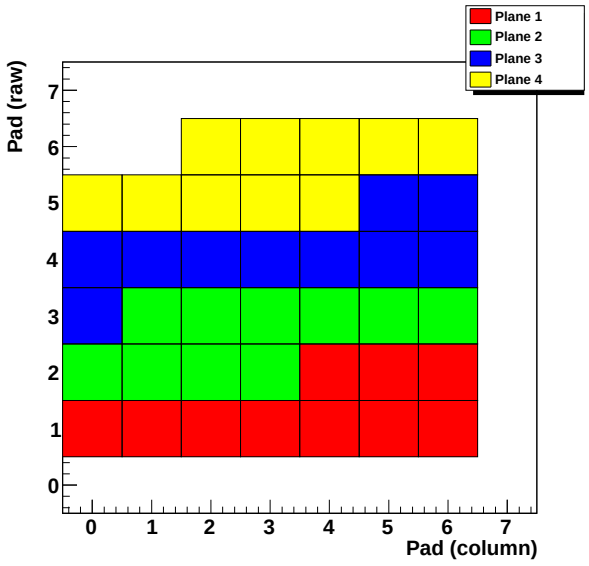

Figure 3.12: The MAPMT-pad mask (already presented in figure 2.16.

column 2, raw 6, seven pads (∼13 cm) far from the good position: in this case the event is registered in the positive peak. This explanation corresponds to a shift in a given direction of the MAPMT with respect to the fiber mask: in this case the

fibers are higher with respect to the MAPMT.

A quantitative study of the cross-talk effect is presented in section 3.2.5.

3.2.2.2 Detection efficiency

The detection efficiency (ϵ) has been defined as:

$$\epsilon = \frac{\text{good events}}{\text{target events}} \tag{3.1}$$

where the "target events" are the particles which have crossed the detector, while the "good events" are the ones measured by each single plane. The error on the efficiencies is evaluated as:

$$\sigma_\epsilon = \sqrt{\frac{\epsilon(1-\epsilon)}{N_2}} \tag{3.2}$$

where $N_2 =$ "target events".

The target events have been identified in this way:

- the track reconstructed by the BCs has been projected on the EMR planes;
- if the first (Y4) and the last (X1) planes have at least one cluster within 3σ from the projected position, the event is accepted.

In the same way, a good event is tagged as good in any other plane if at least one of the clusters is within 3σ from the reconstructed position.

The target events have been defined in this way in order not to underestimate the efficiency: given the BCs geometrical position with respect to EMR, if only the chambers were used to define the target events, this number would include also the particles which decay in the prototype, thus causing a biased value of the efficiency.

Figure 3.13 shows the efficiency as a function of the hit position in each plane: given the particular event selection, the first and last planes are fully efficient; the other planes have an efficiency with an average value of (98.35$\pm$0.37)%.

3.2.3 The digital readout

The digital readout plays a key role in EMR. As already stated in section 2.3, it is performed in two different phases:

1. the MAROC ASIC provides 64 parallel trigger outputs, that are sent by the FPGA and through the digital connectors to the DBB;

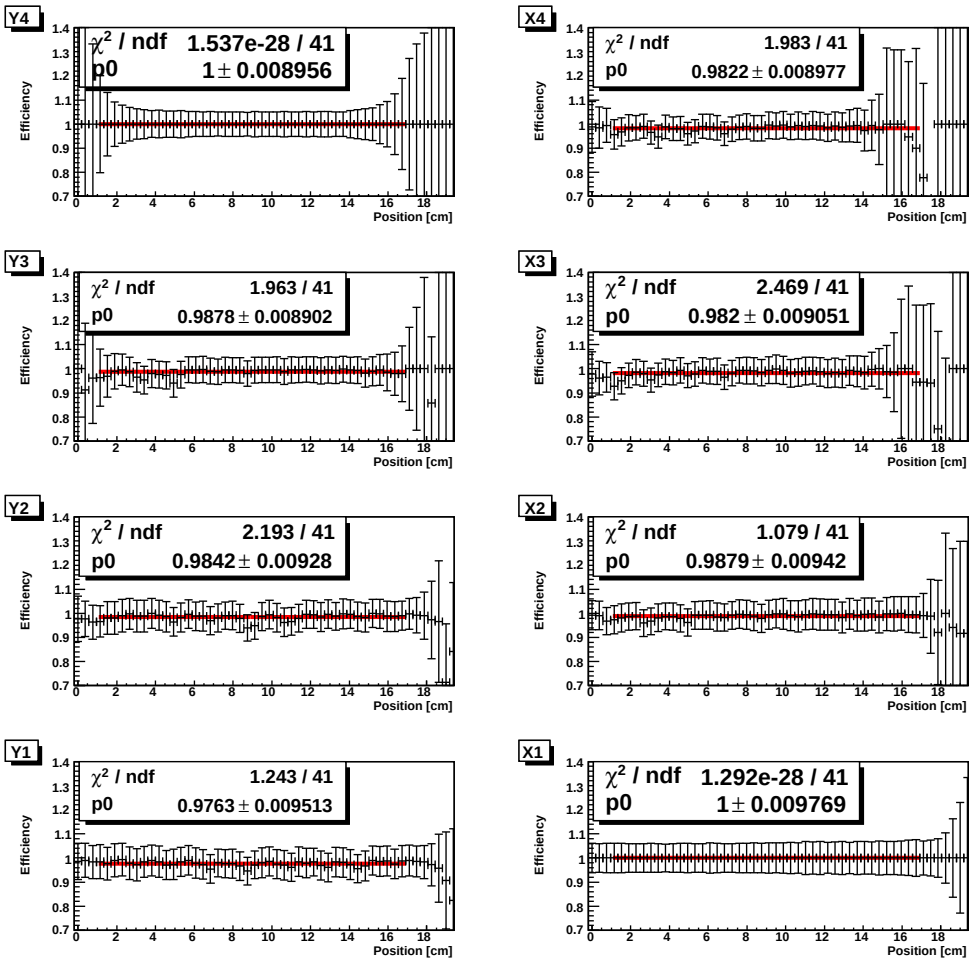

Figure 3.13: The efficiency as a function of the hit position has been evaluated considering all the events with a hit (=cluster) in the first (Y4) and the last (X1) modules. The large errors correspond to the edges of the sensitive area where the statistics is very small.

2. the DBB samples and stores the trigger outputs and sends the digital data to the VRBs with a TLK 1501 gigabit link.

The DBB task is represented in a schematic way in figure 3.14(a): a control FPGA on the board samples the trigger signals in a given time range (the spill gate) with a sampling clock of 400 MHz and provides the leading and trailing edge times with respect to the beginning of the spill gate. A simplified version of the DBB has been implemented for the tests (figure 3.14(b)). It consists of 2 boards, the shift registers. Each board consists of one I/O and one daughter board and reads the digital data of a single FEB (in practice 16 channels per board). In this

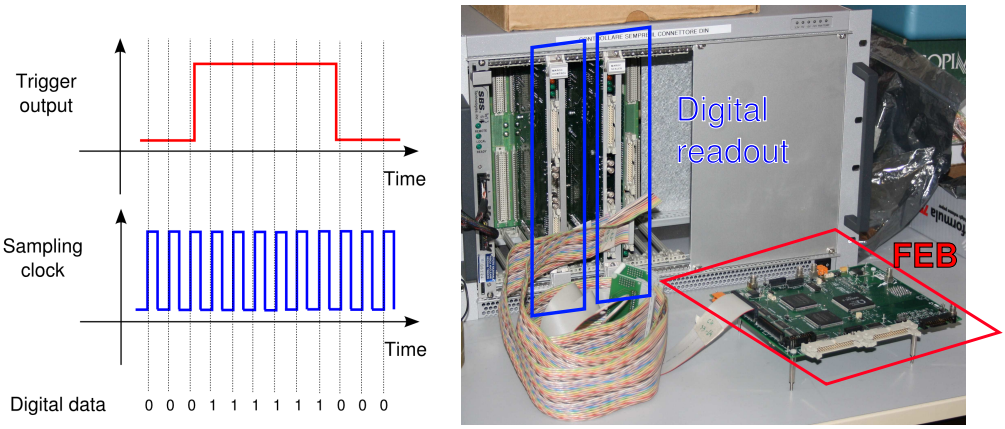

(a) (b)

Figure 3.14: The digital readout: a) the working principle and b) the test setup. The sampling clock has a frequency of 200 MHz.

simplified version the sampling clock has a frequency of 200 MHz. Differently from the final DBB, the system does not store the leading and trailing edges, but the information contained in a time gate of 600 ns is recorded for each event.

More in detail, according to figure 3.14(a), the digital readout in these tests can be described in this way:

- the MAROC ASIC provides 64 parallel trigger outputs: they are HSTL (High Speed Transceiver Logic) signals with a width that is a function of the input (given the ToT). The trigger output signal is high if the input signal is larger than the discriminator threshold: for these tests, a threshold of 1550 mV has been selected;

- the 64 trigger outputs are sent (through the digital connectors and custom cables) to the 4 VME boards (16 channels for each board);

- the VME board FPGAs continuously sample the trigger outputs with a sampling clock of 200 MHz (a sample every 5 ns) and provide a value for each sample: “1” if the trigger output signal is high, “0” if it is low;

- this string of 0s and 1s is readout only in presence of an external trigger: in this case, in fact, a string of 120 bits (600 ns) is readout by the system and converted into a hexadecimal number;

- in the analysis the hexadecimal numbers are re-converted in a string of bits and the signals (the 1s) are expressed in units of time: thus, given the ToT, the digital pulse height can be expressed in ns.

Figure 3.15 shows the digital pulse height distribution for the bars with the maximum digital signal: in this case it is not possible to set a digital threshold in the analysis (as in the analog case) to distinguish the good signals from the noise. These distributions are a function of the discriminator threshold (figure 3.16):

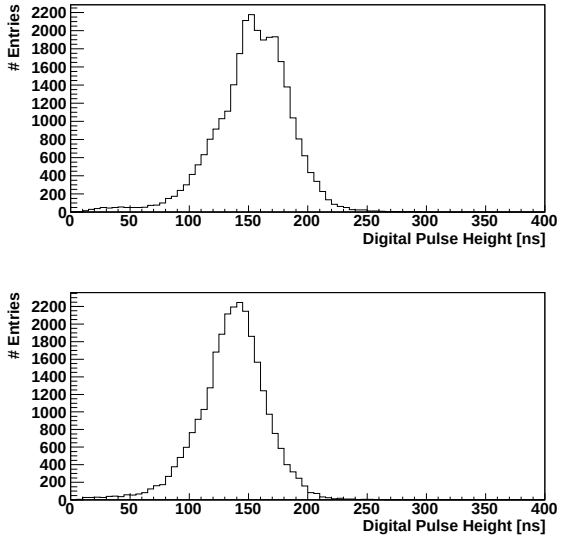

Figure 3.15: The digital pulse height distribution for the bars with the maximum digital signal for a Y plane (top) and for a X one (bottom).

if the threshold is high, the distribution moves to low values; viceversa, if the threshold is low, the pulse height distribution mean value increases, but it can be clearly influenced by noise. The chosen threshold (1550 mV, the top plot) is a good compromise.

Both the analog and digital info are stored allowing to compare their performance, especially for what concerns the tracking variables (spatial resolution and efficiency). Figure 3.17 shows the analog pulse height (black line, already presented in figure 3.6) of the bar with the maximum signal in the event. The red region is the one obtained with all the analog events that have also a digital information: the two distributions overlap from the analog threshold on (blue line, 110 ADC), which thus corresponds to a discriminator threshold of 1550 mV.

This comparison has been performed considering only if the digital output for that bar is present or not. In the same way, it is important to evaluate the digital efficiency (that is different from the detector digital efficiency, computed later on), that is the capability to detect a particle with the digital readout. Referring to equation 3.1, the “target” events are all the events with the bar with the analog maximum signal greater than the analog threshold; the “good” events are defined

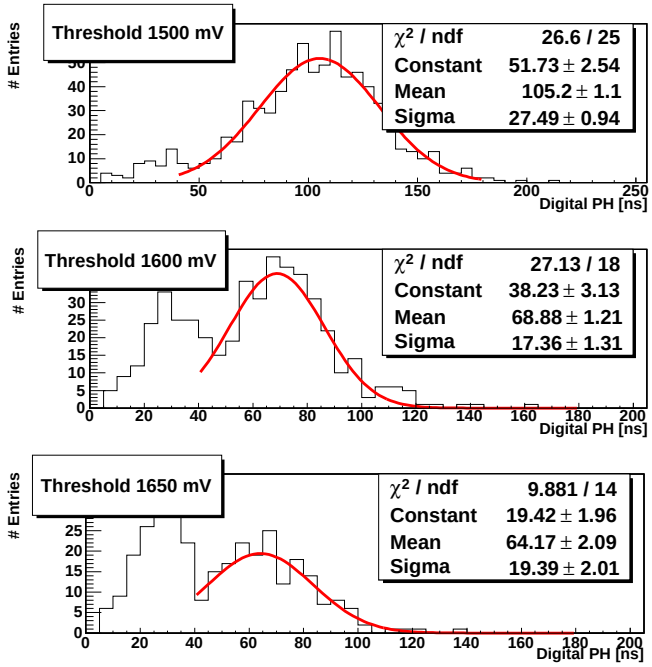

Figure 3.16: The digital pulse height distribution as a function of the discriminator threshold: if the discriminator threshold increases (from top to bottom), the distribution moves to lower values, since the time over threshold is smaller. The peak at lower values is due to the time walk. The chosen threshold for the test run is 1550 mV (top plot).

by the presence (in the same bar) of the largest digital info. In this case, the efficiency is equal to 98.61%. However, if a "good" event is required in any of the bars, the digital efficiency is 99.98%. This fact can be explained considering this example: if two channels have a very similar analog pulse height, the corresponding digital outputs can have the same value, given the digital granularity is smaller than the analog one; thus a possible wrong identification of the digital maximum bar may occur. This is strictly linked to the cross-talk effect: the larger the cross-talk effect (the asymmetries in the residual distributions, as presented in figure 3.10), the smaller the digital efficiency (table 3.1).

It is possible to compute the digital efficiency as a function of the analog pulse height ranges, as presented in figure 3.18: the ranges have been defined fixing the upper limit to 2000 ADC counts and varying the lower value. The efficiency error has been computed considering equation 3.2. As expected, the efficiency reaches 100% above the analog threshold (110 ADC counts).

The correlation between the analog and digital pulse height is presented in figure 3.19(a) and it is the result of the ToT architecture: in fact the digital output

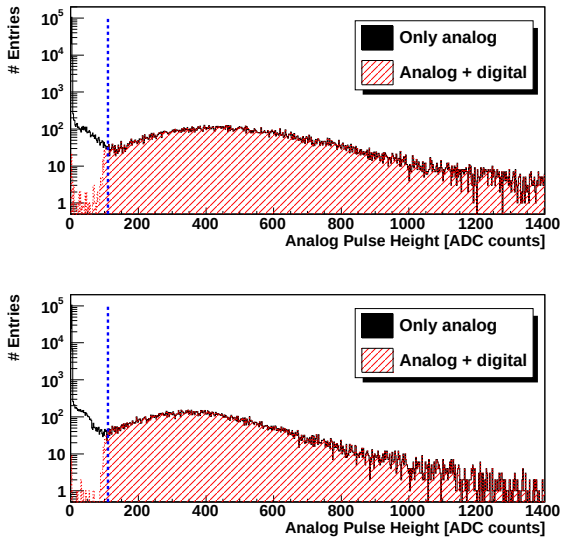

Figure 3.17: The analog pulse height of the bars with the maximum signal considering all the events (black) and the events which have also a digital information (red). The Y planes are collected in the top plot, while the X ones in the bottom one.

Plane	Efficiency(%)
Y4	98.57
X4	98.30
Y3	98.95
X3	97.98
Y2	98.89
X2	98.05
Y1	99.21
X1	99.21
Overall	98.61

Table 3.1: The digital efficiency of the EMR planes: the smaller values occur for the planes with the larger cross-talk contribution (identified by the larger asymmetries in the residual distributions shown in figure 3.10).

width is a function of the analog pulse height. As expected (section A.2.2.2), this correlation can be described by a power-of-4 polynomial law (figure 3.19(b)). This result is fundamental for EMR: even using only the digital information in the final system, a quantity related to the analog pulse height is available and can be

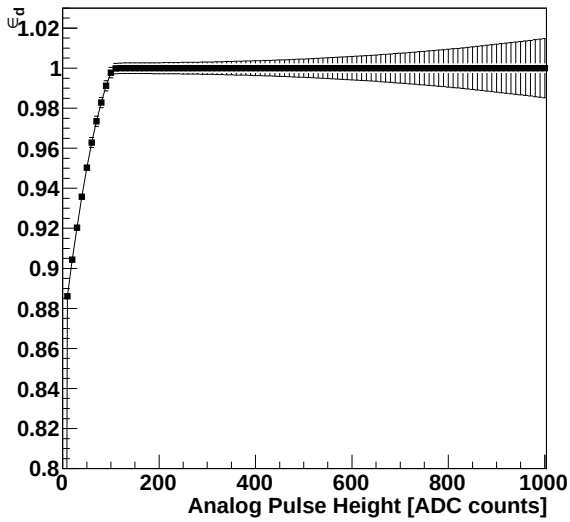

Figure 3.18: The digital efficiency as a function of the analog pulse height. The larger the analog pulse height, the smaller the statistics.

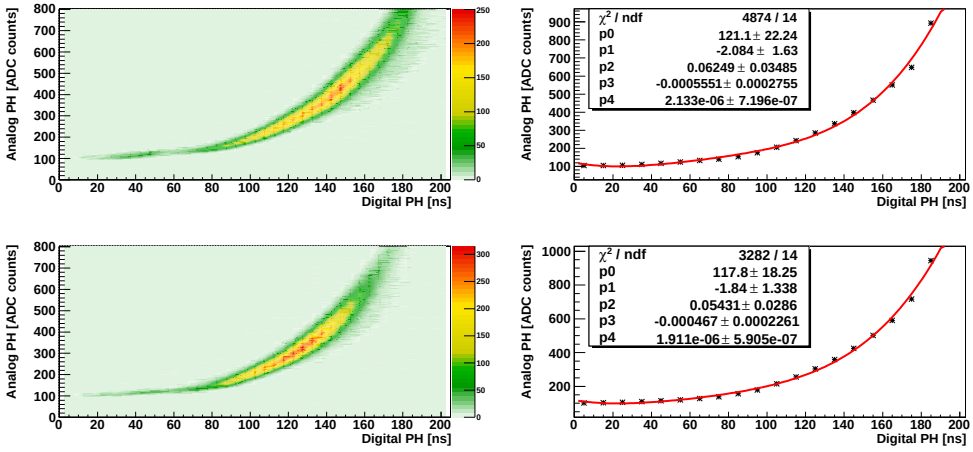

(a) (b)

Figure 3.19: The analog-digital pulse height correlation (a): the correlation can be described by a power-of-4 polynomial law (b). The top plots are related to one Y plane, while the bottom ones to one X plane.

used improving the performance of the detector.

As in the analog case, the measured hit position has been computed by means of a cluster: in this case a cluster consists of a group of contiguous bars which

have a digital information. The number of clusters per plane and the number of bars per cluster are shown in figures 3.20(a) and 3.20(b), respectively.

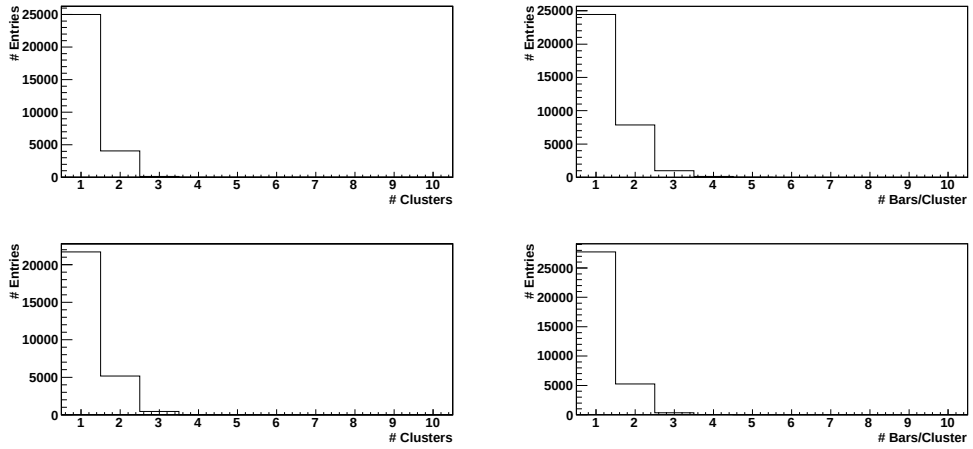

(a) (b)

Figure 3.20: The digital number of clusters per plane (a) and the bars per cluster (b).

The spatial resolution has been evaluated also with the digital data: first it has been computed considering the readout as a pure digital one (in practice not considering the digital pulse height provided by the ToT) and then in an analog way using the ToT info. The pure digital resolution (ρ) is equal to:

$$\rho = \frac{pitch}{\sqrt{12}} \tag{3.3}$$

In this case, given a pitch of 1.9 cm, the spatial resolution is expected to be 5.5 mm. Figure 3.21 shows the residuals of all the planes considering the system as a pure digital one: the obtained values ("Sigma" parameters, of the order of 7-8 mm) are larger than the theoretical one, and this is probably due to the cross-talk and the multiple scattering.

On the other side, exploiting the ToT, the spatial resolution has been evaluated as in the analog case with the charge centroid method (figure 3.22): the data are in perfect agreement. This result is extremely important since it guarantees that in the final detector the digital readout has the same performance of the analog one.

Figure 3.23 presents the digital detection efficiency: the agreement between this case and the analog one (figure 3.13) is excellent.

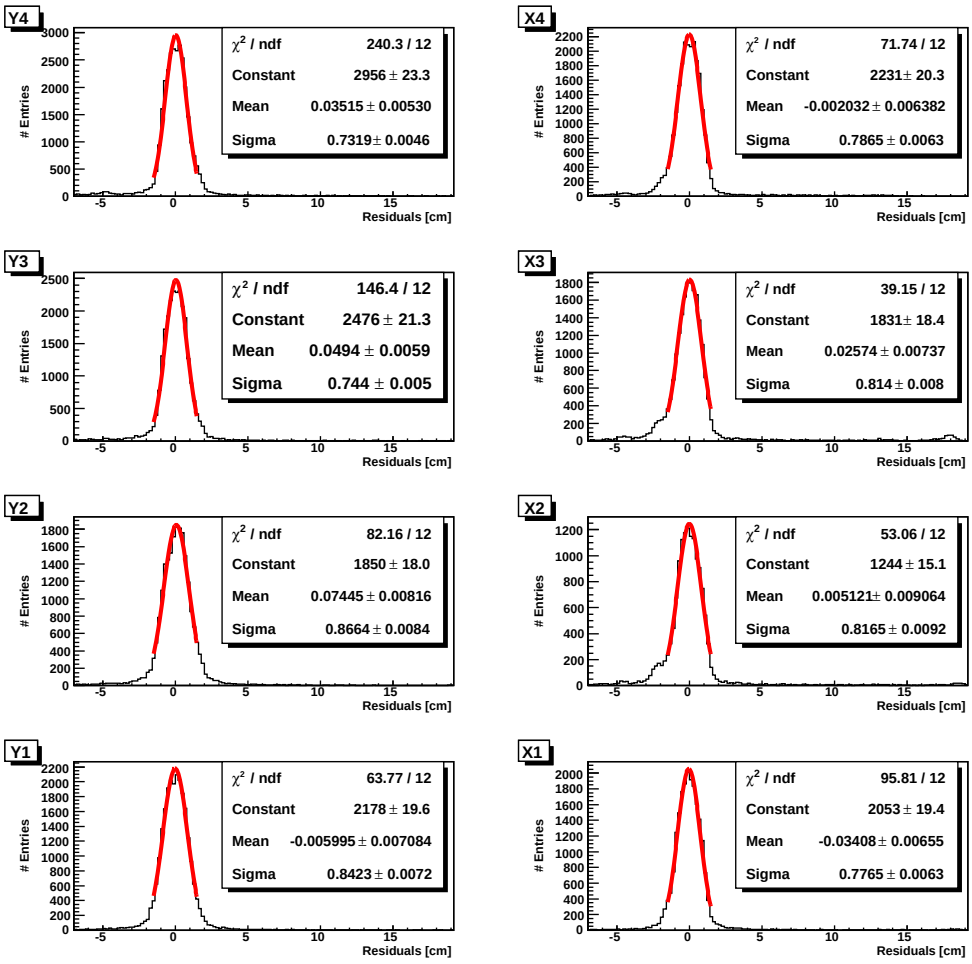

Figure 3.21: The residual distribution considering a pure digital readout.

3.2.4 Analog and digital comparison

The main goal of the tests with the small scale EMR prototype is to measure its performance with the final electronics using both the analog and digital working modes: the EMR tracking capability has been evaluated by means of the spatial resolution and the detection efficiency. The spatial resolution (measured with the residual method) is consistent among the 8 planes: figure 3.24(a) presents the overall values using the analog (black) and digital (red) readout modes. In the first case the average value is (7.46±0.39) mm, while in the second (7.59±0.40) mm, in agreement within 1σ.

As far as the efficiency is concerned, the results obtained with the analog and digital readout modes are summarized in figure 3.24(b): in the first case the aver-

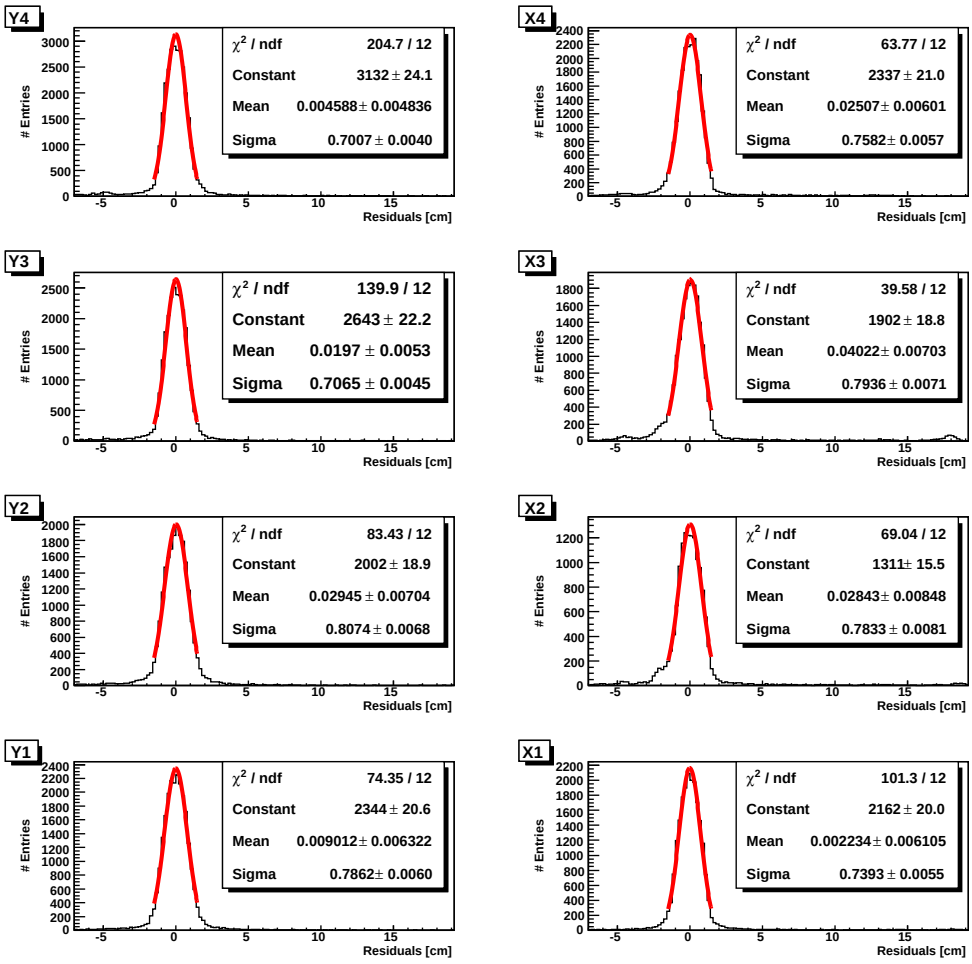

Figure 3.22: The residual distribution considering the ToT.

age value is equal to (98.34±0.43)%, while in the second one to (98.33±0.44)%. Given the particular event selection, only the efficiency of the central layers has been measured.

3.2.5 The cross-talk effect

As already stated, one of the most important problems with a MAPMT readout is the cross-talk effect: the light carried by a fiber can spread on more than one pad. In the EMR prototype each photomultiplier is interfaced with 40 bars arranged in 4 planes (the bar-pad mapping is shown in figure 3.12) and the cross-talk effect causes the peaks presented in figure 3.11(b). The same figure has been obtained for the digital readout mode: thus the effect is independent from the readout mode.

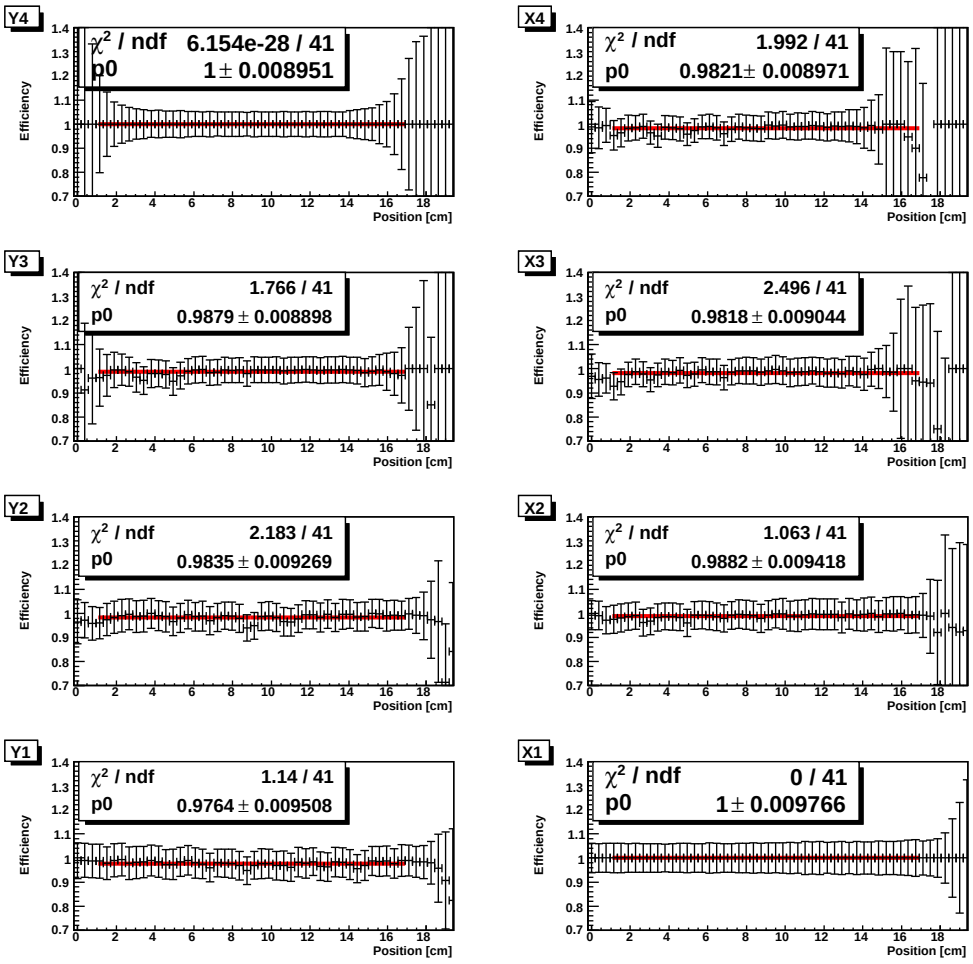

Figure 3.23: The digital efficiency is in perfect agreement with the one computed with the analog readout mode (figure 3.13).

The effect has been studied using the analog readout and the tracking system with the following procedure:

1. for each event the bar signals have been divided in “acceptable” or “not acceptable” (noise) depending on the analog threshold (110 ADC): figure 3.25 shows the pulse height of each bar (for each plane) and the threshold (blue line) for a single event. The “not acceptable” bars have not been taken into account in the analysis;

2. thanks to the tracking system, the “acceptable” bars have been divided in “good” or “not good” bars: the “good” bars are the ones which compose a cluster (one per plane at maximum) whose position is within 3σ of the

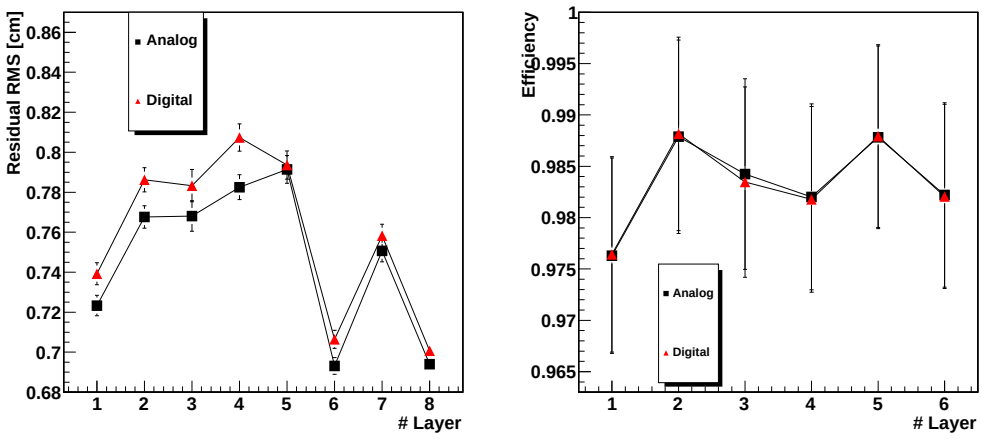

(a) (b)

Figure 3.24: a) The spatial resolution and b) the efficiency for the analog (black) and digital (red) data.

projected one, while the “not good” ones are all the others;

3. for each “good” bar, a 3×3 matrix of neighbouring pads has been taken into account (figure 3.26): a “not good” bar within the matrix has been considered as a “cross-talk” one;

4. the distribution of all the matrices for all the events has been computed (figure 3.27). The central peak corresponds to the “good” bar;

5. the cross-talk contribution of each single pad in the matrix can be computed as the ratio between the events in that pad with respect to the central one (table 3.2).

	PM1			**PM2**	
3.32%	20.80%	6.20%	7.72%	35.33%	2.80%
0.94%	100%	0.11%	0.02%	100%	1.90%
1.01%	2.49%	1.50%	0.43%	2.14%	2.10%

Table 3.2: The cross-talk contribution of each pad of the matrix.

In this case the larger contributions have been measured on the first matrix row in both the PMTs, which corresponds to a downward shift of the photomultipliers, as already presumed in section 3.2.2.

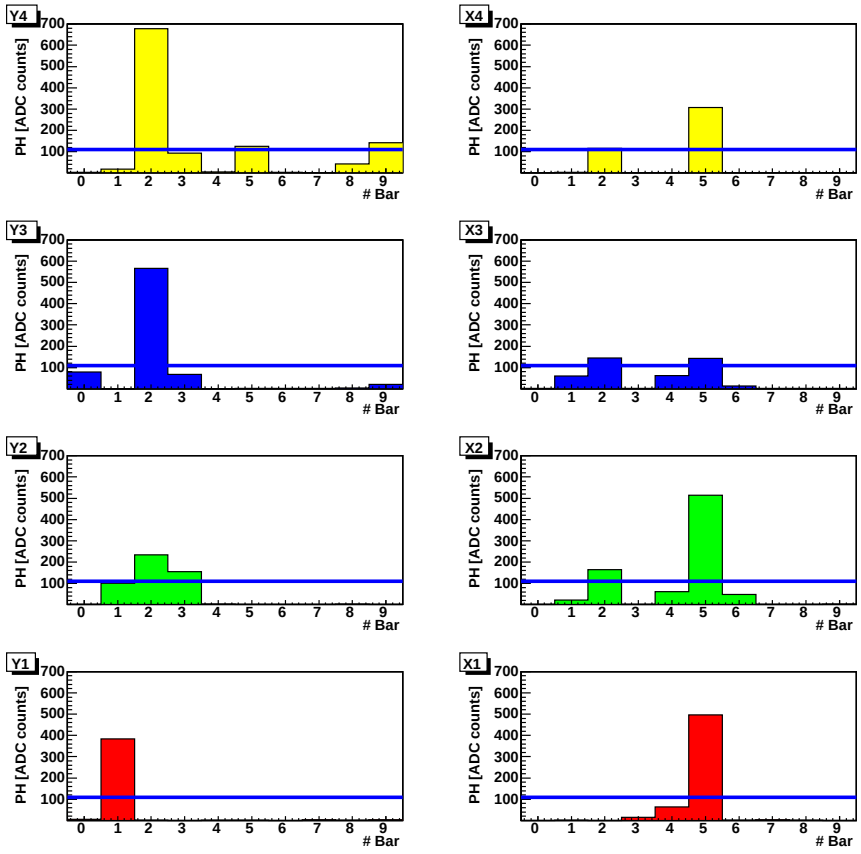

Figure 3.25: The plane profile of an event: the 4 planes of MAPMT 1 are shown on the left, the ones of MAPMT 2 on the right. The bars have been considered "acceptable" if they have a signal larger than the analog threshold (110 ADC, the blue line).

The cross-talk effect can be reduced improving the fiber-MAPMT alignment, but this was not possible in the prototype.

3.3 LEP - Large EMR Prototype

A second EMR prototype called LEP (Large EMR Prototype) has been developed to test the EMR performance as a calorimeter. The detector (presented in section 2.4.2) consists of 48 planes of rectangular bars whose scintillating light is readout with MAPMTs and silicon photomultipliers (SiPMs) on the bars opposite sides. The detector has been tested on the CERN T9 beamline.

This section describes the performance with the MAPMTs. The test goal was

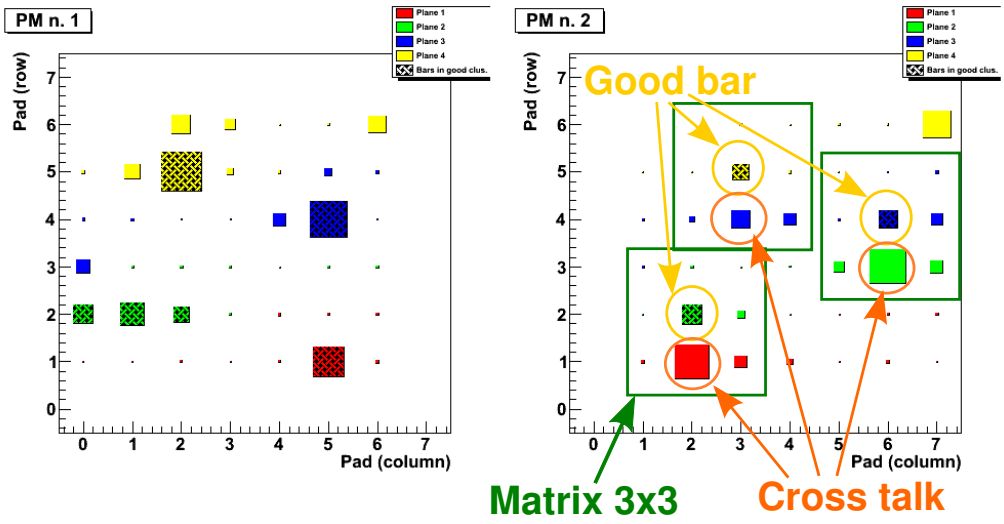

Figure 3.26: An event at the MAPMT pad level (MAPMT 1 on the left, MAPMT 2 on the right): for each "good" bar (yellow), a 3×3 matrix of neighbouring pads (green) has been considered; the "cross-talk" bars (orange) are the ones with a signal larger than the analog threshold but not part of a good cluster.

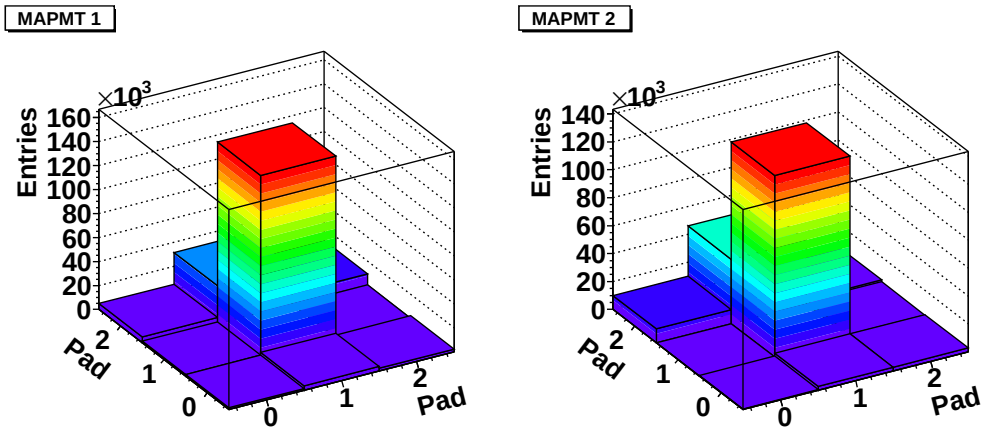

Figure 3.27: The distributions of all the matrices for all the events.

the study of the possibility of discriminating muons and electrons in a 1 GeV/c mixed (muons, pions and electrons) negative beam with a prototype with the same number of radiation lengths of EMR, applying the same algorithms used in the official MICE analysis. Two GEANT4 simulations have been developed: the first one at 1 GeV/c to tune the simulation itself (in particular the detector geometry) as a function of the experimental results; the other one with a 150 MeV/c beam.

3.3.1 Setup and beam

LEP has been tested on the T9 beamline at the CERN East Area with a mixed negative beam with a momentum of 1 GeV/c. The beamtest setup (figure 3.28) consists of a couple of scintillators for the trigger, two large area silicon detectors to track the particles, an electromagnetic calorimeter (DEVA) to evaluate the beam composition and LEP. To identify electrons a threshold Cherenkov detector has been used.

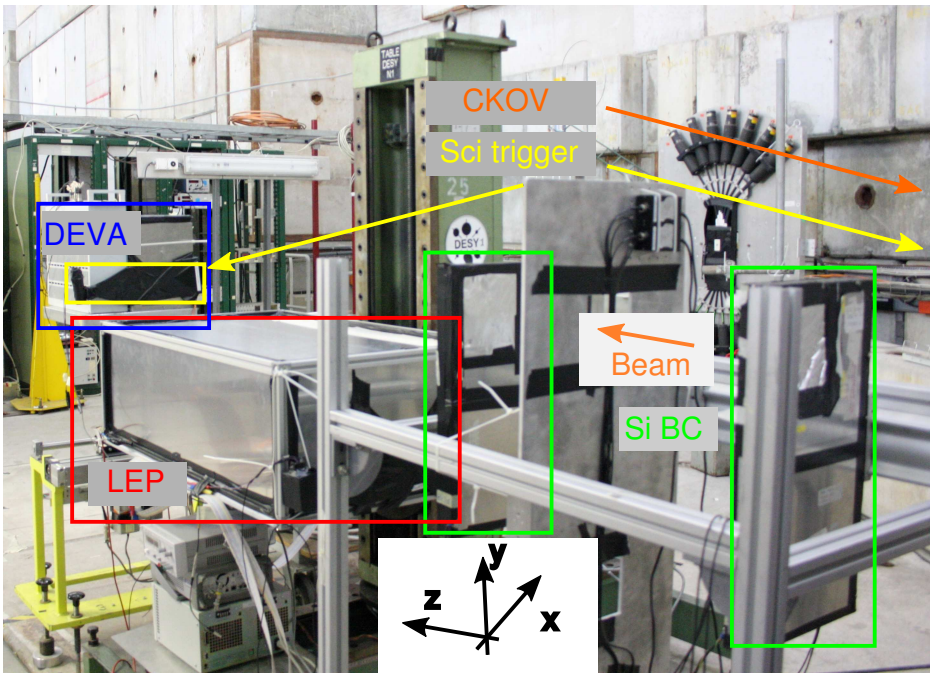

Figure 3.28: The beamtest setup consists of a couple of trigger scintillators, two BCs to track particles, an electromagnetic calorimeter (DEVA) to evaluate the beam composition and LEP; one of the trigger scintillators and the Cherenkov detector are upstream and not shown in the photo.

The trigger is generated by the coincidence of two scintillators with an effective volume of $10\times10\times1$ cm^3 (type 1) and $20\times10\times1$ cm^3 (type 3) (section 3.1.2). The tracking system is based on the beam chambers presented in section 3.1.1.

3.3.1.1 Particle-ID and DAQ

The particle-ID has been performed by two systems: an electromagnetic calorimeter (DEVA) and a Cherenkov detector.

DEVA (figure 3.29(a)) has been used to evaluate the beam composition and to measure the Cherenkov particle-ID capability. DEVA is a $15\times15\times31$ cm^3

sampling calorimeter made of 12 tiles of 2 cm thick scintillator interleaved with 11 lead tiles (eight tiles 0.5 cm thick and three 1 cm thick), for a total of ~ 13 X_0; the overall weight is about 25 kg.

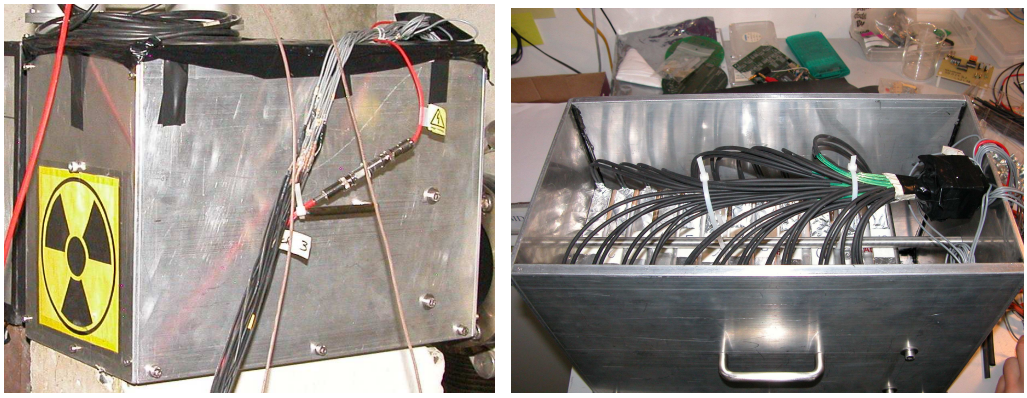

(a) (b)

Figure 3.29: The DEVA electromagnetic calorimeter: a) the overall detector and b) the WLS fiber+MAPMT system to readout the scintillator light.

The scintillator light is collected by 4 2 mm WLS fibers (figure 3.29(b)) and readout by a 16 channel Hamamatsu MAPMT (R5600-M16). The signals are digitized by a CAEN V792 charge-to-digital converter (QDC) and the energy resolution is of the order of $\frac{9\%}{\sqrt{E}}$, as measured at the Beam Test Facility (BTF) of the INFN National Laboratory of Frascati (LNF) for energies lower than 500 MeV.

A 2.5 m long Cherenkov threshold detector placed just before the setup has been used to identify the electrons during the runs with LEP: for 1 GeV/c particles, it has been filled with 0.95 bar of CO_2 [90]; the Cherenkov light is readout by a photomultiplier and its signal is digitized by a channel of the V792 QDC.

The beamtest readout electronics is presented in figure 3.30: as for the small scale prototype case (figure 3.5), it consists of a VME system based on a Bit3 620 board optically connected to a PC, a MAROC control board to configure and readout the analog signals of the FEBs, a V792 QDC for DEVA and the Cherenkov signals and a couple of flash ADCs (CAEN V550).

The BC readout sequence is started by dedicated signals from the MAROC control board and the corresponding analog signals are converted in digital ones by flash ADCs. The V550 ADCs work in zero suppression mode that is only the channels above a given threshold are readout. During the readout, data are transferred from the TA1 ASICs to the ADCs with a 5 MHz clock; in the ADCs, pedestals are subtracted and the result compared with a threshold that depends on the channel noise. In general, less than 5 strips (out of 384) are above threshold,

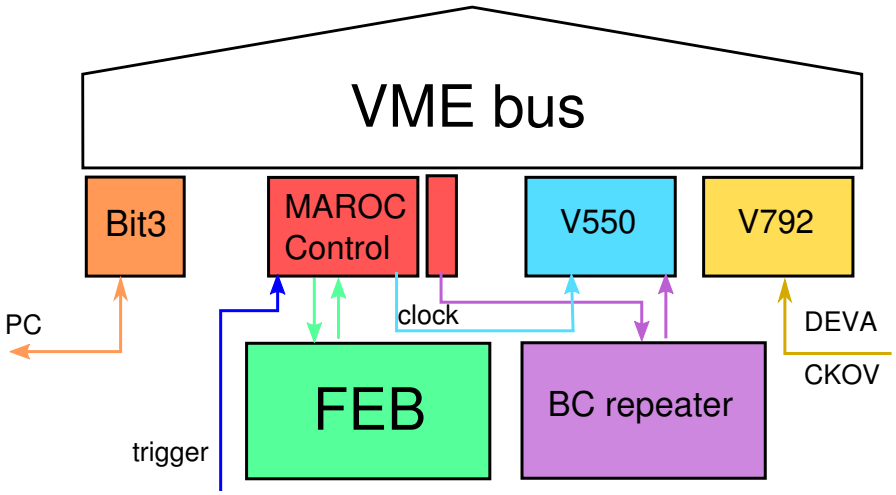

Figure 3.30: The scheme of the readout electronics: the VME system is optically connected to a PC through a SBS Bit3 620. A MAROC control board is used to configure and readout the analog outputs of the MAPMTs and BCs. The BC analog output is digitized by a channel of a CAEN V550 ADC. The DEVA and Cherenkov detector signals are integrated with a V792 QDC.

reducing the readout time dramatically.

3.3.1.2 The beam

The beamtest has been performed at the PS T9 beamline at CERN, one of the lines located in the East Hall (building 157, figure 3.31) [91].

The T9 line provides secondary beams either of negative or positive charged particles (typically μ, π and e) in a momentum range from 0.5 to 15 GeV/c. Particles are produced in the interaction of a primary 24 GeV/c proton beam (accelerated by the Proto Synchrotron - PS) with a target: the beam composition depends on the target material. For the beamtest a target producing both muons and electrons at 1 GeV/c has been required.

The beam features typical intensities of the order of 10^4-10^5 particles per bunch (called spill) for a bunch duration of $\sim$400 ms with a repetition period of 45 s. The secondary beams are selected by a horizontal collimator at the beginning of the line while the focusing and tuning of the beam can be performed with a set of dipole and quadrupole magnets and both vertical and horizontal collimators. The energy of the particle is selected with a bending magnet at the beginning of the line.

The beamtest goal was to measure the particle identification capability of the EMR prototype. The test should have been performed with a beam with a momen-

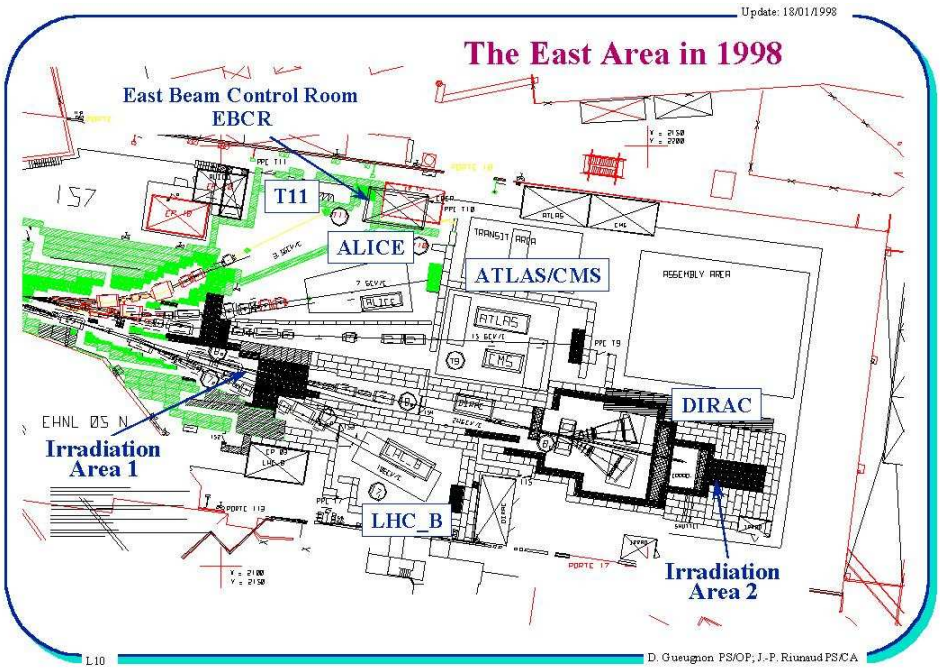

Figure 3.31: The East Hall complex consists of five beamlines: T8 provides a beam for the DIRAC experiment; T7, T9, T10 and T11 are devoted to detector studies and to irradiation tests (T7) [90].

tum of 200 MeV/c and with the same quantity of muons and electrons. However these requests could not be satisfied by the CERN beamlines: the smallest reachable momentum value on T9 is 500 MeV/c, but at this energy the quantity of muons with respect to electrons decreases dramatically. So a 1 GeV/c beam has been chosen as a good compromise.

3.3.1.3 The beam features

The beam features have been evaluated by means of the tracking system and the electromagnetic calorimeter in dedicated runs (in which LEP was not placed on the beam, as shown in figure 3.28). The Gaussian fit of the beam size is presented in figure 3.32: in the horizontal direction (X) the beam RMS is 2.3 cm, while in the vertical one (Y) 3.7 cm.

The beam angular distribution is shown in figure 3.33: the horizontal divergence is 9 mrad, while the vertical one is 5.7 mrad.

The electron identification is performed with the help of the Cherenkov detector whose signal pulse height is presented in figure 3.34(a). The blue dotted line identifies the threshold used in the analysis to discriminate the signal from

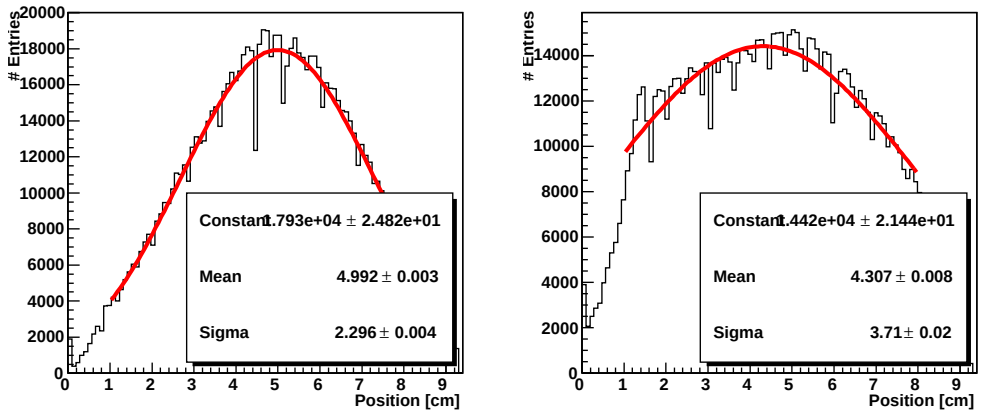

Figure 3.32: The beam size in the horizontal (on the left) and vertical (on the right) directions.

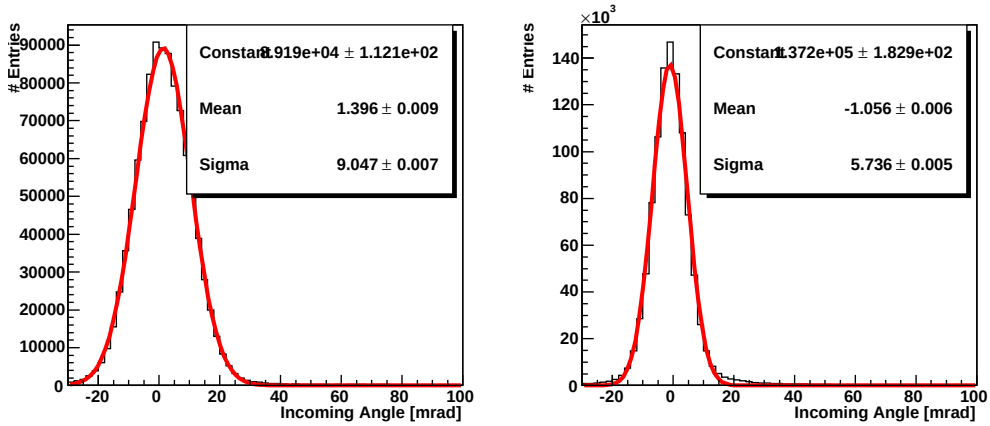

Figure 3.33: The beam angular distribution for the X direction (on the left) and for the Y one (on the right).

the noise or, in this case, the electrons from the other particles.

The overall DEVA energy spectrum is presented in figure 3.34(b) (with the black line) and it is computed summing the 12 tiles information. It presents three regions: the MIP peak (which consists mainly of muons), the electron peak and the pion region (between the two peaks). The same histogram has been evaluated requiring a Cherenkov signal larger than the selected threshold, obtaining in this way the electron peak (the blue line in the plot). The histograms have been obtained considering a central region of 7×7 cm^2 on the DEVA calorimeter in order to exclude the events on the edge of the calorimeter itself since they are character-

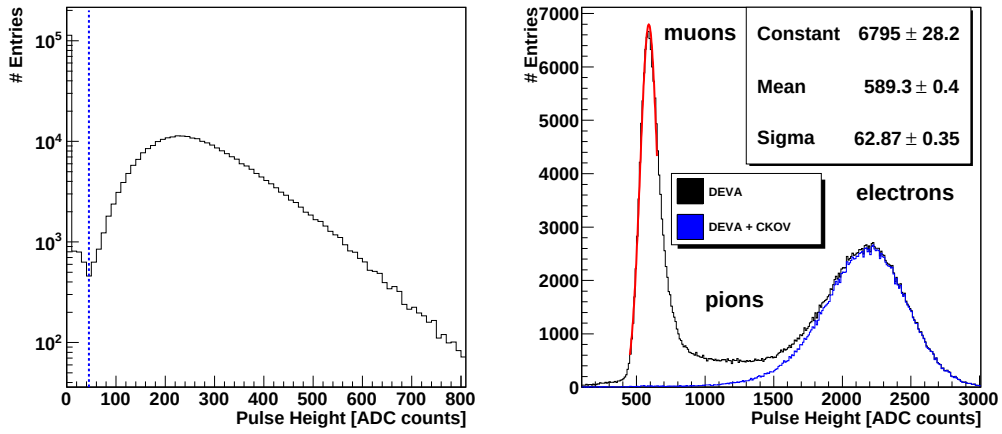

(a) (b)

Figure 3.34: a) The Cherenkov pulse height: the blue dotted line identifies the threshold used to discriminate the electrons (signals above threshold) with respect to the other particles. b) The DEVA energy spectrum (in black) shows three distinct areas: the MIP peak (mainly due to muons), the electron peak (confirmed by the Cherenkov information in blue) and the pion region.

ized by leakage. Considering these results, the particle identification criteria are the following:

- a particle is an **electron** if the Cherenkov signal is larger than the threshold;
- a particle is a **muon** if the Cherenkov signal is smaller than the threshold and its energy in DEVA is the one corresponding to the muon peak, that is in the range $[M - 3\sigma, M + 3\sigma]$, where M and σ are the muon peak mean value and sigma.

According to these definitions, in the 1 GeV/c beam 33% of the events have been identified as muons and 66% as electrons; as far as the pions are concerned, if they have a signal in the Cherenkov detector smaller than the threshold and an energy which falls in the muon peak, they are considered MIPs, otherwise they are not taken into account in the analysis (the probability that they are misidentified as electrons is too small).

Since muons are MIPs, their energy deposit in DEVA is the same with or without the presence of the EMR prototype; in other words DEVA can be used in the tagging. On the other hand, the energy deposit of the electrons in DEVA is different if LEP is placed in the beam: the presence of LEP in fact causes a broader peak in the spectrum. Therefore the Cherenkov detector which is placed

upstream of LEP is the only device that can be used for the electron identification. Its performance has been measured in the test preliminary phase by means of the Cherenkov efficiency defined as:

$$\epsilon_{CKOV} = \frac{N_e}{N_{tot}} \tag{3.4}$$

where N_{tot} is the total number of particles while N_e is the number of electrons defined as the events which have a signal above the Cherenkov threshold. N_e and N_{tot} have been computed in several DEVA pulse height ranges: the ranges have been chosen keeping the upper bound fixed at 3000 ADC counts and increasing the lower edge from 1900 ADC counts on. The Cherenkov efficiency as a function of the energy measured by DEVA in the electron peak region is presented in figure 3.35. The results clearly show that the Cherenkov detector has an efficiency

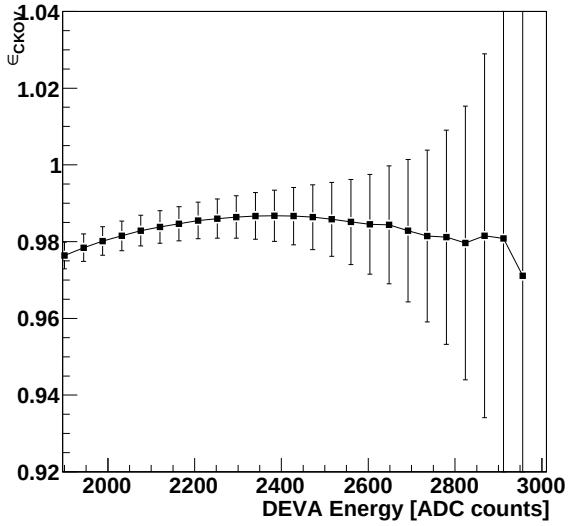

Figure 3.35: The Cherenkov efficiency as a function of the beam energy measured by DEVA. The X axis presents the lower edge of the ranges taken into account. The large error bars are due to the small statistics.

of the order of 98% as far as the electron discrimination is concerned.

3.3.2 Beamtest results

To study the muon/electron discrimination with LEP, the first step of the analysis is the bars signal equalization. Considering the same MIP event, in fact, the analog signal of two bars can be different for several reasons:

- bars: the scintillator light does not reach the MAPMT channel because the WLS fibers are not properly glued inside the bar or a fiber is completely or partially broken;

- fiber-MAPMT interface mask: the WLS fibers are not perfectly glued and polished at the level of the MAPMT mask or the MAPMT is not perfectly aligned with the fibers (inducing the cross-talk effect);

- MAPMT: the MAPMT channels response is intrinsically non uniform (a difference of a factor 2 in the gain is possible).

The channel equalization has been performed computing the pulse height of each of the 192 bars considering only muon events. Given that a momentum of 1 GeV/c is larger than the minimum ionization momentum value, the energy deposited by a muon in each bar is the same [53]. Figure 3.36(a) presents the pulse height of the first layer bars for muon events: the mean value has been computed by means of a fit with a Gaussian law. The pulse height of each channel has been recomputed using a scale factor which is the pulse height of the first LEP bar (the top left plot in figure 3.36(a)). The rescaled pulse height distributions of the same bars are presented in figure 3.36(b). The pulse height distributions for the bar with the maximum signal in the event for the 3 PMTs are presented in figure 3.37; the blue line is the threshold set to distinguish signal from noise.

As for the small scale prototype, the particle hit position on each layer has been reconstructed considering the bar cluster and using the charge centroid method. The number of clusters per layer (computed independently for each layer but represented in a single plot for each PMT) is presented in figure 3.38(a), while the number of bars per cluster in figure 3.38(b). It is possible to note that the number of hit bars is larger for the second PMT: this is expected since the electrons release the larger part of their energy in the middle of LEP, as shown later.

The spatial resolution has been measured using the residual method and the silicon tracking system: the distribution for the first layer (figure 3.39(a)) has been fitted with a Gaussian function and the spatial resolution is 4.6 mm.

The distance between the tracking system and the LEP first layer has been computed by means of the residuals minimization method: the sigma value obtained from the Gaussian fit of the residual is plotted as a function of the distance as presented in figure 3.39(b); a power-of-2 law fitting the distribution has allowed to compute the distance to be 24.26 cm.

The value of the residual RMS as a function of the number of the layer is shown in figure 3.40(a). As expected, the farther the layer, the larger the residual RMS, mainly because of the multiple scattering and the energy loss during the path.

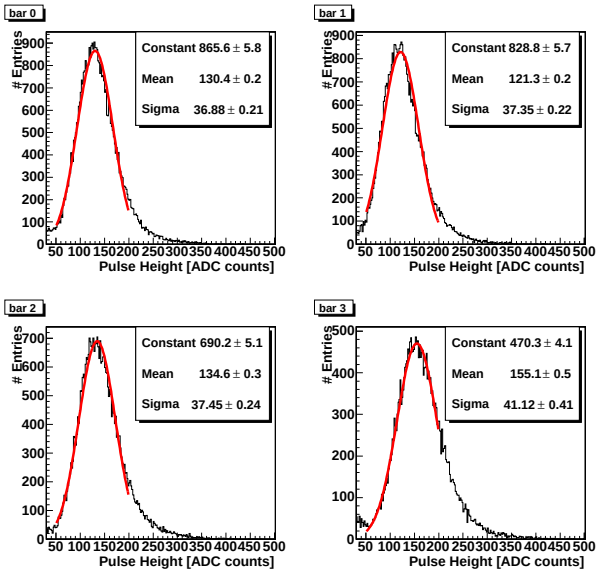

(a)

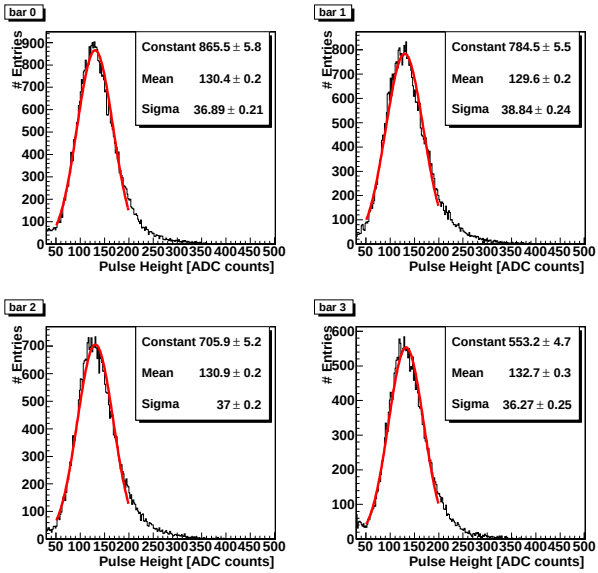

(b)

Figure 3.36: The pulse height for muon events of the 4 bars of the first LEP layer a) before and b) after the channel equalization with respect to the first LEP bar (the top left plot).

To perform the analysis a target region in the center of the first LEP layer has to be identified, in order to exclude the events at the edge of the detector that

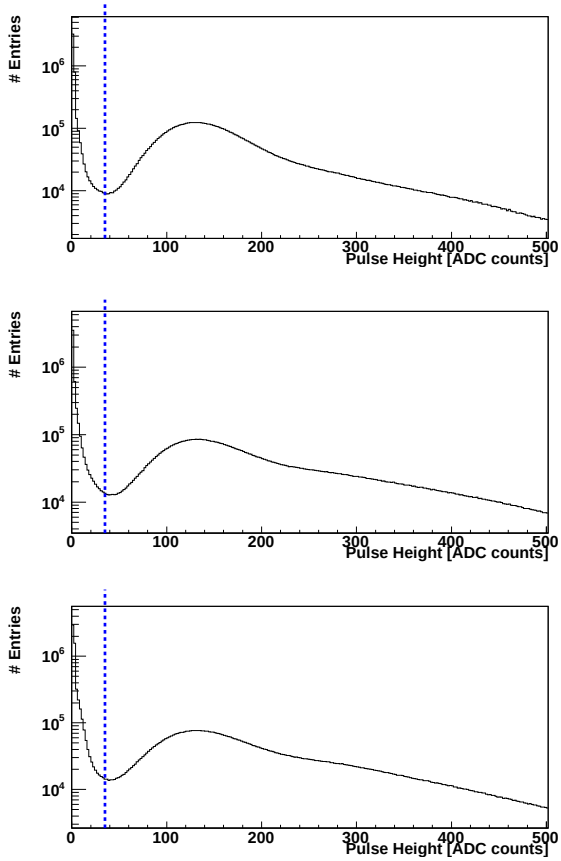

Figure 3.37: The pulse height distributions for the bar with the maximum signal in the event for each PMT. The blue line identifies the analog threshold.

are characterized by an energy leakage. Figure 3.40(b) presents the reconstructed position on the first LEP layer. In the analysis the central beam region is defined by an area of [3,7] cm in the horizontal direction and [4,7] cm in the vertical one.

3.3.2.1 Electron/muon identification with LEP

As described in section 2.4, the algorithm used by the official MICE analysis is based on two variables: the ratio between the energy measured by the layer with the largest energy loss and the one of the first layer, and the number of particles that hit EMR. At 1 GeV/c the first observable is not effective since muons do not release energy following a Bragg-peak distribution, while the particular geometry of LEP does not allow to compute the second observable.

Thus at this momentum value different variables have been studied for the e/μ discrimination purpose: since the tracking capabilities cannot be considered, only

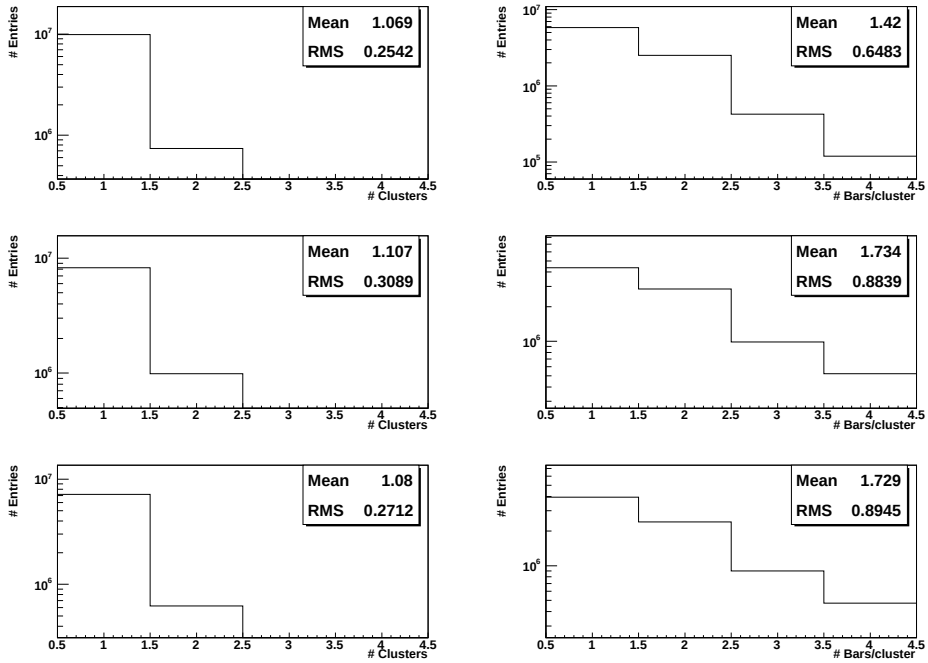

(a) (b)

Figure 3.38: a) The number of clusters per layer and b) the number of bars per cluster. These distributions are computed for each layer and collected in a single plot for each PMT.

the variables related to the energy deposited in the scintillating bars have been taken into account. Among them, the total energy measured by LEP is the most powerful; however, as it will be shown in chapter 4, the energy measured by each layer (and a related quantity) can be used.

Total energy

The total energy measured by LEP is computed as the sum of the pulse heights (without any cut) of all the 192 equalized bars signals. Figure 3.41(a) presents the total energy for all the particles hitting the first layer: the black plot is due to both muons and electrons, while the electron contribution is the blue one. The total energy considering only the central beam region is presented in figure 3.41(b): as before, the black plot is due to all the particles while the blue one just to electrons.

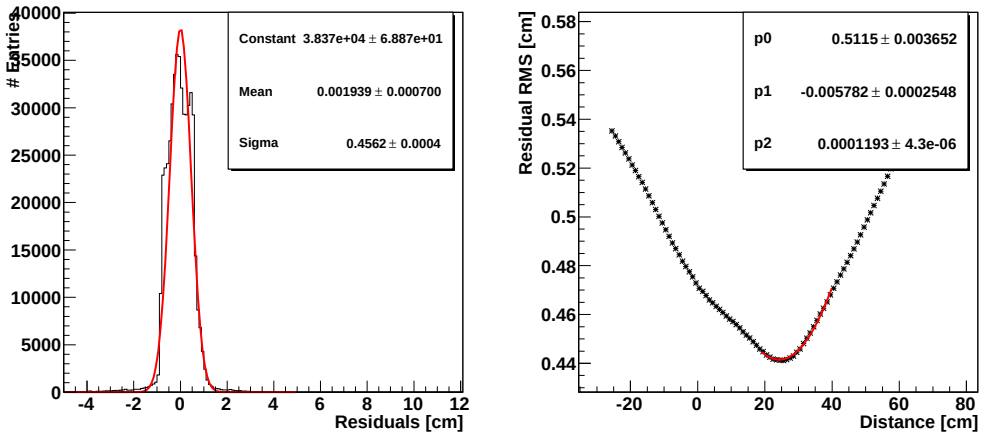

(a) (b)

Figure 3.39: a) The residual distribution for the first layer: the spatial resolution is of the order of 5 mm. b) Residual scan: the residual distributions have been evaluated varying the distance between the tracking system and LEP in the analysis: the minimum corresponds to about 24 cm.

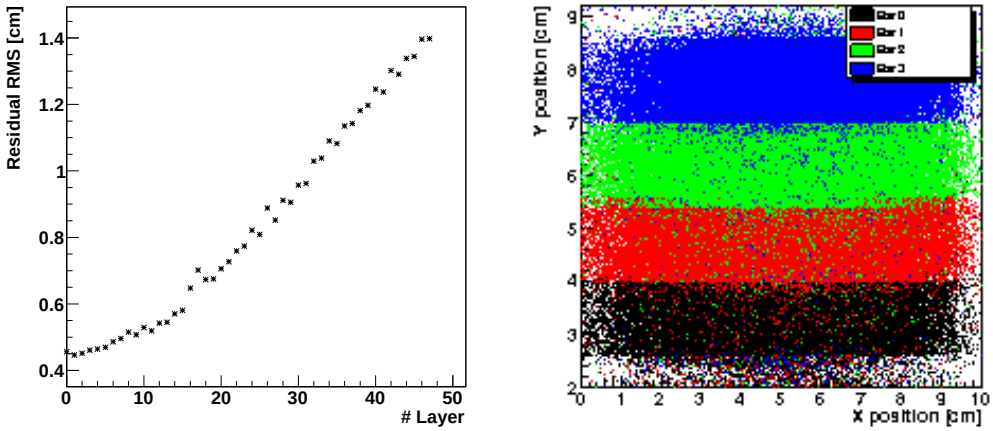

(a) (b)

Figure 3.40: a) The residual distribution as a function of the layer number. b) The reconstructed beam profile on the first layer of LEP: the 4 bars can be perfectly identified.

These distributions allow to compute the electron purity and efficiency defined as:

$$\epsilon_e = \frac{N_e}{N_{tot}}$$
$$P_e = \frac{N_e}{N_e + N_{other}} \tag{3.5}$$

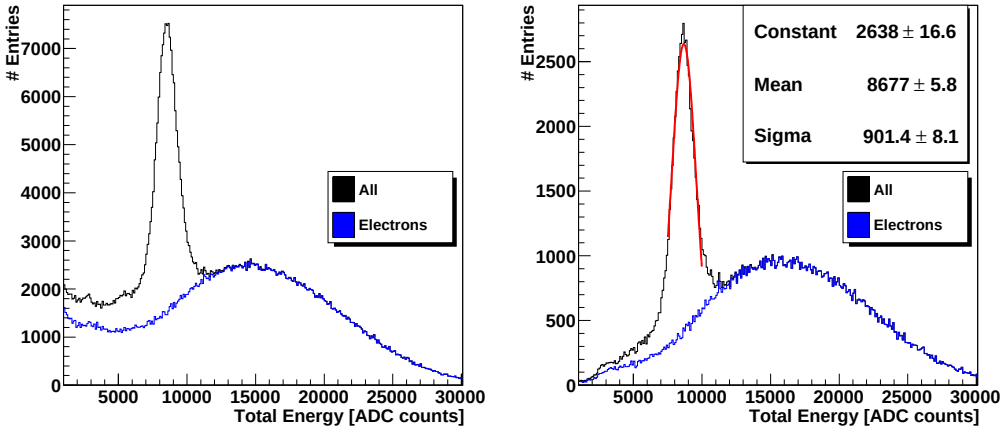

(a) (b)

Figure 3.41: The total energy measured by LEP considering muons and electrons which hit a) the first layer and b) the central beam region. The blue plots are the distributions given by electrons only.

$N_{other} = N_\mu$ is the number of muons (or, to be more precise, MIPs), while N_{tot} is the total number of electrons requiring a Cherenkov signal larger than the threshold. The energy ranges used to compute the variables have been chosen keeping the upper bound fixed at 35000 ADC counts and increasing the lower bound from 10000 ADC counts on; the electron purity as a function of the efficiency is presented in figure 3.42. To give some numbers: the number of electrons (considering all the signals above the Cherenkov threshold) is 144963; in the [10100-35000] ADC counts energy range the number of electrons (blue plot in figure 3.41(b)) is 124047, while the muons (the difference between the black and the blue histograms) are 2882. Therefore the electron efficiency and purity are:

$$\epsilon_e = 0.855 \pm 0.003 \tag{3.6}$$

$$P_e = 0.977 \pm 0.003 \tag{3.7}$$

Energy per layer

Another quantity that can be used to discriminate electrons and muons is related to the energy released in each LEP layer. As in the previous case, the sum of the pulse heights of the 4 bars of each layer (without any cuts) has been computed and only the particles which hit the target area on the first layer have been taken into account. The energy per layer is presented in figure 3.43(a): the muon events are presented in black, while the electron ones in red. In order to compare the two

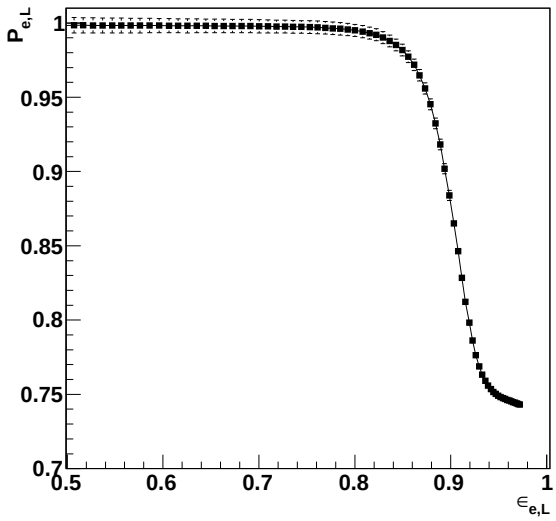

Figure 3.42: The electron purity as a function of the efficiency using LEP.

distributions (since the number of electrons is about 3 times larger than the muons one), they are normalized to the bin with the largest value.

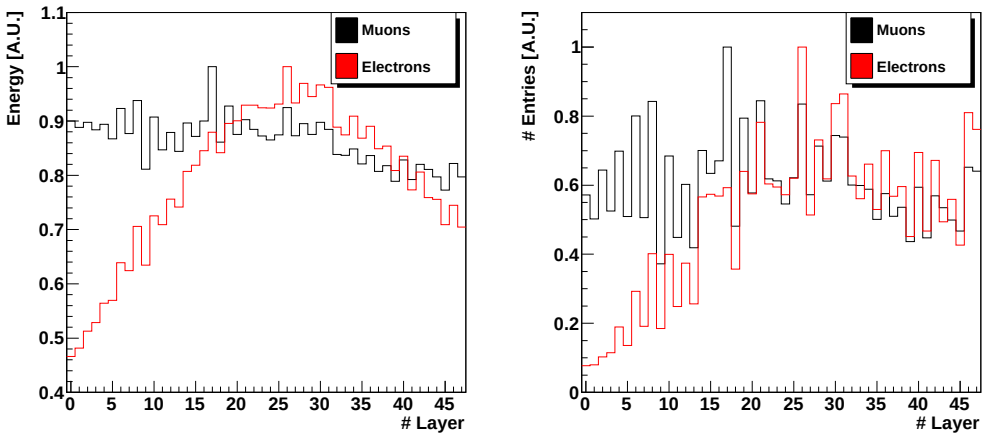

(a) (b)

Figure 3.43: a) The energy measured by each LEP layer normalized to the bin with the largest value and b) the layer with the maximum deposited energy. In both the plots, the black histograms are the ones due to muons, while the red ones to electrons.

The following remarks hold:

- a μ/e^- discrimination with this quantity is hard to perform;
- the electron energy presents a kind of maximum in the second LEP block (from layer 15 to 31). Releasing its energy an electron produces a lot of gammas, and this explains the larger number of clusters and bars per cluster in the second PMT (figure 3.38);
- muons lose about 10% of their energy in LEP, which corresponds to about 100 MeV: since for the Bethe-Bloch formula a particle at the minimum of ionization (e.g. muons at 1 GeV/c) loses about 1.9 MeV/cm in plastic (polystyrene) [53], an energy loss of 170 MeV is expected;
- starting from the energy per layer it is possible to consider another discrimination variable that is the number of the layer which has registered the largest energy loss: figure 3.43(b) presents this distribution that has been normalized (for the comparison) to the bin with the largest value. At 1 GeV this variable is not useful as a discriminator differently from lower momenta, where muons are represented by a narrow peak corresponding to the Bragg one (further details are given in section 3.3.3.1).

3.3.2.2 e/μ identification with LEP: the MICE method

In MICE the muon/electron discrimination is based on both TOF and EMcal, the electromagnetic calorimetric system consisting of EMR and a pre-shower, the KLOE-Light (KL) layer. Focusing only on EMR, as already said the two observables used in the analysis are the ratio between the energy of the layer with the largest value and the energy of the first one and the number of particles that hit the detector itself (section 2.4). Given the particular beamtest momentum and the prototype geometry, these observables are not effective to discriminate muons and electrons: muons do not release their energy following the Bragg-peak distribution, while the prototype sensitive area and the fact that only one direction is measured represent a limit for the second observable. However in this section they have been studied all the same in order to present the MICE analysis method with real data.

The ratio between the energy of the layer with the largest value and the energy of the first layer is presented in figure 3.44 considering only the particles in the central beam area and normalizing the distributions to the bin with the largest value. At 1 GeV/c, muons lose their energy continuously in the detector and their distribution (in black) is close to 1; on the other hand electrons generate a shower in LEP (causing the peak in figure 3.43(a)). A similar electron distribution occurs at lower momenta, but in that case the muon energy ratio is much larger given the Bragg-peak behavior.

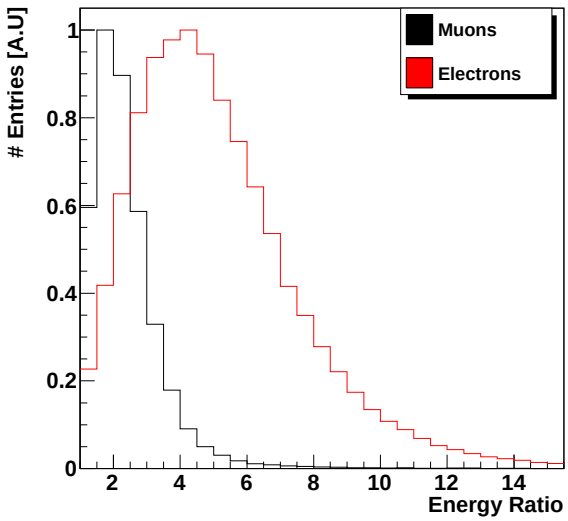

Figure 3.44: The ratio between the energy of the layer with the maximum value and the first one: muons produce the black plot, while electrons the red one. The two distributions are normalized to the bin with the largest value.

As far as the second observable is concerned, LEP is not the ideal prototype for its study:

- the first layer sensitive area is very small (6×19.1 cm^2);
- it measures only one direction (according to the geometry presented in figure 2.17, the vertical one - Y), so no tracking algorithm can be developed;
- the bars have a rectangular shape, so the inefficiency between two adjacent bars is larger than the one in the triangular shape case [80].

However, in order to study the second observable, a dedicated run with LEP in a different position has been performed: the prototype has been turned with two 90° rotations (one anticlockwise in the XZ plane and one clockwise in the YZ plane); the new position is presented in figure 3.45. A $15\times15\times1$ cm^3 lead block acting as a pre-shower has been placed in front of LEP: it corresponds to about 2.65 X_0, close to the 2.5 X_0 of the KL layer.

Two typical muon and electron events are presented in figure 3.46(a) and 3.46(b), respectively: as expected, a single track is present for the muon case, while more than one bar per layer are hit in case of an electron.

The difference in the muon and electron behavior can be shown considering the number of clusters in the first layer (which is now composed by 48 bars), as

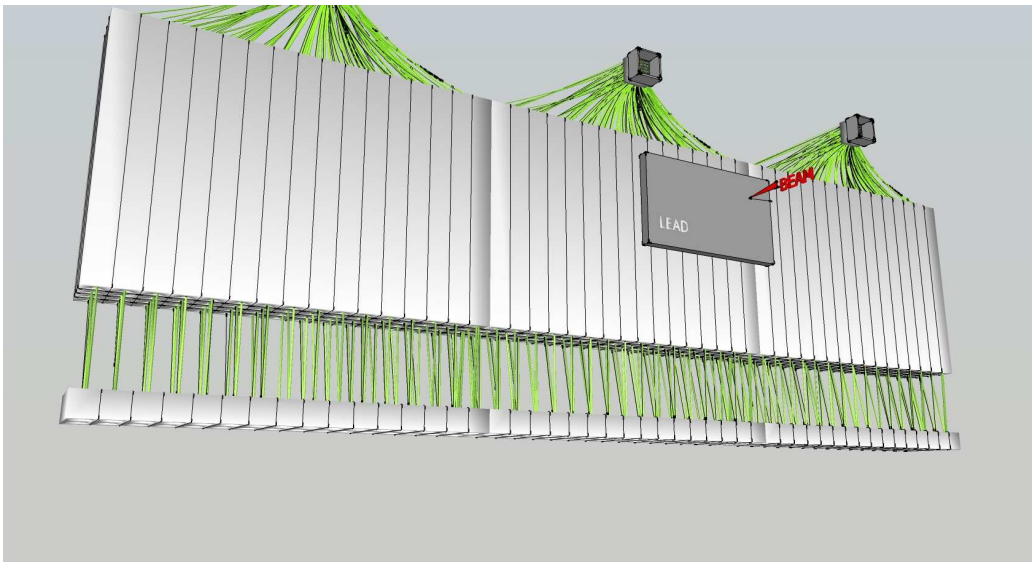

(a)

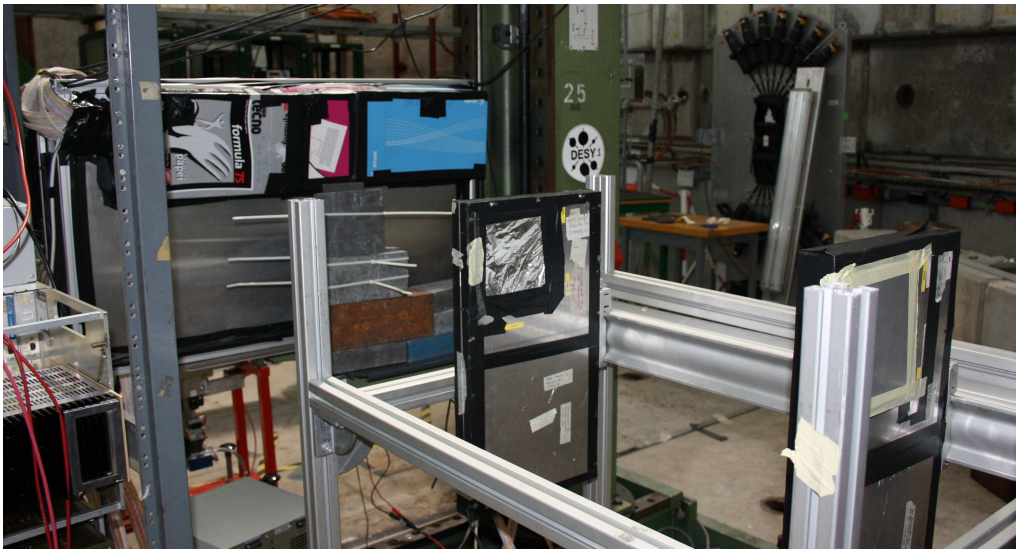

(b)

Figure 3.45: a) A sketch and b) a photo of LEP once turned to study the second MICE official variable. A 1 cm thick 15×15 cm^2 lead block has been placed in front of LEP.

presented in figure 3.47: for muons only one cluster per event is present, while a larger number of clusters occurs in the electron case. The one cluster events in the electron distribution can be due to the fact that two particles can hit the same bar or to an inefficiency of the bar.

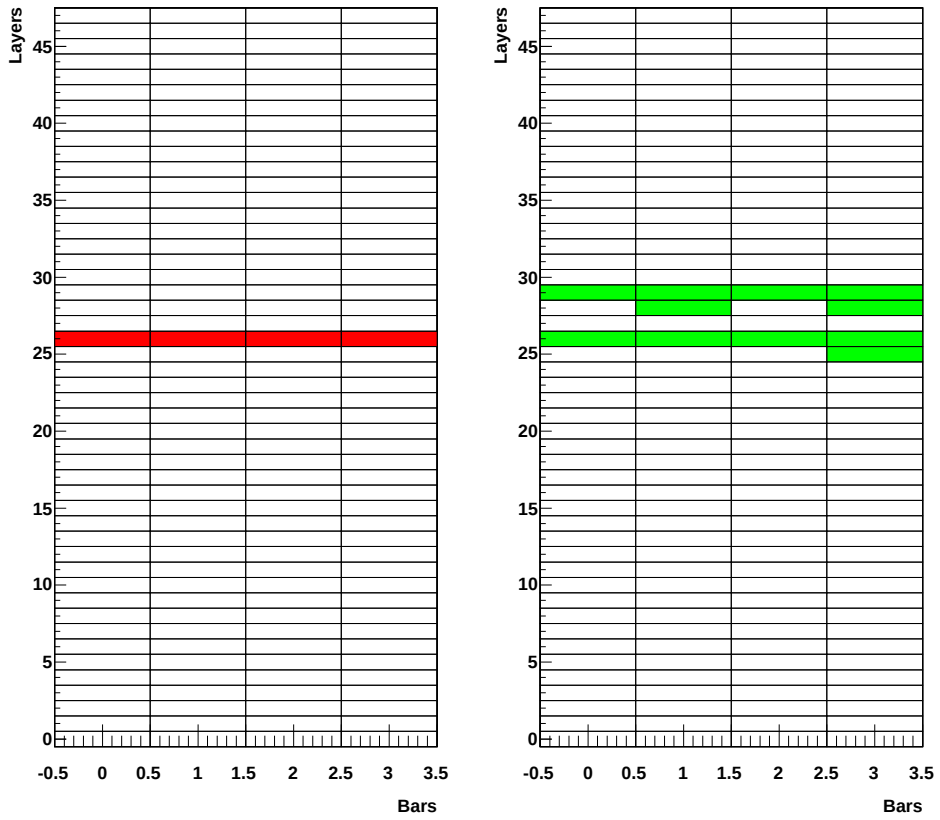

(a) (b)

Figure 3.46: Typical a) muon and b) electron events: the lead causes a shower in the electron case. The beam comes from the left.

3.3.3 LEP simulation

A GEANT4 simulation has been developed both to confirm the experimental results at 1 GeV/c and to study the behavior of LEP at a lower momentum (the 150 MeV/c momentum value has been chosen as an example). For the first goal, the simulation has been tuned on the T9 beam features:

- beam size (RMS): 2.3 cm in the X direction, 3.8 cm in the Y one; the beam is generated 1.5 m before LEP, according to the fact that the Cherenkov detector is placed at this distance;
- divergence (RMS): 9 mrad in the horizontal direction, 5.7 mrad in the vertical one;

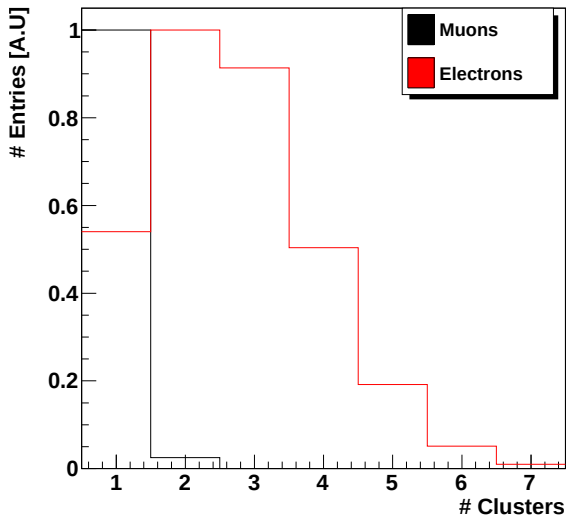

Figure 3.47: The number of clusters in the first layer for muons (black) and electrons (red).

- momentum: 1 GeV/c with a spread of 1%. The nominal spread should be 0.3% [90]; the selected value is conservative and takes into account the presence of the material due to the beam instrumentation;

- particle type: two beams have been generated: 1 million events of muons and 1 million of electrons; according to the beam features, about 56% of each beam hits the first layer of LEP. The percentage of the particles that compose the beam is 33.1% of muons and 65.9% of electrons, as in the experimental case.

A typical muon and electron event at 1 GeV/c are shown in figure 3.48. As expected, a muon crosses the whole detector and releases its energy behaving like a MIP; on the other hand, an electron has an energy deposit characterized by a large number of gammas.

Figure 3.49(a) shows a lateral view of LEP: for mechanical constraints it has been assembled in three blocks (16 layers each) and a space of 1 cm between two contiguous blocks. Moreover, in order to identify the events in the central beam region, a very thin scintillator layer (100 μm thick) has been simulated in front of the first LEP layer (in red in figure 3.49(b)). The thickness has been chosen in order not to disturb the measurement causing a large energy loss or increasing the muon decay probability.

To give some numbers:

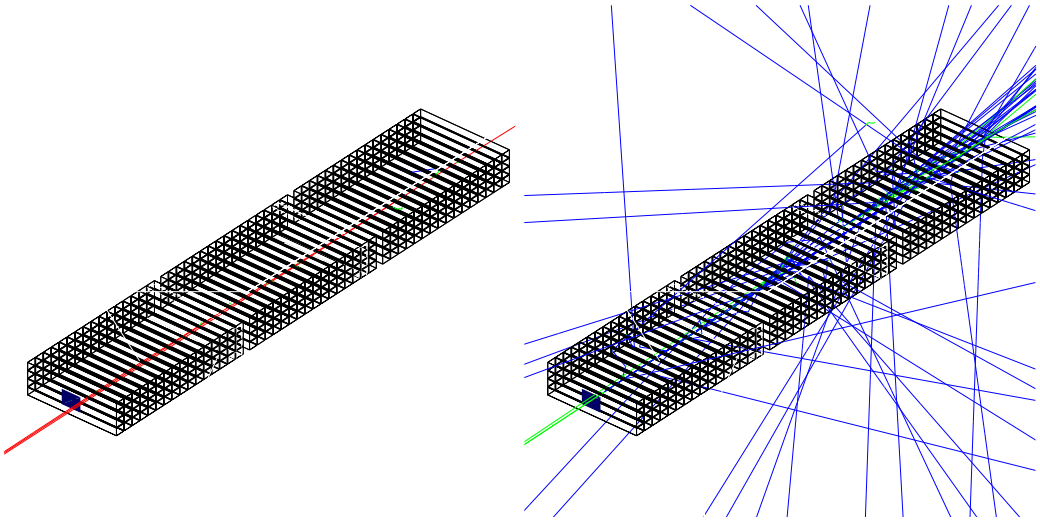

(a) (b)

Figure 3.48: Typical a) muon and b) electron simulated events at 1 GeV/c: muons are drawn in red, electrons in green and gammas in blue.

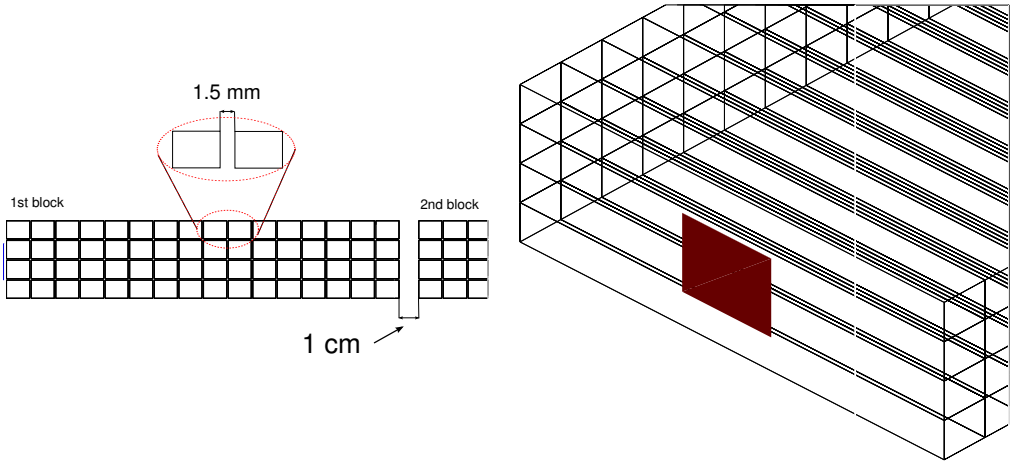

(a) (b)

Figure 3.49: a) LEP is made of three blocks of 64 bars (16 layers) with a space of 1 cm between contiguous blocks and one of 1.5 mm between two adjacent bars (in both directions). b) A very thin scintillator plate (in blue) is placed in front of the first layer to identify the target area used in the experimental analysis.

- about 560000 particles (over 1 million generated) of each type hit the first LEP layer;

- to maintain the experimental beam type percentage, about 285000 muons and 560000 electrons have been analyzed;
- for each particle type, 30% hits the target area;
- 0.3% of the remaining muons decays in electrons before hitting the detector.

Total energy

The total energy measured by LEP is presented in figure 3.50(a) and should be compared with the experimental data shown in figure 3.41(b). The distributions

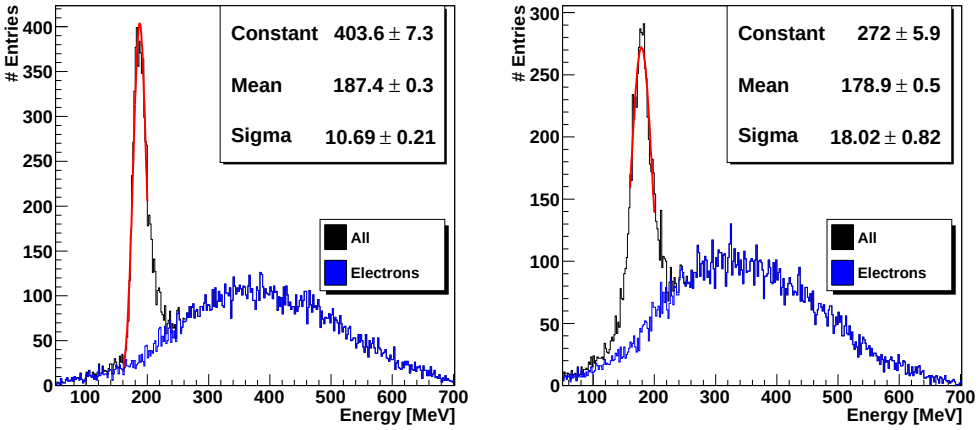

(a) (b)

Figure 3.50: The total energy measured by LEP considering only the events which hit the target area with a) no space or b) a 1.5 mm region between the bars (with more statistics). The blue histograms are the ones due to the electrons.

are very similar, but it is important to note that the simulated MIP peak is narrower than the experimental one. This is independent from the momentum spread if it is smaller than 10% (in any case the momentum spread on the T9 line is smaller than 1% [90]). The main reason of the experimental larger peak is the detector leakage due to the bars inefficiency (e.g. the events on the edge or the space between two bars). For this reason, the simulation has been tuned inserting a dead region among the bars, computed taking into account the spread of the real peak (the RMS is 10.38% of the mean value, figure 3.41(b)): with no space between the bars, the RMS/mean ratio is 6.23%, while a value of about 10% (figure 3.50(b)) is reached considering a space of 1.5 mm. A detailed view of the new simulated LEP geometry is presented in figure 3.49(a).

The purity as a function of the efficiency has been computed with these adjustments (figure 3.51(a)). The very small difference between the muon/electron

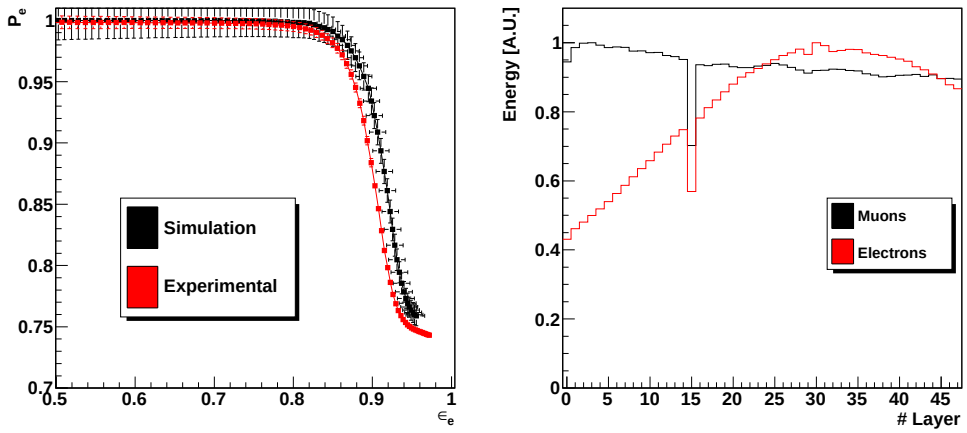

(a) (b)

Figure 3.51: a) The electron purity as a function of the efficiency for experimental (red) data, a muon/electron simulated beam (black) and a mixed (muons, electrons and pions) one (blue). b) The energy measured by each layer (normalized to the bin with the largest value).

beam (in black) and the experimental data (red) can be explained by several factors:

- the Cherenkov efficiency is not 100% (figure 3.35);
- the bar inefficiency: an empirical method has been used to evaluate the distance between two bars, but the intrinsic chain (bar + fiber + MAPMT pad) inefficiency has not been taken into account.

Energy per layer

The energy measured by each layer is presented in figure 3.51(b): differently from the experimental data (figure 3.43(a)), both the muon 10% continuous energy loss and the peak due to the electrons (with a maximum around layer number 32) are visible. The layer with the largest energy deposit for muons and electrons is presented in figure 3.52(a): muons have a uniform distribution, while the electrons generate an electromagnetic shower. The energy loss corresponding to layer 15 (first plane of the second block) is due to the gap among the LEP main blocks.

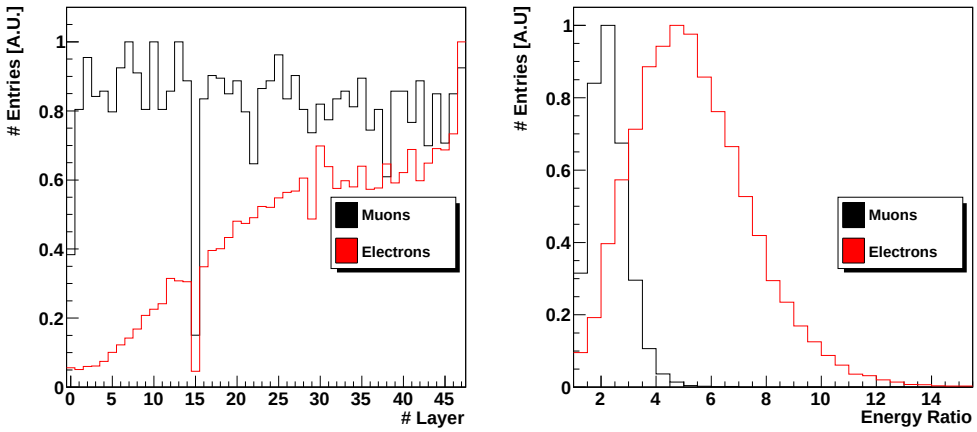

(a) (b)

Figure 3.52: a) The layer with the largest energy deposit and b) the ratio between the energy of this layer and the one of the first layer in simulation. The data have been normalized to the bin with the largest value.

The ratio of the energy of the layer with the maximum and the first one is shown in figure 3.52(b) and it is perfectly comparable with the experimental one (figure 3.44).

3.3.3.1 Predictions at lower momenta

Starting from the simulation developed at 1 GeV/c, a new simulation with the same beam parameters and detector geometry has been performed using a momentum value of 150 MeV/c. This section is not devoted to developing a new method to distinguish muons and electrons at lower momenta, but just to showing the major differences with respect to the previous results.

The total energy is presented in figure 3.53(a): it has to be compared with the experimental (figure 3.41(b)) and simulation (figure 3.50(b)) data obtained at larger momentum. At lower energy LEP is not able to discriminate muons from electrons using this quantity.

However a big difference occurs in the energy per layer distribution (figure 3.53(b)): as expected, muons deposit energy with a Bragg-peak law, so the layer with the maximum deposit can be used to discriminate the two particles (figure 3.54(a)).

As already stated, the energy ratio distribution al lower momenta becomes one of the most powerful discrimination variables: if at a momentum value of 1 GeV/c the muon ratios were lower than the electron ones given the continuous

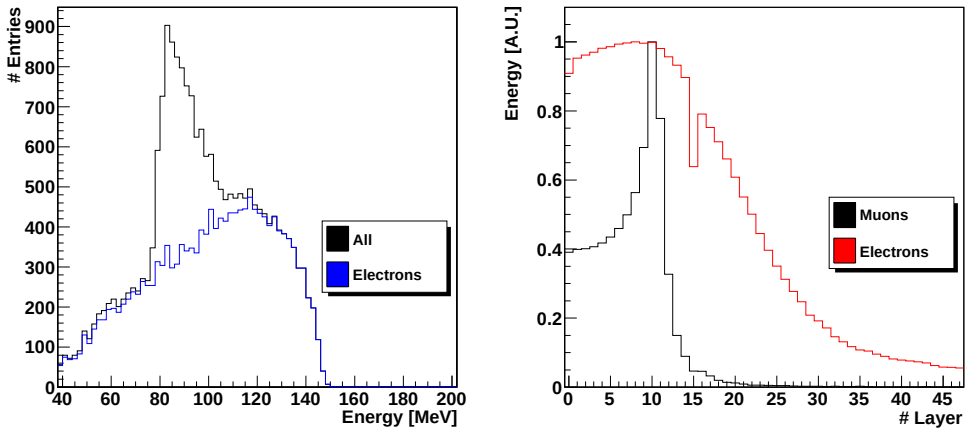

(a) (b)

Figure 3.53: a) The total energy and b) the energy per layer for a 150 MeV/c beam. In the second plot, data have been normalized to the bin with the largest value.

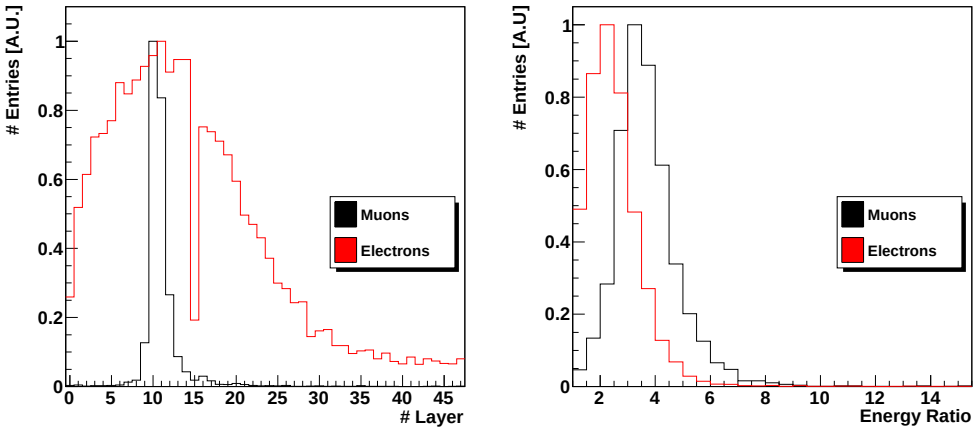

(a) (b)

Figure 3.54: a) The layer with the largest value and b) the ratio between the energy of this layer and the one of the first layer with a 150 MeV/c beam. Data have been normalized to the bin with the largest value.

energy loss, in this case (figure 3.54(b)) the opposite occurs given the Bragg-peak distribution. The MICE collaboration intends to use this variable in the analysis and the expected results obtained with a simple simulation are presented in the next chapter.

Chapter 4

The EMR simulation

MICE intends to measure the muon emittance reduction with a precision of 0.1%. For this reason a particle identification system is foreseen to discriminate muons from the background, consisting mainly of pions and electrons or positrons, depending on the muon sign. In particular the muon-electron discrimination is performed by a TOF system, the KLOE-Light calorimeter and the Electron Muon Ranger. The performance of the complete MICE line (and in particular of the particle-ID system [9]) is being studied with the help of G4MICE [76], a dedicated version of the GEANT4 [77] simulation software.

On the other hand the results presented in this chapter have not been obtained in G4MICE (under the responsibility of a dedicated MICE group), but with a very simple GEANT4 simulation: the goal is not to present the performance of the particle-ID system, but only the behavior of EMR as far as the muon-electron discrimination is concerned. This task has been studied in two ways: one (from now on identified as "EMCal") foresees the presence of EMR and a passive pre-shower to apply the algorithms used by the MICE collaboration; the other ("EMR-only") is based on kinematic cuts using only EMR (that is without the pre-shower) in order to identify other possible variables that can be used by the collaboration and to describe the behavior of EMR for future applications.

Both the studies have considered beams of different momenta. Given the study of the KL+EMR system is one of the activities of the MICE collaboration, only the second method has been deeply investigated varying the charge of the incoming particles and the beam geometrical features.

4.1 EMR and the beam

As already described in chapter 2, the EMR detector consists of 48 planes of extruded 1.1 m long scintillating bars arranged in a x-y geometry; each plane is made

of 59 triangular bars which have been simulated as being made of polystyrene only. Figure 4.1(a) presents the schematic view of the EMCal setup, while the EMR-only one is shown in figure 4.1(b). KL is placed about 50 cm before EMR.

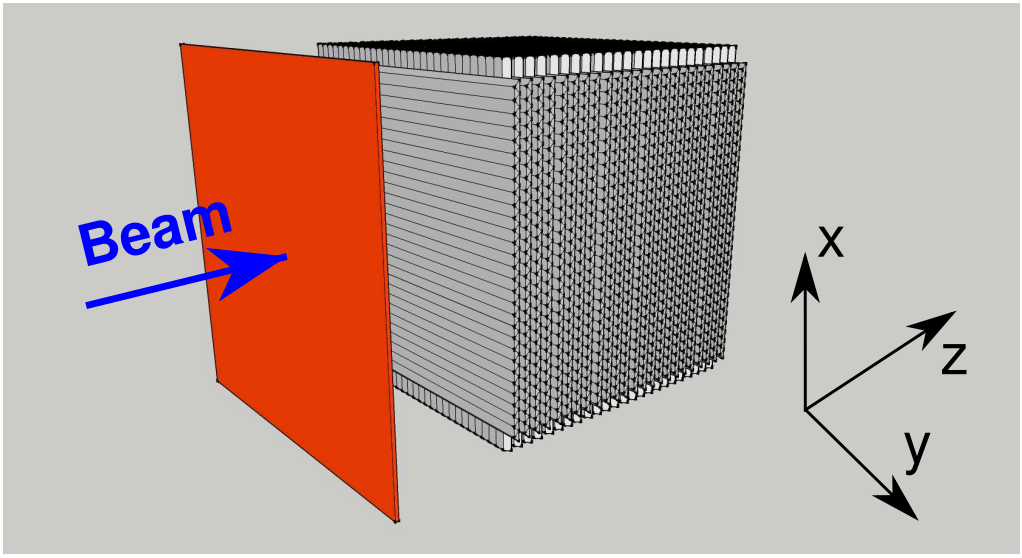

(a)

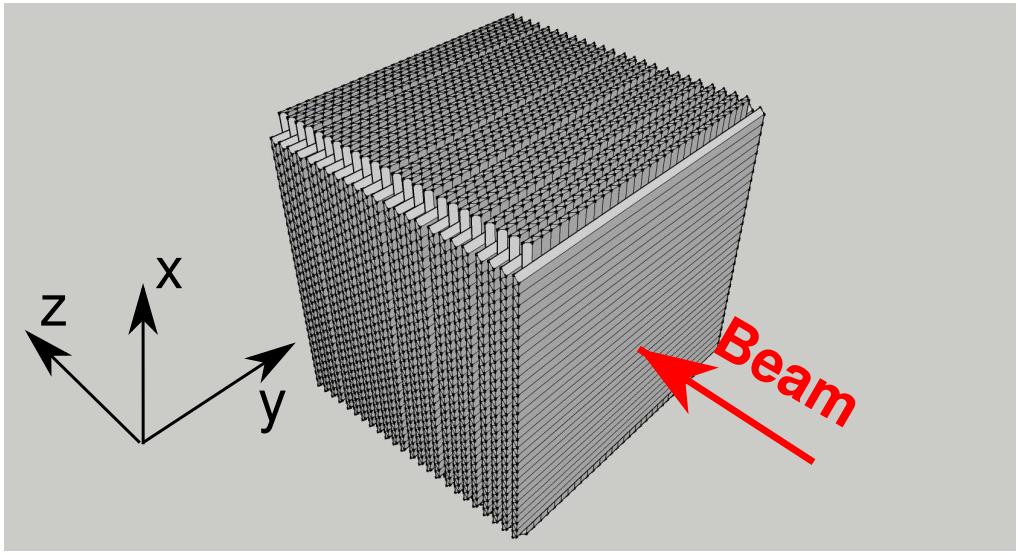

(b)

Figure 4.1: A schematic view of a) the EMCal (with KL in red) and b) the EMR-only simulated systems.

In MICE 80% of the muon-electron discrimination is based on kinematic cuts applied on the information collected by the TOF system; the remaining 20% is

covered by the KLOE-Light detector and EMR. EMR should be able to discriminate muons from electrons in the range 140-240 MeV/c; the incoming muon beam is expected to have a momentum spread of the order of 10%, a RMS (in both directions) of the order of 5 cm and a divergence RMS of the order of 150 mrad [47]. Electrons (or positrons) are produced from the muon decays, so their features are not so easy to describe analytically.

Figures 4.2(a) and 4.2(b) present the beam size and divergence of an incoming muon beam as measured by the first modules of EMR for the largest momentum value (240 MeV/c); both the directions are presented in the plots. The figures

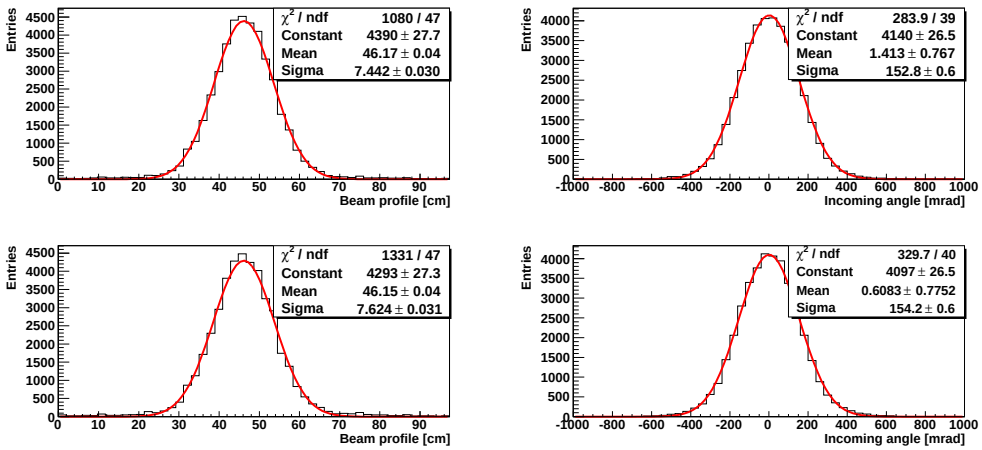

(a) (b)

Figure 4.2: a) The geometrical and b) the divergence distributions of the incoming muon beam in both the directions. The beam size has been measured with the first module (first two planes), while the divergence with the first two modules (using planes 1 and 3 for the X direction and planes 2 and 4 for the Y one).

have been obtained in a preliminary simulation phase generating the beam about 10 cm before the first plane in order to study the EMR detection performance. In the final simulations (for both systems) the beams are generated 1 m upstream of EMR.

Four beams have been generated in the simulations: two muon beams (μ^+, μ^-) and two electron ones (e^+, e^-). As in MICE, the electron beams have been produced in-flight starting from an incoming muon beam: to increase the statistics, for CPU time reasons, the muon mean lifetime has been changed to 0.5 ns. As already stated, the term “electrons” identifies both electrons and positrons, if not otherwise indicated.

As far as the momentum is concerned, four momentum values are taken into account: 140, 170, 200, 240 MeV/c. For each value two different simulations

are performed: one with a momentum spread of 10% for both the simulation systems and the other without any momentum spread for the EMR-only setup (for a comparison with V. Verguilov [92]). The incoming momentum distribution for the 140 MeV/c case is presented in figure 4.3.

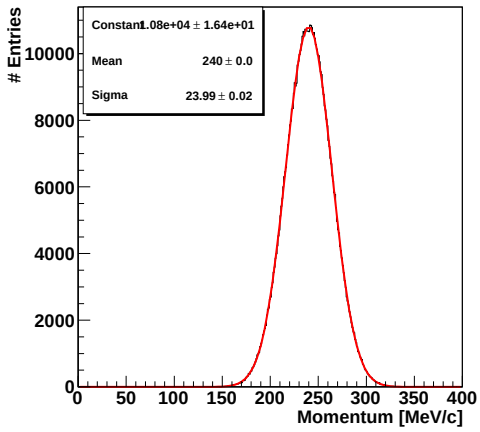

Figure 4.3: The incoming muon beam momentum distribution with a 10% spread.

For each value the Lorentz and β factors have been computed. The Lorentz factor (γ) is defined as:

$$E^2 = \gamma^2 m^2 c^4 = p^2 c^2 + m^2 c^4 \tag{4.1}$$

where E, p, m are the muon energy, momentum and mass respectively, and c the speed of light; the muon mass is 105.56 MeV/c^2 [53]. The β factor is defined as:

$$\beta^2 = \frac{v^2}{c^2} = 1 - \frac{1}{\gamma^2} \tag{4.2}$$

where v is the muon speed. Table 4.1 summarizes the values of the γ and β factors for each momentum value.

p [MeV/c]	γ	β
140	1.66	0.80
170	1.90	0.85
200	2.14	0.88
240	2.48	0.92

Table 4.1: The values of the γ and β factors for each momentum value.

EMR is a fully active detector that is able to measure the whole energy loss plane by plane with the single PMT and the energy of each bar with the MAPMT. The simulation does not take into account the light generation in the bar and its transport to the PMT, but uses directly the energy deposit value in the bar itself. In the MICE official simulation some important experimental effects that are not taken into account in the studies presented in this chapter have to be included; the most important ones are:

- the light dispersion and the cross-talk effects;
- the effect of the electromagnetic noise;
- the cuts on the MAPMT pulse heights to distinguish noise from signal.

These effects have to be taken into account and the final simulation has to be tuned on the experimental data. For these reasons, the efficiencies presented in the following sections are probably overestimated with respect to the experimental ones.

4.2 The EMCal system

The algorithm used by the MICE collaboration to discriminate muons from electrons with the EMCal system is based on two observables: one is related to the energy measured by each EMR layer, while the second depends on the particular pattern of the particle trajectory in the system. This second task is summarized in figure 4.4 which presents a typical muon event in the EMCal system: a muon crosses the KL layer and part of EMR before decaying. Muons deposit their energy with a Bragg-peak behaviour: the longitudinal position of the peak depends on the incoming momentum.

As far as the electrons are concerned, they are generated by in flight muon decays and a typical event is presented in figure 4.5. The electron generates an electromagnetic shower in KL whose photons are detected (together with electrons and positrons) by the first EMR layer.

The simulation numbers can be summarized as follows:

- muon beam: a 1 million event beam of muons is generated 1 m upstream of the first EMR layer. For each momentum value more than 99.9% of the muons hit KL (the rest decays before it);
- electron beam: 1 million muons with a lifetime of 0.5 ns are generated. The electrons at KL are more than 65%, and the percentage depends on the momentum value: the larger the momentum value, the larger the number of electrons given the larger probability to survive after the pre-shower;

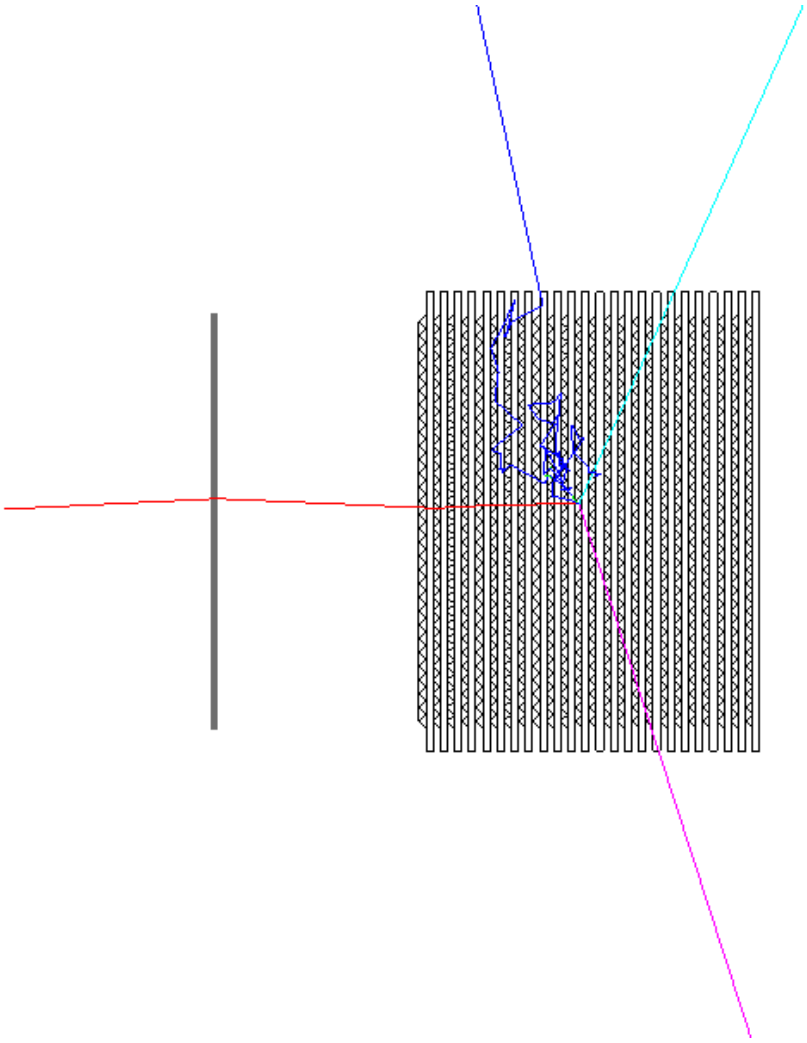

Figure 4.4: A typical 240 MeV/c muon event in the EMCal system: a muon (in red) crosses the KL layer (in gray) and part of EMR and then decays in one electron (in green) and two neutrinos (violet and cyan). A lot of gammas are produced (mainly by the electron) via bremsstrahlung and ionization.

- the same number (650000) of muons and electrons is taken into account in the analysis.

In the following, the results obtained applying the method used by the MICE collaboration are presented. Differently from the method developed with the EMR-only system (section 4.3), not all the possible cases of incoming emittance and particle charge have been studied since it is part of the work of a dedicated group of the MICE collaboration. Only negative particle beams with an incom-

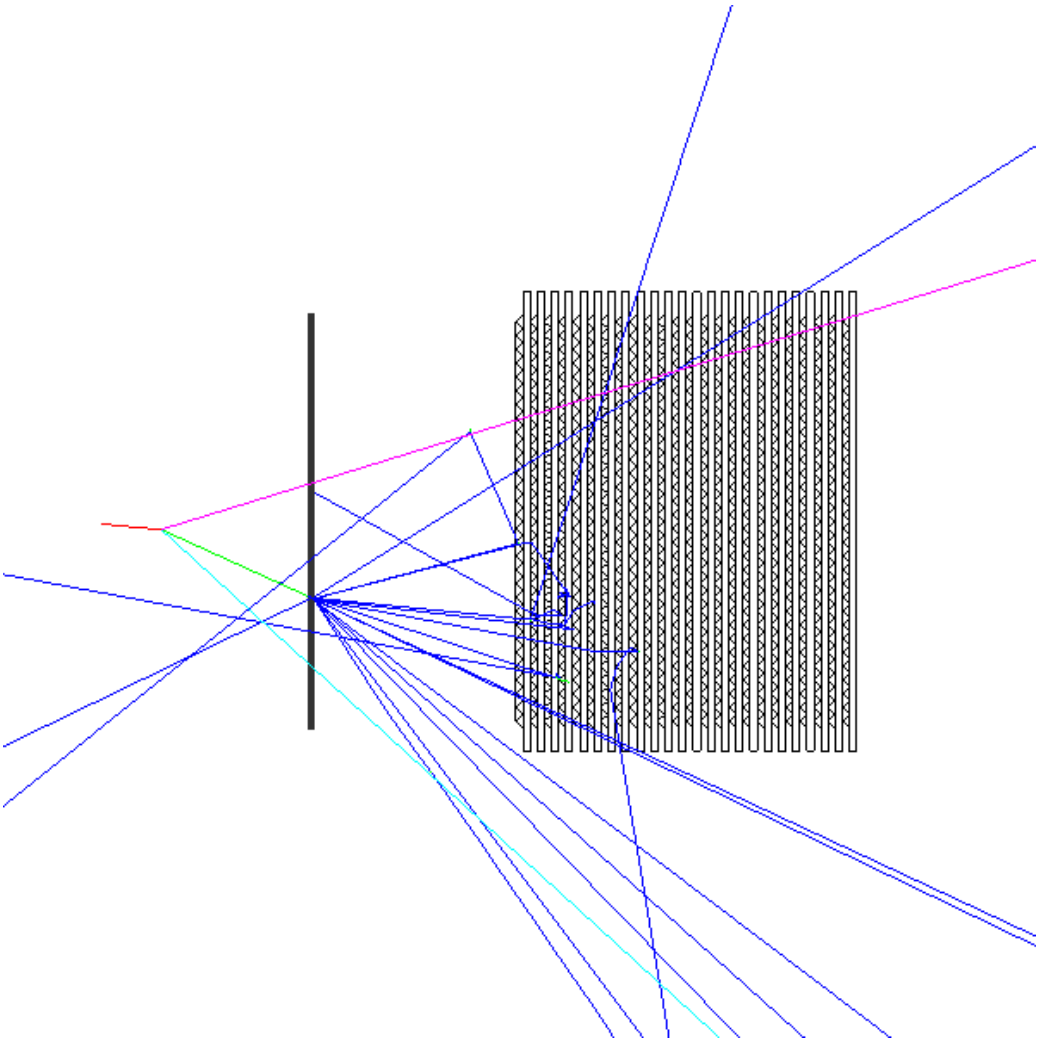

Figure 4.5: A typical electron event in the EMCal system: an electron (in green), produced by the muon decay (red), generates a shower in the KL detector that is detected by EMR.

ing emittance of 2.38π·mm·rad (divergence = 150 mrad, beam size = 5 cm) and a momentum spread of 10% have been considered. Moreover, if not otherwise indicated, the 240 MeV/c case is used to describe the results of the analysis.

The energy measured by each EMR layer is presented in figure 4.6(a). As expected, muons (black) release their energy following the Bragg-peak distribution, while the electrons (red) have a continuous energy loss. The plot considers the average distribution of all the events. Thus the number of the layer with the largest energy loss can be considered. In the muon case a peak appears (the mean

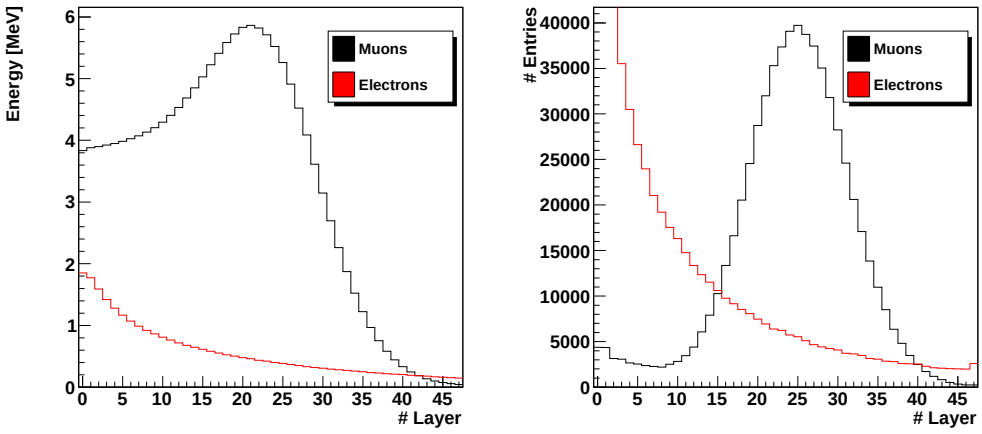

(a) (b)

Figure 4.6: a) The average energy per layer and b) the layer with the largest energy value for muons (black) and electrons (red) for all the events.

position depends on the incoming momentum), while in the electron one the first layer is the one with the largest energy deposit.

4.2.1 Energy ratio

The energy ratio is defined as the ratio between the energy of the layer with the largest energy loss and the one of the first layer; for muons it is presented in figure 4.7(a). To be more rigorous, in the plots the energy ratio (R_E) has been computed with the following definition:

$$R_E = \frac{E_{\text{max layer}} - E_{\text{first layer}}}{E_{\text{first layer}}} \tag{4.3}$$

The muon distribution presents two peaks: a larger one around 3 and a smaller one at about 0.5. The detector leakage is responsible of the small peak: if, for example, only the events that hit the first EMR module in a central region of 40×40 cm^2 are taken into account, the small peak disappears (the red distribution in figure 4.7(a)). The same conclusion can be reached considering the energy ratio distribution as a function of the number of the layer with the largest energy loss (figure 4.7(b)): the smaller peak corresponds to the first layers, the ones hit by particles before escaping the detector.

The comparison between the muon and electron distributions is presented in figure 4.8(a): as expected, this quantity is excellent for the discrimination. As presented in chapter 3, the discrimination capability can be quantitatively expressed

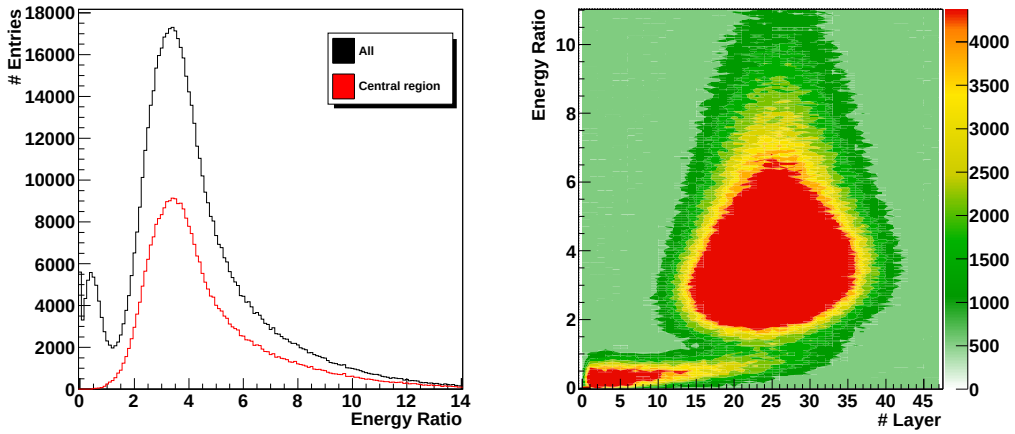

(a) (b)

Figure 4.7: The energy ratio distributions for muons considering all the events (black) and the events in a central EMR region (red). b) The energy ratio as a function of the layer with the largest energy loss.

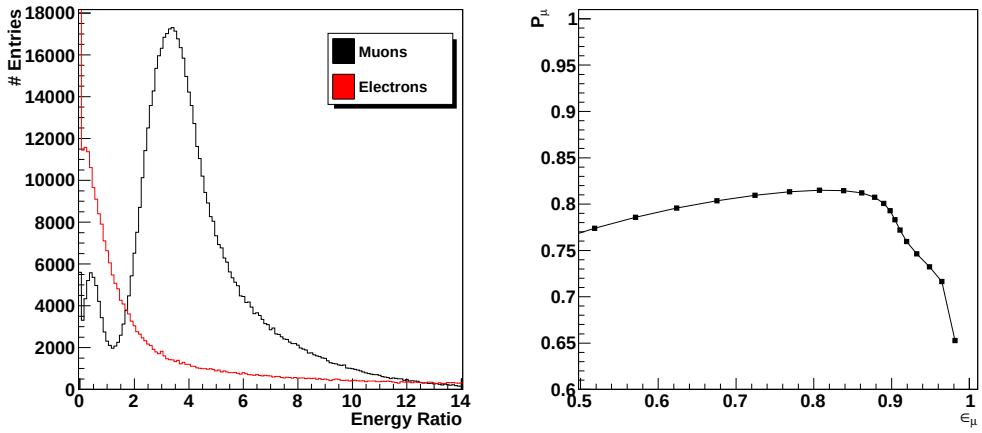

(a) (b)

Figure 4.8: a) The energy ratio distributions for muons (black) and electrons (red). b) The muon purity as a function of the efficiency considering only the first observable of the algorithm used by the MICE collaboration.

by the muon purity (P_μ) as a function of the efficiency (ϵ_μ) defined as:

$$P_\mu = \frac{N_\mu}{N_\mu + N_e}$$
$$\epsilon_\mu = \frac{N_\mu}{N_{tot}} \tag{4.4}$$

where N_{tot} is the number of generated muons that have been analyzed ($N_{tot} = 650000$), while N_μ and N_e are the number of muons and electrons in different energy ratio ranges. The errors on the two quantities have been computed according to equation 3.2. The ranges have been chosen keeping the upper bound fixed at R_e=40 and increasing the lower edge from 0 on. The muon purity as a function of the efficiency is presented in figure 4.8(b): the largest purity value ($P_{\mu,max} = 0.815 \pm 0.002$) is reached with an efficiency of $\epsilon_{\mu,max} = 0.807 \pm 0.001$.

4.2.2 Tracking

The second observable used by the MICE collaboration is based on the pattern recognition. Before decaying, a muon is expected to have a single track in the detector, while electrons generate a shower, so more particles have to be detected. In this thesis work the algorithm to identify all the particle tracks has not been developed: the method, in fact, requires also the information from KL which is not provided by this thesis simulation.

Some preliminary results can be obtained considering the EMR tracking capability, in particular the number of clusters and the number of bars per cluster. As already stated in chapter 3, a cluster is a group of contiguous bars which have measured a particle energy loss. In this particular case no cuts on the pulse height have been applied since no MAPMT noise has been simulated, thus no signal is present in the bars that have not been hit by particles.

The number of clusters for the first two EMR planes (the ones measuring the horizontal and vertical directions, respectively) for muons and electrons are presented in figure 4.9(a). As expected, muons are identified by a single cluster in the first layers, while electrons have a larger number of clusters per plane given the photons produced in the pre-shower. As far as the bars per cluster are concerned (figure 4.9(b)), given the particular bar shape, the expected value for a single cluster event is 2.

The muon purity as a function of the efficiency has been computed for the energy ratio variable including also the constraints that a muon event features a single cluster and two bars per cluster in the first two layers: the results for each momentum value are presented in figure 4.10. The following remarks hold:

- even without considering the kinematic cuts (provided by the TOF system) and the KL information, for higher momenta the purity reaches large numbers (close to the required value of 99.93%) maintaining the efficiency larger than 50%;

- at smaller momenta the presence of KL reduces the muon-electron discrimination capabilities of EMCal since part of the energy is lost in the pre-

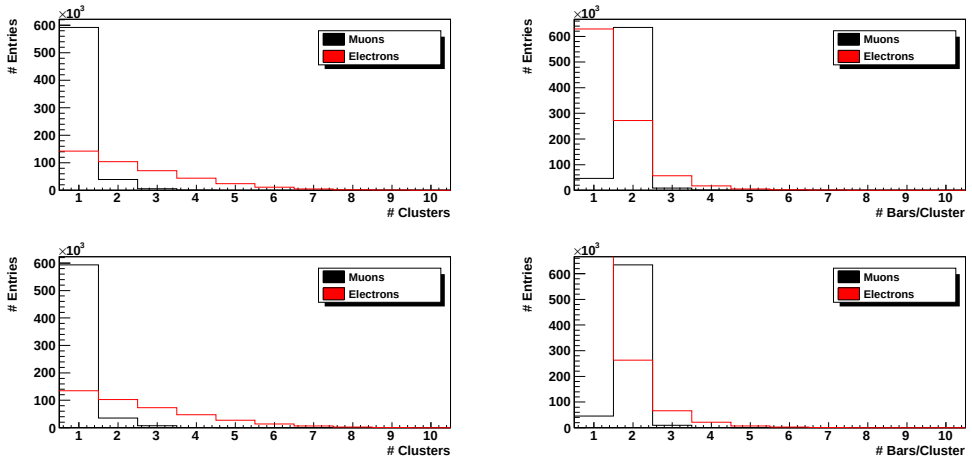

(a) (b)

Figure 4.9: a) The number of clusters and b) the number of bars per cluster for muons (black) and electrons (red) computed in the first EMR module: the top plots refer to the X direction (first plane), while the bottom plots to the Y one (second plane).

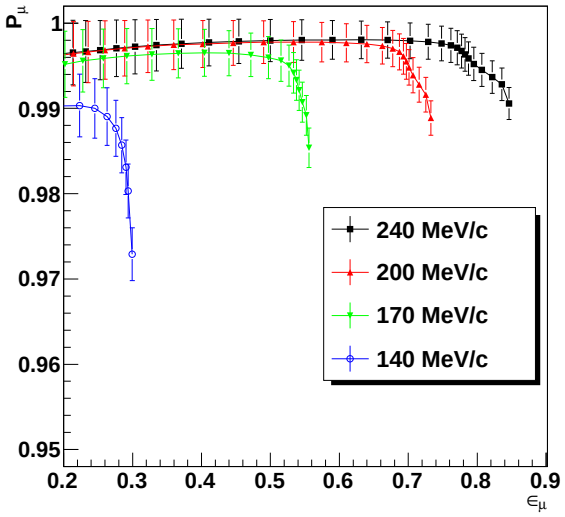

Figure 4.10: The muon purity as a function of the efficiency for four momentum values considering the algorithm used by the MICE collaboration.

shower itself. A possible solution could be to use only EMR as presented in the next section.

4.3 The EMR-only system

This section deals with a preliminary study of a possible method to distinguish muons from electrons using only EMR. The goal is twofold:

- to study the performance of a fully active scintillator detector for future applications;
- to investigate another possible algorithm that can be used in MICE in a wide range of momenta.

As already stated, the analysis on the EMCal simulation (presented in the previous section) is performed by a dedicated group of the MICE collaboration, so not all the possible beam cases have been considered in this thesis work. Viceversa, all possible beam cases have to be considered to illustrate the discrimination capabilities with the newer algorithm presented in this section, the one developed with the new detector system (the EMR-only one). Thus positive and negative particles, four momentum values without or with a 10% of momentum spread and two different emittance values (3π and 6π·mm·rad) have been simulated. The beams without a momentum spread have been used to show the discrimination in a limit case and to compare the data with some preliminary ones presented in [92].

Since the major problems in the EMCal system occur at smaller momenta, the μ^+ 140 MeV/c case has been chosen as an example to present the analysis.

As already stated, for the Bethe-Bloch theory a muon with a momentum in the range 140-240 MeV/c loses its energy with a distribution presenting the characteristic Bragg peak. Figure 4.11 summarizes the deposited energy for the different momenta as a function of the layer number (and thus of the amount of crossed material). Figure 4.11(a) shows the results obtained with four different momenta with no spread, while figure 4.11(b) presents the same data considering a momentum spread of 10%. Both the distributions have been computed considering all the events. From the figures it is possible to assert that the number of scintillating layers in EMR is large enough to stop the particle also without KL.

The corresponding results for the electron case are shown in figure 4.12: as expected, muons and electrons have different behaviors in the detector. It is important to note that the distributions in figure 4.12 are quite similar: the original muon momentum spread is a negligible contribution to the momentum distribution of the final electron beam. The comparison of the energy loss per layer for muons and electrons is presented in figure 4.13.

The new discrimination algorithm developed in this work requires the definition of a series of kinematic variables depending either on the calorimeter capability or on the particle tracking; no pattern recognition has been taken into consideration.

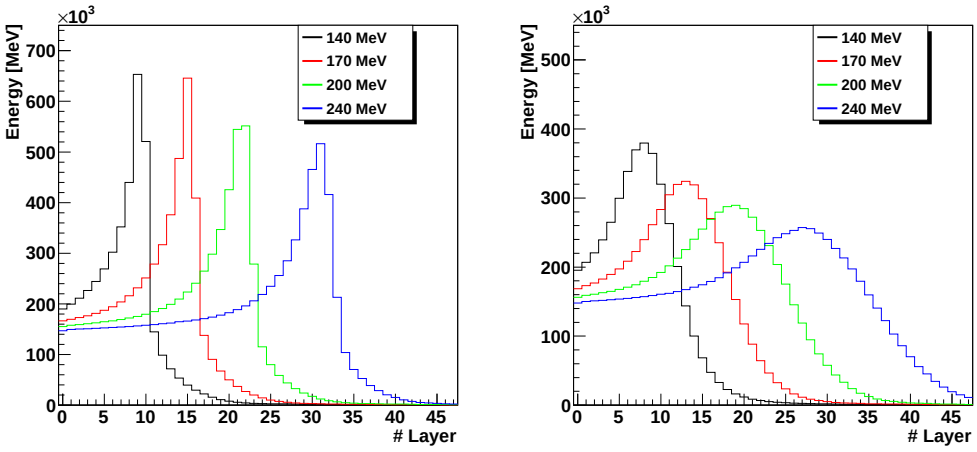

(a) (b)

Figure 4.11: The energy loss distributions as a function of the layer number for muons with five different momenta without (a) and with (b) a momentum spread considering all the events (that is the energy on the vertical axis is the sum of the energy of all the simulated events).

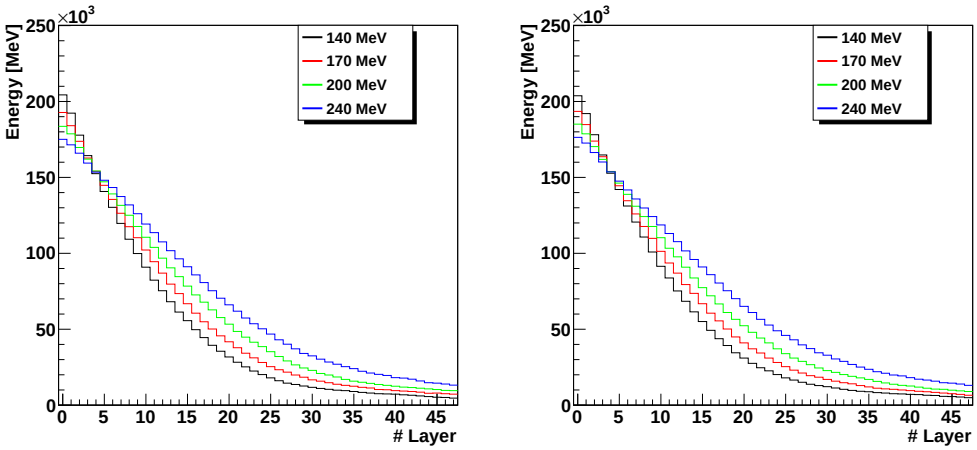

(a) (b)

Figure 4.12: The energy loss distribution as a function of the layer number for electrons generated in the muons decay for five different momenta. The original muon beams are generated without (a) and with (b) a momentum spread.

Such kinematic variables are the following:

- the *total energy* to measure the energy deposited in the whole EMR;

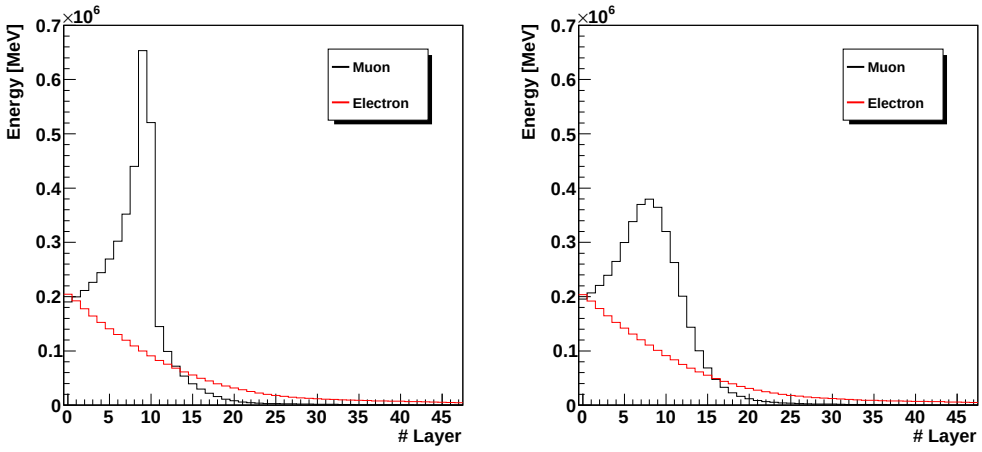

(a) (b)

Figure 4.13: The energy loss as a function of the layer number for 140 MeV/c muon and electron beams, without (a) and with (b) the momentum spread.

- the *six-plane energy* to measure the energy loss in a block of six layers;
- the *maximum layer* to identify the number of the layer which detects the largest energy loss;
- the *hit bars* to identify the number of bars hit by each particle;
- the *angular distribution* to measure the divergence of the beam in the front layers.

The first three variables are pure calorimetric ones (based on the longitudinal segmentation), while the last two require a fine transversal segmentation (the tracking geometry).

For each variable the muon and the electron distributions are shown; the analysis is divided in two phases:

1. a particular variable range in which the muon distribution is clearly different from the electron one is selected and three efficiencies are computed;
2. the variable range is varied and the purity (P_μ) as a function of the muon efficiency (ϵ_μ) is evaluated.

Focusing on the first issue, the three efficiencies are defined in the following way:

- the discrimination inefficiency (ϵ_D) is the ratio between the electrons (N_e) and muons (N_μ) present in a given variable range (identified in the plots by the blue lines):

$$\epsilon_D = \frac{N_e}{N_\mu}$$

- the electron rejection inefficiency (ϵ_e) is defined as the ratio between the electrons in a variable range and the total number of generated ones:

$$\epsilon_e = \frac{N_e}{N_{tot}}$$

- the muon efficiency (ϵ_μ) is defined as the ratio between the muons in a variable range and the total number of generated ones:

$$\epsilon_\mu = \frac{N_\mu}{N_{tot}}$$

The error on the efficiency is evaluated with equation 3.2.

In the following sections, the efficiencies and the purity obtained with each kinematic variable are presented: the cuts have been applied independently for each variable starting from the original data sample. The results obtained with all the variables used at the same time are described in the last section.

4.3.1 The total energy

The total energy distributions for muons and electrons are presented in figure 4.14 and are computed as the sum of the energy deposited in each EMR bar. In EMR the total energy can be measured in two ways: using the information of the single PMTs or using the data collected by each single bar.

Table 4.2 summarizes the electron inefficiency and muon efficiency for the μ^+ case. This kinematic variable is efficient for higher momentum values and similar results are obtained for an emittance of 6π·mm·rad and for the μ^- case.

The purity as a function of the muon efficiency for the total energy variable is presented in figure 4.15.

4.3.2 The six-plane energy

The second kinematic variable is the total energy measured in a block of six layers: since EMR consists of 48 planes, 8 distributions have to be considered. The number of layers (6) per block has been chosen considering the distribution in figure 4.11(b): a smaller number would result in the non-inclusion of the muon Bragg

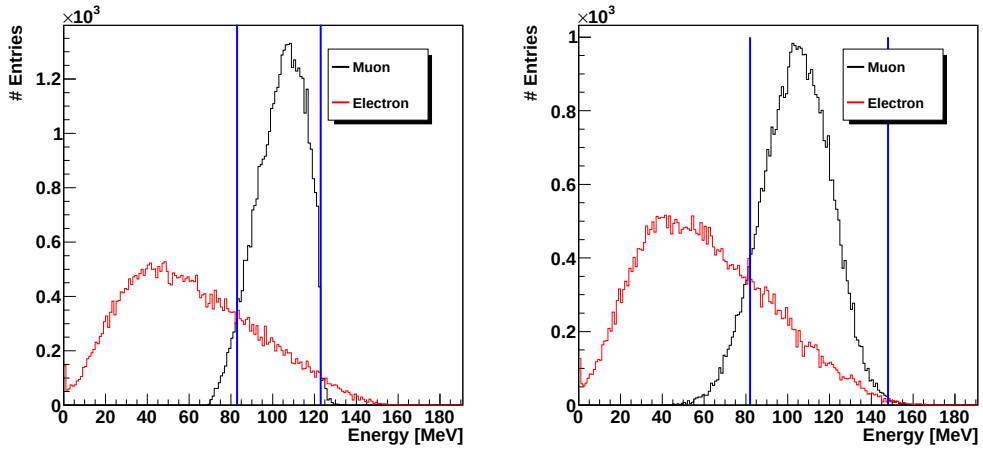

(a) (b)

Figure 4.14: The distributions of the total energy deposited by muons (black) and electrons (red) a) without and b) with a momentum spread. The blue lines identify the kinematic cuts.

μ	Emittance [mm · rad]	Momentum [MeV/c]	ϵ_e **(%)**	ϵ_μ **(%)**
+	3π	140 (NS)	21.36 ± 0.25	94.56 ± 0.68
+	3π	170 (NS)	15.13 ± 0.21	97.28 ± 0.69
+	3π	200 (NS)	10.43 ± 0.17	98.28 ± 0.70
+	3π	240 (NS)	6.63 ± 0.13	99.27 ± 0.70
+	3π	140 (S)	24.98 ± 0.28	90.46 ± 0.66
+	3π	170 (S)	18.86 ± 0.24	93.31 ± 0.67
+	3π	200 (S)	15.04 ± 0.21	95.20 ± 0.68
+	3π	240 (S)	11.36 ± 0.18	96.68 ± 0.69

Table 4.2: The electron inefficiency and muon efficiency after the total energy cut for an incoming μ^+ beam. These data have been collected for each momentum value and considering the distributions without (NS) and with (S) a 10% momentum spread for an emittance of 3π·mm·rad.

peak, while a larger one would take into account the events out of the peak. The position of the six-plane block varies as a function of the momentum: for example for the 140 MeV/c case the second block (the layers from 7 to 12) is considered, for the 240 MeV/c the fifth block (planes 37-42) and so on. The distributions for the first case are shown in figure 4.16.

This variable is more efficient with respect to the total energy one since it is

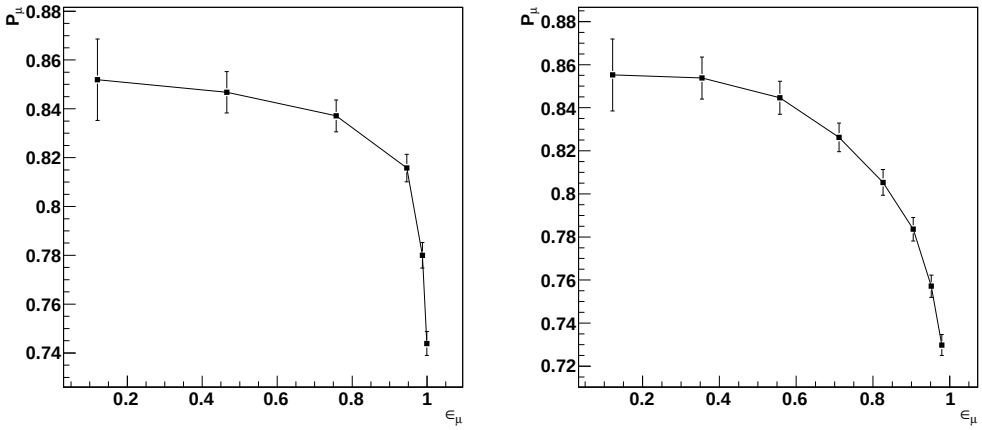

(a) (b)

Figure 4.15: The purity as a function of the muon efficiency for the total energy variable for the beams a) without and b) with a momentum spread.

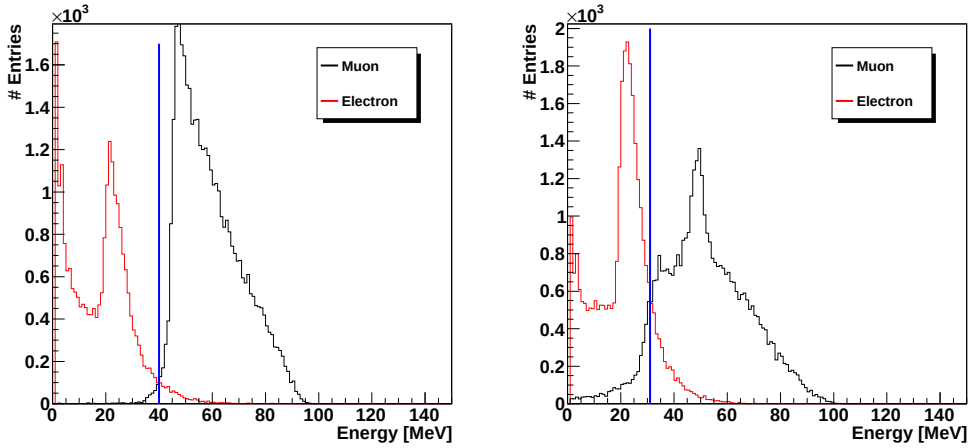

(a) (b)

Figure 4.16: The distributions of the six-plane energy measured for 140 MeV/c muons (black) and electrons (red) a) without and b) with a momentum spread. The blue lines identify the kinematic cuts.

chosen depending on the momentum value, as presented in table 4.3 for the μ^+ case; no differences are found for the μ^- case or for beams with an emittance of 6π·mm·rad.

This cut is particularly effective, as shown by the purity as a function of the muon efficiency presented in figure 4.17.

μ	Emittance [mm · rad]	Momentum [MeV/c]	ϵ_e **(%)**	ϵ_μ **(%)**
+	3π	140 (NS)	1.88 ± 0.07	99.42 ± 0.70
+	3π	170 (NS)	2.01 ± 0.07	99.08 ± 0.70
+	3π	200 (NS)	1.67 ± 0.07	99.10 ± 0.70
+	3π	240 (NS)	5.91 ± 0.13	99.53 ± 0.70
+	3π	140 (S)	9.74 ± 0.16	90.17 ± 0.65
+	3π	170 (S)	9.76 ± 0.16	82.55 ± 0.61
+	3π	200 (S)	10.29 ± 0.17	81.98 ± 0.61
+	3π	240 (S)	12.79 ± 0.19	91.61 ± 0.66

Table 4.3: The electron inefficiency and muon efficiency after the six-plane energy cut for an incoming μ^+ beam.

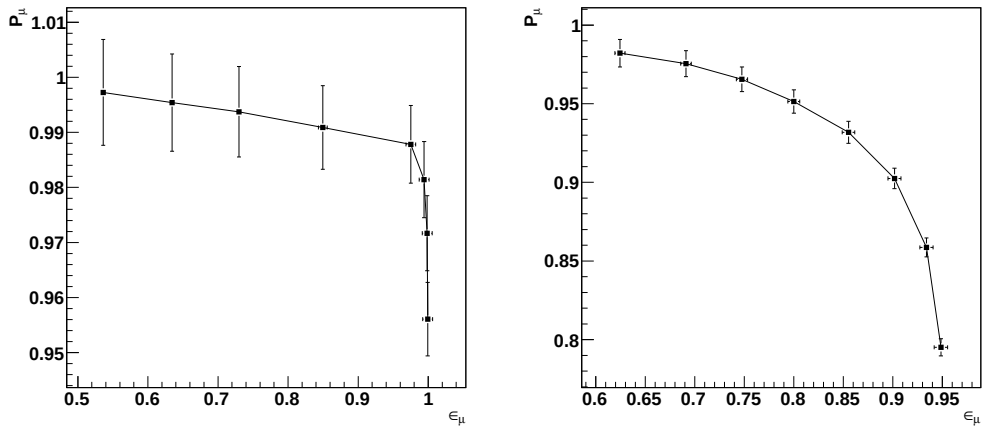

(a) (b)

Figure 4.17: The purity as a function of the muon efficiency for the six-plane energy variable for the beams a) without and b) with a momentum spread.

4.3.3 The maximum layer

According to the analysis presented in chapter 3 and section 4.2, the distribution of the layer measuring the largest energy loss can be used to discriminate muons and electrons as presented in figure 4.18.

Table 4.4 summarizes the results obtained for the μ^+ case; no differences are present in the μ^- case or for beams with an emittance of 6π·mm·rad.

The purity as a function of the muon efficiency for the maximum layer variable is presented in figure 4.19.

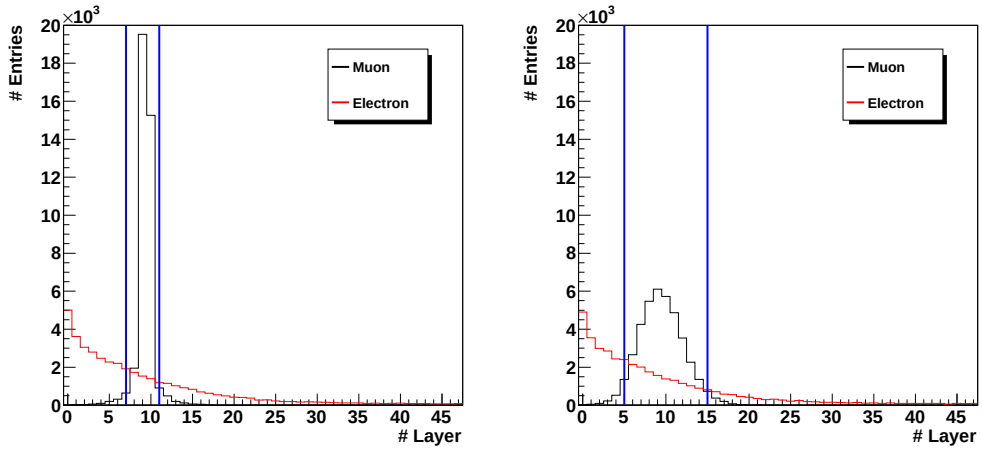

(a) (b)

Figure 4.18: The distributions of the layer number with the largest energy loss for muons (black) and electrons (red) a) without and b) with a momentum spread. The blue lines identify the kinematic cuts.

μ	Emittance [mm · rad]	Momentum [MeV/c]	ϵ_e **(%)**	ϵ_μ **(%)**
+	3π	140 (NS)	11.64 ± 0.18	91.84 ± 0.66
+	3π	170 (NS)	8.64 ± 0.15	93.12 ± 0.67
+	3π	200 (NS)	8.02 ± 0.15	96.28 ± 0.69
+	3π	240 (NS)	5.23 ± 0.12	96.57 ± 0.69
+	3π	140 (S)	33.10 ± 0.33	90.60 ± 0.66
+	3π	170 (S)	28.33 ± 0.30	93.09 ± 0.67
+	3π	200 (S)	22.52 ± 0.26	93.42 ± 0.67
+	3π	240 (S)	17.73 ± 0.23	94.11 ± 0.68

Table 4.4: The electron inefficiency and muon efficiency after the maximum layer cut for an incoming μ^+ beam.

4.3.4 The hit bars

The fourth observable is the number of bars which have detected an energy loss in the 48 layers: the distributions for positive muons and positrons are shown in figure 4.20.

The contribution of each particle type can be evaluated with the help of the simulation: the black plot in figure 4.20(a) (also presented in figure 4.21(a)) is the sum of the bars hit by positive muons, positrons and photons (plots b, c and

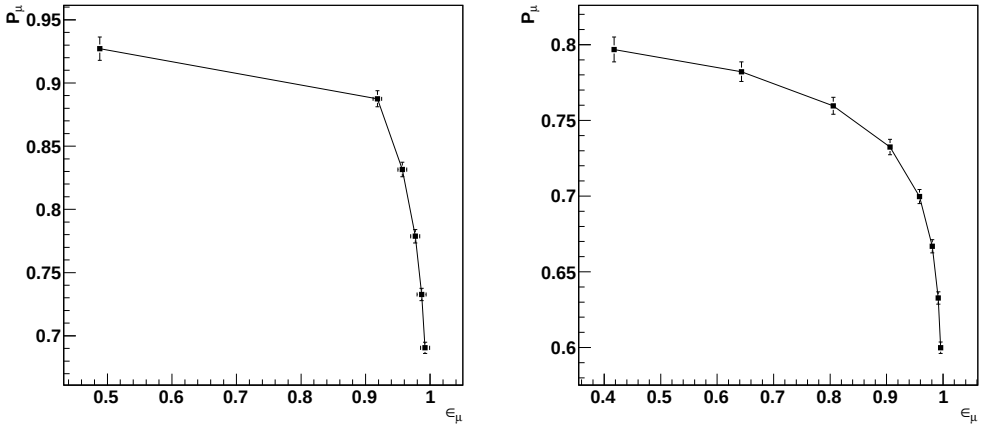

(a) (b)

Figure 4.19: The purity as a function of the muon efficiency for the maximum layer variable for the beams a) without and b) with a momentum spread.

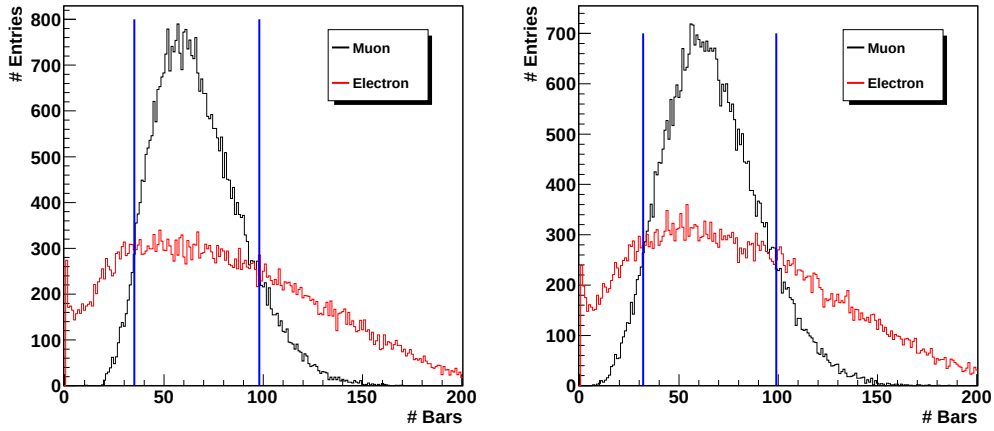

(a) (b)

Figure 4.20: The number of bars which have detected an energy loss for positive muons (black) and positrons (red) a) without and b) with a momentum spread.

d respectively in figure 4.21). A positive muon hits a certain number of bars (in this case $\sim$ 21, figure 4.21(b)) before decaying inside EMR; the generated positron loses energy in different bars depending on its original momentum and the ionization probability (figure 4.21(c)). The positron distribution presented in figure 4.20(a) (in red) is the result of the sum of the positron and photon plots presented in figures 4.21(c) and 4.21(d).

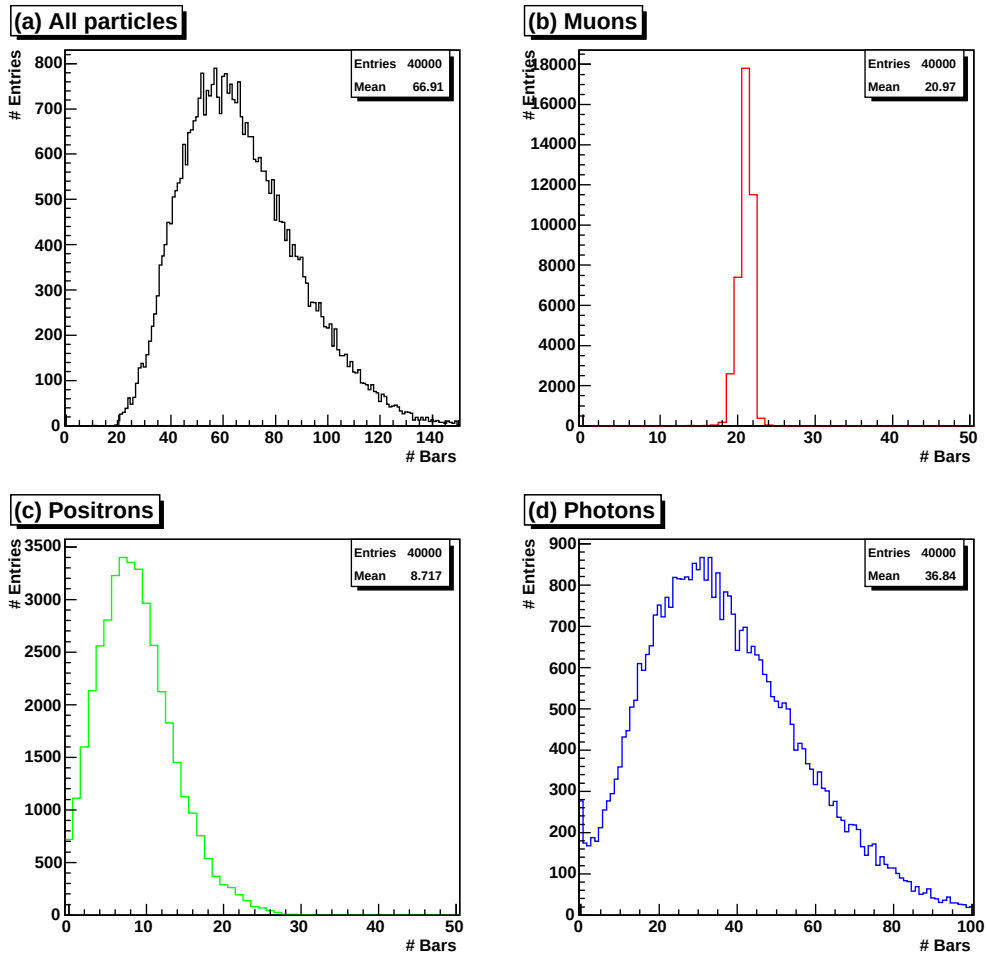

Figure 4.21: The number of hit bars distribution (top left, a) for the μ^+ is the sum of the muons (top right, b), positrons (bottom left, c) and photons (bottom right, d) distributions.

The physical process that generates the hit bar distribution is different depending on the incoming particle charge sign. The difference can be explained by the annihilation: a positron annihilation occurs in EMR and produces two gammas (the large photon distribution in figure 4.21), while an electron loses its energy along its travel in matter, thus explaining the larger distribution for electrons with respect to the photon one in figure 4.22.

However the particle discrimination performance is independent from the muon sign: in other words the results obtained for the positive and negative cases are equivalent. Table 4.5 presents the efficiencies obtained in the μ^+ case, varying the incoming beam emittance, momentum value and spread. It is important to note

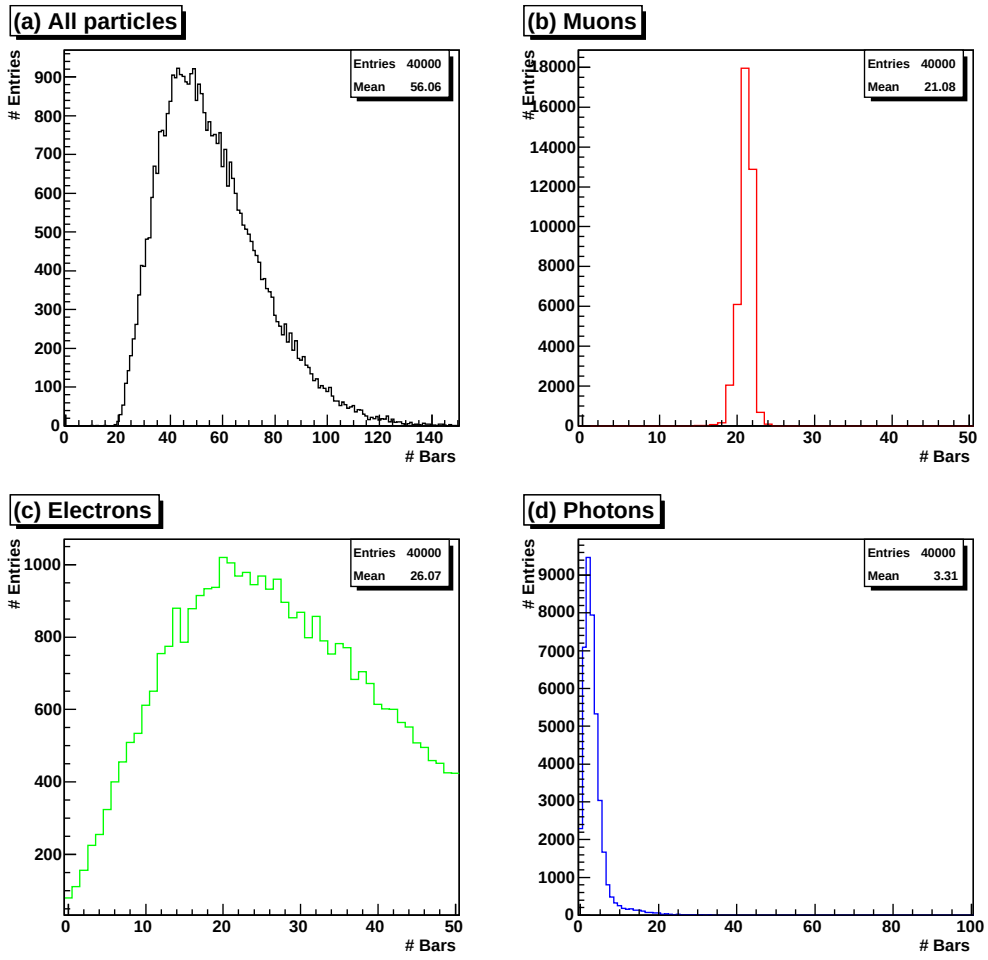

Figure 4.22: The number of hit bars distribution (a) for the μ^- is the sum of the muon (b), electron (c) and photons (d) distributions.

that this variable does not have a great discriminating power, but, from a certain point of view, this is good news since in EMR the number of hit bars is computed measuring the MAPMT signals: the larger the noise, the larger the error on this variable. To use this variable in MICE, a deep investigation on the noise contribution must be performed.

The purity as a function of the muon efficiency for the number of hit bars variable for the 3π·mm·rad 140 MeV/c μ^+ case is presented in figure 4.23.

μ	Emittance [mm · rad]	Momentum [MeV/c]	ϵ_e **(%)**	ϵ_μ **(%)**
+	3π	140 (NS)	45.00 ± 0.40	85.42 ± 0.63
+	3π	170 (NS)	38.45 ± 0.36	85.27 ± 0.63
+	3π	200 (NS)	37.51 ± 0.36	89.06 ± 0.65
+	3π	240 (NS)	33.24 ± 0.33	89.73 ± 0.65
+	3π	140 (S)	48.22 ± 0.42	83.94 ± 0.62
+	3π	170 (S)	42.08 ± 0.39	84.37 ± 0.62
+	3π	200 (S)	39.10 ± 0.37	86.86 ± 0.64
+	3π	240 (S)	35.99 ± 0.35	89.75 ± 0.65

Table 4.5: The electron inefficiency and muon efficiency after the hit bars cut for an incoming μ^+ beam.

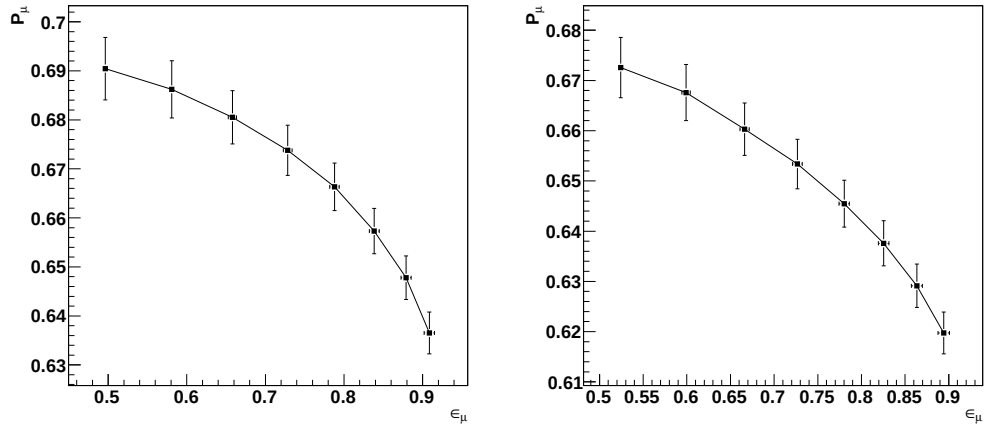

(a) (b)

Figure 4.23: The purity as a function of the muon efficiency for the hit bars variable for the beams a) without and b) with a momentum spread.

4.3.5 The angular distribution

The last kinematic variable is the angular distribution (in both directions) measured with the first two modules (first 4 planes). The angular distribution is computed considering the hit position given by the clusters, which in fact can be more than one per plane because of the decay products and the photons. In order to consider just the clusters which correspond to the incoming charged particles, the pulse height of each cluster in one EMR plane has been computed. Figure 4.24(a) presents the distribution for the first layer in case of an incoming muon beam,

while the electron case is shown in figure 4.24(b). From the figures it is possible

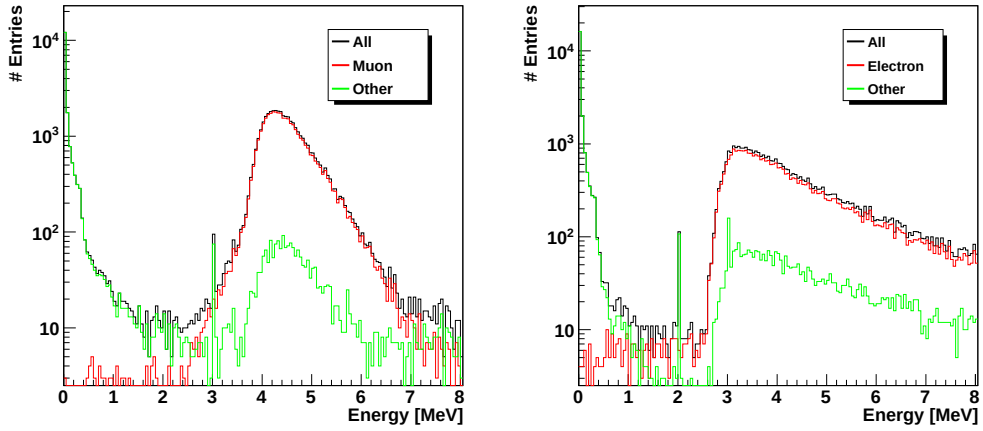

(a) (b)

Figure 4.24: The energy of each cluster in the first EMR layer for an incoming a) muon and b) electron beam without momentum spread.

to note that selecting the clusters with the larger pulse height, the probability to identify the cluster as the one due to the incoming charged particle is very high. As an example, considering the 140 MeV/c positive muons case, 92% of the clusters with the largest pulse height are correctly identified as muons.

The angular distributions for both directions are presented in figure 4.25: since the electrons are generated in a decay, their divergence is larger with respect to the muons one. Table 4.6 summarizes the efficiencies for the 3π μ^+ case; no differences are present in the other cases.

The purity as a function of the muon efficiency for the divergence variable is presented in figure 4.26.

4.3.6 Results with cuts

Applying the cuts on all the kinematic variables at the same time, the resulting efficiencies are the ones summarized in tables 4.7 and 4.8 for the μ^+ and μ^- cases respectively considering all the beam types.

Summarizing:

- the discrimination efficiency (1-ϵ_D) is very high in any condition: the worst value is 99.60%;
- the larger the momentum value, the larger the fraction of survived muons (ϵ_μ).

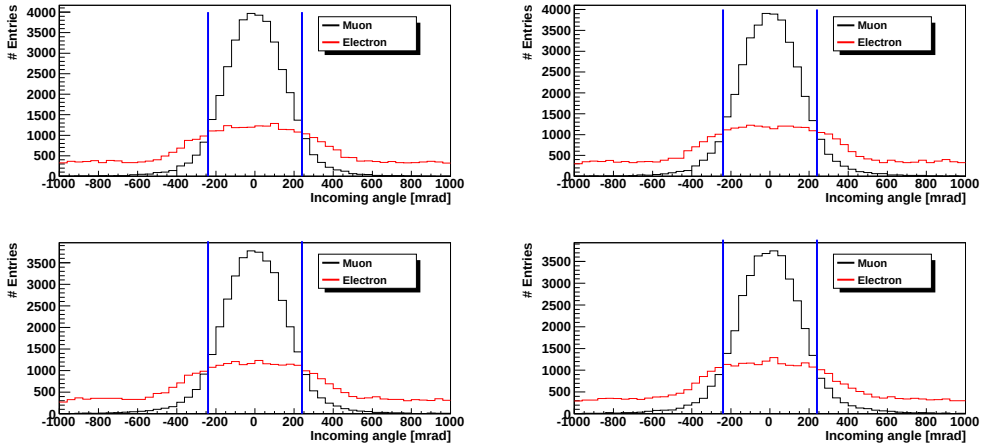

(a) (b)

Figure 4.25: The angular distributions for the vertical (top) and horizontal (bottom) directions for muons (black) and electrons (red) a) without and b) with a momentum spread. The blue lines identify the kinematic cuts.

μ	Emittance [mm · rad]	Momentum [MeV/c]	ϵ_e **(%)**	ϵ_μ **(%)**
+	3π	140 (NS)	19.68 ± 0.24	79.84 ± 0.60
+	3π	170 (NS)	23.32 ± 0.27	85.17 ± 0.63
+	3π	200 (NS)	27.62 ± 0.30	85.76 ± 0.63
+	3π	240 (NS)	32.05 ± 0.33	85.67 ± 0.63
+	3π	140 (S)	19.83 ± 0.24	78.07 ± 0.59
+	3π	170 (S)	23.49 ± 0.27	83.97 ± 0.62
+	3π	200 (S)	27.53 ± 0.30	85.35 ± 0.63
+	3π	240 (S)	32.02 ± 0.33	85.71 ± 0.63

Table 4.6: The electron inefficiency and muon efficiency after the divergence cut for an incoming μ^+ beam.

Focusing on the particle discrimination, the purity as a function of the muon efficiency applying all the cuts at the same time for the 3π·mm·rad μ^+ case is presented in figure 4.27. The results obtained with the use of EMR-only are consistent with the EMCal system ones. The largest efficiency value is of the order of 70-80% and it is smaller with respect to the value obtained with each single variable (e.g. almost 100% for the six-plane variable, figure 4.15), but with a purity which is close to 100%.

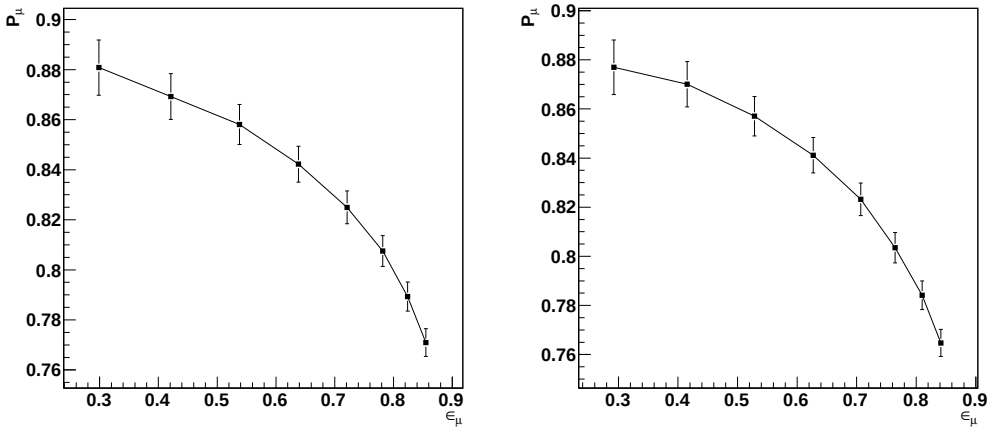

(a) (b)

Figure 4.26: The purity as a function of the muon efficiency for the divergence variable for the beams a) without and b) with a momentum spread.

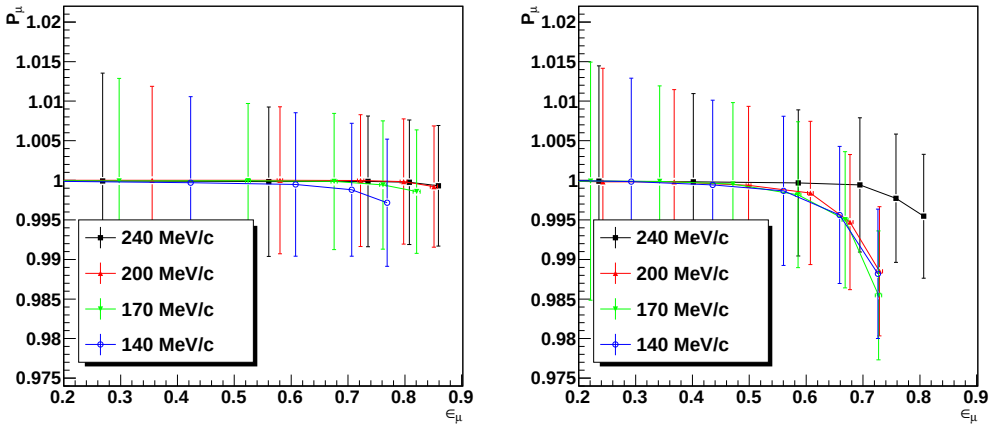

(a) (b)

Figure 4.27: The purity as a function of the muon efficiency applying all the cuts at the same time for beams a) without and b) with a momentum spread.

μ	Emittance [mm · rad]	Momentum [MeV/c]	ϵ_D **(%)**	ϵ_e **(%)**	ϵ_μ **(%)**
+	3π	140 (NS)	0.05 ± 0.01	0.03 ± 0.01	58.84 ± 0.48
+	3π	170 (NS)	0.01 ± 0.01	0.01 ± 0.01	66.88 ± 0.53
+	3π	200 (NS)	0.00 ± 0.00	0.00 ± 0.00	73.03 ± 0.56
+	3π	240 (NS)	0.01 ± 0.00	0.01 ± 0.00	74.38 ± 0.57
+	3π	140 (S)	0.17 ± 0.03	0.10 ± 0.02	56.41 ± 0.47
+	3π	170 (S)	0.19 ± 0.03	0.11 ± 0.02	59.95 ± 0.49
+	3π	200 (S)	0.18 ± 0.03	0.11 ± 0.02	62.25 ± 0.50
+	3π	240 (S)	0.07 ± 0.02	0.05 ± 0.01	70.64 ± 0.55
+	6π	140 (NS)	0.02 ± 0.01	0.01 ± 0.01	58.58 ± 0.48
+	6π	170 (NS)	0.02 ± 0.01	0.01 ± 0.01	68.08 ± 0.53
+	6π	200 (NS)	0.02 ± 0.01	0.01 ± 0.01	73.16 ± 0.56
+	6π	240 (NS)	0.01 ± 0.00	0.01 ± 0.00	74.03 ± 0.57
+	6π	140 (S)	0.18 ± 0.03	0.10 ± 0.02	57.42 ± 0.48
+	6π	170 (S)	0.23 ± 0.03	0.14 ± 0.02	60.41 ± 0.49
+	6π	200 (S)	0.25 ± 0.03	0.16 ± 0.02	62.91 ± 0.51
+	6π	240 (S)	0.13 ± 0.02	0.09 ± 0.02	68.64 ± 0.54

Table 4.7: The discrimination, rejection and muon efficiencies for an incoming μ^+ beam for each momentum value and considering the distributions without (NS) and with (S) a 10% momentum spread; the incoming beam emittance has been varied from 3π to 6π·mm·rad.

μ	Emittance [mm · rad]	Momentum [MeV/c]	ϵ_D **(%)**	ϵ_e **(%)**	ϵ_μ **(%)**
-	3π	140 (NS)	0.06 ± 0.02	0.03 ± 0.01	58.06 ± 0.48
-	3π	170 (NS)	0.05 ± 0.01	0.03 ± 0.01	69.26 ± 0.54
-	3π	200 (NS)	0.01 ± 0.01	0.01 ± 0.00	72.49 ± 0.56
-	3π	240 (NS)	0.02 ± 0.01	0.01 ± 0.01	76.77 ± 0.58
-	3π	140 (S)	0.24 ± 0.03	0.13 ± 0.02	55.27 ± 0.46
-	3π	170 (S)	0.40 ± 0.04	0.25 ± 0.02	61.72 ± 0.50
-	3π	200 (S)	0.25 ± 0.03	0.15 ± 0.02	62.56 ± 0.50
-	3π	240 (S)	0.10 ± 0.02	0.07 ± 0.01	70.29 ± 0.55
-	6π	140 (NS)	0.06 ± 0.02	0.04 ± 0.01	56.88 ± 0.47
-	6π	170 (NS)	0.05 ± 0.01	0.03 ± 0.01	66.64 ± 0.53
-	6π	200 (NS)	0.04 ± 0.01	0.03 ± 0.01	75.14 ± 0.57
-	6π	240 (NS)	0.03 ± 0.01	0.02 ± 0.01	76.92 ± 0.58
-	6π	140 (S)	0.26 ± 0.03	0.15 ± 0.02	57.73 ± 0.48
-	6π	170 (S)	0.40 ± 0.04	0.25 ± 0.02	61.45 ± 0.50
-	6π	200 (S)	0.28 ± 0.03	0.17 ± 0.02	62.72 ± 0.51
-	6π	240 (S)	0.13 ± 0.02	0.09 ± 0.02	70.66 ± 0.55

Table 4.8: The discrimination, rejection and muon efficiencies for incoming μ^- beams.

Chapter 5

The commissioning phase

The first Electron Muon Ranger data taking is foreseen in May-June 2012 [93] after a commissioning phase that is divided in two parts: the test of the layers with cosmic rays at the University of Geneva (UNIGE) during the manufacturing of the detector and the tests after the installation of part of the detector at RAL. At the time of this thesis work, part of the commissioning has been performed and the results are presented in this chapter.

The first EMR planes have been tested with cosmic rays at UNIGE: these tests have demonstrated to be fundamental to identify the failure of the bars or of the fibers before their installation in the EMR box and to evaluate the tracking performance of the detector. Moreover the layers have been used to develop the final mechanics (electronics boards holders, aluminum frames, patch panels). The tests, started in 2010, used a setup similar to the one presented in section 3.2 for the small scale prototype, in order to track the particle that hits a EMR module. The results obtained with these studies and with optical tests[1] allowed to fix the final bar assembly procedure in which the scintillating bar light is brought out to the PMTs through clear fibers attached to the bars with connectors [81]. The results of the UNIGE tests of a few planes is presented in section 5.1. Similar tests are scheduled for the beginning of 2012: the 48 planes will be studied using the final frontend and readout electronics (thus without the BC for the tracking) just before their shipment to RAL.

The second part of the commissioning is related to the installation of the detector at RAL. This task is twofold: the assembly of the detector in the KL frame (and the corresponding installation of the cables for signals and power) and the implementation of the EMR control and readout in the MICE DAQ (DATE). These issues have been partially performed in July 2011 when six planes have been placed on the MICE line identifying the mechanical constraints for the final installation;

[1] In the optical tests the fibers have been illuminated on one side with a light source while on the other side the light yield is measured with a CCD camera [81].

moreover a preliminary version of the DAQ has been developed. Using DATE and the DAQ system of the UNIGE tests, the detector has been tested both with cosmic rays and a mixed beam; the results are presented in section 5.2.

5.1 Tests at UNIGE

All the EMR planes have to be tested with cosmic rays at the University of Geneva before the final data taking. Two different phases have been foreseen:

- the test of a few modules (1 or 2) in terms of efficiency, spatial resolution and cross-talk with a setup based on high resolution silicon detectors. This test allowed the definition of the assembly procedure. The modules were also used to develop the mechanics (supports, electronics board holders, patch panels) and to test the readout electronics;
- the test of the 48 planes installed in the EMR box readout by the final electronics (without using the silicon tracking system).

The first tests started in 2010 and will be finished for the beginning of 2012. When all the modules will be completed and tested, the whole detector will be assembled, tested with the final electronics and with cosmic rays and sent to RAL for its installation on the MICE line.

An example of the first tests is presented in this section, from the description of the setup to the results.

5.1.1 The setup

A schematic drawing of the UNIGE setup is presented in figure 5.1: it consists of a 10×10 cm^2 plastic scintillator used for the trigger and a couple of 9.5×9.5 cm^2 silicon detectors for the particle tracking placed below the EMR modules.

A typical test foresees the presence of two modules: the four layers (figure 5.2) are hosted in a black wooden box that guarantees the light tightness. The planes under test had the bars with the final shape but not with the final method to bring out the scintillating light to the PMTs. Thanks to some optical tests on these planes, in fact, the originally used “single WLS fiber” system has been substituted with the “connectors+clear fibers” one (figure 2.4(c)) [81]. Because of a problem during the assembly, only the fibers of three planes had been glued on the MAPMT masks and polished, so in the analysis one of the layers cannot be taken into account.

The MAPMT signals are readout by the final FrontEnd board version (section 2.3.1). The analog and digital readout modes are performed with the small

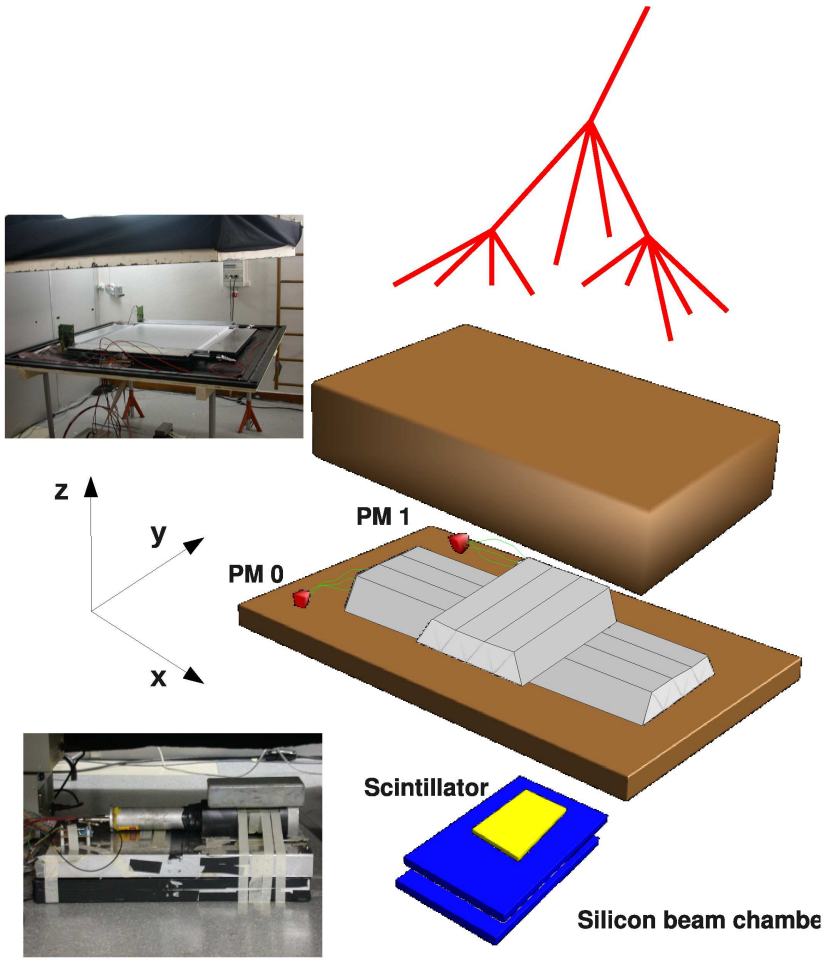

Figure 5.1: A sketch of the UNIGE setup: on its journey a cosmic ray hits the EMR modules, a plastic scintillator for the trigger (in yellow) and a couple of silicon detectors (in blue).

scale prototype DAQ architecture (figure 3.5), that is based on a VME system which hosts a SBS Bit3 card for the data transmission, one I/O board (the MAROC control, consisting of one VME card and a piggy-back one) to configure and read-out the four scintillating planes and the BCs and two I/O boards (the shift register cards) to record the digital information of a single FEB. Four EMR planes are readout by a single VME card (the main part of the MAROC control board, while the piggy-back one is devoted to the BCs readout). As far as the EMR digital readout is concerned, the DAQ allows only one FEB to be readout in this way, thus in the UNIGE tests only one plane has been readout with both the analog and digital modes. The tests of the digital parts of the other FEBs have been per-

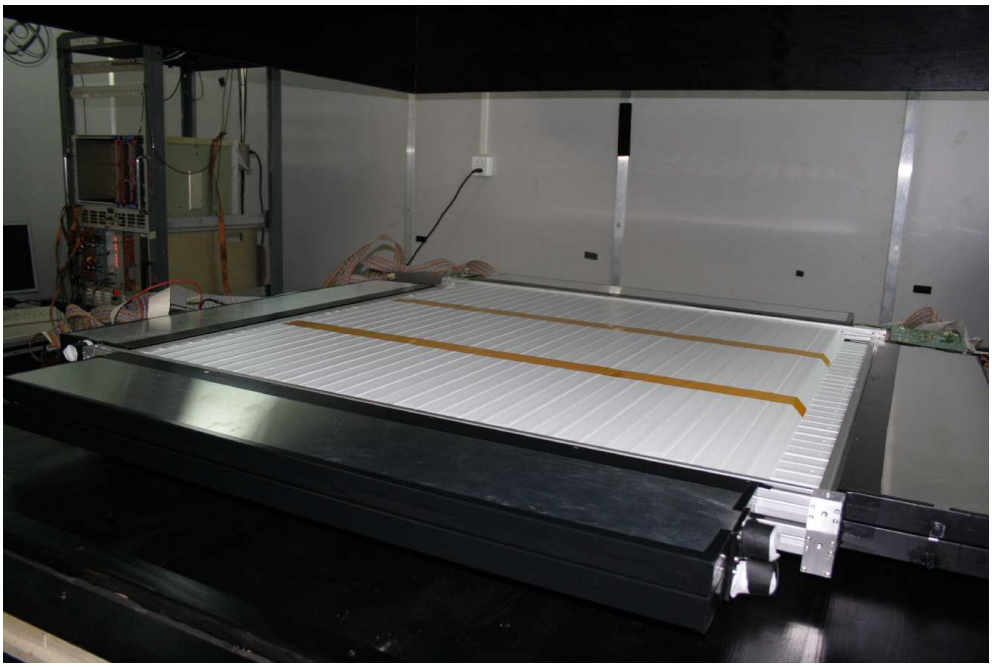

Figure 5.2: Four EMR planes under test at UNIGE.

formed directly at RAL (see section 5.2 for further details), even if all the FEBs functionalities had been previously verified on bench (appendix A).

The test procedure is similar to the one performed with the small scale prototype: a typical data taking consists in the acquisition of 200 events of pedestal and a high statistics run of real events.

5.1.2 The results of the UNIGE test

The analysis of the UNIGE data is very similar to the one implemented for the small scale prototype since the tracking capabilities are the only features that can be evaluated with these tests. The first important quantity to analyze is the pulse height distribution of the bar with the largest signal in the event for each MAPMT. The distributions (presented in figure 5.3) are used to identify a threshold (the blue lines in the plots) to distinguish the good signals from the noise ones. As already stated, the fibers of the third layer (the bottom left histogram in figure 5.3) are not connected to the plastic mask, thus the distribution corresponds to the noise contribution of the electronics (which typically is of the order of a few ADC counts). From now on, if not otherwise indicated, the results obtained with one module will be used as an example of the analysis since no differences are present among the layers themselves.

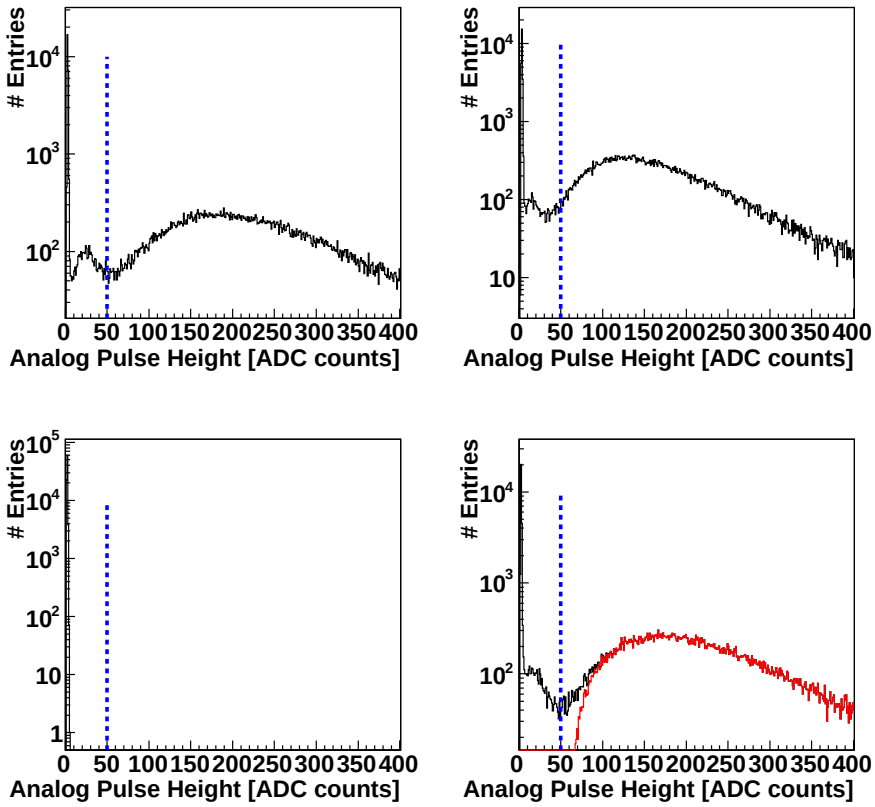

Figure 5.3: The analog pulse height of the bar with the largest signal of the four modules under test at the University of Geneva. The blue dotted line identifies the threshold used in the analysis to discriminate the signal from the noise. The third layer is not connected to the MAPMT. The fourth module is readout both in the analog and digital way: the red line corresponds to the events in which the bar has also a digital information.

The fourth plane (the bottom right plot in figure 5.3) has been readout both in the analog and digital way: the red line in the plot identifies the events in which the bars with the largest signal have also a digital information. The discriminator threshold roughly corresponds to an analog pulse height of about 100 ADC counts. The digital efficiency (see section 3.2.3 for further details) has been evaluated as a function of the analog pulse height (figure 5.4): as expected, an efficiency of 100% is reached around a pulse height value of 100 ADC counts.

Exploiting the Time-over-Threshold architecture implemented in the MAROC ASIC, the digital pulse height can be measured: the distribution, presented in figure 5.5(a), has to be compared with the small scale prototype one (figure 3.15).

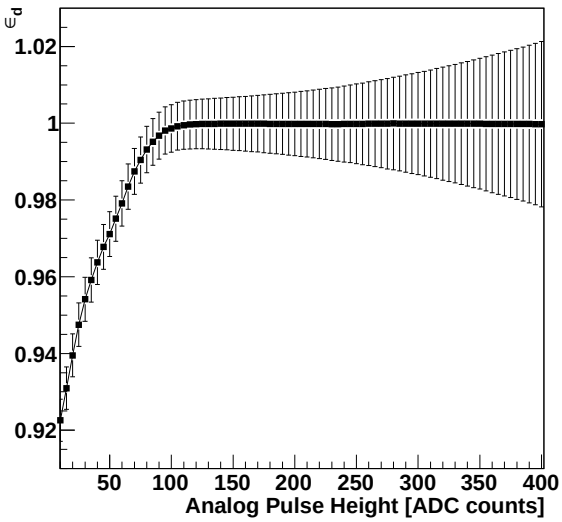

Figure 5.4: The digital efficiency as a function of the analog pulse height. The large errors at the larger pulse height values are due to the small statistics.

It is clear that the two distributions have a Gaussian-like shape, but the mean

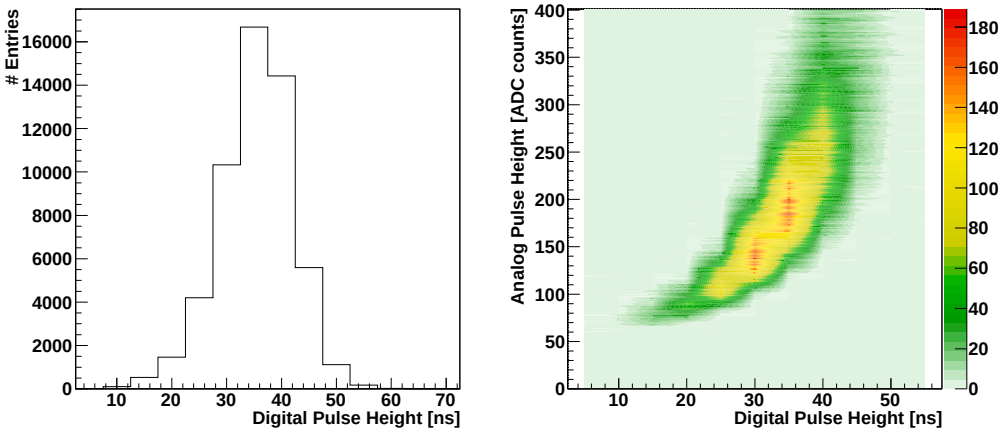

(a) (b)

Figure 5.5: a) The digital pulse height distribution. b) The correlation between the analog and digital pulse height.

value is smaller in the UNIGE case. This is due to the MAROC ASIC version: in MAROC2 (the one used for the prototype) the digital pulse height range was larger with respect to the MAROC3 one. A wider range means a larger granularity;

the smaller ranger can represent a limit: in fact, in the MAROC3 case, two bars have a different digital information if the difference of their analog pulse height is larger than in the MAROC2 one. However the correlation between the analog and digital pulse height is still valid (as presented in figure 5.5(b)) and this guarantees an improvement of the detection capability with respect to a pure digital system.

The particle hit position is computed by means of the clusters: in the analog case a cluster consists of the contiguous bars with an analog signal larger than the analog threshold (the blue lines in figure 5.3) while in the digital case all the bars which have a digital information are taken into account in the cluster computation. The number of clusters per plane has been computed both for the analog (figure 5.6(a)) and digital (figure 5.6(b)) readout modes: the two distributions show no significant difference. As already stated for the small scale prototype, the

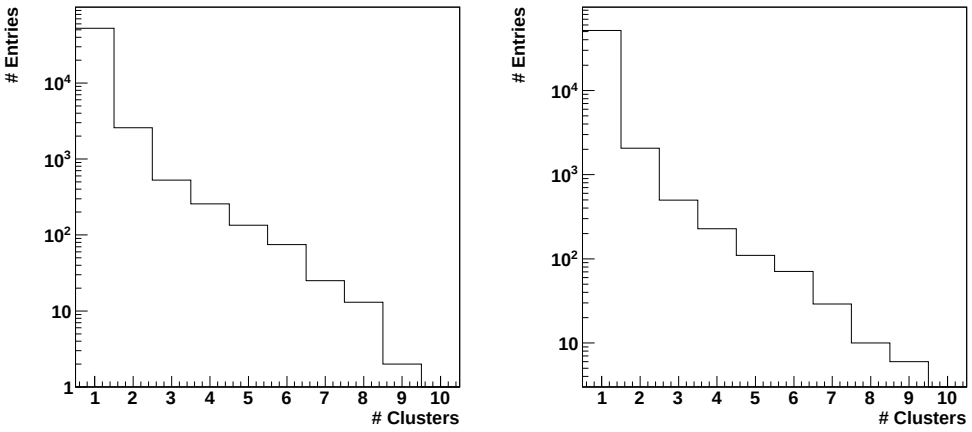

(a) (b)

Figure 5.6: The number of clusters per plane computed with a) the analog and b) the digital readout mode.

larger number of clusters per plane is probably due to the cross-talk effect, even if in this case the probability of a multi event in the plane is larger given the layer larger sensitive area. The number of bars per cluster is presented in figure 5.7(a) for the analog readout mode and in figure 5.7(b) for the digital one. Given the particular geometry, the expected number of bars per cluster is two, as in the analog case. The two distributions are different because of the pulse height threshold: in the analog case the threshold corresponds to about 50 ADC counts, while in the digital one it is about 100 ADC counts. This means that part of the events considered in the analog case that release a small amount of energy (as en example all the events that impinge on the edge of a bar) are not taken into account in the digital one. Varying the analog threshold from 50 to 100 ADC counts (the red

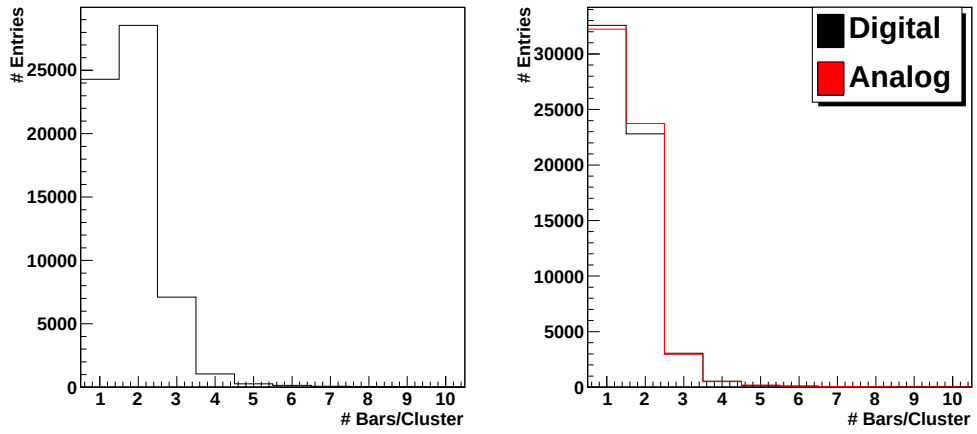

(a) (b)

Figure 5.7: The number of bars per cluster per plane computed with a) the analog and b) the digital readout mode. The red histogram in figure (b) identifies the number of bars per cluster computed in the analog mode varying the threshold from 50 to 100 ADC counts.

histogram in figure 5.7(b)), the two distributions are equivalent. However, in the rest of the analysis the analog threshold will be set to 50 ADC counts.

The cosmic profiles detected with both modules are presented in figure 5.8: the hit position on each plane has been computed with the charge centroid method for the single cluster events. The distributions present a larger number of events in the center of the plane (as expected by the cosmic rays distribution) and some holes (the most important around 10 cm) due to a low efficiency value as presented later on.

The EMR tracking capabilities are based on two quantities: the spatial resolution and the efficiency. The first one is evaluated by means of the residual using the BC tracking system, following the method developed for the small scale prototype presented in section 3.2. The residual distributions for the single cluster events are presented in figure 5.9(a) for the analog case and in figure 5.9(b) for the digital one: the distributions can be fitted with a Gaussian law, allowing to evaluate a spatial resolution (the “Sigma” parameter) of the order of 6.5 mm. As already described, the distances between the BCs and the layers have been evaluated minimizing the residual RMS value.

The two readout modes provide two different values: the digital residual RMS is larger with respect to the analog one because the charge centroid method is less effective given that not all bars above the analog threshold contribute to the digital cluster (as presented in figure 5.7). However both the spatial resolution

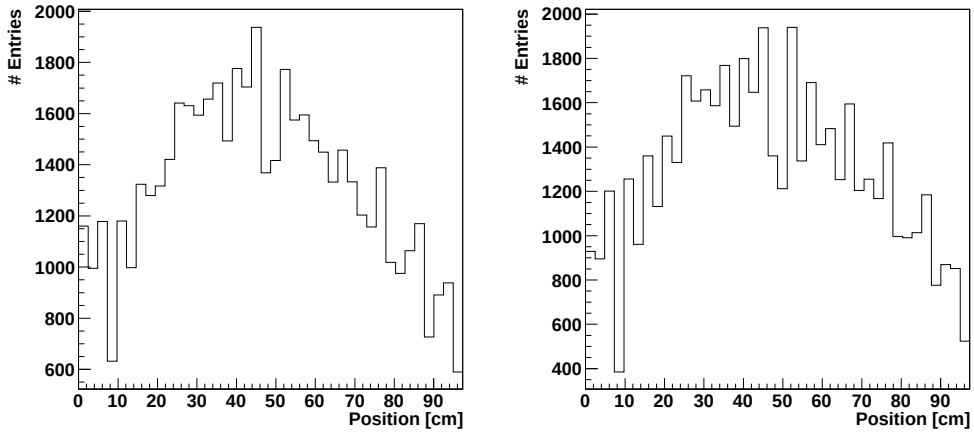

(a) (b)

Figure 5.8: The cosmic profile computed with a) the analog and b) the digital readout modes.

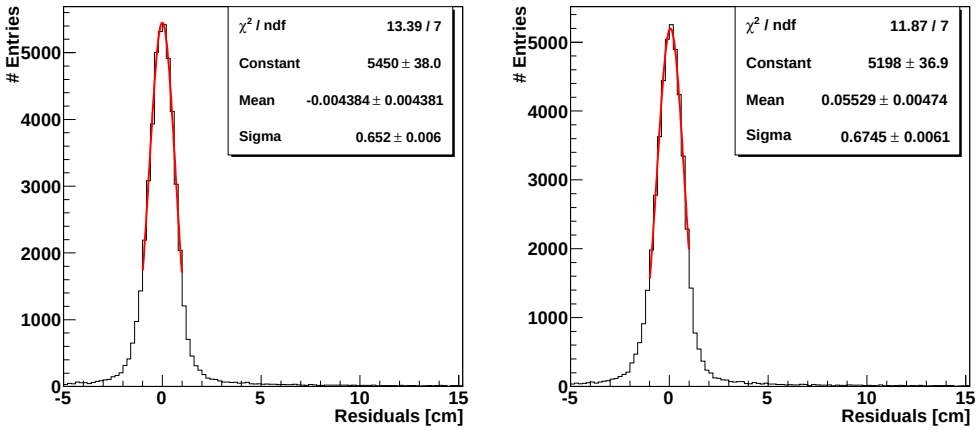

(a) (b)

Figure 5.9: The residual distribution computed with a) the analog and b) the digital readout modes.

overall plots demonstrate that the MAPMT-mask alignment has been improved with respect to the prototypes: figure 5.10 presents the residual distribution (in logarithmic scale) considering all the clusters in the plane. The same distribution for the small scale prototype case (figure 3.11(b)) presented several lateral peaks due to the cross-talk effect that in this case are absent.

The detection efficiency has been computed following the method developed

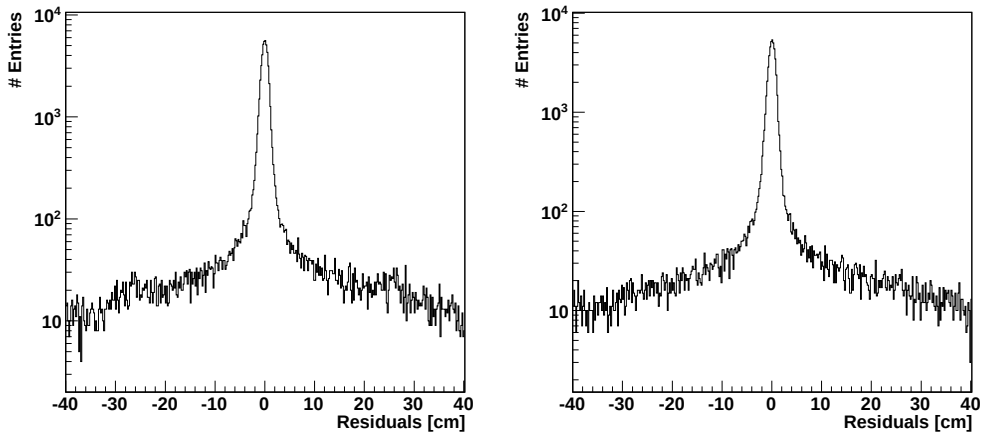

(a) (b)

Figure 5.10: The residual distribution in logarithmic scale for all the clusters computed with a) the analog and b) the digital readout mode.

for the prototype: referring to equation 3.1, the "target events" are all the events that have a single cluster in the BCs and a single cluster in two EMR planes, requiring also that the positions reconstructed by the EMR planes are at less than 3σ from the reconstructed hit position on the planes themselves; the "good events" are the events with a single cluster in the third plane with a residual within 3σ from the expected value. The efficiency as a function of the hit position is presented in figure 5.11: the average value is around 97%. As in the spatial resolution case, the digital value is smaller than the analog one because of the different pulse height threshold. It is important also to note the smaller efficiency region at about 10 cm that explains the cosmic ray profile distribution presented in figure 5.8.

The goal of the UNIGE tests is to verify the bar assembly procedure and not to compare the readout modes performances (already presented with the small scale prototype, section 3.2.3). For this reason, two different thresholds have been used for the analog and digital cases. In the tests performed at RAL presented in the next section, the discriminator threshold has been lowered to be equal to the analog one.

5.2 Commissioning tests at RAL

The second part of the EMR commissioning phase has been performed on the MICE line. The commissioning of EMR at RAL requires EMR to be installed in the KL frame, the readout to be included in the MICE DAQ (DATE) and the

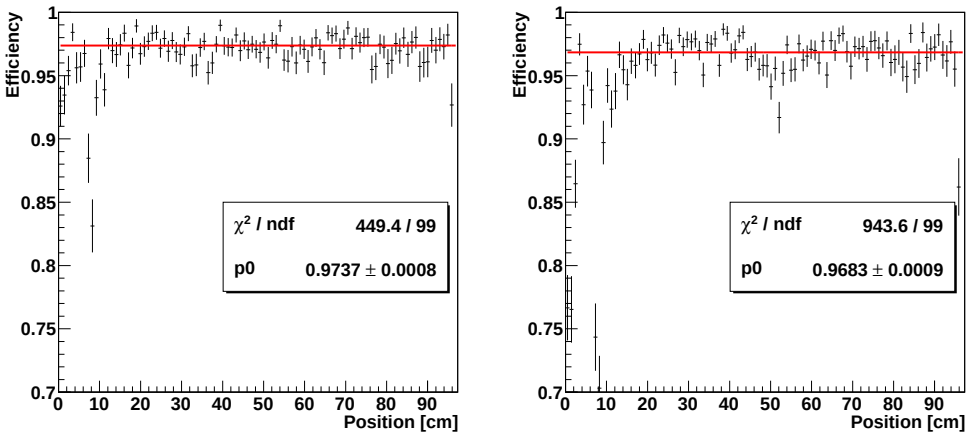

(a) (b)

Figure 5.11: The efficiency as a function of the hit position computed with a) the analog and b) the digital readout modes.

detector performances to be evaluated with dedicated beams. In order to speed up the final installation foreseen for May 2012, a few of these tasks have been performed in July 2011: six EMR planes have been placed in the final box and installed on the line, the readout has been included in DATE and some preliminary results have been obtained with cosmic rays and a mixed (pion/muon/electron) beam. The readout has been performed independently by two systems: DATE and a "UNIGE-like" system, a simplified version of the VME DAQ used for the cosmic rays tests. Because of the low beam particle rate, the EMR performances have been evaluated both using beams and cosmic rays.

In this section, after a brief introduction on the setup, the preliminary results obtained with both the DAQ systems are presented.

5.2.1 EMR at RAL: the setup

Six EMR layers have been installed in July 2011 at RAL. At that time the MICE collaboration had completed the tasks foreseen for Step I (figure 1.31) and was in an intermediate status between Step II and III: in fact, the TOF2 stations, KL and part of EMR had been installed, but the first spectrometer was not available. Given the particular situation, EMR has been installed at the beginning of the beamline (figure 5.12(a)), almost in the same position where the first spectrometer will be placed. As presented in figure 5.12(b), the EMR box has been located in the KL aluminum frame just downstream of the last TOF station and all the cables have been pulled.

(a)

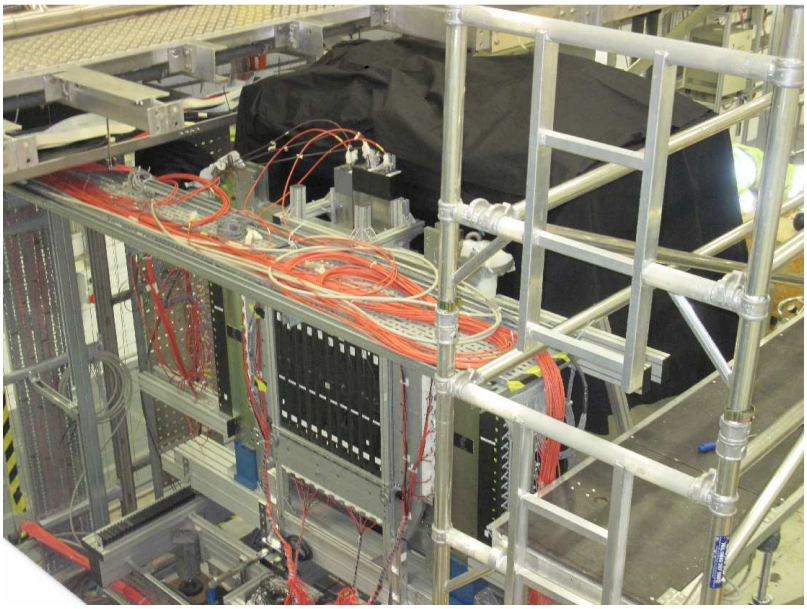

(b)

Figure 5.12: EMR at RAL: a) for the 2011 commissioning tests six planes have been installed at the beginning of the MICE line; b) EMR installed in the KL frame, just downstream of the TOF2 station.

The data have been acquired with two independent DAQ systems: DATE and a

"UNIGE-like" one, the same system used for the UNIGE tests without the readout of the silicon beam chambers. In these tests only the four internal planes have been readout: the coincidence of the first and last plane outputs has been used as a trigger signal for the second DAQ system (more details are presented later on), while the trigger for DATE was given by a dedicated combination of the TOF system and KL, chosen depending on the beam type (cosmic rays or the MICE beam).

As far as the beam is concerned, the original idea was to separately test the detector with cosmic rays and a mixed muon/pion 200 MeV/c beam. However some problems with the line target forced the use of both the particle types in the same run: in fact the typical event rate for the cosmic rays was of the order of 10 Hz, while the beam one of 1 Hz. In conclusion, there was no possibility to collect enough statistics exploiting just the beam events.

The analysis presented in the following has been performed on the data collected with the UNIGE-like system; as fas as DATE is concerned, just a few raw data plots will be shown.

5.2.2 Results with cosmic rays and the mixed beam

The analysis performed on the RAL data is similar to the UNIGE one (section 5.1), apart from the evaluation of the spatial resolution and efficiency given the absence of the silicon tracking system. The pulse height of two MAPMTs is presented in figure 5.13(a): the distributions have been obtained considering the bar with the largest energy deposit in each event. This distribution has been computed to discriminate the good signals from the noise ones setting an analog threshold (the blue dotted line) in the analysis. Differently from the other setups (e.g. the UNIGE tests - figure 5.3 - or the prototype ones), the modules under tests are sandwiched between two planes which cover the overall sensitive area, so the interaction probability is very high and the number of noise events is small.

A comparison between the analog and digital readout modes has been performed for the four internal planes under test. Only a single FEB per run has been readout with both the systems; figure 5.13(a) presents the results obtained with the second board (bottom plot). The analog pulse height of the bar with the largest analog signal and with a digital information is represented by the red line. The digital efficiency as a function of the analog pulse height is presented in figure 5.13(b). In this case, the discriminator threshold value has been set to be the same of the analog one.

The digital pulse height is shown in figure 5.14(a). Thanks to the ToT architecture, it is a function of the analog pulse height (figure 5.14(b)).

The cluster computation has been used to reconstruct the cosmic and beam profile. The number of clusters is presented in figure 5.15(a) for two planes: as

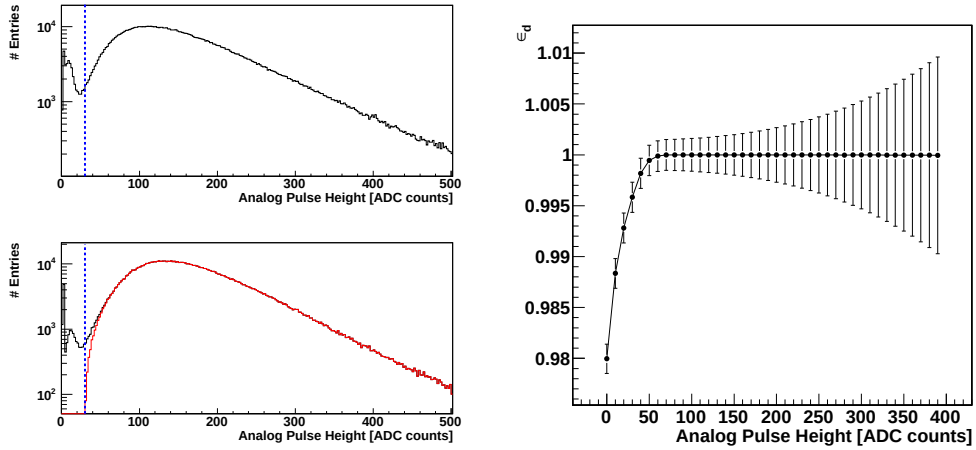

(a) (b)

Figure 5.13: a) The pulse height distribution for one vertical (top) and one horizontal (bottom) planes. The analog threshold (blue dotted line) in the analysis has been set to 30 ADC counts. The analog pulse height in presence of a digital information in the bar is indicated by the red line in the bottom plot. b) The digital efficiency as a function of the analog pulse height.

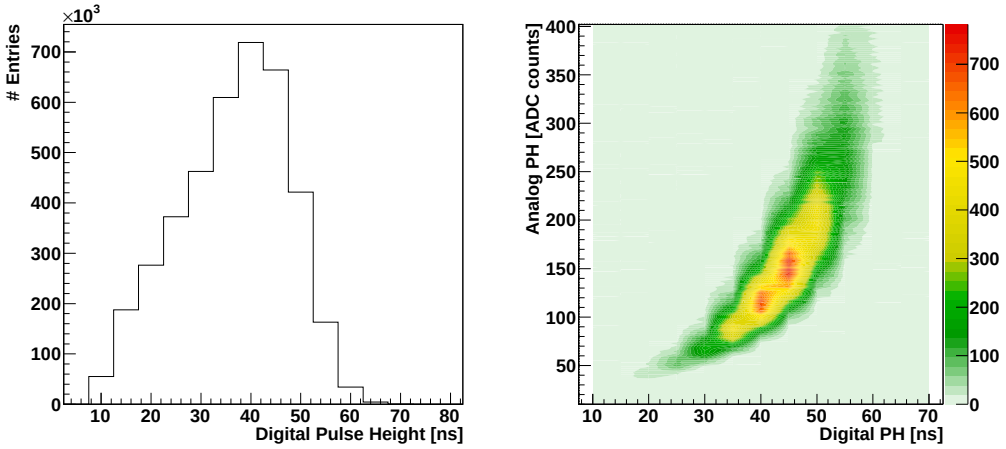

(a) (b)

Figure 5.14: a) The digital pulse height and b) the correlation between the analog and digital pulse height.

expected, the majority of the events has a single cluster, but also a larger number of clusters is possible. In the small scale prototype a large number of clusters per event has been explained by the presence of the cross-talk effect. On the other

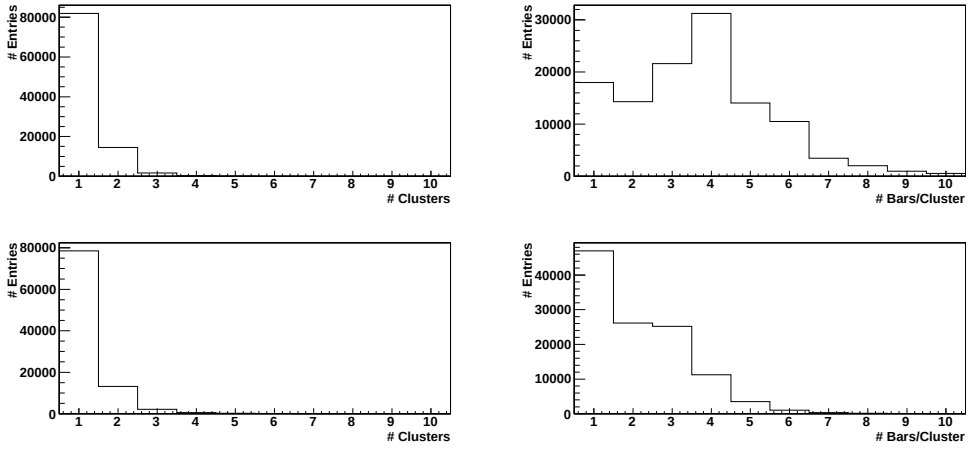

(a) (b)

Figure 5.15: a) The number of clusters and b) the number of bars per cluster for one Y (top) and one X (bottom) plane.

hand, in this case the trigger area is large enough to allow two independent events to be recorded at the same time.

The number of bars per cluster is shown in figure 5.15(b). The distributions can be explained considering the particular trigger system whose sketch is presented in figure 5.16. Given the cosmic rays angular distributions[2], the most probable cosmic ray event is perpendicular to the Z direction (the one that defines the motion along the beam). Thus, given the trigger architecture, the most probable events are the ones represented by the red lines in figure 5.16: the planes which measure the vertical (Y) direction (as an example the third layer from the left in the figure) have a larger number of hit bars (at least 4), while in the horizontal coordinate the most probable event is orthogonal to the planes.

As in the UNIGE tests case, the cosmic and beam profiles have been computed considering all the events with a single cluster whose position is the barycenter of the charge. The distributions for one plane per direction are presented in figure 5.17.

In order to select the particles more orthogonal to the EMR planes (the ones parallel to the z direction), another trigger system has been implemented. Figure 5.18 presents the second trigger architecture: together with the first and last EMR layers, the signal of a TOF2 scintillator (placed about 50-60 cm upstream of the first EMR plane) has been used in coincidence. The red lines identify the most probable particle events.

[2]The muon angular distribution at the sea level is proportional to $\cos^2\theta$, where θ is the Zenith angle [53].

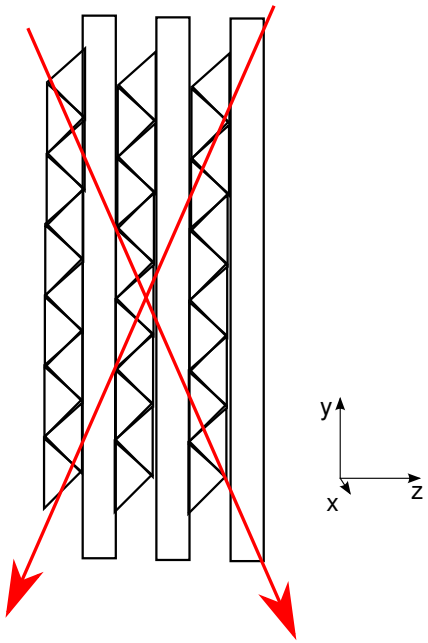

Figure 5.16: The most probable cosmic ray events (in red) come from the top of the detector and cross the scintillating planes, hitting a large number of bars.

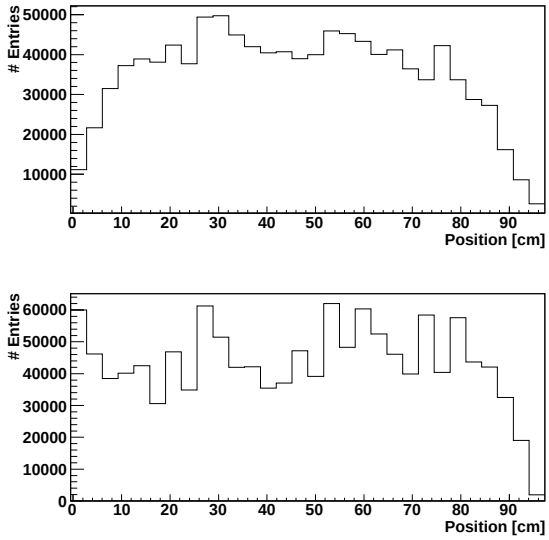

Figure 5.17: The cosmic and beam profile for the vertical (top) and horizontal (bottom) directions.

The same analysis has been performed on this set of data. The number of

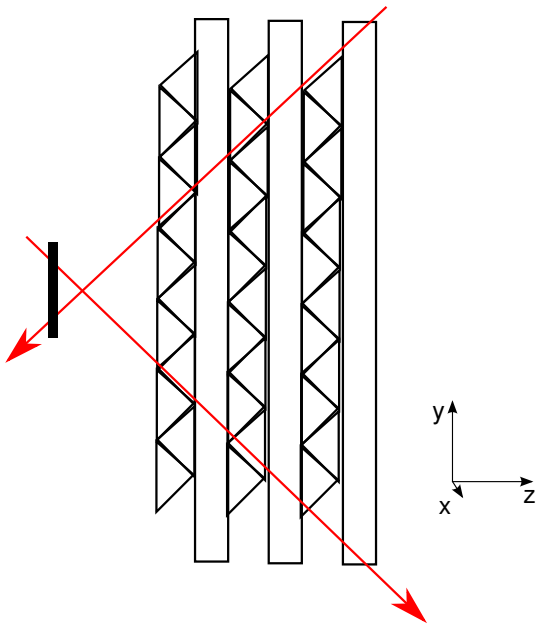

Figure 5.18: The second trigger system is based on the coincidence of the first and last EMR layers and a TOF2 scintillator (50 cm in the X direction, 10 cm in the Y one).

clusters per plane is presented in figure 5.19(a): the distribution is very similar to the one obtained with the first trigger since no large differences are expected. On

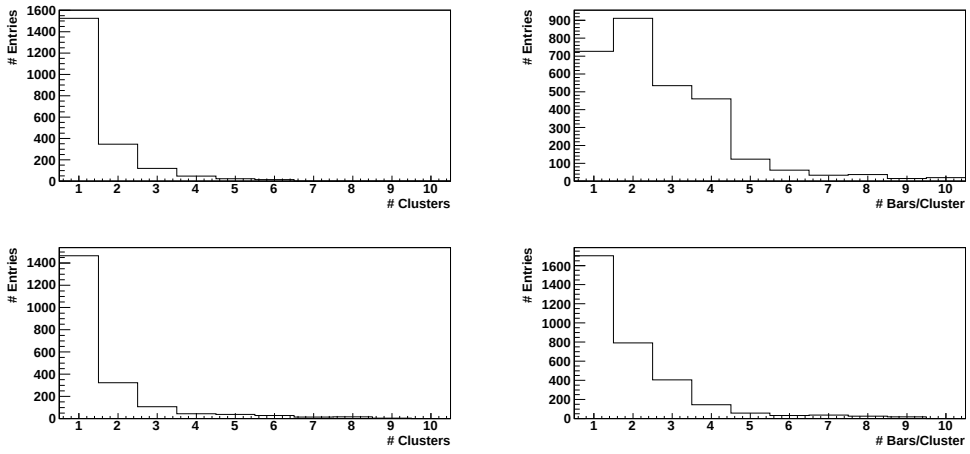

(a) (b)

Figure 5.19: a) The number of clusters and b) the number of bars per cluster for one Y (top) and one X (bottom) planes using the second trigger type.

the other hand, a smaller number of bars per cluster was expected in the vertical direction with respect to the previous trigger configuration. This fact is confirmed by the distribution presented in figure 5.19(b).

Also the cosmic profile has been measured and the results are summarized in figure 5.20. As expected, the top plot is different with respect to the one pre-

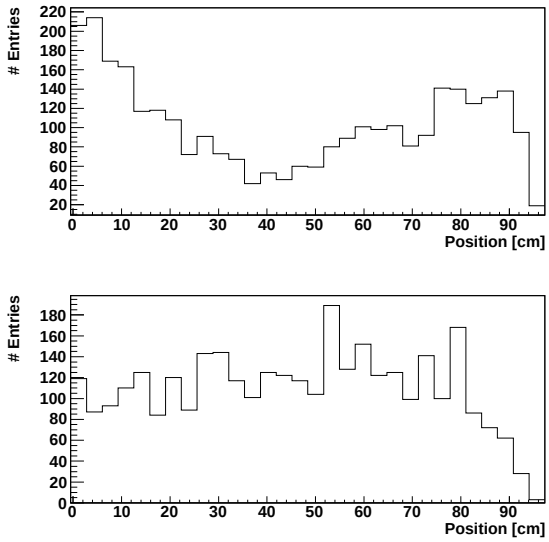

Figure 5.20: The cosmic and beam profile for the vertical (top) and horizontal (bottom) directions using the second trigger type.

sented in figure 5.17: given the most probable events (identified by the red lines in figure 5.18), the particles hit the vertical plane close to the edges.

The four inner planes have been readout also with the DATE system. This was the very first time that the final electronics chain (FEB+DBB+VRB+DATE) has been used. The analysis of the data recorded with DATE is still ongoing, so just a few preliminary results are available [94]. The first one is the distribution of the leading edge time of the EMR events (see section 2.3.2) with respect to the spill gate signal (figure 5.21(a)). In practice the plot represents the time arrival distribution of the particles recorded by EMR (typically cosmic rays, in blue) with respect to the end of the spill gate represented by the red line.

The DBBs compute at the same time the number of triggers per spill detected by EMR and provided by the MICE DAQ. In a spill gate, in fact, the DBBs receive the trigger signals from the general DAQ system (that is generated by a dedicated combination of TOF, CKOV and other detectors); but, at the same time, they check if there is a digital information in the bars that are readout. The comparison of the two distributions is presented in figure 5.21(b). The two distributions should be

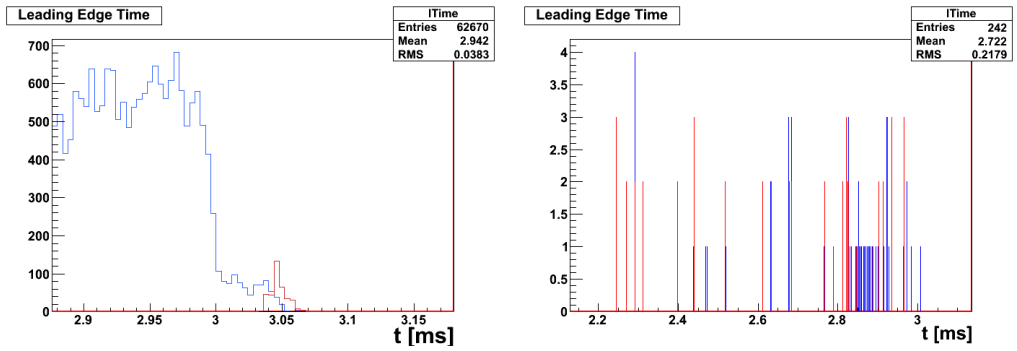

(a) (b)

Figure 5.21: a) The leading edge time for the EMR events (in blue) and the spill width (in red) and b) the number of particle triggers recorded by EMR (in blue) and by the MICE DAQ (in red) [94].

the same, but this is it not the case and the problem has to be investigated.

Chapter 6

Conclusions and outlooks

Neutrino physics is still one of the most fascinating research fields in high energy physics. Fundamental questions such as the neutrino mass or its mixing can lead to unexplored theoretical regions, even questioning the Standard Model. The study of the neutrino requires the development of both heavy and large detectors and dedicated sources, able to produce neutrino beams with well defined features such as a Neutrino Factory.

The necessity of a Neutrino Factory is analyzed in the first chapter of this thesis. Natural and artificial sources like the Sun, the atmosphere, nuclear reactors and particle accelerators on one hand have led to fundamental results, but on the other they are limited in terms of intensity, energy and flavor composition. To optimize the detector design and to face the unanswered questions, a pure neutrino beam with high intensity and a well-defined energy should be used. In a Neutrino Factory two of the listed limits are intrinsically solved: the neutrinos are produced from the decay of a muon beam whose energy and shape can be set. For what concerns the intensity, a huge amount of muons have to be stored in a ring but this is complicated by this particle short lifetime. In other words the muon cooling represents a key element not only for the Neutrino factory but also for a Muon Collider. A possible solution is being investigated by the MICE collaboration and it is based on an innovative technique called ionization cooling.

MICE is currently under commissioning at the Rutherford Appleton Laboratory. The aim of the experiment is to cool a pure muon beam (by a factor 10%) exploiting the ionization cooling technique in which the particles lose transversal momentum hitting a light absorber (liquid hydrogen), while the longitudinal one is restored through radiofrequency cavities. The cooling capability is evaluated with two 4 T spectrometers (based on fiber trackers) measuring the emittance before and after the cooling section with a precision of 0.1% and, therefore, the emittance reduction with a precision of 1%. This goal can be achieved selecting the muons, discriminating them from the background that is mainly made of pi-

ons and electrons. Thus in the experimental line a Particle-ID system is needed: upstream of the cooling channel a TOF system and Cherenkov detectors identify the muons and the pions, while downstream the muon/electron discrimination is ensured by a TOF system, a pre-shower (KLOE-Light) and the Electron Muon Ranger.

The heart of this thesis work is represented by EMR and its evolution, from the design to the prototype tests, from a Monte Carlo simulation to the preliminary results in the commissioning phase. EMR is a fully active detector based on 1.1 m long scintillating bars with a triangular shape whose light is carried out by one WLS fiber and is readout by two PMT systems: on one side the 59 fibers of a plane are readout by a single anode PMT, while on the other the light of each single bar is measured by an anode of a MAPMT. This dual readout has been implemented to distinguish the two detector main tasks: the calorimetric capability is ensured by the single PMTs measuring the whole energy deposited in each plane, while the track of each particle is reconstructed starting from the signals recorded by the MAPMT pads. The single PMTs signals are readout by 8 channel WaveForm Digitizers, while a dedicated frontend electronics has been developed for the MAPMTs, based on the so-called FrontEnd Board and Digitizer and Buffer Board. Each FEB hosts a MAROC ASIC that processes the 64 PMT signals in parallel and provides 64 digital outputs that are sampled, stored and sent to the VME readout system through the DBBs.

The EMR tracking and calorimetric capabilities have been evaluated using two different prototypes: the small scale prototype is roughly a cube consisting of 8 planes of 10 scintillating bars each (with a rectangular shape and organized in a x-y configuration), while LEP is made of 48 planes of 4 bars each. The light of both the prototypes bars is brought out by WLS fibers interfaced to the MAPMTs and the FEBs. The first prototype has been tested with cosmic rays: the tracking capabilities have been expressed by means of the spatial resolution (of the order of 7 mm) and of the efficiency (larger than 98%). Moreover the cross-talk effect (due to the misalignment between the MAPMT and the fiber plastic mask) has been studied and the results have been used to finalize the EMR design. The muon/electron discrimination has been evaluated with the Large EMR Prototype with a 1 GeV/c beam on the PS T9 line at CERN. Although the beam momentum is different (in MICE the momentum value is in the range 140-240 MeV/c), the experimental results have been used to tune a Monte Carlo simulation to study the performance at lower momenta.

Two simplified Monte Carlo simulations of EMR are presented in the fourth chapter: the EMCal system (based on KL and EMR) has allowed to present the discrimination algorithm proposed by the MICE collaboration, while the EMR-only system has been simulated to understand the EMR performance identifying a few kinematic variables that can help the background rejection. Both the simu-

lated systems are characterized by good results in terms of discrimination, even if the analysis is still in a preliminary phase.

The last chapter of the thesis is dedicated to the commissioning phase of EMR: in particular the first part deals with the tests with cosmic rays performed at the University of Geneva to check the bar assembly procedure, while the second part describes the installation of six planes on the MICE line at RAL. The UNIGE tests are based on the study of the tracking capability: as for the small scale prototype, the spatial resolution (of the order of 6.5 mm) and the efficiency (about 97%) have been computed. The results have shown that the bar triangular shape improves the uniformity of the efficiency over the whole plane, while the spatial resolution is enough good. Six planes have been installed on the MICE line at RAL in order to plan the installation of the detector in its final frame downstream of KL and to implement the EMR configuration and readout in the final DAQ system (DATE). The performance of the detector with cosmic rays and a mixed beam has been evaluated with the DAQ used for the UNIGE tests and the results are consistent with the expected ones. On the other hand, the readout and configuration task for the EMR electronics have been implemented in DATE and the analysis of the results is still ongoing.

The oscillation study is fundamental to investigate the neutrino physics. For this reason several detector systems and techniques have been proposed in the last years, among which the so-called *magnetized scintillation detectors* are very important. These far detectors (thus placed at the end of a baseline) are based on scintillating material (to have a large energy resolution) located in a magnetic field to separate and identify the charged particles produced by the neutrinos: the oscillation phenomenon is thus studied via the golden, silver and platinum channels. To make an example, if in a Neutrino Factory a μ^+ decays (thus producing ν_e and $\overline{\nu_\mu}$ neutrinos), the oscillation is demonstrated by the detection of a μ^- in the detector. Two of the most important magnetized scintillator detectors are MIND (Magnetized Iron Neutrino Detector) and TASD (Totally Active Scintillator Detector): the first one is made of scintillator interleaved by lead or iron, while the second one is a fully active detector. Thus EMR may represent the first step towards a TASD.

MIND has been proposed in 2000; it is a 20 m diameter 20 m long cylinder made of 6 cm wide iron rods interleaved with 2 cm scintillating rods [9]. The scintillator is readout on both ends to determine the hit position along the scintillator. A superconducting coil generates a magnetic field of 1 T inside the iron.

The first TASD design was proposed in 2006 [95] and foresees a detector made of long scintillating bars arranged in a x-y geometry with a triangular shape (figure 6.1(a)). Such a detector has been designed starting from the layout of the the NOνA one [85], with two important differences:

- each bar is 15 m long, for a total detector thickness of about 150 m and a mass of 22.5 kton. A possible design has been simulated with GEANT4 as presented in figure 6.1(b);

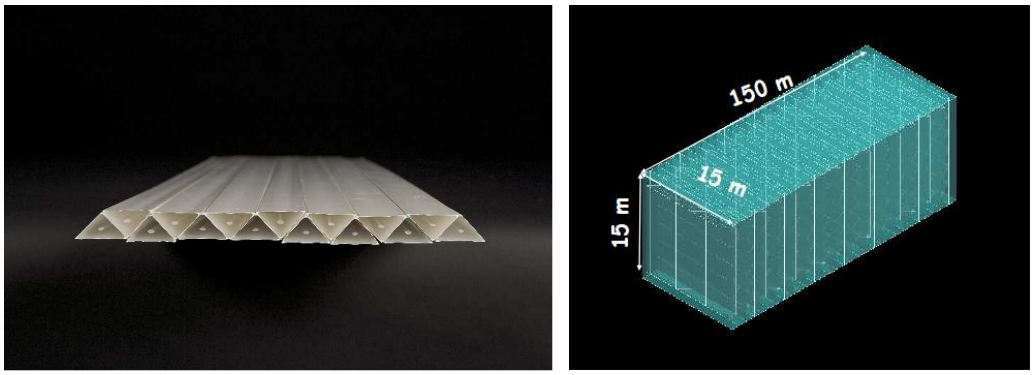

(a) (b)

Figure 6.1: The TASD detector: a) the 15 m long scintillating bars with a triangular shape [96] and b) the final detector in a GEANT4 simulation [9].

- the detector is positioned in a 0.5 T magnetic field perpendicular to the beam axis.

In a TASD, the energy and the tracks of the neutrino charged parts are measured in the energy range between 100 MeV/c and 15 GeV/c: thanks to the scintillator architecture, the energy resolution is better than in MIND and it is of the order of $\Delta E/E \lesssim 10\%/\sqrt{E[\mathrm{GeV}]}$, while the low density of the material and fine granularity increases the efficiency of the muon charge measurement at lower momenta [9]. Last but not least, the large number of hits per track allows to separate the neutral pions from the electrons.

EMR could represent the first step towards a TASD since it can be considered a prototype for future tests. In these tests the problemes related to the develop of a TASD have to be studied:

- magnetic field: the large dimensions of the detector require the development of a non conventional system to generate the magnetic field. Among the possible solutions one can list the high-Tc (high-Temperature superconductors)[1], even if the costs at the moment are too large, or the superconducting transmission line (STL), in which a superconducting cable is inserted in a coaxial helium cryostat, eliminating the presence of a large bulky cryostat

[1]The high-temperature superconductors are materials that have a superconducting transition temperature above 30 K.

[9]. EMR with a different readout system (e.g. the Silicon PhotoMultipliers, see later on) can be used as a large prototype to test the two solutions;

- long bars: the detection uniformity, the light attenuation and the mechanics are just an example of the open questions related to the length of the bars;

- readout system: in a magnetic field the scintillating light can be readout by dedicated (and expensive) MAPMTs (the fine-mesh ones) or with solid state systems, such as the Silicon PhotoMultipliers. Following this idea, LEP (section 3.3) integrates both the MAPMT and SiPM readout, allowing a comparison of the devices.

The golden and platinum channels can be also investigated with a liquid argon Time Projection Chamber (TPC), made of massive (up to 100 kton) dense material that provides highly uniform and accurate imaging [9]. However the large dimension of the TPC requires a dedicated study concerning the high voltage of the long drift lengths, the readout and the embedding in the magnetic field; moreover a lAr TPC is very expensive.

Appendix A

Tests on the MAROC ASIC

The MAPMT electronics is based on the FrontEnd Board (FEB): the heart of the board is represented by the 64 channel MAROC ASIC, developed by the Omega group (LAL[1], Orsay) for the ATLAS[2] luminometer [84]. The ASIC has been designed in the AMS SiGe 0.35 μm technology and the active area measures about 16 mm^2. Each ASIC channel consists of a pre-amplifier, slow and fast shapers, a discriminator and a sample & hold circuit; the ASIC provides 64 parallel digital outputs and one multiplexed analog one. The prototype version of the FEB (the one used for the prototype tests described in chapter 3) has been developed to host both the version 2 and 3 of the ASIC: the third release has minor improvements with respect to version 2, apart from an embedded 12 bit ADC (to digitize the analog output) that in version 2 does not work, but that anyway has not been used in the EMR electronics design.

After a brief introduction on the ASIC, this appendix describes the tests on a prototype frontend board (figure 2.13(b)) to study the MAROC performance. The MAROC used in the tests is the version 3 one.

A.1 The MAROC ASIC

The performances of the MAROC ASIC have been evaluated with some tests on bench to compare the results with the ones described in the ASIC datasheet [97]. More in detail, the goal of the test has been the evaluation of the analog and the digital readout mode considering all the MAROC settings.

The signal in a single MAROC channel (figure A.1) follows the following steps: a MAPMT (or a calibration) signal is sent to the input capacitor of the channel; the signal is pre-amplified (with a 8-bit tunable gain) and a current mirror

[1] Laboratoire de l'accélérateur Linéaire, Orsay: http://http://omega.in2p3.fr/

[2] A Toroidal LHC ApparatuS is one of the LHC experiments.

feeds the analog (red), the digital (yellow) and the sum (green) parts. The analog part consists of a tunable pre-buffer and a RC slow shaper, two sample & hold circuits and a 12-bit Wilkinson ADC. The digital part consists of a fast shaper (bipolar, unipolar or half-bipolar) and a discriminator with a tunable threshold; the sum output allows to measure the pre-amplifier signal.

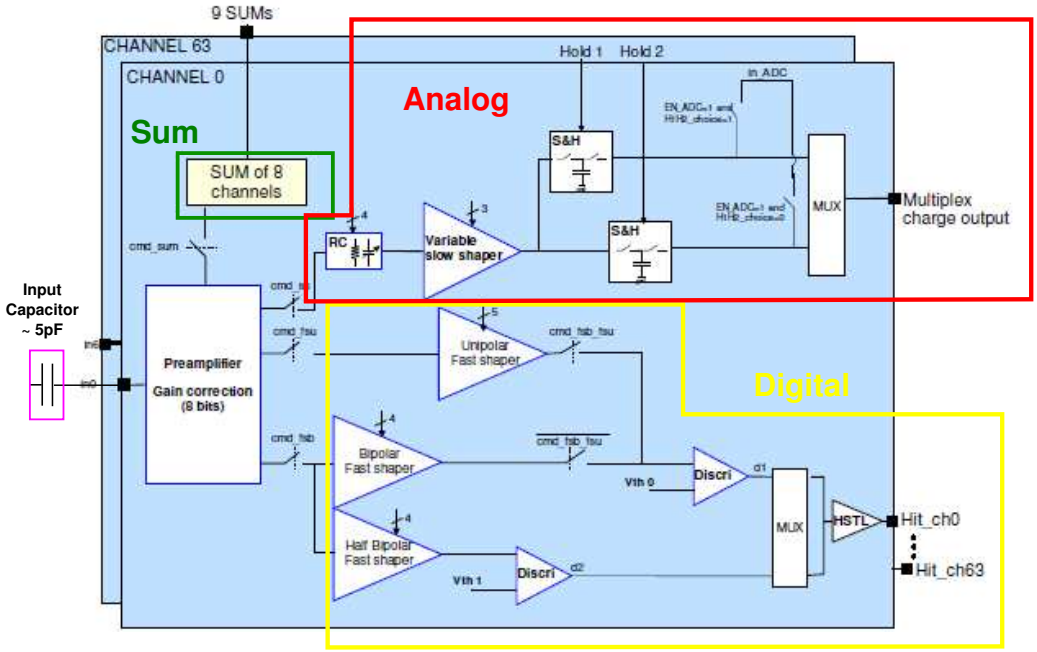

Figure A.1: The schematic view of a MAROC channel [97], which consists of three main parts: analog (red), digital (yellow) and sum (green).

All the channel settings can be selected sending a string of 829 bits to the ASIC during the configuration phase. The bit list is summarized in table A.1 [97].

A.2 Tests on bench

The prototype FEB has been tested on bench evaluating the MAROC analog and digital readout modes as a function of a calibration signal. The setup is presented in figure A.2. The calibration signal features have been chosen depending on the test and have been generated with a pulse generator. A VME Input/Output (I/O) board (MAROC control) is used to configure and readout the FEB under test; it receives the generator TTL[3] synchronized signal that is used as a trigger. Each

[3]TTL is the acronym of TransistorTransistor Logic.

Bit	Name	Description
1-2	dummy	not used
3	slope DAC	change DAC0 slope
4[...]13	DAC1 threshold	
14[...]23	DAC0 threshold	
24[...]27	ADC param.	not used in EMR design
28[...]155	Mask discriminator outputs	enable/disable digital outputs
156[...]190	General parameters	Select shaper and sample & hold circuit Select feedback capacitors/resistors
191[...]198	Gain 64	select gain of channel n. 64
199	Sum 64	enable sum output channel n. 64
200[...]765	Gain-sum	select gain and sum of other 63 channels
766[...]829	C-test all ch.	enable calibration input

Table A.1: The list of the MAROC3 configuration bits [97].

leading edge of the digital signals is counted in two possible ways: by means of four I/O boards (16 channels per board, only the input connectors are used) or directly in the control FPGA on the FEB (this last case is the one presented in figure A.2).

A.2.1 The analog part

The hold scan, the shaper scan and the test on the linearity are the so-called analog tests. The test procedure consists of a pedestal run (a run with a random trigger) with no signal (to evaluate the electronics baseline) and of a calibration run in which a calibration signal is sent to the input capacitor of each channel. The global response (that is the average of all the 64 channels) has been computed. An example of the obtained distribution is shown in figure A.3: it has been fitted with a Gaussian function to measure the mean position.

In the hold and shaper scans the pedestal value has been subtracted from the measured one; in the linearity test only the measured one has been considered.

A.2.1.1 The hold scan

The hold scan allows to evaluate the analog output shape varying the “sample & hold” time. This shape is a function of the pre-amplifier, pre-buffer and shaper parameters, which have been set in the following way (for further details see next sections):

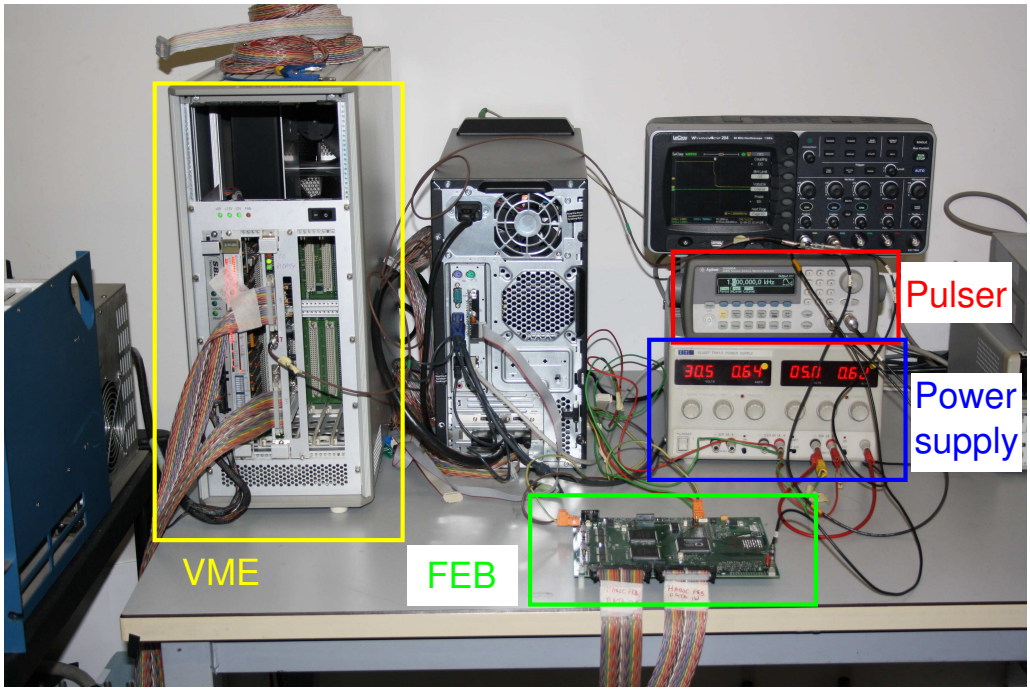

Figure A.2: Test on bench setup: the calibration signal is generated by a pulse generator and directly sent to the ASIC through a FEB input LEMO connector. The generator synchronized signal is used like a trigger and sent to the MAROC control board.

- pre-amplifier gain = 64 (the so called unitary gain);
- the three shaper capacitors (C) have been set to 1;
- the four pre-buffer capacitors (C_{buf}) have been set to 0.

A square pulse with a frequency of 1 kHz and an amplitude of 1 V has been used as a calibration signal.

Figure A.4 presents the hold scan performed with three different boards (three MAROC ASICs): the analog output signal has a peaking time of the order of $\sim$70 ns, and it is consistent in the different boards.

A.2.1.2 The shaper scan

The analog slow shaper circuit is shown in figure A.5(a): C0, C1 and C2 are switches associated to three different feedback capacitors (300, 600 and 1200 fC, respectively); the capacitors can be independently switched ON (1) or OFF (0) by dedicated bits (see section A.1).

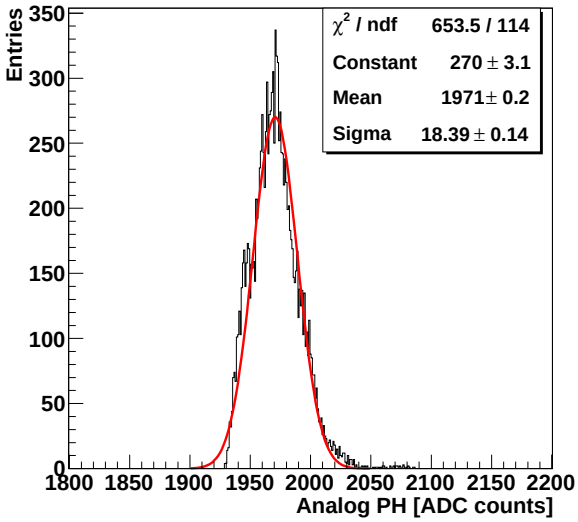

Figure A.3: Example of the analog output: the Gaussian distribution is the global response of the 64 channels to a calibration signal.

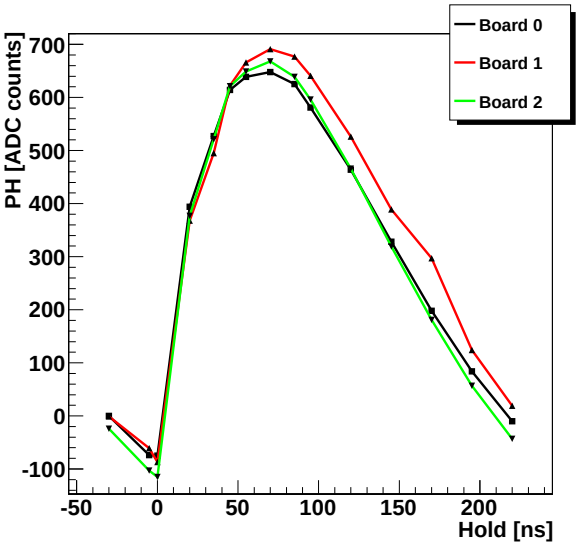

Figure A.4: The hold scan of three different boards.

The shaper scan is used to evaluate the analog shape of the signal in the same way as performed for the hold scan with all the possible feedback capacitors. For these measurements, the unitary gain has been chosen and the pre-buffer capacitors have been set to 1 (in order to use the slowest signals, see later on). The plot in

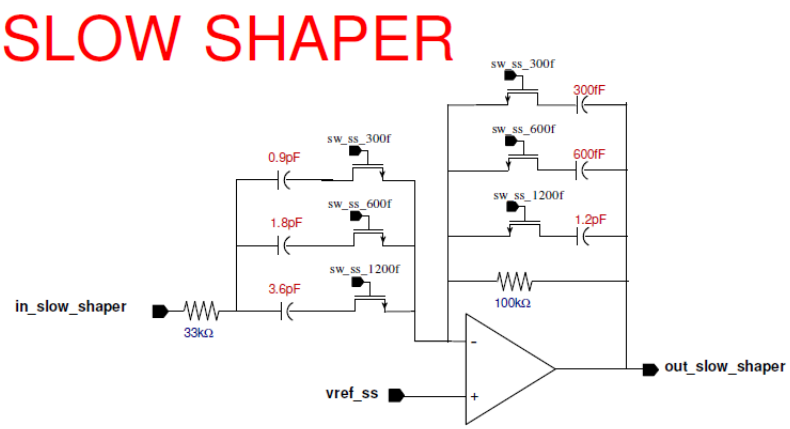

(a)

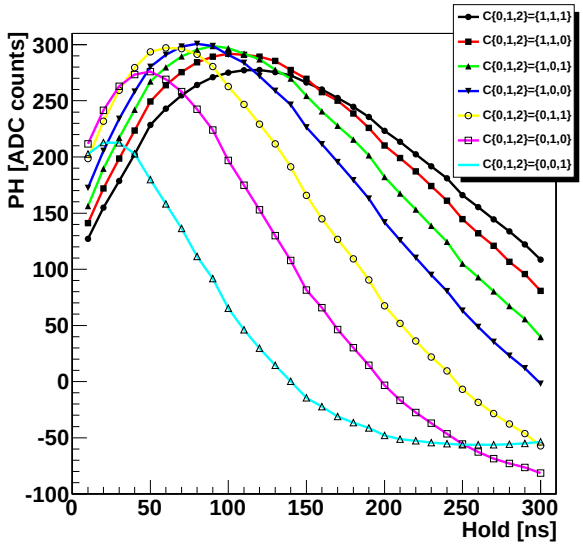

(b)

Figure A.5: a) The slow shaper circuit: C0, C1 and C2 are the switches associated to feedback capacitors of 300, 600 and 1200 fC [97]. b) The hold scan with different shaper settings.

figure A.5(b) shows the different cases: when all the feedback capacitors are used (or, in other words, when all the switches are on, that means C{0,1,2}={1,1,1}) the signal is the slowest; the larger the feedback capacitor value, the smaller the peaking time. With C{0,1,2}={0,0,0} (all the switches off) the ASIC does not work.

The analog output is also a function of the pre-buffer settings: the pre-buffer is

a RC circuit (figure A.6(a)) which feeds the slow shaper. It consists of a 50 kΩ resistor and a tunable capacitance. The value of the capacitance is selected enabling (1) or disabling (0) four switches which correspond to capacitors of (2, 1, 0.5, 0.25) pF. The hold scan has been performed with different pre-buffer settings con-

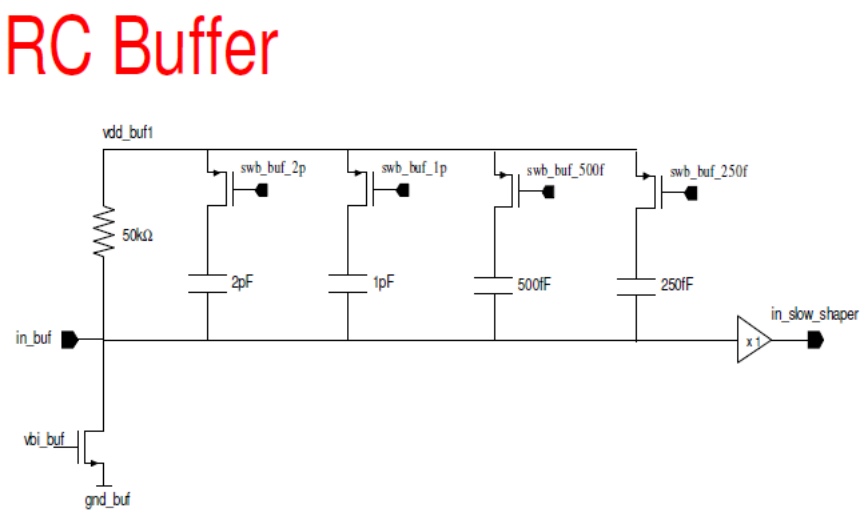

(a)

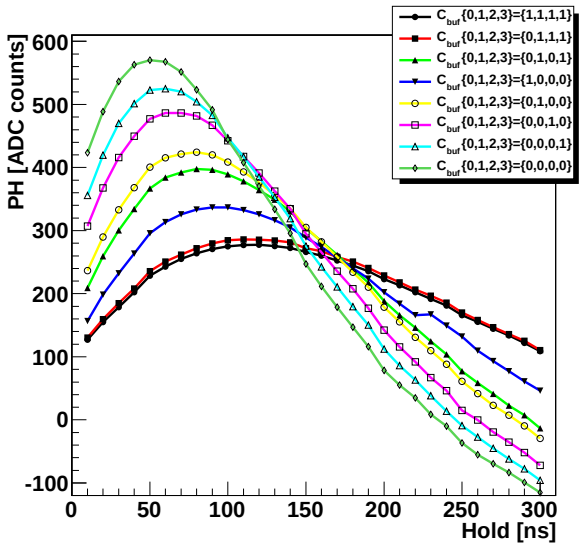

(b)

Figure A.6: a) The pre-buffer circuit: C_{buf}[0-3] are switches associated to capacitors of 2, 1, 0.5, 0.25 pC [97]. b) The hold scan with different pre-buffer settings.

sidering the unitary gain and shaper capacitors set to 1 (slowest case). The scans

are presented in figure A.6(b): the larger the capacitance, the larger the peaking time, but also the smaller the maximum value of the pulse height. During the tests presented in chapters 3 and 5, the slowest case is used: although this corresponds to the smallest value for the pulse height, it ensures time enough for the trigger signal to be generated and distributed to the MAROC. In a faster configuration, in fact, the sampling would be performed on the trailing edge of the analog signal.

A.2.1.3 The linearity

The analog output has been measured as a function of different input amplitudes in a configuration with the slowest shaper settings and a hold of ∼70 ns. Figure A.7(a) shows the outputs with 4 different gains (16, 32, 64 (=unitary gain) and 128) for an input signal up to 6 V; the output values are in raw ADC counts (without the pedestal subtraction) to be sure that a saturation is due to the MAROC and not to the ADC (in this case the raw number is equal to 4096). The MAROC

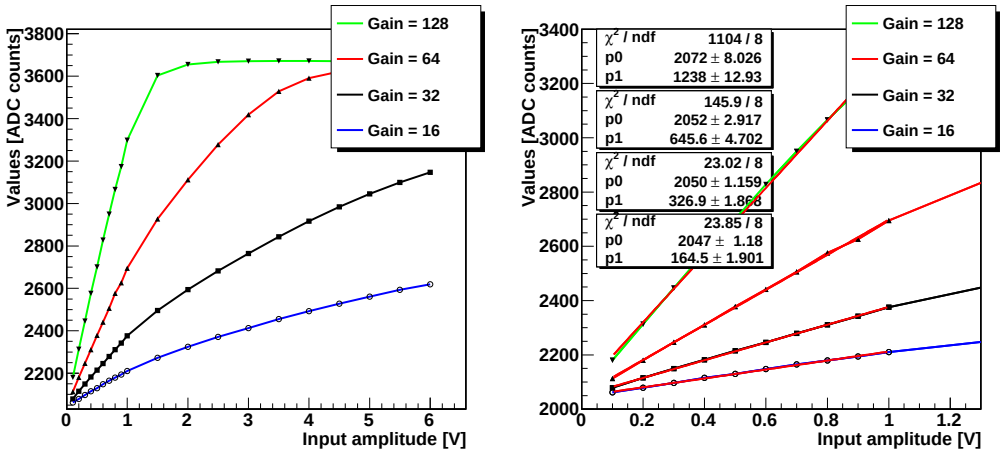

(a) (b)

Figure A.7: a) The linearity tests with a gain of 128, 64, 32, 16. b) The ASIC is linear up to 1 V.

outputs saturate when a gain of 128 or 64 is used but only with an input amplitude larger than 1 V (∼5 pC). Up to this value, as shown in figure A.7(b), the outputs have a linear trend. Moreover, the values of the linear fit slopes (the P1 parameter) reproduce correctly the gain ratio.

In EMR the MAPMT signal amplitudes depend on the high voltage; however the values are typically of the order of a few hundreds of mV.

A.2.2 The digital part

The digital part (as shown in figure A.1) consists basically of a fast shaper and a discriminator. More in detail, the current mirror feeds (at the same time) a unipolar (FSU), a bipolar (FSB1) and a half-bipolar (FSB2) fast shaper and the wanted output can be selected by the control bits (section A.1). As in the slow shaper case, several shaper configurations can be selected enabling different feedback capacitors and resistors. The most important test of the digital part is the threshold scan, that is the study of the response of the digital output as a function of the discriminator threshold. In the ASIC a Time over Threshold architecture has been implemented: with such a system, the analog and digital responses are correlated since the digital output width is a function of the analog pulse height.

A.2.2.1 The threshold scan

The most important test of the digital part is the threshold scan, which consists in sending a train of calibration signals (that is a train of squared pulses with a frequency of 1 kHz) to all the channels, varying the discriminator threshold and measuring the corresponding counting rate. An example of a threshold scan for a calibration signal of 350 mV using the bipolar fast shaper (FSB1) is shown in figure A.8(a). Since the gate in which pulses are counted is generated via software

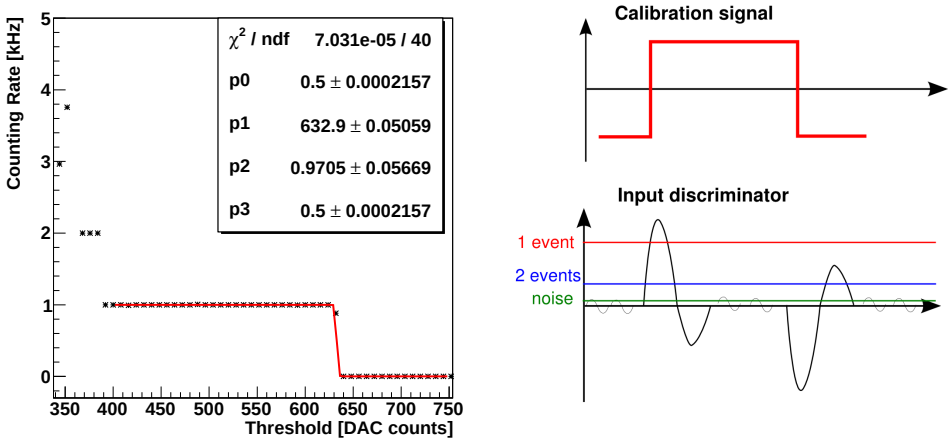

(a) (b)

Figure A.8: a) The threshold scan of one channel with an input signal amplitude of 350 mV. b) The threshold scan principle with the problem of the double-counting.

(and this is not precise), the counting rate (and not the number of pulses) has been considered.

The scan can be explained considering figure A.8(b). The signal train is sent to the input capacitors and the corresponding discriminator input consists of a large positive signal followed by an undershoot; in the same way a similar signal is obtained with the falling edge (a large negative signal followed by an overshoot). During the scan, the threshold increases in the positive range: thus the undershoot of the pulse rising edge is not considered, differently from the overshoot of the falling one. In this case the counting rate is double, as shown in figure A.8(a) in the threshold range between 360 and 380 DAC counts.

From 390 DAC counts on the threshold scan is described by a step function:

$$rate = P0 * \mathrm{erf}(-(x - P1) * P2) + P3$$

where $P0$ (function range) = $P3$ (offset) $\approx$ 0.5 kHz and erf() is the error function:

$$\mathrm{erf} = \frac{2}{\sqrt{\pi}} \int_0^{\pi} e^{-t^2} \mathrm{d}t$$

$P1$ is the position of the inflection of the curve and it is a function of the calibration amplitude. Performing a scan with different amplitudes, the plot presented in figure A.9 has been obtained for each of the 64 channels. The correlation be-

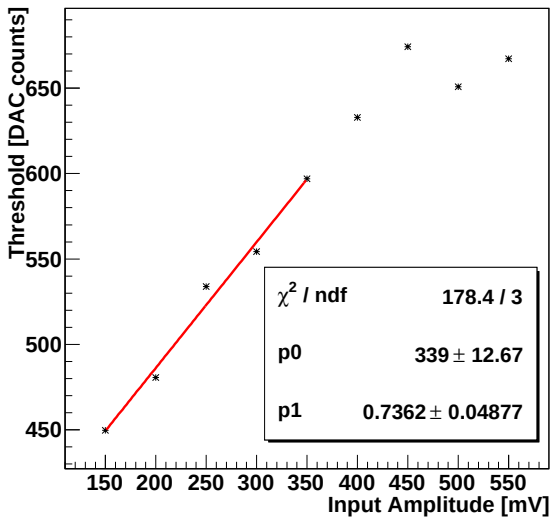

Figure A.9: The correlation between the calibration signal amplitude and the discriminator threshold for one of the 64 channels. The fit has been considered up to 350 mV in order to avoid any saturation problem at the discriminator level.

tween the calibration input amplitude and the corresponding discriminator threshold has been fitted with a linear function to obtain the gain (the slope, indicated

by the $P1$ parameter) and the offset (the zero threshold, $P0$) of each channel. The overall distributions of these two quantities are shown in figure A.10(a): the spread ($= \frac{sigma}{mean}$) of the 64 channels for the gain is (8.3±1.1)%, while for the offset is (4.4±0.6)%.

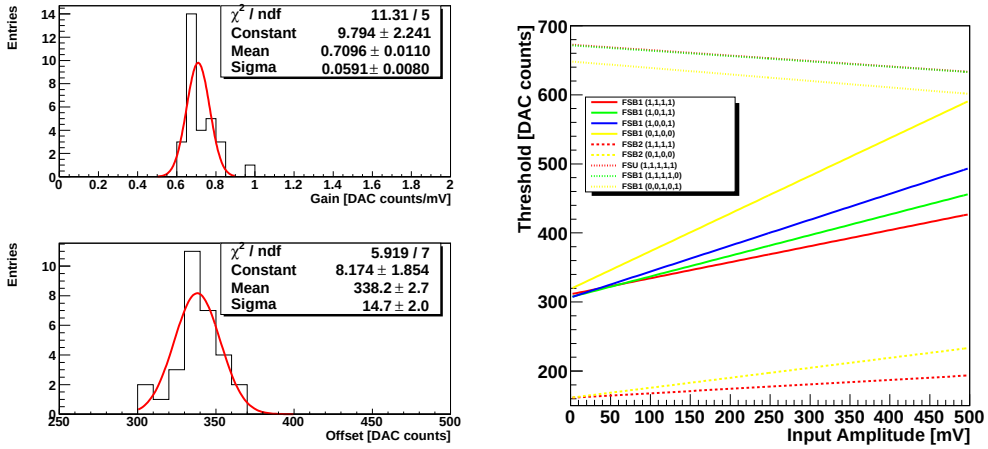

(a) (b)

Figure A.10: a) The gain and the offset distributions for FSB1: the gain spread is 8.3%, while the offset one 4.4%. b) The gain and offset for different fast shaper parameters.

The results presented in figure A.10(a) are the ones of the bipolar fast shaper (FSB1) with all the capacitors set to 1. The gain and the offset are a function of the shaper parameters (feedback capacitors and resistors) and the shaper: figure A.10(b) presents the gain and offset values for the unipolar (FSU), bipolar (FSB1) and half-bipolar (FSB2) fast shapers with different parameters.

A.2.2.2 The Time over Threshold measurement

Typically the digital output is represented by a pulse. In the MAROC ASIC the pulse width is a function of the input because of the Time over Threshold (ToT) architecture. The ToT principle is explained in figure A.11: the larger the input, the longer the time in which the signal stays above threshold. In other words, the discriminator output is not a fixed width signal, but it is correlated with the analog shape. The correlation between the input amplitude and the digital width is shown in figure A.12: different input amplitudes have been selected and the corresponding digital output width has been measured with an oscilloscope. The correlation is described by a power-of-4 polynomial law:

$$y = P4\,x^4 + P3\,x^3 + P2\,x^2 + P1\,x + P0$$

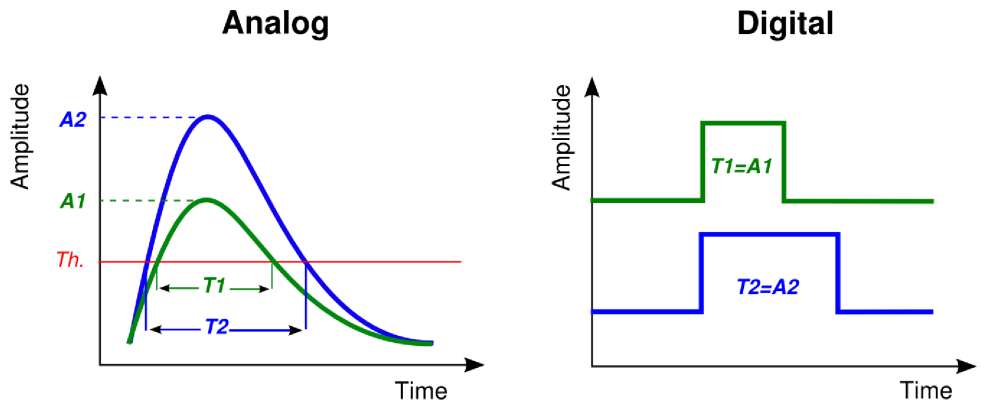

Figure A.11: The ToT principle: the digital output width is a function of the input amplitude.

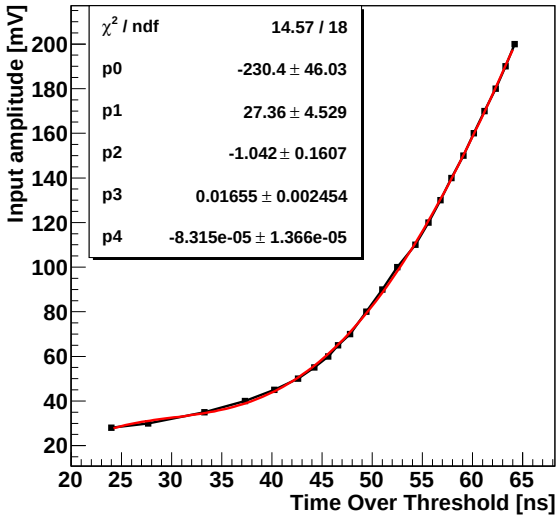

Figure A.12: The ToT measurement: the correlation between the input amplitude and the digital output width is described by a power-of-4 polynomial law.

where y is the input amplitude and x the digital output width.

List of acronyms

$0\nu\beta\beta$	Neutrinoless Double Beta Decay
ADC	Analog to Digital Converter
AFC	Absorber Focusing Coil
AGILE	Astro-rivelatore Gamma a Immagini LEggero
AGS	Alternating Gradient Synchrotron
ALICE	A Larger Ion Collider Experiment
ASI	Agenzia Spaziale Italiana (Italian Space Agency)
ASIC	Application Specific Integrated Circuit
BC	Beam Chamber
BGA	Ball Grid Array
BTF	Beam Test Facility
Cat	Category
CC	Charged Current
CERN	European Organization for Nuclear Research (Conseil Europeen pour la Recherche Nucleaire)
CKM	Cabibbo-Kobayashi-Maskawa
CMB	Cosmic Microwave Background
CKOV	CherenKOV detector
CP	Charge-Parity
CPU	Central Processing Unit
DAQ	Data AcQuisition
DATE	Data Acquisition and Test Environment
DBB	Digitizer and Buffer Board
DIS	Deep Inelastic Scattering
DONUT	Direct Observation of the NU Tau

DPNC Departement de Physique Nucleaire et Corpuscolaire

EMcal Electron Muon calorimeter
EMR Electron Muon Ranger
ES Elastic Scattering

FADC Flash Analog to Digital Converter
FEB FrontEnd Board
FIFO First In First Out
FNAL Fermi National Accelerator Laboratory
FODO FOcus DefOcus
FOFO FOcus FOcus
FPGA Field Programmable Gate Array

GEANT GEometry ANd Tracking
GALLEX GALLium EXperiment
GNO Gallium Neutrino Observatory
GUT Grand Unified Theory

High-Tc High-Temperature superconductors
HSTL High Speed Transceiver Logic

ID IDentification
I/O Input/Output

KamLAND Kamioka Liquid scintillator AntiNeutrino Detector
KEK Koh Ene Ken
(National Laboratory for High Energy Physics)
KL KLOE-Light
KLOE K LOng Experiment

LBL Long BaseLine
LED Light-Emitting Diode
LEP Large EMR Prototype
LHC Large Hadron Collider
LMA Large Mixing Angle
LNF Laboratori Nazionali di Frascati
LNGS Laboratori Nazionali del Gran Sasso

MAPMT Multi-Anode PhotoMultiplier Tube
MAROC Multi Anode ReadOut Chip

MICE Muon Ionization Cooling Experiment
MINERνA Main INjector ExpeRiment for ν-A
MIP Minimum Ionization Particle
MSW Mikheyev-Smirnov-Wolfenstein
MWE Meter Water Equivalent

NC Neutral Current
ND Near Detector
NuFact Neutrino Factory
NuMI Neutrinos at the Main Injector

OPERA Oscillation Project with Emulsion tRacking Apparatus

PAW Physics Analysis Workstation
PC Personal Computer
PCB Printed-Circuit Board
PMMA PolyMethylMethAcrylate
PMNS Pontecorvo-Maki-Nakagawa-Sakata
PMT PhotoMultiplier Tube
PQFP Plastic Quad Flat Pack
PS Proton Synchrotron
PSI Paul Scherrer Institute
PVC Polyvinyl Chloride

QDC Charge-to-Digital Converter
QFT Quantum Field Theory

RAL Rutherford Appleton Laboratory
RF RadioFrequency (cavity)
RFCC RadioFrequency and Coupling Coil
RMS Root Mean Squared

SAGE Soviet-American Gallium Experiment
SBL Short BaseLine
SciFi Scintillating Fiber tracker
SLAC Stanford Linear Accelerator Center
SM Standard Model
SMA SubMiniature version A
SNO Sudbury Neutrino Observatory
SSM Standard Solar Model
STL Superconducting Transmission Line

Super-K	Super-Kamiokande
SW	SandWich
TASD	Totally Active Scintillator Detector
Tcl	Tool command language
TDC	Time-To-Digital Converter
TOF	Time-Of-Flight
ToT	Time over Threshold
TTL	Transistor-Transistor Logic
UNIGE	UNIversity of GEneva
USA	United States of America
UV	UltraViolet
V-A	Vector-Axial
VCB	VME Configuration Board
VLPC	Visible Light Photon Counter
VME	Versa Module Eurocard
VRB	VME Readout Board
WFD	WaveForm Digitizer
WLS	Wave Length Shifter
WMAP	Wilkinson Microwave Anisotropy Probe

List of Figures

List of Tables

Bibliography

[1] K. Zuber, “Neutrino Physics”, Taylor & Francis, 2003.

[2] K. Winter, “Neutrino Physics”, Cambridge University Press, 2000.

[3] W. Pauli, “Letter to a physicists gathering at Tubingen”, 1930,
The English version can be found here: *http://www.pp.rhul.ac.uk/∼ptd/TEACHING/PH2510/pauli-letter.html*.

[4] J. Chadwick, “Possible Existence of a Neutron”, *Nature* 129: 312, 1932.

[5] E. Fermi, “An attempt of a theory of beta radiation”, *Z. Phys.* 88: 161–177, 1934.

[6] B. Pontecorvo, “Inverse β-process”, PD-205, 1946, unpublished.

[7] P. Ramond, “Introduction to Neutrinos”, *arXiv:hep-ph/0001007*, 2000.

[8] C. L. Cowan *et al.*, “Detection of the Free Neutrino: a Confirmation”, *Science* 124(3212): 103–104, 1956.

[9] A. R. Sandstrom, “Background and Instrumentation in MICE”, Ph.D. thesis, University of Geneva, 2007.

[10] N. G. Cooper, “The Reines-Cowan Experiments”, Los Alamos Science, 1997.

[11] M. Goldhaber *et al.*, “Helicity of Neutrinos”, *Phys. Rev.* 109(3): 1015–1017, 1958.

[12] T. D. Lee *et al.*, “Parity Nonconservation and a Two-Component Theory of the Neutrino”, *Phys. Rev.* 105: 1671–1675, 1957.

[13] S. Sakata *et al.*, “On the Correlations between Mesons and Yukawa Particles”, *Prog. Theo. Physics* 1(4): 109–124, 1946.

[14] G. Danby *et al.*, "Observation of High-Energy Neutrino Reactions and the Existence of Two Kinds of Neutrinos", *Phys. Rev. Lett.* 9(1): 36–44, 1962.

[15] K. Kodama *et al.*, "Observation of tau neutrino interactions", *Phys. Lett. B* 504(3): 218–224, 2001.

[16] M. Blennow, "Theoretical and Phenomenological Studies of Neutrino Physics", Ph.D. thesis, Royal Institute of Technology, Stockholm, 2007.

[17] C. Giunti *et al.*, "Fundamentals of neutrino physics and astrophysics", Oxford University Press, 2007.

[18] M. Cozzi, "Study of pion identification in the Emulsion Cloud Chambers of the OPERA experiment", Ph.D. thesis, University of Bologna, Italy, 2005.

[19] C. Salvioni, "Optimization of the single module of detection for the CUORE-0 experiment", Ph.D. thesis, University of Insubria, Italy, 2010.

[20] E. Majorana, "Teoria simmetrica dell'elettrone e del positrone", *Nuovo Cim.* 14: 171, 1937.

[21] V. Vignati, "Model of the Response Function of the CUORE Bolometers", Ph.D. thesis, University of Roma 1, Italy, 2010.

[22] B. Pontecorvo, "Mesonium and anti-mesonium", *Sov. Phys. JETP* 6: 429, 1957.

[23] M. Maki *et al.*, "Remarks on the Unified Model of Elementary Particles", *Prog. Theo. Physics* 28(5): 870–880, 1962.

[24] R. Slansky *et al.*, "The Oscillating Neutrino", Los Alamos Science, 1997.

[25] M. C. Gonzalez-Garcia *et al.*, "Phenomenology with massive neutrinos", *Phys. Rep.* 460(1-3): 1–129, 2008.

[26] L. Wolfenstein, "Neutrino oscillations in matter", *Phys. Rev. D* 17: 2369–2374, 1978.

[27] S. Mikheyev *et al.*, "Resonant amplification of ν oscillations in matter and solar-neutrino spectroscopy", *Nuovo Cim. C* 9: 17–26, 1986.

[28] A. D. Giovanni, "Study and realization of a Resistive Plate Chamber system for the VETO planes and the Magnetic Spectrometers of the OPERA experiment", Ph.D. thesis, University of l'Aquila, Italy, 2008.

[29] J. N. Bahcall, "Solar neutrinos: an overview", *Phys. Rep.* 333-334: 47–62, 2000.

[30] R. Davis, "A review of the Homestake solar neutrino experiment", *Prog. in Part. and Nucl. Phys.* 32: 13 – 32, 1994.

[31] T. A. Kirsten, "GALLEX solar neutrino results and status of GNO", *Nucl. Phys. B - Proc. Suppl.* 77(1-3): 26 – 34, 1999.

[32] J. N. Abdurashitov *et al.*, "Measurement of the solar neutrino capture rate in SAGE", *Nucl. Phys. B - Proc. Suppl.* 118: 39 – 46, 2003.

[33] Y. Suzuki, "Kamiokande solar neutrino results", *Nucl. Phys. B - Proc. Suppl.* 38(1-3): 54 – 59, 1995.

[34] SNO Collaboration, "Electron Energy Spectra, Fluxes, and Day-Night Asymmetries of ^{8}B Solar Neutrinos from the 391-Day Salt Phase SNO Data Set", *Phys Rev. C* 72: 055502, 2005.

[35] A. Strumia *et al.*, "Neutrino masses and mixings and...", *arXiv:hep-ph/0606054v3* 2010.

[36] S. Fukuda *et al.*, "The Super-Kamiokande detector", *Nucl. Instr. and Meth. in Phys. Res. A* 501(2-3): 418 – 462, 2003.

[37] S. M. Bilenky, "A Lecture on Neutrino Masses, Mixing and Oscillations", *arXiv:hep-ph/0210128* 2002.

[38] K. Eguchi *et al.*, "First Results from KamLAND: Evidence for Reactor Antineutrino Disappearance", *Phys. Rev. Lett.* 90: 021802, 2003.

[39] S. Abe *et al.*, "Precision Measurement of Neutrino Oscillation Parameters with KamLAND", *Phys. Rev. Lett.* 100: 221803, 2008.

[40] M. Apollonio *et al.*, "Search for neutrino oscillations on a long base-line at the CHOOZ nuclear power station", *Eur. Phys. J. C* 27: 331–374, 2003.

[41] M. H. Ahn *et al.*, "Measurement of neutrino oscillation by the K2K experiment", *Phys. Rev. D* 74: 072003, 2006.

[42] P. Adamson *et al.*, "Measurement of Neutrino Oscillations with the MINOS Detectors in the NuMI Beam", *Phys. Rev. Lett.* 101: 131802, 2008.

[43] N. Agafonova *et al.*, "Observation of a first ν_τ candidate event in the OPERA experiment in the CNGS beam", *Phys. Lett. B* 691(3): 138–145, 2010.

[44] M. Tegmark *et al.*, "Cosmological parameters from SDSS and WMAP", *Phys. Rev. D* 69: 103501, 2004.

[45] K. S. Hirata *et al.*, "Observation in the Kamiokande-II detector of the neutrino burst from supernova SN1987A", *Phys. Rev. D* 38: 448–458, 1988.

[46] A. Bandyopadhyay *et al.*, "Physics at a future neutrino factory and superbeam facility", *Rep. Prog. Phys.* 72(10): 106201, 2009.

[47] The MICE collaboration, "An International Muon Ionization Cooling Experiment", *Proposal to the Rutherford Appleton Laboratory*, 2003.

[48] D. M. Kaplan, "Muon collider/neutrino factory: status and prospects", *Nucl. Instr. and Meth. in Phys. Res. A* 453(1-2): 37–48, 2000.

[49] C. M. Ankenbrandt *et al.*, "Status of muon collider research and development and future plans", *Phys. Rev. ST Accel. Beams* 2: 081001, 1999.

[50] C. Albright, "Physics at a Neutrino Factory", *arXiv:hep-ex/0008064v2*, 2000.

[51] M. Lindner, "The Physics Potential of Future Long Baseline Neutrino Oscillation Experiments", *arXiv:hep-ph/0210377v2*, 2002.

[52] D. Neuffer, "Principles and Applications of Muon Cooling", *Part. Acc.* 14(1-2): 75–90, 1983.

[53] Particle Data Group, "Review of Particle Physics", *Jour. Phys. G* 37(7A): 1–1422, 2010.

[54] D. Neuffer, "Introduction to muon cooling", *Nucl. Instr. and Meth. in Phys. Res. A* 532(1-2): 26–31, 2004.

[55] The $\mu^+\mu-$ Collider Collaboration, "Muon Muon Collider: a feasibility study", BNL-52503, 1996.

[56] D. Brandt, "Introduction to Accelerators", *http://cas.web.cern.ch/cas/Spain-2006/PDFs/Brandt.pdf*, 2006.

[57] S. Yang, "MICE Design Office", *http://www.physics.ox.ac.uk/design/MICE/ mice_page.htm*, 2007.

[58] R. B. Palmer, Neutrino Factory Draft Parameters, Mucool note-46, 1999.

[59] S. Ishimoto *et al.*, "Liquid Hydrogen Absorber for MICE", Technical report, LBNL-3914E, 2010.

[60] M. A. C. Cummings *et al.*, "Progress on the Liquid hydrogen absorber for the MICE cooling section", Proceedings of PAC 2005, Knoxville, USA, 2005.

[61] The MICE collaboration, "MICE cooling section layout", *http://mice-overview.web.cern.ch/mice-overview/images/channelayout_strip.ppt*, 2005.

[62] D. E. Baynham *et al.*, "A Liquid Cryogen Absorber for MICE", *AIP Conf. Proc.* 823(1): 1068–1075, 2006.

[63] A. DeMello *et al.*, "Progress on MICE RFCC module for the MICE experiment", Proceedings of PAC 2011, New York, USA, 2011.

[64] H. Sakamoto, "Status of the MICE Tracker System", Technical report, MICE-310, 2010.

[65] M. A. Green *et al.*, "Progress on the MICE tracker solenoid", Technical report, MICE-157, 2006.

[66] M. Ellis, "MICE Tracker Status", *http://www.cap.bnl.gov/mumu/conf/MC-090125/talks/MEllis1-090125.pdf*, 2009.

[67] S. Virostek, "Spectrometer Solenoid Fabrication & Testing Update", *Talk at the 24th MICE Collaboration Meeting*, 2009.

[68] R. Bertoni *et al.*, "The design and commissioning of the MICE upstream time-of-flight system", *Nucl. Instr. and Meth. in Phys. Res. A* 615(1): 14–26, 2010.

[69] R. Bertoni *et al.*, "The construction of the MICE TOF2 detector", Technical report, MICE-286, 2010.

[70] M. Bonesini *et al.*, "The design of MICE TOF0 detector", Technical report, MICE-145, 2006.

[71] D. Orestano, "The detector system of the MICE experiment", *Nucl. Instr. and Meth. in Phys. Res. A* 617(1-3): 45–47, 2010.

[72] L. Cremaldi *et al.*, "A Cherenkov Radiation Detector With High Density Aerogels", *IEEE Trans. on Nucl. Sci.* 56(3): 1475–1478, 2009.

[73] L. Cremaldi, "CKOV Update", *Talk at the 21st MICE Collaboration Meeting*, 2008.

[74] F. Ambrosino *et al.*, "Calibration and performances of the KLOE calorimeter", *Nucl. Instr. and Meth. in Phys. Res. A* 598(1): 239–243, 2009.

[75] The MICE Collaboration, "MICE STATUS REPORT September 2010", Technical report, MICE-316, 2010.

[76] C. Rogers *et al.*, "Simulation of MICE using G4MICE", Proceedings of EPAC 2006, Edinburgh, Scotland, 2006.

[77] S. Agostinelli *et al.*, "Geant4-a simulation toolkit", *Nucl. Instr. and Meth. in Phys. Res. A* 506: 250–303, 2003.

[78] S. Boyd, "MINERνA: A High Statistics Neutrino Scattering Experiment in the NuMI Neutrino Beam", *Nucl. Phys. B - Proc. Suppl.* 139(0): 311–316, 2005.

[79] A. Pla-Dalmau *et al.*, "Low-cost extruded plastic scintillator", *Nucl. Instr. and Meth. in Phys. Res. A* 466(3): 482–491, 2001.

[80] D. Lietti, "The Electron Muon Ranger for the MICE Experiment", Master's thesis, University of Insubria, Como, 2010.

[81] R. Asfandiyarov *et al.*, "Modifications to the EMR design", Technical report, MICE-357, 2011.

[82] H. Wisting, "MICE EMR Prototype Efficiency and PMT Calibration", Master's thesis, Norwegian University of Science and Technology, 2010.

[83] T. Anticic *et al.*, "Commissioning of the ALICE data acquisition system", *Jour. Phys.: Conf. Ser* 119(2): 022006, 2008.

[84] S. Franz *et al.*, "ATLAS ALFA-measuring absolute luminosity with scintillating fibres", *Nucl. Instr. and Meth. in Phys. Res. A* 610(1): 35–40, 2009.

[85] The NOνa Collaboration, "Proposal to Build a 30 Kiloton Off-Axis Detector to Study $\nu_\mu \rightarrow \nu_e$ Oscillations in the NνMI Beamline", *arXiv:hep-ex/0503053v1*, 2005.

[86] G. Barbiellini *et al.*, "The AGILE silicon tracker: testbeam results of the prototype silicon detector", *Nucl. Instr. and Meth. in Phys. Res. A* 490(1-2): 146–158, 2002.

[87] M. Prest *et al.*, "The AGILE silicon tracker: an innovative γ-ray instrument for space", *Nucl. Instr. and Meth. in Phys. Res. A* 501(1): 280–287, 2003.

[88] S. Hasan, "Bent silicon crystals for the LHC collimation studies with an ultrarelativistic proton beam", Master's thesis, University of Insubria, Como, 2007.

[89] D. Bolognini *et al.*, "Tests of the MICE Electron Muon Ranger frontend electronics with a small scale prototype", *Nucl. Instr. and Meth. in Phys. Res. A* 646(1): 108–117, 2011.

[90] L. Gatignon, "http://gatignon.web.cern.ch/gatignon/EastArea/", 2011.

[91] L. Durieu *et al.*, "The CERN PS east area in the LHC era", Proceedings of PAC 1997, Vancouver, Canada, 1997.

[92] V. Verguilov, "EMR Simulation", *Talk at the 29th MICE Collaboration Meeting*, 2011.

[93] R. Asfandiyarov, "Electron-Muon Ranger (EMR) - Status of the EMR Project", *Talk at the 31st MICE Collaboration Meeting*, 2011.

[94] R. Asfandiyarov, "Electron-Muon Ranger (EMR) - First Tests at RAL", *Talk at the 30th MICE Collaboration Meeting*, 2011.

[95] T. Abe *et al.*, "International Scoping Study (ISS) for a future neutrino factory and Super-Beam facility. Detectors and flux instrumentation for future neutrino facilities", *Jour. Instr.* 4(05): T05001, 2009.

[96] M. Ellis *et al.*, "Performance of a Magnetised Scintillating Detector for a Neutrino Factory", *Talk at the International Scoping Study meeting*, 2006.

[97] Omega group, "MAROC Datasheet", Private communication, 2009.

Acknowledgments

There are a lot of people that I would like to thank for their contribution to this thesis work. First of all the organizations which have supported the described research: CERN, INFN (section of Milano Bicocca and Trieste), the University of Insubria and the University of Geneva. Many thanks to the MICE collaboration and in particular to EMR group at UNIGE, both led by prof. Alain Blondel. In particular many thanks to Ruslan for the help during the installations at UNIGE and RAL.

Many many thanks to Michela, Erik and the Insulab group for the help, the opportunities and the time spent in these six years.

And now, after a thesis in English, I would like to write my last words in Italian...

Passo all'Italiano perchè in fondo a te, lettore, che hai saltato le 220 pagine di questa tesi interessano più i ringraziamenti e vuoi leggere qualcosa di più dei semplici "Grazie" ufficiali. E soprattutto vuoi cercare il tuo nome o un riferimento a te qui dentro. Spero solo di accontentarti.

Un grazie a te, Michela, che sei stata correlatore occulto (triennale), relatore (specialistica) e tutor (dottorato) in questi 6 anni passati insieme. Grazie per avermi aiutato, spronato, incoraggiato, sostenuto, per aver discusso per ore su un decimale o su un metodo di analisi. Grazie per la fiducia (io e Said eravamo due "pivelli" quando ci lasciasti a lavorare da soli ad H8 nel lontano 2007) e grazie per le conferenze all'Elba! In realtà c'e' un grazie che raggruppa tutto: mi hai insegnato un lavoro, e questo non lo scorderò mai. **Grazie**.

Grazie a te, Erik, per l'aiuto, per le tue conoscenze, per la pazienza e per mille altri motivi. **Grazie**.

Grazie all'Insulab group per le ore ed ore ed ore ed ore passate insieme in laboratorio. Grazie ai vecchi ed ai nuovi, ma grazie soprattutto a due di voi: Said per le ore di parole spese in questi anni; e grazie a te, Alessandro "Mente" Berra, perchè dopo 9 anni di studio, scherzi, incazzature (e bestemmie connesse) ed insulti (da parte mia, scusa...) siamo ancora amici. **Grazie**.

Grazie a voi, mamma, papà, Ele, nonna e zia. Di solito si ringraziano i famigliari perchè ci hanno supportato e sopportato. Si, il supporto è stato tanto, ma

grazie veramente per avermi sopportato. Grazie per non avermi sempre mandato a quel paese, anche quando me lo meritavo... E grazie a te, Emanuela, per la quantità di cene e pranzi che mi hai offerto e per l'aiuto che mi hai dato. Cucinare qualche volta non sarà mai sufficiente per saldare il mio debito. **Grazie**.

Eccoci qua. Lo so, stavi aspettando questo momento da tutta una tesi. Mi hai chiesto dei ringraziamenti quando ancora non avevo in mano il titolo! Ed ora sono qui a pensare quali parole usare. Ma sono certo che qualunque frase non esprimerebbe la mia gratitudine nei tuoi confronti. Ma ci provo lo stesso. Grazie per l'aiuto a questa tesi (LEP non sarebbe esistito se tu non mi avessi dato una mano), per i testbeam e per l'anaDst.C (e milioni di altre cose!). Ma soprattutto grazie per avermi aiutato nella vita: perchè mi stai accanto, perchè mi fai ridere, o per quello che provo nel farti ridere. A te dedico questa tesi perchè sei una persona speciale e non potrei vivere senza te. **Grazie, Laura!**